BERGISCHE
UNIVERSITÄT
WUPPERTAL

Laser Additive Manufacturing of oxide-dispersion strengthened steels

Dissertation

to obtain the doctoral degree

Dr.-Ing.

In the

School of Mechanical Engineering and Safety Engineering

University of Wuppertal

Submitted by

Markus Benjamin Wilms

from Aachen

Wuppertal, 2023

This thesis has been carried out at the Chair for Materials and Additive Manufacturing of the University of Wuppertal (BUW) under the supervision of Prof. Dr. Bilal Gökce and the Fraunhofer-Institute for Laser Technology (ILT) in Aachen under the supervision of Dr. Konrad Wissenbach and Dr. Andreas Weisheit. It is partially based on the collaborative project “AProLAM” funded jointly by the Fraunhofer Society and the Max Planck Society in their strategic cooperation framework. This thesis has been accepted by the University of Wuppertal (BUW) for publication.

Location and date of the doctoral disputation:

Wuppertal, 18.10.2023 (09:15, Room: VW.12.001)

Chairman:

Prof. Dr.-Ing. Axel Schumacher
University of Wuppertal

Referees:

Prof. Dr. Bilal Gökce
University of Wuppertal

Prof. Dr.-Ing. Arne Röttger
University of Wuppertal

Prof. Dr.-Ing. Swantje Bargmann
University of Wuppertal

I. Foreword

My sincere gratitude goes to my supervisors Prof. Dr. Bilal Gökce (BUW), Dr. Konrad Wissenbach and Dr. Andreas Weisheit (ILT) for their guidance over the years as well as the opportunity to pursue my theories and concepts. I would like to thank my colleagues from the Chair of Materials and Additive Manufacturing at BUW: Dr. Silja-Katharina Rittinghaus, Dr. Carlos Doñate-Buendia, Dr. Ingo Erdmann, Mareen Goßling, Inna Khairani, Shabbir Tahir, Farbod Riahi, Hamed Shokri, Claudia Kirchner and Daniel Behrens. Equally, I thank my collegues from ILT as well as neighbouring institutes and companies, who enriched my time at the ILT over the last years: Herbert Horn-Solle, Tim Biermann, Gerhard Backes, Jochen Kittel, Wolfgang Küppers, Stefan Jung, Harald Dickler, Sadagopan Tharmakulasingam, Dominik Dobrzanski, Rudolf Meier, Stephanie Linnenbrink, Andreas Vogelpoth, Friedrich Wopen, Dr. Norbert Pirch, Christian Budde, Josef Kemmerling, Christian Hannemann, Susanne Wollgarten, Rui João Santos Batista, Ratmar Frömbgen and Barbara Jacobs.

The thesis would not have been possible without the support other researchers, namely Dr. Philipp Kürnsteiner, Prof. Dr. Eric Jägle, Dr. Priyanshu Bajaj, Dr. Christian Haase, Dr. Torsten Fischer and Dr. Ulrike Hecht. Special thanks go to my former students Niklas Fögen, Mareen Goßling, Nathalie Al-Achkar, Paula Baquero, Patrick Köhnen, Christian Brunner-Schwer and Duc Chu for their support in the lab. Last but not least, my sincere gratitudes go to people who always inspired me over the last years: Dr. Gesa Rolink, Dr. Sabrina Vogt, Dr. Silja-Katharina Rittinghaus, Rebar Hama-Saleh and Veronica Molina.

Many of these people became friends over the last years and I would not like to miss them. Lastly, I would like to thank my friends Paul Romanowski, Lars Stötera, Lucas Golombek, Alain Schäfer, Sandra Böhle and my family for countless good times and their everlasting support.

II. Abstract

The development of high-performance materials for highly efficient propulsion systems and modern energy generation technologies, such as nuclear fusion technology, is becoming increasingly important as fossile resources become scarcer. Metal-ceramic composites show in particular potential for these applications, as they combine the processability characteristics of metals with the high-temperature properties of ceramic materials. One group of metal-ceramic composites are the so-called oxide dispersion strengthened steels (ODS steels), which are characterized by the dispersion of nano-scaled oxide particles in a typically corrosion-resistant steel matrix.

In this thesis, the fabrication of an oxide dispersion strengthened (ODS) steel, based on the commercial alloy PM2000, developed by Plansee SE, is investigated using the laser-based additive manufacturing processes of Laser Powder Bed Fusion (L-PBF), Laser Directed Energy Deposition (L-DED), and a High-Speed Laser Cladding (HSLC). Different process and solidification environments are created by the utilization of the respective additive manufacturing processes, allowing the evaluation of different solidification conditions on the microstructure formation, size and distribution of the introduced oxide nanoparticles as well as the influence on mechanical properties in ambient and high-temperature atmospheres. One main objective will be the effective suppression of agglomeration mechanism of oxide nanoparticles during the molten phase, in order to minimize the nanoparticles' size after solidification. However, the successful manufacturing of ODS materials by additive manufacturing technologies requires the production of suitable powder composites, which will be performed by the conventionally established method of mechanical alloying (MA) and the innovative laser-based process methodology of Laser Synthesis and Processing of Colloids (LSPC). LSPC offers the advantage of loading metallic micrometer-sized powders with nano-scaled oxide particles via a pH-controlled process without the application of external mechanical forces, ensuring the retention of the spherical shape of the inert-gas atomized metallic powder particles and thus improving the processability by additive manufacturing processes.

Specimens fabricated by the various additive manufacturing technologies are subjected to extensive microstructural characterizations on different length scales. Light optical and scanning electron microscopy are used to characterize the grain structure of the corrosion-resistant steel matrix and the distribution of nano-scaled oxide particles. In addition, electron backscatter diffraction (EBSD) and X-ray diffraction (XRD) investigations are used to examine the local and global texture properties of the created microstructures. The chemical composition is determined by X-ray fluorescence analysis (XRF) as well as energy dispersive X-ray spectroscopy (EDX). On the nanometer scale, transmission electron microscopy (TEM) as well as Atom Probe Tomography (APT) investigations are used to study the dislocation interactions with dispersed nanoparticles and to determine the nanoparticle compounds formed during processing. In addition, mechanical characterizations are performed, which will focus on the spatially resolved measurement of Vickers hardness and the determination of the compressive

strength at room temperature and 600°C. The results of the mechanical characterization will be linked to the microstructural properties to derive potential improvements for manufacturing of ODS materials by additive manufacturing technologies.

III. Abbrevations

Abbrevation	Long name	Abbrevation	Long name
AAMA	Adhesive Agent Mechanical Alloying	GARS	Gas Atomization Reaction Synthesis
AM	Additive Manufacturing	HAADF	High-angle Annular Dark Field
APT	Atom Probe Tomography	HAGB	High-angle Grain Boundary
ASTM	American Society for Testing and Materials	HE	Hot Extrusion
BD	Build Direction	HIP	Hot Isostatic Pressing
BFSTEM	Bright Field Scanning Transmission Electron Microscopy	HSLC	High-speed Laser Cladding
BPP	Beam Parameter Product	HRTEM	High Resolution Transmission Electron Microscopy
BSE	Backscattered Electrons	IEP	Isoelectric Point
CAD	Computer-aided Design	IPF	Inverse Pole Figure
CLD	Condensed Layer Deposition	LACS	Laser Assisted Cold Spray Deposition
CMOS	Complementary Metal-oxide-semiconductor	LAGB	Low-angle Grain Boundary
CS	Cold Spray Deposition	L-DED	Laser Directed Energy Deposition
CT	Computer Tomogaphy	LOM	Light Optical Microscopy
DD	Diffusion Deposition	L-PBF	Laser Powder Bed Fusion
DLS	Dynamic Light Scattering	LSPC	Laser Synthesis and Processing of Colloids
DPA	Displacement Per Atom	MA	Mechanical Alloying
EBSD	Electron backscatter diffraction	MMC	Metal Matrix Composite
EDS	Energy-dispersive X-ray Spectroscopy	NA	Numeric Aperture
ED	Electrostatic Deposition	NC	Numerical Control
EHLA	(German) Extremes Hochgeschwindigkeits-Laserauftragschweißen	NP	Nanoparticles
EPMA	Electron Probe Microanalysis	PBR	Pilling-Bedworth-Ratio
EB-PBF	Electron Beam Powder Bed Fusion	PVD	Physical Vapour Deposition
FBR	Fluidized Bed Reactor	RAF	Reduced Activation-Ferritic
FEM	Finite Element Modelling	RAFM	Reduced Activation-Ferritic/Martensitic

RAM	Resonant Acoustic Mixing	TD	Traverse Direction
RFMS	Radio Frequency Magnetron Sputtering	USP	Ultra Short Pulse
RPA	Revolution Powder Analyser	UV-Vis	Ultraviolet-Visible Light Spectroscopy
SD	Scanning Direction	VED	Volume Energy Density
SE	Secondary Electrons	VIGA	Vacuum Inert Gas Atomization
SEM	Scanning Electron Microscopy	WAAM	Wire Arc Additive Manufacturing
SPS	Spark Plasma Sintering	XRD	X-ray Diffraction Analysis
STARS	Surface Treatment of Gas Atomized Powder & Reactive Synthesis	XRF	X-ray Fluorescence Analysis
TEM	Transmission Electron microscopy	YSZ	Yttrium-stabilized Zirconia

IV. Table of contents

1 Scope of the thesis

The objective of this thesis is to systematically explore the laser-based additive manufacturing route for manufacturing of ODS alloys. Based on an extensive literature research, which is shown in the introduction section (Chapter 1-4) a material system based on the conventional and available PM2000 alloy by Plansee SE, composed of a stainless ferritic steel with the the chemical composition of Fe20Cr4.5Al0.5Ti (wt.%) and the reinforcement phase of yttrium(III) oxide (Y_2O_3) is selected as an exemplary material to study the different process characteristics of the laser additive manufacturing processes of laser based powder bed fusion (L-PBF) and the laser directed energy deposition process (L-DED) as well as the high-speed directed energy deposition process of high-speed laser cladding (HSLC) on the microstructure formation. Prior to additive manufacturing processing with the respective AM processes suitable composite powder materials, composed of the metallic and ceramic component are synthesized using the widely established solid-state based of Mechanical Alloying (MA) and the advanced liquid-based manufacturing process of Laser Synthesis and Processing of Colloids (LSPC), including an electrostatic deposition (ED) process (Chapter 5), which is expected to allow the production of spherical powder composites with homogeneous oxide nanoparticle dispersion on the surface of the metallic powder particles, resulting in equally improved printability and homogeneous nanoparticle dispersion in printed parts. After printing of the MA- and LSPC-generated powder materials (Chapter 6) extensive microstructural characterizations including grain structure and texture analysis as well as the determination of oxide nanoparticles' size, dispersion and chemistry is performed (Chapter 6) and compared with non-reinforced stainless steel material.

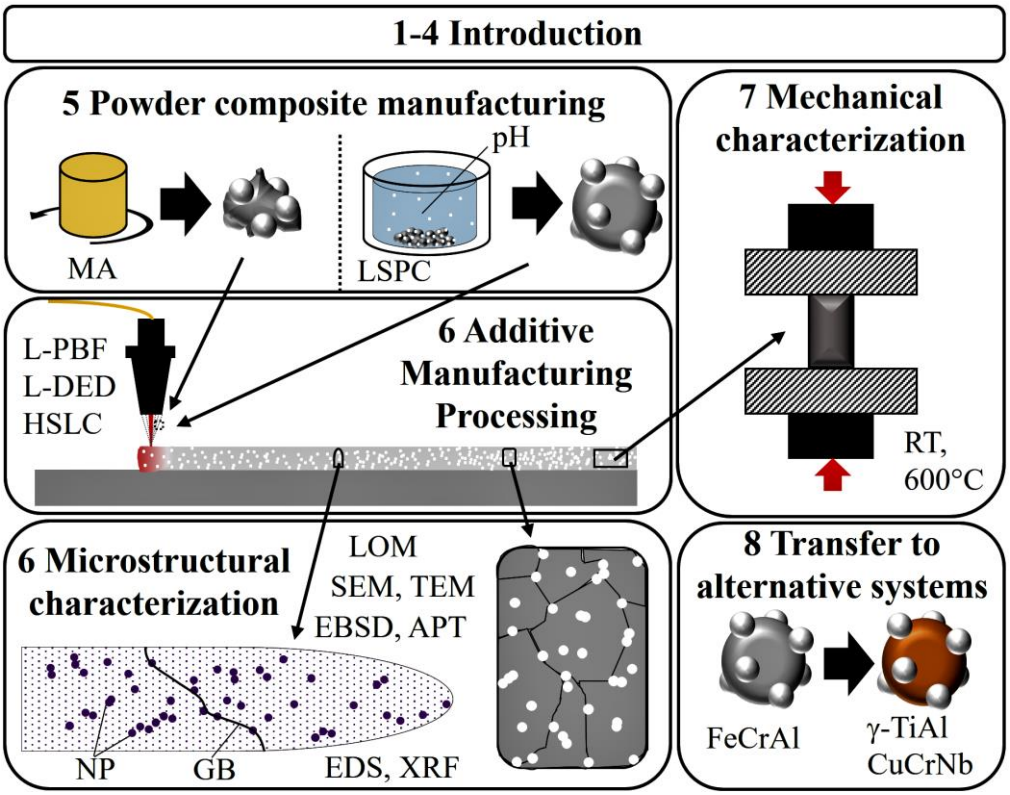

Fig. 1: Outline of the thesis including the numbers, denoting the respective chapters of this thesis.

The process parameters of the respective AM processes are developed towards minimized incidents of defect formation (e.g., porosity or crack formation) in printed parts as well as homogeneous nanoparticle dispersion and smallest nanoparticles' size (< 50 nm), as it is expected to result in optimized mechanical properties. The mechanical characterization of printed specimen (Chapter 7), including compression testing in room and high temperature environments (600°C), is correlated to the microstructures produced with the respective AM processes. In Chapter 8 the developed methodology of introducing oxide nanoparticles in additively manufactured material is demonstrated for the two alternative material systems of a γ-TiAl-based turbine blade material and a high strength copper material, based on the Cu-Cr-Nb alloy system.

The thesis aims to answer the following lead questions:

1) Can a homogeneous dispersion of nano-scaled oxide particles (10 - 100 nm) in a metallic matrix be achieved by laser additive manufacturing technologies and which process conditions allow the formation of the finest nanoparticle structures?

2) How does the introduction of oxide nanoparticles affect the solidification microstructure of the ferritic stainless steel regarding grain size and defect formation?

3) How do the mechanical properties of the ODS steels produced by LAM correlate with the microstructure and the selected manufacturing process and its solidification conditions?

4) Is the elaborated additive manufacturing route of an oxide-dispersion strengthened stainless steel transferable to other metallic alloy systems?

2 Introduction

Contains content from the following publication:

Additive manufacturing of oxide-dispersion strengthened alloys: Materials, synthesis and manufacturing

M. B. Wilms, S.-K. Rittinghaus, M. Goßling, B. Gökce*

Chair of Material Science and Additive Manufacturing, School of Mechanical Engineering and Safety Engineering, University of Wuppertal, Gaußstr. 20, 42119 Wuppertal, Germany

Article Information

Article history:
Received 27 March 2022
Accepted 14 November 2022
Available online 26 November 2022

DOI: 10.1016/j.pmatsci.2022.101049
Progress in Material Science

*Corresponding author
bilal.goekce@uni-wuppertal.de

Abstract

Oxide dispersion strengthened (ODS) alloys are characterized by nanoscale oxide particles homogeneously dispersed in a metallic matrix. They have been developed driven by technological applications such as gas turbines that require increased material strength and creep properties at elevated temperatures, as well as increased resistance to high-energy neutron atmospheres as needed in modern nuclear reactors. Additive manufacturing (AM) offers the possibility to sustainably shorten the conventional sinter-based process chain of ODS materials and is additionally capable of the direct production of complex components. This work aims to critically review the current state of additive manufacturing of ODS alloys, which is mainly based on singular studies and the deduction of influence factors. Challenges in production are emphasized such as the production of suitable powder materials and consolidation techniques including in-situ manufacturing techniques. A main emphasis of this review are process-related influences on the final ODS material and its microstructural features as well as mechanical performance. Different classes of ODS alloys are presented and discussed along with their fields of use. Current drawbacks of ODS alloys are highlighted, enabling a focused development required for the widespread application of this class of materials.

Own contribution: Conceptualization, literature research, writing and editing of the original draft and revised manuscript.

In 2021, the European Commission reveals the Green Deal program, which aims at a drastic reduction of emissions up to full carbon neutrality in 2050. [1] In order to achieve these aims the efficiency of combustion engines for energy generation (Fig. 2a,b) and turbomachinery applications (Fig. 2c,d) have to be increased either by higher operating temperatures of combustion engines [2, 3] or the utilization of alternative fuels, such as hydrogen. Hydrogen combusts with higher flame speed and temperatures than natural gas [4, 5] resulting in higher maximum temperatures and pressures in combustion chambers [6] and thus demands creep-resistant high-temperature materials for these components. [7] Oxide dispersion strengthened (ODS) alloys are a potential candidate for this particular application, due to their homogeneous dispersion of oxide nanoparticles in a metallic matrix alloy, typically enhancing mechanical properties over a large temperature range by impeding dislocation motion through the mechanisms of Hall-Petch or Orowan, respectively. [8, 9, 10, 11] Moreover, ODS alloys are known to withstand the extreme conditions in nuclear power plants and therefore are considered as high-performance materials for safe and sustainable use in the field of nuclear fusion, which, due to recent advances [12], may replace nuclear power plants in the future.

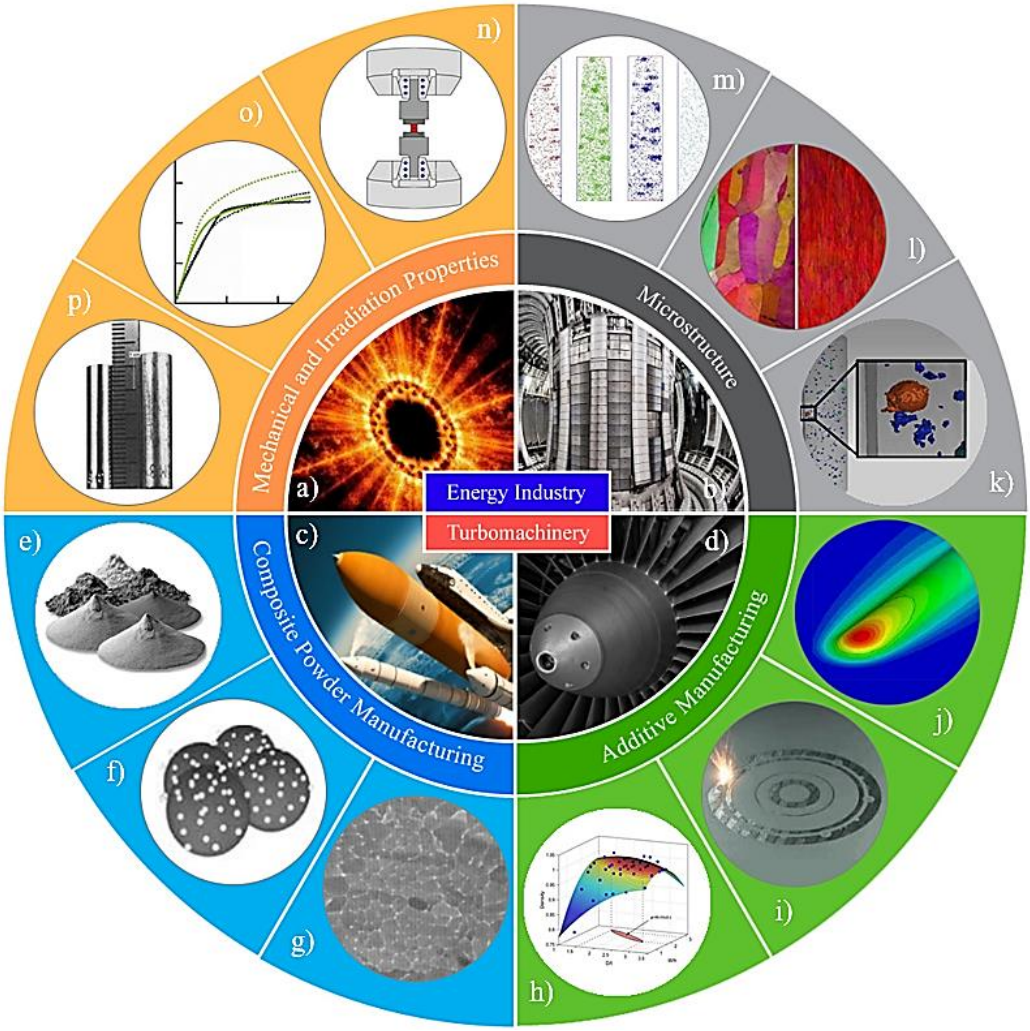

Fig. 2: Additive manufacturing of ODS materials. Application of ODS materials for energy industry for nuclear fusion (a) in a Tokamak-type reactor (b) and turbomachinery applications: Space aircraft (c) and turbofan engines (d). Manufacturing and characterization of tailored powder feedstocks for production of ODS materials by AM processes. e) Composite powders with optimized rheological properties. f) Schematic depiction of micro-scaled metallic particles homogeneously decorated with nano-scaled oxide nanoparticles. Reprinted with permission from [13]. g) Cross-section SEM analysis of a gas-atomization reaction synthesis (GARS) manufactured powder particle for AM production of ODS materials. Reprinted with permission from [14]. h) Depiction of process parameter development. Reprinted with permission from [15]. i) Process observation during AM. j) FEM modelling of the thermal profile of the L-PBF process of an ODS steel. Reprinted with permission from [13]. k) Microstructural characterization by computer tomography (CT) for the detection of pores in AM manufactured ODS steel. Reprinted with permission from [16]. l) Inverse pole figures from electron backscatter diffraction examination of AM manufactured ODS steels (l). Reprinted with permission from [13]. m) Volume reconstructions from atom probe tomography (APT) measurements of ODS steels (m). Reprinted with permission from [17]. n) Schematic illustration of a hot compression test setup. Reprinted with permission from [16]. o) Compressive strength-strain curves. Reprinted with permission from [16]. p) Photograph of irradiated and non-irradiated 316L material showing swelling behavior. Reprinted with permission from [18].

However, the conventional manufacturing route of oxide-dispersion strengthened parts via powder metallurgy involves multiple process steps, including composite powder manufacturing via mechanical alloying processes, consolidation via different sintering techniques, subsequent heat treatment procedures and final subtractive shaping. Powder-based Additive Manufacturing (AM) is a promising prospective production route for ODS materials, since it allows the near-net-shaped consolidation directly from tailored powder materials (Fig. 2e-g) and thus a significant shortening of the

manufacturing route of ODS alloys. Despite AM being an established technique for manufacturing metallic components from various alloys, regularly used alloys were initially developed for conventional manufacturing processes (e.g., casting). Thus, they are not optimized for the characteristic process environments in additive manufacturing processes and therefore cannot fully exploit the potential of this manufacturing technique. [19] The development of adapted alloys for additive manufacturing processes, in general, is complex and requires a careful selection of process parameters (Fig. 2h), process observation (Fig. 2i), accurate modelling of the complex temperature profiles [20] and solidification conditions (Fig. 2j) [21], and flow conditions of the melt pool [22, 23]. Based on these models, adapted alloy concepts with superior performance of additively manufactured conventional alloys can be developed. [24, 25, 26, 27, 28, 29, 30, 31, 32, 33] However, the production of superior materials by AM processes additionally requires extensive microstructural (Fig. 2m-k) and mechanical characterizations (Fig. 2n-p) to guide the process development toward optimized material properties. In addition to the holistic development of new alloy concepts, the modification of established alloy systems by integrating nano-scaled exogenous particles (e.g., oxides) offers the possibility of adapting conventional alloys for additive manufacturing processes. [34] Nanoparticles can conduct manifold functions and therefore offer the potential to challenge several material-related problems in additive manufacturing processes. They can be used to manipulate the powder materials absorption for specific energy sources, e.g., laser beams [35, 36, 37], and improve flowability properties [37, 38, 39]. During the melting stage, nanoparticles can change the melt pool dimensions, flow characteristics [40] and keyhole formation [41]. Additionally, nanoparticular entities can modify solidification conditions, i.e., by acting as active nucleation sites promoting heterogeneous nucleation and suppressing the formation of defects in crack-sensitive materials, like high-strength aluminum [42, 43, 44], titanium alloys [45], nickel-based alloys [46] and refractory materials [47].

AM technologies are being adopted in more and more industries, specifically in aerospace [48, 49, 50, 51], automotive [48, 51], energy [51] and biomedical branches [48, 49, 50], and are applied to produce an increasing number of highly complex and customized products. The increasing application of AM in industrial applications is accompanied by intensive research activities in this particular research area, which is reflected in the constant growth of scientific publications. [52, 53, 54] In particular, most publications are in the research field of material science, which demonstrates the demand for new material concepts tailored to additive manufacturing. [55, 56, 57, 58] This allows concluding that not only AM can be used to improve the processing of existing ODS materials, but conversely, ODS can help to exploit the potential of additive manufacturing. The unification of these two research fields is thus a significant step in materials development, as demonstrated by the research activities of the last years. However, the successful fabrication of ODS materials via additive manufacturing techniques is challenging. It requires a careful selection of powder manufacturing techniques, suited process design, and subsequent correlation of microstructural features with resulting mechanical properties.

3 Oxide-dispersion strengthened (ODS) alloys

Oxide-dispersion strengthened (ODS) alloys represent a particular class of metal matrix composites (MMC) and have been developed in the previous century, driven by several technological applications, such as gas turbines [59] requiring enhanced material strength and creep properties at elevated temperatures [60] as well as increased resistance towards high-energy neutron flux found in modern nuclear reactors. [61, 62, 63, 64, 65] Oxide-dispersion strengthened alloys are characterized by nano-scaled oxide particles homogeneously dispersed in a metallic matrix resulting in exceptional mechanical properties in high-temperature environments [66, 67, 68, 69] and pronounced resistance towards high-energy neutron irradiation [70].

3.1 Mechanical properties of ODS alloys

The mechanical properties of ODS alloys are governed by the mechanism of solid solution hardening, which is mainly determined by the chemical composition of the matrix alloy, and by dispersion hardening caused by the dispersion of oxide nanoparticles in the matrix alloy [71], particularly in the vicinity of grain boundaries. [72] Dispersion hardening in ODS alloys is attributed to the Orowan mechanism, which describes the bypassing mechanism of non-cuttable nanoparticles by the formation of dislocation loops of an advancing dislocation line (Fig. 3a). [73] Thus, the effectiveness of hardening by dispersoids mainly depend on the number density, size distribution and coherency [74, 75, 76] of embedded nanoparticles within the surrounding metallic matrix. Coherent nanoparticles are preferable by lowering the driving force for bypass mechanisms by dislocation climbing processes. [77] The strength contribution by the dispersed nanoparticles can be estimated by (1). [78]

$$\sigma_{OR} = \frac{0.4M}{\pi\sqrt{1-\nu}} \cdot \frac{Gb}{L} \cdot \ln\frac{\sqrt{\frac{2}{3}\cdot d_p}}{b} \qquad (1)$$

where ν is the Poisson's ratio, M the Taylor factor, G the shear modulus, b the Burgers vector, d_p the average particle diameter, and L the average interparticle spacing according to (2):

$$L = \sqrt{\frac{2}{3}\cdot d_p}\left(\sqrt{\frac{\pi}{4\nu_p} - 1}\right) \qquad (2)$$

where ν_p is the volume fraction of the nano-sized precipitates.

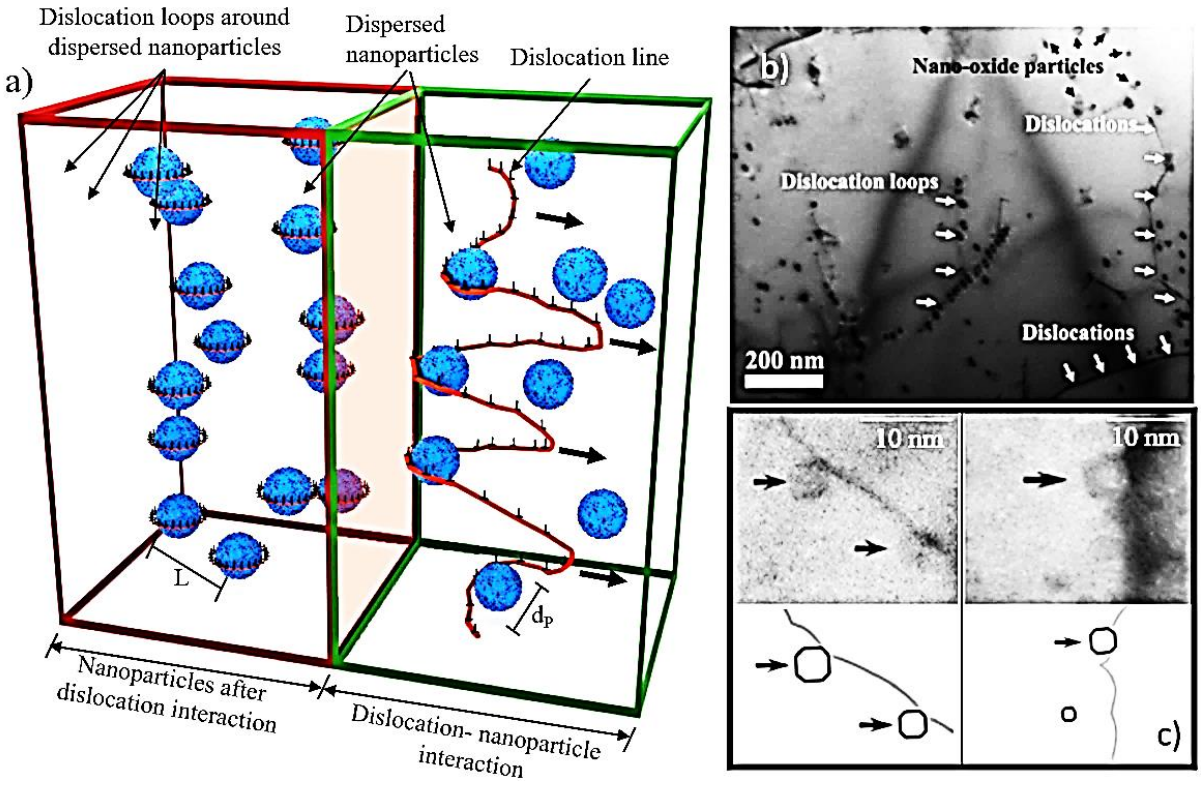

Fig. 3: a) Schematic depiction of the Orowan mechanism in oxide-dispersion strengthened alloys displaying dispersed nanoparticles during (green box) and after interaction with a dislocation line (red box). b) TEM images of nanoparticle interaction with nano-scaled oxide particles in a Fe-18Cr-2W-0.5Ti-0.3Y_2O_3 (wt.%) ODS steel. Reprinted with permission from [79]. c) High-magnification BFSTEM images of dislocations attached to nanoparticles in a 14YWT ODS steel. Reprinted with permission from [80].

Dispersed oxide nanoparticles located on grain boundaries additionally enable pinning of grain boundaries (Fig. 2b,c) [81, 82] and effectively suppress equally dislocation creep and diffusional creep assisted grain boundary sliding (GBS) mechanisms [83]. The latter is considered as the predominant deformation mechanism of polycrystalline superalloys at low strain rates in high temperature environments [84, 85] and thus is decisive for material degradation at high service temperatures over long time periods. The inhibition of GBS mechanisms by dispersed oxide nanoparticles becomes even more important for fine-grained microstructures, which are typically encountered in additively manufactured materials, as diffusion creep rates and pronounced grain boundary sliding is observed, compared to coarse-grained materials. [86] Thereby, the stabilization of grain boundary structures in high temperature environments over long time periods effectively inhibits recrystallization processes [87, 88, 89, 90], which is also enabled by extraordinary coarsening resistance at high temperatures [91, 92, 93, 94] probably by extremely low interfacial energy of the oxide nanoparticle clusters [95] in combination with low solubility of the oxide species in the metal matrix [96, 97] and their high melting point [98]. Therefore, ODS alloys are characterized by increased strength in the room and high temperature regimes compared to their non-reinforced counterparts. [81, 99, 100, 101, 102, 103, 104] and show exceptional creep resistance [104, 105, 106], which can be described by the Rösler-Arzt model [107]. However, the integration of a higher volume fraction of nanoparticles (> 0.5 vol.%) is typically

associated with a deterioration of the ductility [74], resulting in brittle material behavior at low- and room temperatures. [108, 109]

3.2 Irradiation properties of ODS alloys

The homogeneous dispersion of nano-scaled oxide particles in a metallic matrix allows the improvement of mechanical properties and it enhances the resistance of the alloy toward high-energy neutron radiation, which is typically present in nuclear power plants. [110, 111, 112] The interfaces of embedded nano-scaled oxides with the surrounding metallic matrix act as effective traps for radiation-induced crystal lattice defects, i.e., spallation-induced point defects and allow their recombination. [113, 114, 115]

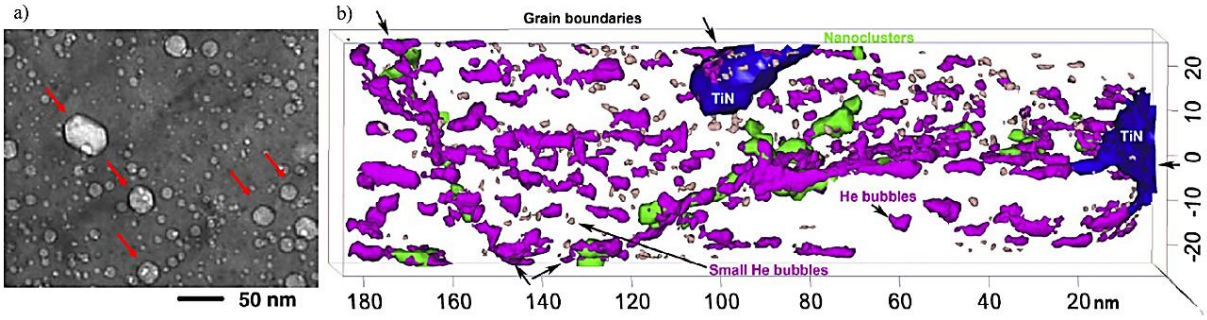

Fig. 4: a) TEM image of a dual-ion irradiated (60 dpa) RAF steel showing cavities (indicated with red arrows) formed by helium gas generated upon ion irradiation. Reprinted with permission from [119]. b) Volume reconstruction from APT measurements of a He implanted 14YWT ODS steel after annealing for 100 h at 750°C. Reprinted with permission from [120].

Additionally, the interface acts as a sink for elemental helium gas (Fig. 4a,b), formed by neutron-capturing events induced transmutation reactions [116, 117, 118, 119, 120], effectively inhibiting macroscopic degradation effects such as swelling [121, 122].The sink strength of cavities can be calculated according to Zinkle et al.: (3) [115]

$$S_C = 4\pi r_C N_C (1 + S^{\frac{1}{2}} r_C) Z_C \qquad (3)$$

where S_C is the cumulative sink strength, Z_C the cavity sink capture efficiency, N_C the number density, r_C the radius of the cavities and by Sivak et al.: (4) [121]

$$k^2 = \frac{2d}{(\lambda^2 \langle N \rangle)} \qquad (4)$$

where λ is the particle jump length, ⟨N⟩ the average number of particle jumps until the absorption by the sink and d the dimensionality of motion. The high number density of sinks presents in ODS materials allow the microstructure to withstand high doses of high-energy irradiation, as shown by Edmondson et al. [122]. Accordingly, for effective protection from high-energy neutron radiation, ultrafine dispersion of nano-scaled oxide particles is required to form a large number of interfaces. [80, 115, 123, 124] Further information of the impact of high-energy irradiation on ODS alloys and nanoparticle behavior can be found in reference. [125]

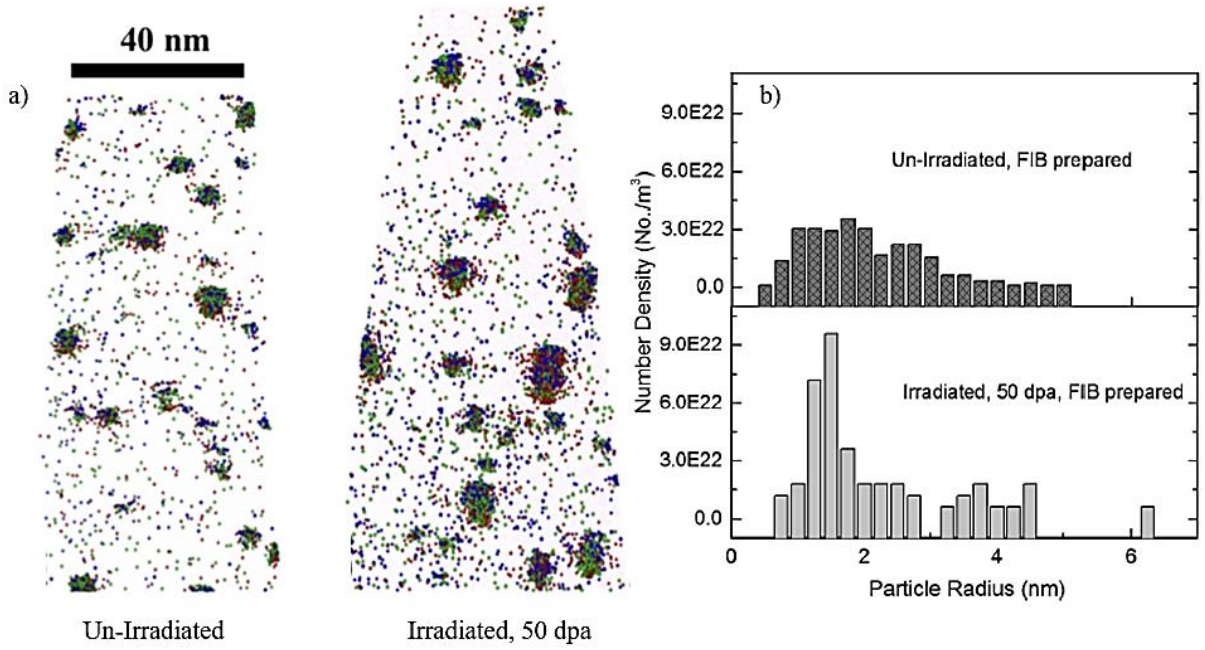

Fig. 4: a) Volume reconstruction from atom probe tomography (APT) measurements of a hot extruded 14YT (Fe-14Cr-0.2Ti-0.3Y_2O_3, wt.%) alloy in un-irradiated and irradiated state. b) Corresponding histogram plots of the number density of nanoparticles as a function of the particle radius in un-irradiated and irradiated state. Irradiation was performed at 700°C using 5 MeV Fe^{3+} ions up to a dose of 50 dpa. Reprinted with permission from [122].

3.3 Oxide compound compositions in ODS alloys

The properties of ODS alloys regarding mechanical and irradiation properties are primarily determined by the selected oxide composition and phase and the compatibility of the oxide with the matrix alloy. The unique property combination of ODS alloys stems from mechanisms governed by the interface between oxide and metallic matrix. The coherency between nanoparticles and the matrix alloy plays a significant role in interacting with advancing dislocations, as pointed out in chapter 2.1. However, the oxide nanoparticles also must show high thermodynamic stability and low solubility in the surrounding matrix alloy, effectively suppressing coarsening mechanisms at high operating temperatures over long time periods.

3.3.1 Yttrium-based oxides

Yttrium (III) oxide (Y_2O_3) is the most commonly used and, therefore, the best-studied oxide compound in ODS alloys, because this compound is empirically found to be one of the most thermodynamically stable oxide compounds with an extremely low standard enthalpy of formation of ($\Delta_f H^{Y_2O_3}$ = -1905.31 kJ mol^{-1} [126]) and low solubility in Fe-Cr alloys (< 0.07 wt.% in a Fe-25Cr wt.% alloy at room temperature) [127]. Therefore, Y_2O_3-based dispersoids in Fe-based ODS alloys are considered resistant to coarsening effects at temperatures of 1200 - 1300°C [128, 129, 130, 131]. Despite the poor wettability of Y_2O_3 with metallic melts and a typically incoherent interface with metallic lattices [132], nano-scaled Y_2O_3 dispersoids exhibit a strong orientation correlation with the matrix in Fe-Cr alloys [67] up to full coherency. Coherency is rapidly lost upon larger dispersoid sizes (> 20 nm [129]), e.g., as a result of

agglomeration or coarsening. [94, 129, 130] The addition of other elements to the matrix alloy, e.g., titanium [130, 131], zirconium [133, 134, 135], hafnium [136, 137], silicon [138], vanadium [139, 140], and tantalum [133, 140] promote the formation of complex yttrium-based oxides (Y_x-X_y-O_z, X= Ti, Al, Zr, Hf, Si, V, Ta) (Fig. 5a-h) with lower standard formation enthalpy and different crystallographic structures (Table 1). Other elements like carbon deteriorate the effectiveness of zirconium and hafnium as nanoparticle refining agents by forming the respective carbides (ZrC and HfC respectively). [141] Scandium substitutes yttrium to form Sc-Ti-O structured oxides in titanium alloyed ODS steel [142], which is presumably attributed to the chemical similarity of yttrium and scandium, both belonging to the same transition metal group. The addition of aluminum or titanium allows the formation of cubic-structured partially [75] or fully [76, 143] coherent $Y_xTi_yO_z$ (e.g., pyrochlore-type $Y_2Ti_2O_7$) and $Y_xAl_yO_z$ (e.g., $Y_3Al_5O_{12}$) nanoparticles, respectively. Commercial ODS alloys typically contain significant concentrations of titanium or aluminum.

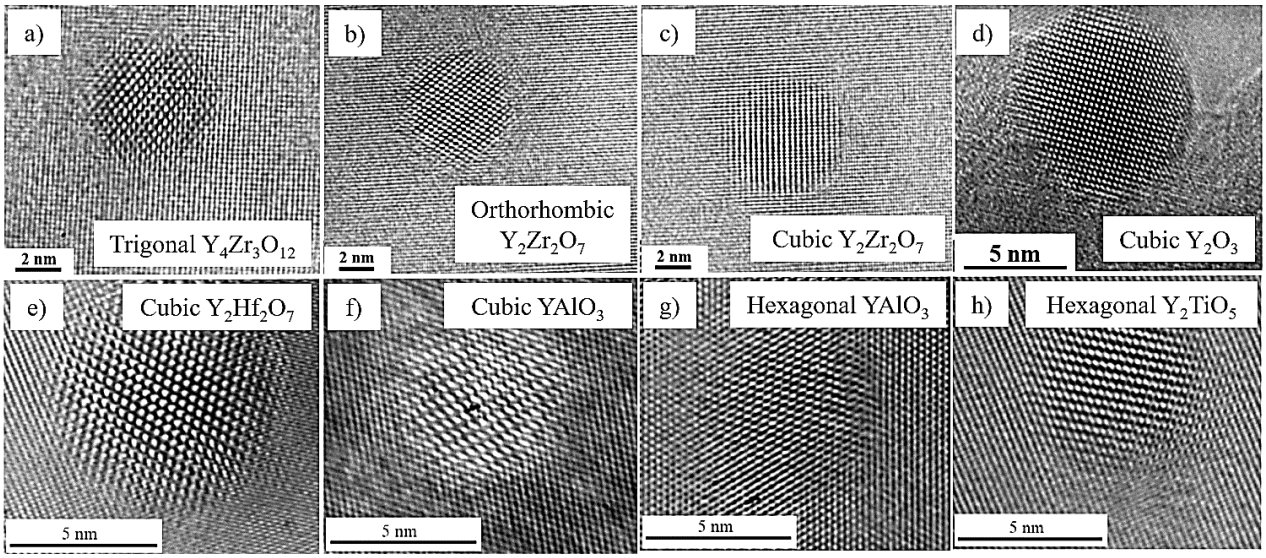

Fig. 5: HRTEM images of different yttrium-based nano-scaled oxide particles coherent with the surrounding bcc-structured Fe-Cr steel matrix, manufactured from mechanically alloyed and subsequently hot-extruded material. a-c) reprinted with permission from [143]. d) Reprinted with permission from [144]. e-h) Reprinted with permission from [145].

Consequently, the refinement of the oxide particles by titanium [130, 131, 146], zirconium [133, 134, 135] and hafnium [136] increases both strength and resistance toward high-energy neutron irradiation. Despite its low standard formation enthalpy, aluminum has only a minor refining effect on the nanoparticles, so the strength gain is lower. [147] In the combined addition of oxidative elements, the formation of the compound with the lower standard enthalpy of formation in each case is energetically preferred. [148, 149, 150, 151]

Table 1: Yttrium-based oxide compounds in ODS alloys with their standard enthalpy of formation ΔH_f^0, the crystallographic structure and the formation mechanism as used in literature for ODS alloys. The references column list the studies, where the respective oxide compounds were detected in ODS alloys. (n.r.: not reported)

Alloying element	Oxide compound	ΔH_f^0	Crystallographic structure	Formation mechanism	References
-	Y_2O_3	-1905 kJ/mol [126]	cubic	4 Y + 3 O_2 → 2 Y_2O_3 [152]	143
Titanium	Y_2TiO_5	-2674 kJ/mol [153]	orthorhombic	Y_2O_3 + TiO_2 → Y_2TiO_5 [152]	154, 155, 156, 157, 158, 159, 160, 161
	$Y_2Ti_2O_7$	-3874 kJ/mol [162]	cubic	Y_2O_3 + 2 TiO_2 → $Y_2Ti_2O_7$ [163]	91, 108, 143, 144, 145, 146, 158, 162, 164, 165, 166, 167, 174
Aluminum	$Y_4Al_2O_9$ (YAM)	-5546 kJ /mol [163]	monoclinic	2 Y_2O_3 + Al_2O_3 → $Y_4Al_2O_9$ [163]	144, 147, 157, 166, 169, 170, 178
	$Y_3Al_5O_{12}$ (YAG)	-7197 kJ/mol [163]	cubic	3 Y_2O_3 + 5 Al_2O_3 → 2 $Y_3Al_5O_{12}$ [152]	147, 157, 158, 159, 170, 171
	$YAlO_3$ (YAH)	-1827 kJ/mol [163]	hexagonal	Y_2O_3 + Al_2O_3 → 2 $YAlO_3$ [163]	159, 160, 172
Zirconium	$Y_4Zr_3O_{12}$	n.r.	trigonal	2 Y_2O_3 + 3 ZrO_2 → $Y_4Zr_3O_{12}$	143, 145, 148, 161, 164, 165, 166, 167, 170, 172, 173, 179, 180
	$Y_2Zr_2O_7$	n.r.	cubic	Y_2O_3 + 2 ZrO_2 → $Y_2Zr_2O_7$	143, 173
Silicon	Y_2SiO_5	-2869 kJ/mol [177]	monoclinic	Y_2O_3 + SiO_2 → Y_2SiO_5	138
	$Y_2Si_2O_7$	-3820 kJ/mol [178]	monoclinic	Y_2O_3 + 2 SiO_2 → $Y_2Si_2O_7$	138, 169
Hafnium	$Y_2Hf_2O_7$	n.r.	cubic	Y_2O_3 + 2 HfO_2 → $Y_2Hf_2O_7$ [152]	143, 169, 177, 181, 182, 183, 184, 185
Tantalum	Y_3TaO_7	n.r.	cubic	3 Y_2O_3 + Ta_2O_5 → 2 Y_3TaO_7	177
Vanadium	$Y_8V_2O_{17}$	n.r.	monoclinic	4 Y_2O_3 + V_2O_5 → $Y_8V_2O_{17}$	177
Niobium	Y_3NbO_7	n.r.	cubic	3 Y_2O_3 + Nb_2O_5 → 2 Y_3NbO_7	177

3.3.2 Alternative oxide compounds in ODS alloys

In addition to the widely used oxide compound of Y_2O_3 in ODS alloys, alternative oxide compounds exist, exhibiting high stability in high temperature regimes and therefore are considered candidates for dispersion phases in ODS alloys. Most of these oxides are based on different rare earth (RE) elements, such as cerium [180, 186, 187, 188, 189] and lanthanum [180, 190, 191, 192]. These oxides show a behavior comparable to that of yttrium oxide, e.g. by the formation of pyrochlore-structured complex

oxide compounds in titanium alloyed steels, e.g. $La_2Ti_2O_7$ and $Ce_2Ti_2O_7$ [181]. Oxide compounds of ZrO_2 [193, 194, 195, 196], HfO_2 [197] and Al_2O_3 [198, 199] are also feasible due to their high thermodynamic stability; however, the formation of complex oxide structures is not observed. (Table 2)

Table 2: Overview of alternative (non-yttrium-based) oxide compounds used in ODS alloys with the resulting oxide compound determined after consolidation by the used consolidation process. The references column lists the studies, where the respective oxide compounds are detected in ODS alloys. L-DED: Laser directed energy deposition. L-PBF: Laser powder bed fusion.

Oxide compound	Oxide load	Matrix alloy	Consolidation process	Resulting oxide compound	Reference
CeO_2	0.3 wt.%	Fe-14Cr-2W-0.3Ti	Spark Plasma Sintering	$Ce_2Ti_2O_7$	180
CeO_2	0.7 wt.%	Fe-12Cr-6.3Al-0.5Ti	Spark Plasma Sintering	Ce_2O_3, Al_2O_3	188
CeO_2	0-4 wt.%	Ni-16Cr-8Fe-4.5Si-3.3B	L-DED	Ce_2O_3	187
CeO_2	n.r.	Fe-22Cr-5Al	Laser Remelting	n.r.	186
La_2O_3	0.3 wt.%	Fe-14Cr-2W-0.3Ti	Spark Plasma Sintering	$La_2Ti_2O_7$	180
La_2O_3	0.5 wt.%	Fe-14Cr-1Ti-0.3Mo	Spark Plasma Sintering	La-Ti-Cr-O	191
La_2O_3	5 wt.%	Al	Hot Pressing	La_2O_3	192
ZrO_2	0.5 wt.%	316L	Arc Plasma Sintering	n.r.	193
ZrO_2	0.35 wt.%	Fe-9Cr-2W	Spark Plasma Sintering	n.r.	196
ZrO_2	0.3 wt.%	Fe-21Cr-9Mn-6Ni-0.4Ti	Vacuum Hot Pressing	n.r.	194
ZrO_2	20-60 vol.%	Cu	Spark Plasma Sintering	n.r.	195
Al_2O_3	8 wt.%	Fe-15Cr-1Mo-2.5C-1Si	L-DED	n.r.	198
Al_2O_3	1-3 vol.%	Ti-6Al-4V	L-PBF	n.r.	200
Al_2O_3	0.2-1 wt.%	Co-27Cr-4.5Mo-2.3Ni	L-DED	$CoAl_2O_4$	201
HfO_2	0.3 wt.%	Fe-14Cr-2W-0.35Ti	L-DED	n.r.	197
Ta_2O_5	1; 3 vol.%	Ti-6Al-4V	L-PBF	n.r.	200

In conclusion, a large library of different oxide nanoparticle species has been applied in ODS materials. Oxide nanoparticles can be manipulated by alloying the matrix alloy with additional elements and thus tune the nanoparticle size typically toward refined structures. However, research in this field does not include the adaptation of nanoparticle and matrix alloys for each other. Machine learning approaches, exemplary shown by Martin et al. [42], may pose a powerful tool to identify suitable nanoparticle species for given matrix alloy, allowing the development of superior ODS materials.

3.4 Matrix materials in ODS alloys

The concept of dispersion strengthening by dispersion of nano-scaled oxide particles can be applied to all crystalline structured materials. Accordingly, this concept may be used for enhancing mechanical and irradiation properties for a wide variety of metallic material groups, such as structural materials like ferritic [68] and austenitic [202] steels, nickel-based alloys, light metals based on magnesium [203], aluminum [192, 204, 205, 206, 207] and titanium [208] as well as refractory alloys based on tungsten [209, 210] and molybdenum [211, 212]. However, the mechanical properties of special alloys, such as abrasive resistant cobalt alloys [213, 214], high conductivity materials based on copper [195, 215, 216, 217], and even advanced high entropy alloys [218, 219, 220] also benefit from dispersed nanoparticles in their matrix in terms of material strength.

3.4.1 Steel-based ODS alloys

Steels are the most commonly used structural materials in technical applications and are widely used in engineering sectors. One reason is the broad spectrum of properties ranging from high-strength to corrosion- and high-temperature resistant grades. The steadily increasing demand for radiation-resistant materials for the application and modern nuclear power plants or future nuclear fusion power plants [60] and highly efficient combustion engines [59] promoted the development of Fe-based ODS alloys in the 80s of the last century. Today, many of commercial ODS alloys exist, which are often based on RAFM (reduced activation ferritic/martensitic) steels. These steels are characterized by the absence of easily activated alloying elements. [221, 222] In addition to RAFM steels, austenitic grades gained increasing interest for structural applications. [223, 224] In Table 3, commercial representatives of iron-based ODS alloys are listed.

Table 3: Commercially available ODS steels and their chemical composition in wt.%.

Alloy designation	Fe	Cr	W	Mo	Ti	Al	Ta	Mn	V	Y_2O_3	Reference
12YWT	Bal.	12	2.5	-	0.4	-	-	-	-	0.25	89
14YWT	Bal.	14	3	-	0.4	-	-	-	-	0.25	225
MA957	Bal.	14	-	0.3	0.9	-	-	-	-	0.25	66
ODS Eurofer97	Bal.	9	1	-	-	-	0.14	0.5	0.2	0.3	226
MA956	Bal.	20	-	-	0.5	4.5	-	-	-	0.5	226
PM2000	Bal.	19	-	-	0.5	5.5	-	-	-	0.5	227

Based on the chemical composition of the ODS steels shown in Table 3, two groups can be identified: While titanium alloyed ODS steels (e.g. 14YWT) are typically characterized by the dispersion of fine (< 10 nm) [66] oxide particles in the steel matrix, leading to enhanced material strength, aluminum alloyed ODS steel grades (e.g. PM2000) contain larger oxide particles (< 50 nm) [228] exhibiting higher corrosion resistance [229, 230], especially towards aqueous media [231] and oxidation resistance in air atmospheres up to temperatures of 1450°C [232] at the cost of reduced material strength [147, 162].

3.4.2 Nickel-based ODS alloys

Nickel-based superalloys are widely used in aerospace and power plant engineering applications. They are vital materials in combustion engines due to their exceptional high-temperature strength and creep properties. The additional reinforcement of nickel-based superalloys by nano-scaled oxide particles aims to improve mechanical properties such as strength and creep resistance in high-temperature regimes. For this reason, commercially available nickel-based alloys, e.g., Alloy625 [233] and Hastelloy X [46] are considered matrix alloys for oxide-dispersion strengthened nickel-based alloys. Additionally, γ'-reinforced nickel-based alloys (e.g., Alloy718 [234]) containing the γ'-forming agents titanium and aluminium are used due to their exceptional high-temperature properties. Few commercially available nickel-based ODS alloys were developed particularly for turbomachinery applications using nano-scaled Y_2O_3 as the reinforcement phase. (Table 4)

Table 4: Commercially available nickel-based ODS alloys and their chemical composition in wt.%.

Alloy designation	Ni	Cr	Fe	W	Mo	Ta	Ti	Al	Y_2O_3	Reference
PM1000	Bal.	20	3	-	-	-	0.5	0.3	0.6	235
PM3030	Bal.	17	-	3.5	2	2	-	6.6	1.1	236
MA6000	Bal.	15	1	4	2	2	2.5	4.5	1.1	237
MA758	Bal.	30	1	-	-	-	0.5	0.3	0.6	237
MA754	Bal.	20	1	-	-	-	0.5	0.3	0.6	226

Interestingly, in nickel-based ODS alloys, similarly structured oxide compounds compared to ODS steels are observed, e.g., pyrochlore-structured $Y_2Ti_2O_7$ [238, 239, 240] and $Y_4Al_2O_9$ [241] phases, indicating similar formation mechanisms of complex oxide nanoparticles. Refinement of the nanoparticles‘ size is observed by adding specific elements, such as hafnium [183, 242], which allow the formation of complex oxide nanoparticles similar to ODS steels. Accordingly increased material strength in high-temperature atmospheres is encountered by addition of hafnium. [237] One significant difference compared to ODS steels is a remarkable grain refinement induced by nano-scaled oxide particles in nickel-based alloys [46, 238], which may be attributed to their effect as heterogeneous nucleation sites.

3.4.3 Intermetallic ODS alloys

Intermetallic alloys offer high specific strengths and outstanding oxidation resistance in high-temperature environments superior to conventional nickel-based alloys, consequently drawing tremendous interest for aerospace applications. In particular, the groups of aluminides based on titanium (γ-TiAl) and iron (FeAl), as well as silicides based on molybdenum (Mo-Si) and vanadium (V-Si), are considered as substitute materials for nickel-based superalloys in modern combustion engines. [243] Comparable to nickel-based alloys, the dispersion of nano-scaled oxide particles in an intermetallic matrix aims to enhance the mechanical properties in high-temperature environments further. The

dispersion of various nano-scaled oxide particle species, e.g., Y_2O_3 [244, 245, 246, 247, 248], ZrO_2 [249, 250], La_2O_3 [249], and Er_2O_3 [251], leads to higher hardness and correspondingly to superior strength in room temperature and high-temperature environments compared to their non-reinforced counterparts. Additionally, incorporating of nano-scaled dispersoids facilitates a remarkable refinement of the grain structure [245, 246, 252], which is stabilized up to high temperatures [253]. Large amounts of aluminum in iron and titanium aluminides promote complex structured oxide compounds, e.g., $Y_3Al_5O_{12}$ and $Y_4Al_2O_9$ [247, 253, 254], similar to the formation mechanisms observed in iron- and nickel-based ODS alloys. Intermetallic alloys are still largely part of current research activities. Yet, no commercial oxide-dispersion strengthened alloys based on intermetallic alloy systems exist up to this date.

4 Additive Manufacturing of ODS alloys

In Additive Manufacturing (AM), metal parts are built in a layer-by-layer-based process, typically from metallic powder or wire feedstocks. The revolutionary potential of AM lies in the feasibility of producing parts of arbitrarily complex shapes directly from computer-aided design (CAD) data, additionally minimizing the need for subtractive manufacturing and waste compared to conventional manufacturing. [49, 50, 255] This shortens the time from the design of a part to its use to a minimum and is essential to save material, specifically on metallic products based on expensive and scarce alloying elements. Today, many different AM methods for manufacturing metals and composites are available. However, the AM methods of powder bed fusion (PBF) and directed energy deposition (DED) have gained the most attention over the last years. In PBF-based processes a high energy beam, typically a laser or an electron beam, is scanned over a thin pre-spread powder layer, melting the powder material locally. This process allows the fabrication of complex parts with high precision in an entire inert atmosphere. In the DED process, a powder feeding system is used to introduce powder materials into a melt pool on the surface of a substrate generated by an external heat source (e.g., laser beam, plasma torch, or electric arc). In contrast to PBF processes, local shielding gas atmospheres are created to protect the melt pool from undesired reactions with the atmosphere in DED processes. [49] As next-generation manufacturing processes, additive manufacturing processes are in principle suitable for the production of composite materials due to their unique process characteristics of small-scaled melt pools, dynamic flow conditions, and rapid solidification. Thus, many studies display the feasibility of PBF and DED processes for manufacturing metal-ceramic MMCs by effective dispersion of carbide [10, 36, 37, 256-284], boride [9, 11, 285-295], and nitride [296-303] compounds in metallic matrices.

MMCs, such as ODS alloys, are conventionally manufactured by a series of powder metallurgical processes (Fig. 6 upper panel), including a mechanical alloying (MA) process to produce a powder composite of metallic and oxide ceramic components followed by a consolidation process based on various sintering techniques, such as hot isostatic pressing (HIP) [304], hot extrusion (HE) [304], and advanced sintering processes, such as field-activated sintering (SPS) [128, 304, 305, 306, 307, 308, 309]. Conventional metallurgical processes, e.g. casting, involving a liquid stage are typically not suitable for

the production of ODS alloys since agglomeration and flotation mechanisms of dispersed oxide nanoparticles prevent the homogeneous distribution of nano-scaled oxide phases in the metallic matrix. Only liquid metallurgy processes with highly dynamic melt pool flows [310, 311] and rapid solidification conditions [312, 313] are feasible due to the effective suppression of agglomeration and flotation effects of dispersed nanoparticles. AM processes unite rapid solidification and dynamic melt flow characteristics and therefore principally represent a manufacturing technique feasible for the manufacturing of ODS alloys. However, AM processes also involve a strong overheating of the melt pool formed [13, 314] by spontaneous melting of the metallic component from the composite powder material, resulting in the liberation of oxide nanoparticles into formed melt pool. It is pointed out by numberous research groups, that oxide nanoparticles, i.e., Y_2O_3, may decompose due to the high melt pool temperatures in AM processes, releasing elemental yttrium and oxygen into the melt pool [244, 314, 315, 316, 317, 318, 319, 320, 321, 322]. This behavior is indicated by the formation of Y-rich intermetallic precipitates in steels [319, 321] as well as nickel superalloys [316] and may be enhanced by the melting point depression of nanoparticles compared to bulk material [323]. In this scenario, the nano-scaled oxide particles are formed by precipitation during cooling and solidification of the melt pool, as shown by Eo et al. [324] by numerical modelling and the prevention of agglomeration is facilitated by the rapid solidification kinetics and the turbulent melt pool dynamics. Boegelein et al. [325] demonstrate that the residual supersaturation of yttrium and oxygen in the metallic matrix after solidification can be reduced by subsequent annealing procedure, resulting in the formation of additional oxide precipitates. Thus, AM processes allow the simultaneous synthesis and shaping of ODS alloys, enabling a significant reduction of precess steps of the complex conventional manufacturing route of ODS alloys. [326] (Fig. 6 lower panel) It is noted, that additively manufactured parts may be exposed to further post processing steps like polishing procedures [327] and hot isostatic pressing (HIP) for reduction of porosity [328] or enhancement of mechanical properties [329].

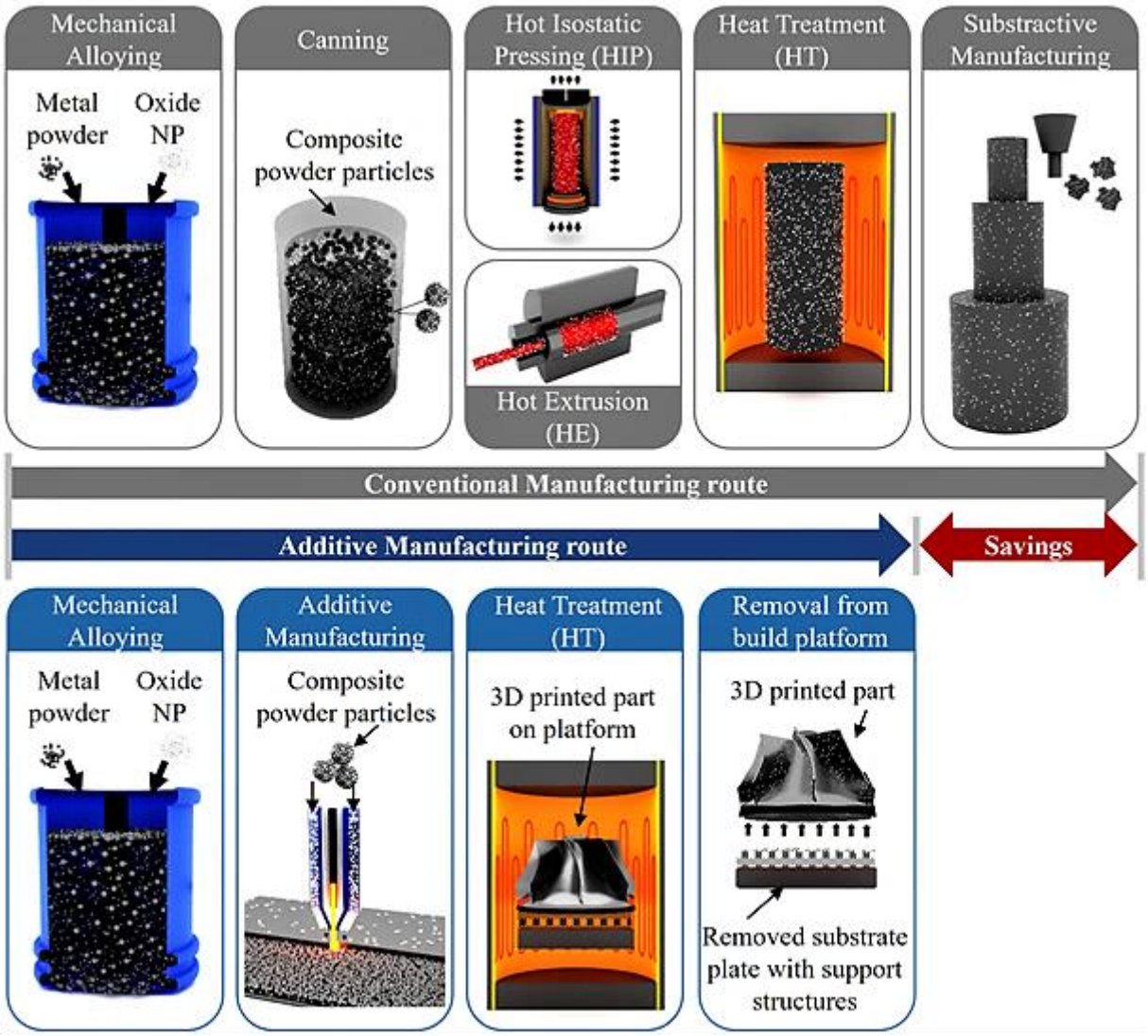

Fig. 6: Conventional manufacturing route [330] in comparison to the additive manufacturing route of ODS alloys. The conventional manufacturing route includes the composite powder manufacturing process of mechanical alloying (MA) followed by canning and subsequent powder metallurgical consolidation processes of hot isostatic pressing (HIP) and hot extrusion (HE). After consolidation furnace-based heat treatments and subtractive shaping of a part are necessary. The additive manufacturing route also uses composite powder feedstock i.e. from mechanical alloying processes. Additive manufacturing processes typically combine consolidation and shaping, followed by a subsequent heat treatment.

Both the conventional and AM routes for ODS alloys are based on the processing of powder materials. Simple mixing processes of micro-scaled metal particles and nano-scaled oxide particles typically lead to an inhomogeneous distribution of oxide particles within or on the bulk powder and results in inhomogeneous dispersion within the consolidated ODS alloy. [199] Therefore, the fabrication of suitable composite powders with homogeneous distributions of metallic and ceramic components is essential for the successful synthesis of ODS alloys by AM processes.

4.1 Manufacturing of ODS powder composites for AM

The successful and reliable manufacturing of parts using AM processes is significantly influenced by the material properties of the utilized powder. Therefore, high demands are imposed for powder materials used in AM processes. [58, 331, 332] These demands differ significantly from the powder properties used in sintering processes. In general, spherical powder morphologies are required for the reliable processing of metallic powder materials in AM due to their superior flowability properties that are needed for the powder deposition and recoating step [331, 333, 334]. Spherical powder morphologies are typically achieved by inert gas atomization processes [335] and plasma spheroidization processes [336]. In addition, bulk properties, such as flowability and bulk density, and optical properties, such as absorption characteristics, play a critical role in reproducible results. [331] High bulk densities, resembling denser packing of the powder bed, typically result in less porosity [37, 337] of printed parts. The influence of powder particle properties on absorption for a heat source (e.g. a laser beam) will be discussed in section 4.2.

In AM of ODS materials, the nano-scaled ceramic component typically must be added to the metallic powder material via additional process steps prior to the additive processing. Thereby, simple mixing of micro-scaled metallic and nano-scaled oxide powder materials leads to an inhomogeneous distribution of the reinforcement phase in printed components [199] and could also be disadvantageous with regard to safety regulations. Accordingly, various powder composite manufacturing techniques are proposed in the literature to manufacture suitable powder composites allowing the reliable fabrication of ODS alloys by AM processes (Fig. 7). [338] These composite powder manufacturing techniques include solid-based, liquid-based, and gas-based processes.

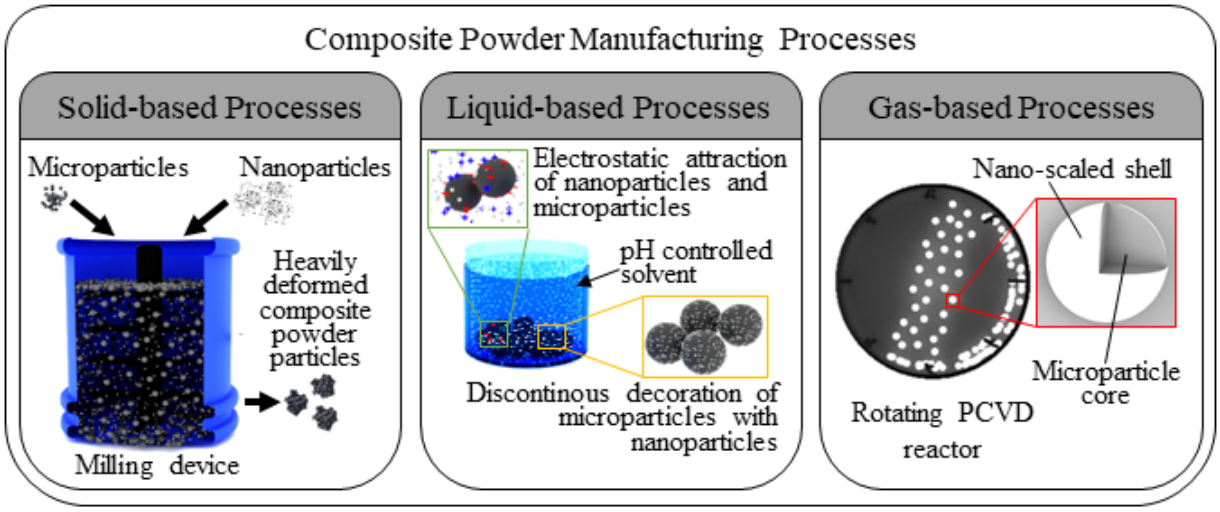

Fig. 7: Classification of composite powder manufacturing techniques including the mechanical alloying (MA) process as a representative for a solid-based composite powder manufacturing process, the process of electrostatic deposition (ED) as a representative of a liquid-based composite powder manufacturing process, and the process of PCVD (PVD) as a representative for gas-based composite powder manufacturing processes.

4.1.1 Solid-state based manufacturing of composite powder materials

The synthesis of composite powders for ODS materials is conventionally performed by solid-state reactions (Fig. 7 left box) incorporating the application of external forces on the powder components. [339, 340] The process of mechanical alloying (MA) is a widely used solid-state grinding process in which powder materials are mixed, crushed and cold-welded with the aid of grinding balls [339, 340, 341] in high-energy grinding aggregates, such as vibrating mills [342], planetary mills [10, 343] and attritor mills [344, 345, 346]. The competing mechanisms of crushing and cold welding reach a state of equilibrium over several hours. [347, 348, 349] The nano-scaled oxide phase decomposes as a result of the repeating impact of the grinding balls and either forms a supersaturated solid solution with the metallic powder component [251, 348, 349, 350, 351] or amorphizes [351]. This state, which is far from thermodynamic equilibrium, is relieved upon heat induction in the subsequent consolidation process by precipitation of nano-scaled oxide particles in the matrix alloy. [174, 178, 352, 353] To avoid unwanted reactions with atmospheric gases during the mechanical alloying process, either an inert gas [354] or reducing atmosphere to remove excess oxygen inside the milling containers is created. [355, 356] Mechanically alloyed powder materials typically do not meet the requirements for powder materials suitable for AM processes because the exposure to external forces during the MA process leads to severe deformation (Fig. 8c,d) of initially spherical powder particles (Fig. 8a,b) and their surface, impairing its flowability [357] and reducing the process windows for successful manufacturing of ODS materials via AM [358].

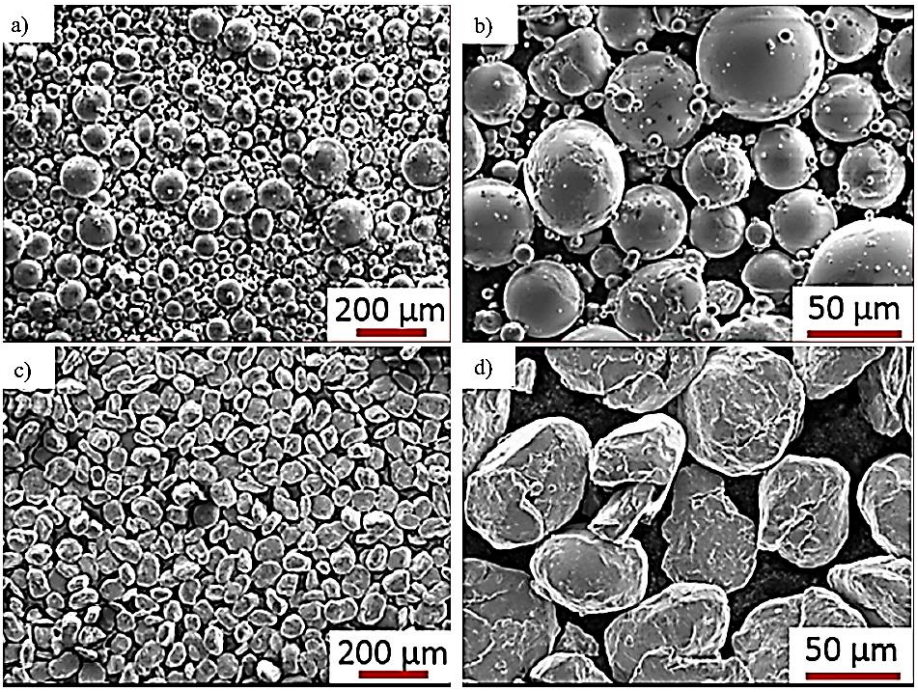

Fig. 8: a,b) SEM images of an inert gas atomized Fe-14Cr stainless steel powder with spherical morphology, shown with different magnification. c,d) SEM images of the Fe-14Cr stainless steel powder with 0.3 wt.% Y_2O_3 and 0.3 wt.% TiH_2 after MA for 176 h in hydrogen atmosphere showing non-spherical powder particles. Reprinted with permission from [358].

The adaption of MA by utilizing "adhesive agents", such as polyvinyl alcohol, allows a significant reduction of required milling forces to produce a powder composite consisting of slightly deformed metallic powder particles decorated with ceramic nanoparticles (AAMA). [359] The most promising solid-state fabrication process for powder composites is characterized by applying a resonant acoustic mixing technique (RAM), allowing the deposition of nano-scaled reinforcement phases on micrometer-scale metal particles without altering the spherical metal powder morphology. [360]

4.1.2 Liquid-based manufacturing techniques for powder composites

Liquid-based manufacturing techniques (Fig. 7, middle box) represent another group of processes used to synthesize powder composites for AM of ODS materials by incorporating a liquid phase during the powder manufacturing process. Typically, the micrometer-sized metallic and the nano-scaled powder components are dispersed in an organic [199] or inorganic [361] fluid allowing a homogeneous distribution of both phases within the liquid. The deposition of the nano-scaled oxide particles onto the surface of the metallic powder particles can be achieved by controlled evaporation of the fluid and subsequent diffusion deposition (DD) [199, 362] or by the aid of electrostatic attraction of metallic and ceramic powder components. In water, the electrostatic attraction can be enabled by controlling the pH value to achieve opposite charges of the metallic and ceramic components (electrostatic deposition, ED) allowing the homogeneous decoration of metallic particles with different loadings of ceramic nanoparticles. (Fig. 9a-e) [361, 363]

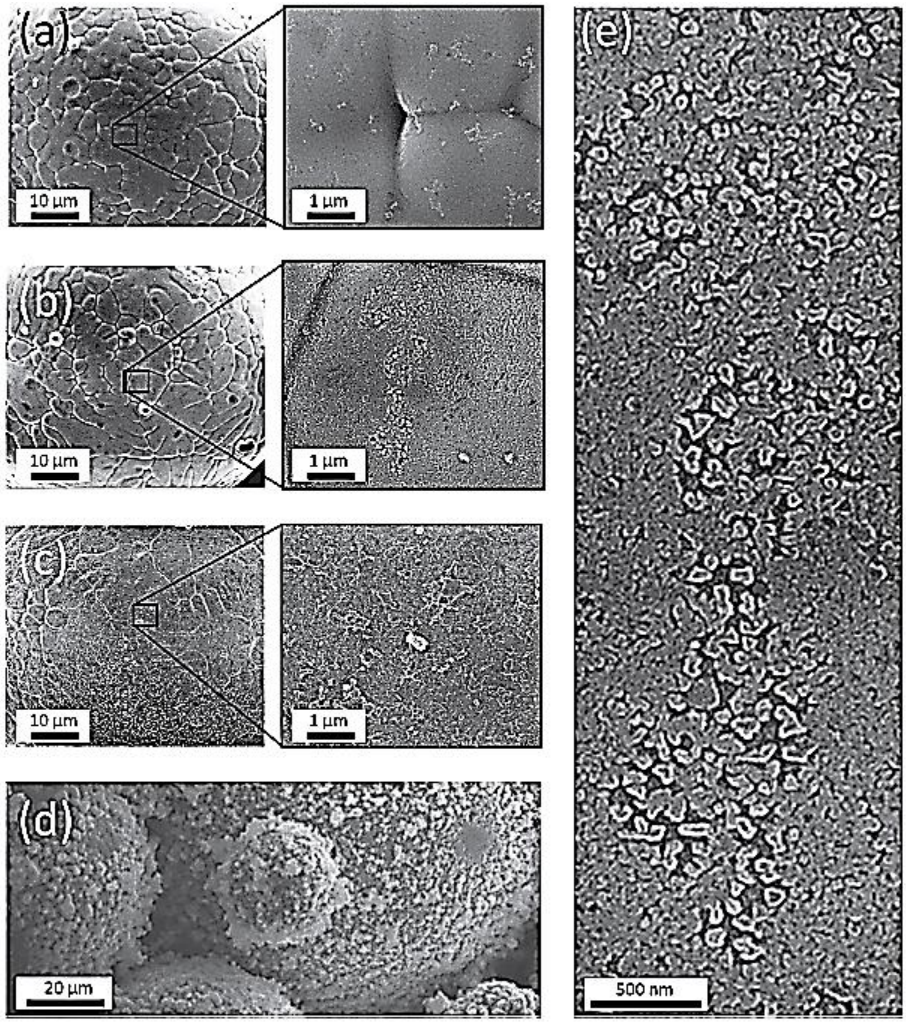

Fig. 9: SEM images of stainless steel micropowders with different loadings of Y_2O_3 nanoparticles. a) Raw stainless steel micropowder. b) 0.02 wt.% loading. c) 0.3 wt.% loading. d) 5 wt.% loading. e) Magnification of the compound shown in b). Reprinted with permission from [361].

An alternative approach is the utility of a condensed layer deposition (CLD) methodology to manufacture metallic particles with uniform deposition of nanocoatings by chemical reactions using special precursor compounds. [364] However, subsequent furnace-based calcination processes are necessary. [45, 365, 366, 367, 368] Liquid-based power composite manufacturing techniques offer tremendous advantages over solid-state processes retaining the initial morphology of the powder particles by the absence of external forces on the powder particles at the cost of comparably weak bonding between metallic and ceramic component and possible chemical reactions between the (oxidation-prone) powder particles and the fluid used, which may pose new challenges towards powder handling or powder re-coating process steps during AM. However, powder compounds manufactured with the methodology described in [361, 362, 363] have been successfully used in L-DED and L-PBF processes to manufacture ODS steels with an increased strength of approx. 30% compared to non-reinforced steel, proving the potential of this technology. [13, 16, 361]

4.1.3 Gas-based powder manufacturing techniques for powder composites

Gas-based synthesis techniques (Fig. 7, right box) are characterized by the use of oxygen-containing gases, which provide the oxygen required for the formation of nano-scaled oxides. In this context, the oxygen input can be performed already during the production of metallic powder materials with inert gas atomization processes by adding oxygen to the atomization gas (e.g., Ar-O_2 mixtures). This process, known as gas atomization reaction synthesis (GARS), allows the in-situ formation of nano-scaled oxides upon atomization of a Fe-Cr-Y alloy inside the generated powder particles (Fig. 10a,b). Due to the high oxygen affinity for the yttrium contained in the master alloy, selective oxidation with the formation of Y_2O_3 nanoparticles occurs, as shown by Rieken et al. [14]. Accordingly, using oxygen-contaminated inert gases or oxygen-containing feedstock promotes the formation of oxides during gas atomization. It results in oxygen-containing powder material [369, 370, 371, 372, 373, 374, 375, 376], which allows the formation of nano-scaled oxide dispersoids during AM processes. [377, 378, 379, 380] However, the integration of oxygen can also be achieved after powder production by oxidation of powder particles in furnaces by the process of surface treatment of gas atomized powder & reactive synthesis (STARS) [381, 382, 383, 384, 385] or fluidized bed reactors (FBR) [37], which allows the formation of oxides on the surface of metallic particles (Fig. 10c,d). This simple concept is, for example, also suitable for the production of nitride-dispersion strengthened materials. [386] Comparable deposits of oxides on the surface of metallic powder materials are also observed on powder exposed to oxidation processes during long-term storage [387], handling of powder materials [388], as well as recycling [376, 389, 390, 391, 392, 393] of used powder materials, which can promote significant oxygen input into the AM process and unintentionally cause the production of oxide-dispersion strengthened materials. Since these methodologies are based on oxidation processes, a careful selection of the master alloy is required to promote the formation of desired oxide compounds. In addition to the gas-based manufacturing processes based on oxidation reactions, conventional coating processes such as physical vapor deposition (PVD) [393, 394] and sputtering techniques (RFMS) [395] offer the possibility to deposit nano-scaled coatings consisting of oxide compounds on metallic powder particles independent of their respective oxygen affinity.

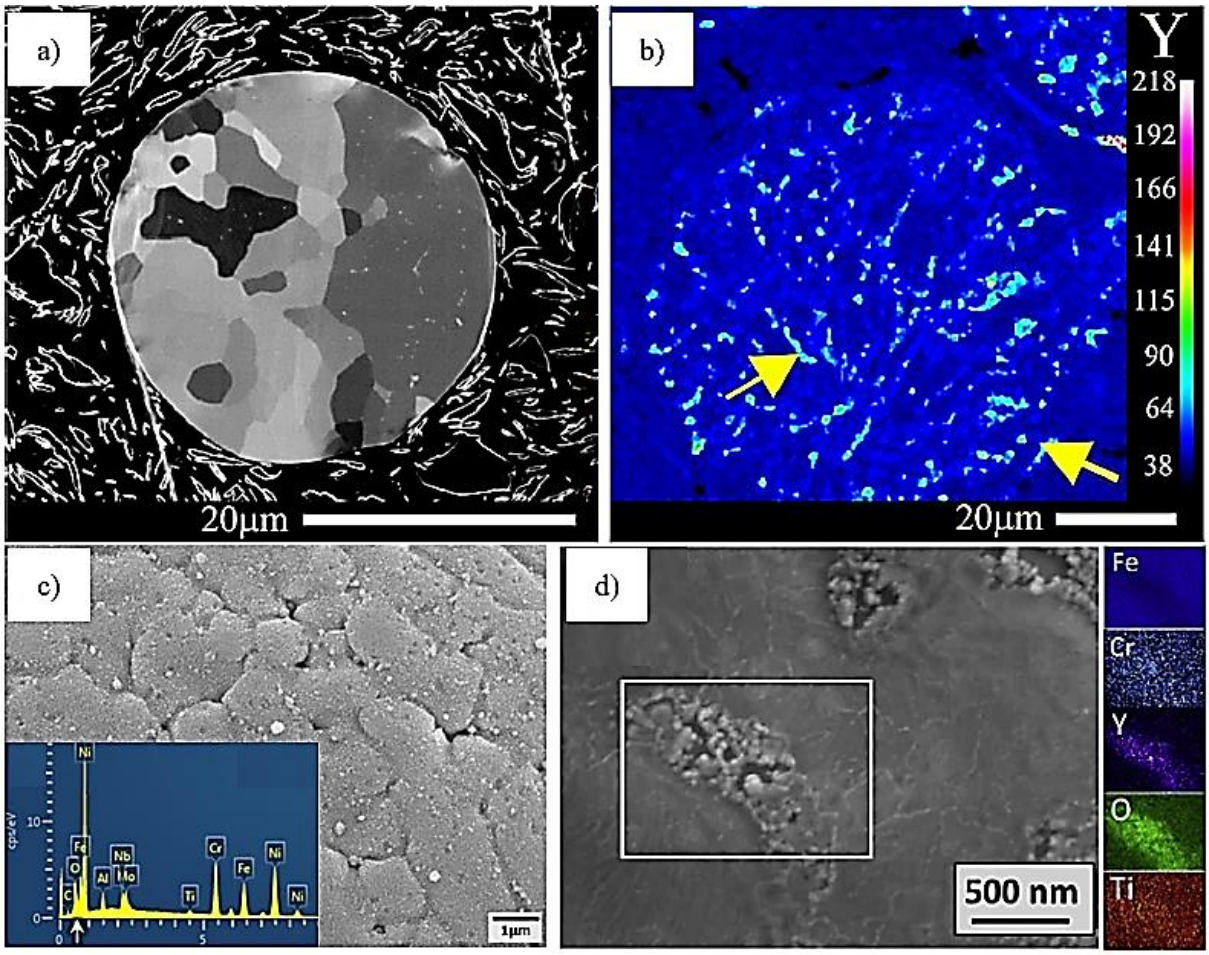

Fig. 10: a) ,b) Gallium ion contrast image of a cross-section of a GARS powder particle and corresponding EPMA chemical mapping with yttrium presence indicated by yellow arrows. The scale depicts the intensity of the yttrium signal. Reprinted with permission from [321]. c) SEM micrographs of a reused IN®718 powder particle with distributed sub-nanometer oxide particles on the surface proved by the superimposed EDS spectrum. Reprinted with permission from [376]. d) SEM image of a steel powder particle after surface oxidation with EDS maps of the white box area. Reprinted with permission from [381].

In Table 5, an overview of the assessed composite powder manufacturing techniques is presented showing characteristic process properties regarding the scalability and composite powder properties.

Table 5: Overview of current techniques for manufacturing of powder composites for AM of ODS materials.

	Method	Degree of host powder morphology retained	Flowability of the powder compound formed	Homogeneity of oxide particle dispersion	Scalability of oxide loading	Productivity / Scalability of powder composite production
Solid-state powder composite manufacturing process	Mixing (M)	Low	Low	Low	Low	High
	Mechanical Alloying (MA)	Low	Low	Medium	Medium	High
	Adhesive agent assisted Mechanical Alloying (AAMA)	Medium	Medium	Medium	Medium	High
	Resonant Acoustic Mixing (RAM)	High	High	High	Medium	Medium
Liquid-based powder composite manufacturing process	Diffusion Deposition (DD)	High	Medium	High	Low	Medium
	Electrostatic Deposition (ED)	High	Medium	High	High	Medium
	Condensed Layer Deposition (CLD)	High	High	High	High	Medium
Gas-based powder composite manufacturing process	Gas Atomization Reaction Synthesis (GARS)	High	High	Low	Medium	High
	Surface Treatment of Gas Atomized powder & Reactive Synthesis (STARS)	High	Medium	Low	Medium	Medium
	Fluidizing Bed Deposition (FBD)	High	Medium	Medium	Low	Medium
	Physical Vapor Deposition (PVD)	High	High	Medium	High	Low
	Radio Frequency Magnetron Sputtering (RFMS)	High	High	Medium	Low	Low

4.2 Consolidation of composite ODS powders via AM

The consolidation of powder composites can be performed by various AM processes, which can be differentiated either by the energy form provided or by the process principle of powder bed based- and blown powder processes (Fig. 11). Whereas the powder bed-based process and directed energy deposition processes are characterized by the introduction of thermal energy provided by high-energy laser- (L-DED, L-PBF) and electron beam sources (EB-PBF) or via plasma torches and electric arcs (WAAM) [49], cold spray deposition techniques use the high kinetic energy of particles to form dense depositions on a substrate material.

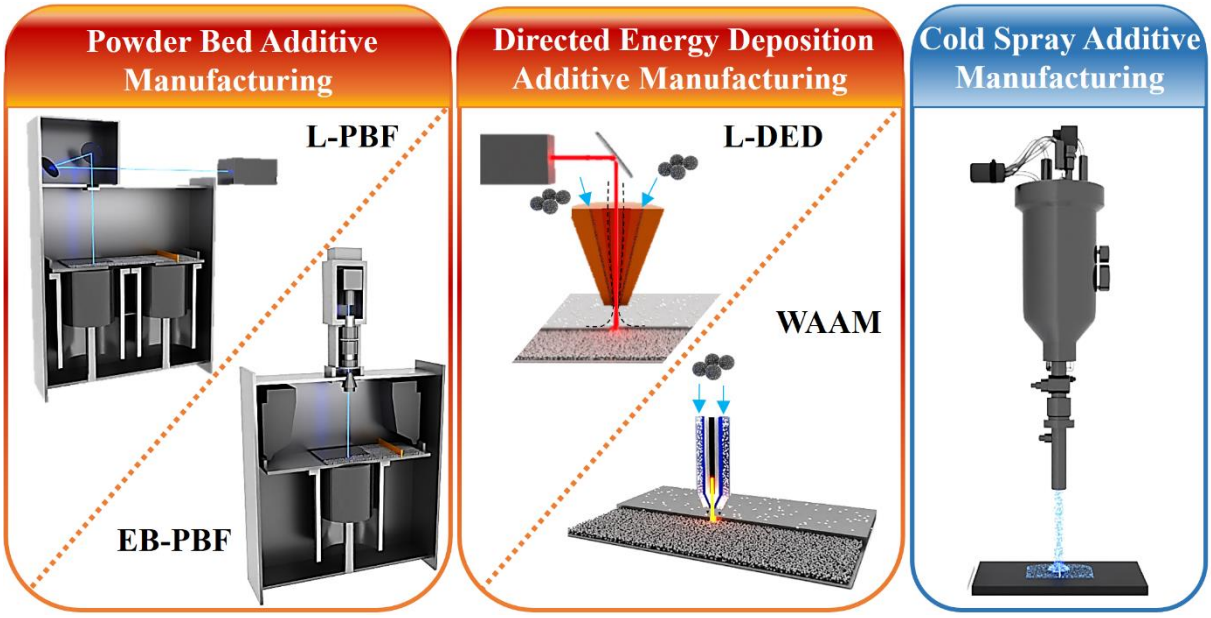

Fig. 11: Consolidation processes in additive manufacturing of ODS alloys: Orange boxes: Thermal powder-bed based of laser powder bed fusion (L-PBF) and electron beam powder bed fusion (EB-PBF) as well as directed energy deposition processes of laser directed energy deposition (L-DED) and wire arc additive manufacturing (WAAM). Blue box: Athermal cold spray deposition process.

Thermal additive manufacturing processes are characterized by three subsequent states of the interaction of composite powder particles with high-energy radiation, the behavior of nanoparticles in the melt pool, and the interaction of nanoparticles with the advancing solidification front, which govern the final distribution and size of nanoparticles in the solidified metallic matrix alloy.

Interaction of composite powder particles with high-energy radiation

Upon exposure of the composite powder particles to the high-energy radiation, e.g., lasers, the ratio of absorption and reflection determines the energy amount transferred by the laser beam into the powder material und thus the melting behavior of the powder material. Absorption and reflection are significantly influenced by the powder species and furthermore properties of the composite powder material, such as powder morphology [396], particle size distribution [397, 398], and surface condition, e.g., coatings [37]. (Fig. 12a,b) The matrix metal alloy has a characteristic absorption ratio for used laser wavelength (Fig. 12c), as shown by Brandau et al. [399]. Absorbed energy is transformed to heat, which

dissipated throughout the exposed powder particles via heat conduction [400], which can also be considered a material property. The absorption ratio of the powder material additionally depends on geometrical aspects, such as the morphology of the powder material. Irregular shaped powder particles as well as fine grained power sizes increase the probability of multiple relections boosting the overall absorbance ratio of the powder material. [396, 397, 398, 399] The absorption ratio for radiation is furthermore influenced by the surface condition of the powder particles. Coating the powder particles' surface with high absorbent compounds with high absorption for the used wavelength aids the absorptivity of the powder material significantly. [35, 36, 37, 199] However, the covering of powder particles with other compounds, i.e., oxide layers, may also reduce the absorptivity. [399] (Fig. 12d) Therefore, the status of powder materials needs to be considered before application in AM processes.

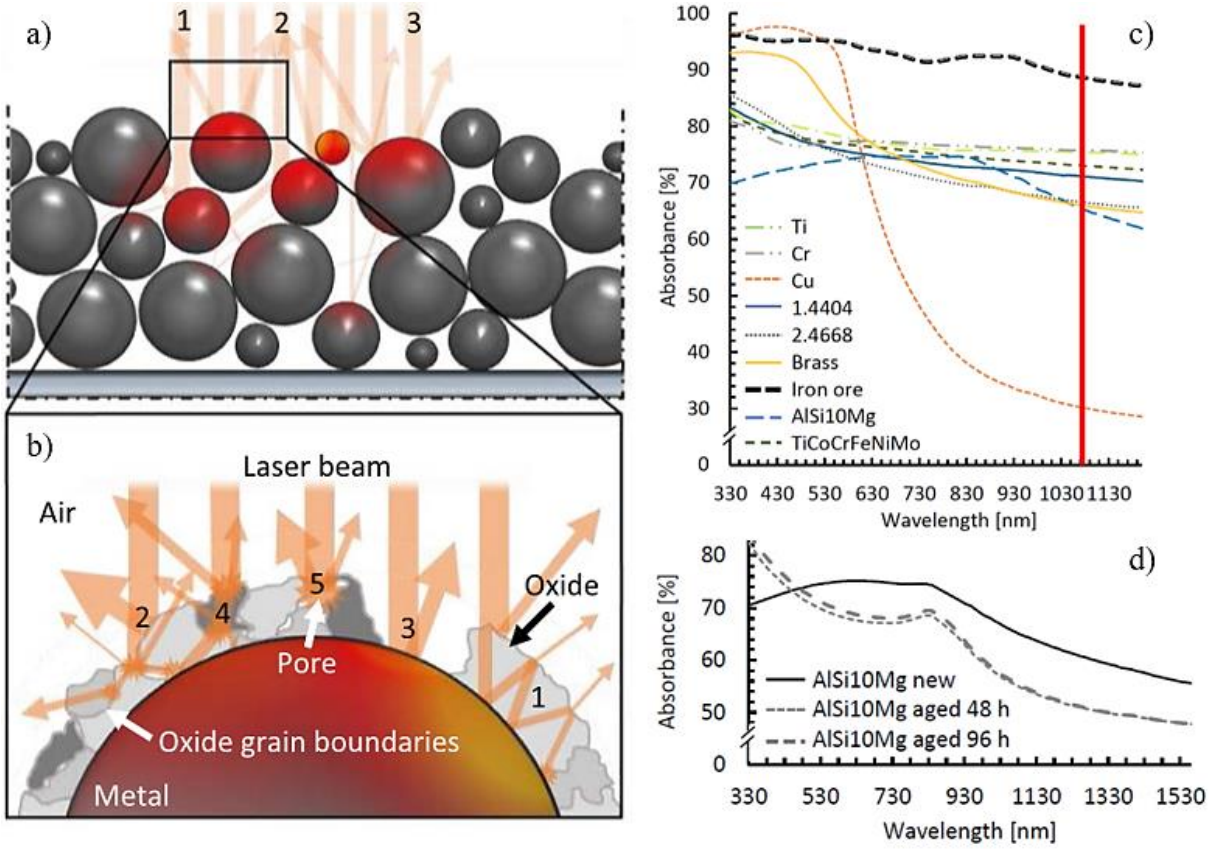

Fig. 12: a) Schematic of absorption and scattering of laser radiation on metal powder surfaces. b) Schematic of a magnified view of a powder particle with oxide accumulation on the surface with incident laser beam and different scattering and reflection events. c) Absorbance spectra of various powder materials ("1.4404" corresponds to 316L stainless steel and "2.4668" to IN®718) for laser irradiation wavelengths from 330 nm – 1130 nm. d) Absorbance spectra for new and aged AlSi10Mg powder material for laser irradiation wavelengths from 330 nm – 1130 nm. Reprinted with permission from [399].

Nanoparticle behavior in the melt pool

Exposing powder composite particles, consisting of metallic and ceramic components, to high-energy irradiation leads to the selective melting of the metallic component, which typically exhibits a lower melting temperature than the oxide phase, and forms the melt pool together with the partially molten substrate material. The nano-scaled oxide particles are released into the liquid melt pool and influenced

by the dynamic melt flow conditions typically encountered in AM processes. The flow conditions in AM processes are governed by a complex interplay of time-dependent forces, such as gravitational and buoyancy forces, as well as recoil and Marangoni forces [20, 401, 402, 403], which are influenced by the process conditions, e.g., process parameters [404].

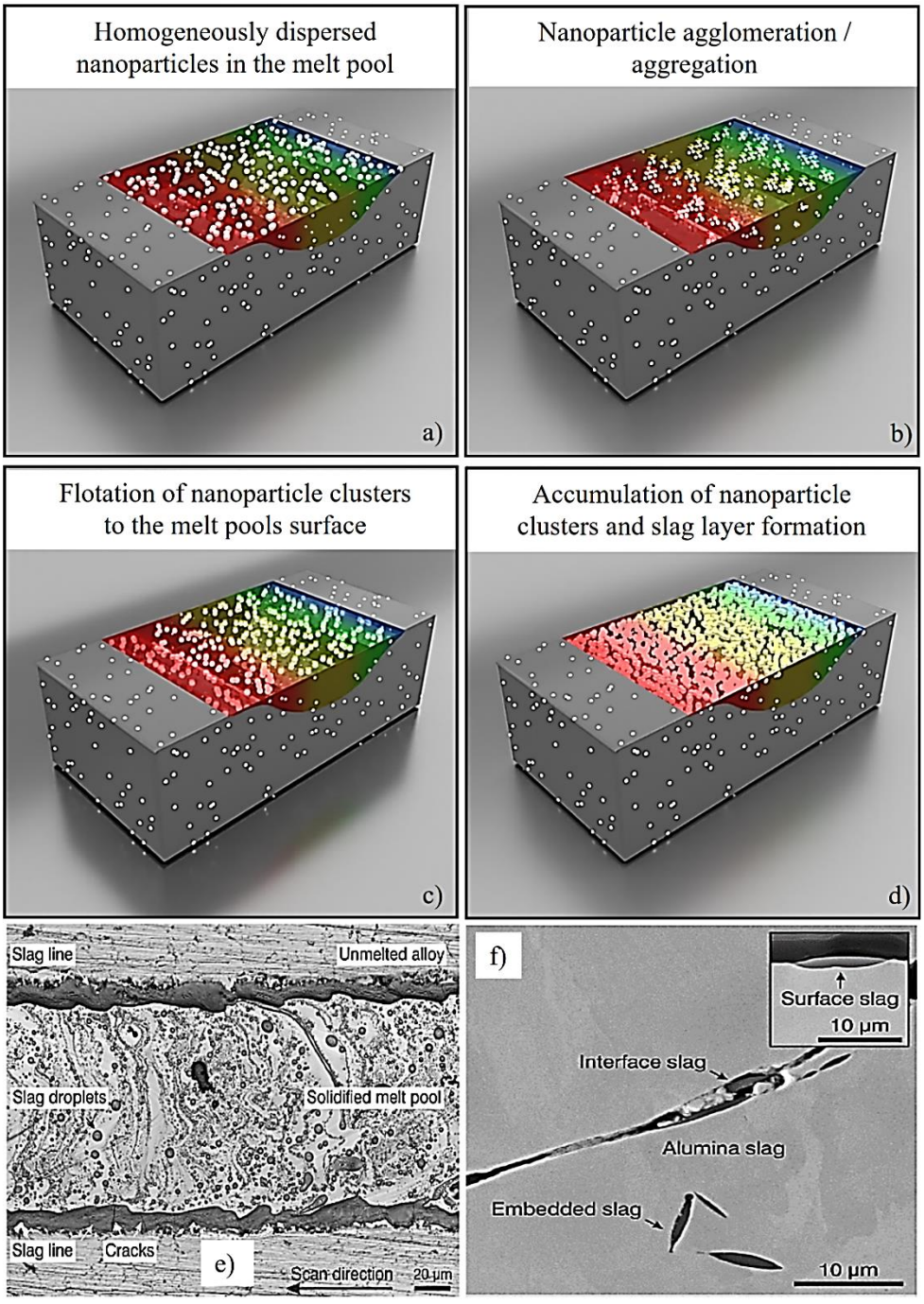

Fig. 13: Schematic illustration of oxide nanoparticle behavior in the melt pool during thermal AM processes and formation process of slag layers. a) Homogeneously distributed nanoparticles in a melt pool. b) Nanoparticle agglomeration driven by van der Waals forces. c) Flotation of nanoparticle agglomerates by buoyancy forces. d) Accumulation of floated nanoparticle agglomerates and formation of slag layers. e) Scanning laser micrograph of the surface of single laser scans on a SPS-consolidated Ni-8Cr-5.5Al-1Ti (wt.%) Y_2O_3 specimen. Reprinted with permission from [316]. f) BSE-SEM images of

entrapped alumina slag at free interfaces in an additively manufactured Ni-8Cr-5.5Al-1Ti (wt.%) alloy. Reprinted with permission from [408].

Nano-scaled particles are believed to follow the melt current due to their low mass, which is also reflected in as negligible considered buoyancy and gravitational forces in modelling approaches. [405] However, nanoparticles dispersed in the melt pool show strong tendencies towards agglomeration and aggregation due to their high surface area, high interfacial energy with the surrounding metallic melt and van der Waals forces. [406, 407] Advanced progress of agglomeration and aggregation tendencies enhance buoyancy forces of the agglomerated/aggregated nanoparticles. (Fig. 13a-d)

Increased buoyancy forces lead to pronounced flotation of nanoparticles, resulting in the formation of slag layers on the melt pool surface. (Fig. 13d-e)) [198, 316, 317, 409, 410, 411, 412], which may be entrapped between deposited layers upon subsequent deposition of additional layers. [317] Accordingly, preventing the agglomeration of nanoparticles, which is typically driven by van der Waals forces [413], with highly dynamic flow conditions is essential for the successful dispersion of nano-scaled oxides in the metallic matrix. While evaporation-induced recoil flows are typically dominant in the keyhole-welding mode, Marangoni flow is the governing flow mechanism in the conduction-welding mode. [414] Marangoni flows stem from different surface tensions due to alternating spatial melt pool temperatures, typically caused by inhomogeneous intensity distribution of the heat source (e.g., Gaussian laser beam profiles) and different cooling conditions across the melt pools area. While melt pools in AM processes are typically characterized by an outward flow profile [272, 403], the introduction of certain elements such as oxygen [414, 415, 416, 417, 418, 419, 420] or sulfur [421] change the surface tension temperature coefficient, resulting in a reversed flow direction inside the molten pool and thus significantly altering the thermal distributions and thus the solidification conditions.

The complex behavior of nanoparticles during the melting stage in AM processes has not been understood well. One reason may due to the fact, that the direct observation of nanoparticle movement during melting and solidification i.e. by camera systems is not possible. In-situ X-ray techniques, which are currently used for exploration of melt pool and cooling dynamics [422, 423], pore formation mechanisms [424, 425] and keyhole behavior [425], are principally capable of detecting particle movement in melt pools but are currently limited to resolution on the micrometer scale, making the detection of single oxide nanoparticles challenging. Thus, computational modelling offers an effective tool to predict nanoparticle behavior under different process environments and therefore guide the process development toward efficienct of nanoparticle dispersion. Xu and coworkers performed the first simulations on L-PBF processing of ODS steels, showing the potential of tracking nanoparticle movement in AM of ODS materials. (Fig. 14a,b), [413]

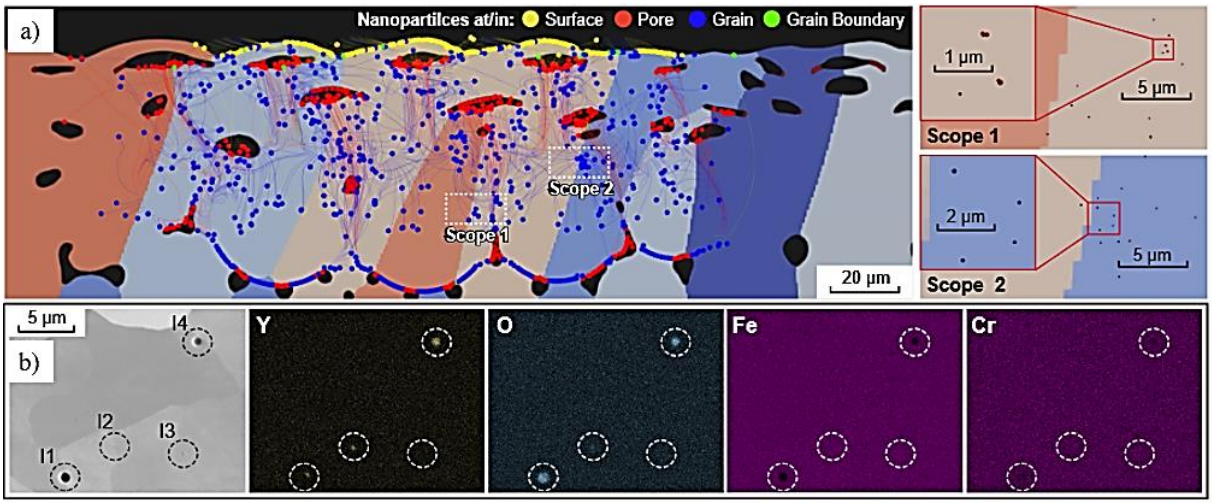

Fig. 14: a) Left: 2D- modeling of the movement of Y_2O_3 nanoparticles in a L-PBF-processed PM2000 ODS steel with 0.005 wt.% Y_2O_3 showing nanoparticle movement (indicated by lines) and their final position after solidification (spheres) in the steel matrix. Approx. 55% of the nanoparticles are captured inside grains (blue spheres), approx. 2% are located at grain boundaries (green spheres). Additionally, a large amount of nanoparticles accumulate in pores with approx. 13% (red spheres) and on the melt pool surface with approx. 30% (yellow spheres). Right: Regional magnification of dispersed nanoparticles in selected scopes (Scope 1 and 2) in realistic scale. b) SEM backscatter electron image with the corresponding EDS maps of yttrium, oxygen, iron, and chromium of the L-PBF processed PM2000 specimen showing enrichments of yttrium and oxygen enrichment and corresponding depletion of iron and chromium in nanoparticle agglomerates. Reprinted with permission from [413].

Nanoparticle interaction with advancing solidification fronts

The formation of small melt pools in AM processes, e.g., by utilizing of highly focused laser radiation, is typically accompanied by high cooling rates and high solidification front velocities. Successful incorporation of nanoparticles into the solidifying metallic matrix via the process of engulfment requires exceeding the critical solidification front velocity, which, among other factors, depends on the size of the nanoparticles. Small nanoparticle sizes require high solidification front velocities for successful incorporation by engulfment mechanisms during solidification. [426, 427] Low solidification front velocities promote pushing of the nanoparticles ahead of the solidification front [426, 427, 428, 429, 430], resulting in ineffective dispersion of nanoparticles in the metallic matrix and confirming the necessity of high cooling rates for homogeneous dispersion of nano-scaled oxide particles in AM of ODS alloys. (Fig. 15) It should be noted, that the solidification front velocity may vary significantly across different regions of the dendrites. [426]

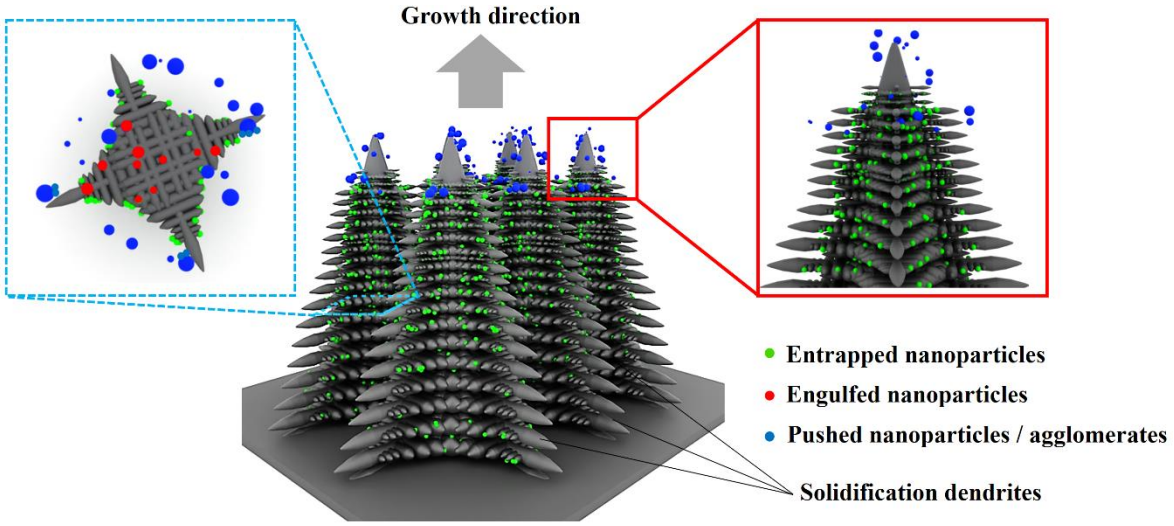

Fig. 15: Illustrative depiction of the interaction of nanoparticles with dendrites during solidification in AM showing engulfed nanoparticles inside dendrite structures and entrapped nanoparticles (green spheres) between dendrite arms. Right box: Nanoparticle agglomerates (blue spheres) are pushed in front of the dendrite tip. Left box: Cross section of a dendrite with engulfed nanoparticles (red spheres) inside the dendrites.

Alloys that are characterized by dendritic solidification additionally allow the trapping of nanoparticles between dendrite branches (Fig. 15), which facilitates nanoparticle incorporation at the cost of spatial nanoparticle enrichment in the interdendritic regions. [431, 432]

4.2.1 Powder bed-based AM of ODS alloys

Powder bed-based AM processes are the most widely used AM processes in research and industrial applications and are characterized by the high-precision production of components. Manufacturing is performed with focused, high-energy laser (L-PBF) or electron beams (EB-PBF), which selectively irradiate the powder bed consisting of powder composites. While the L-PBF process occurs in an inert gas atmosphere, interactions between the formed melt pool and the gas atmosphere cannot be excluded, in contrast to the EB-PBF operating under vacuum conditions. Powder-bed processes are characterized by extremely high solidification rates (L-PBF: 10^4-10^7 K/s [433, 434], EB-PBF: 10^4-10^6 K/s [435, 436]), and high Marangoni flows, due to large thermal gradients, allowing the effective dispersion of present nanoparticles in the melt pool. The successful fabrication of ODS alloys using powder bed-based AM processes (Table 6 ,7) is mainly governed by the selected matrix alloy, determining the process window and the tendency towards defect formation, e.g., cracking behavior. Accordingly, crack-tolerant matrix materials, such as aluminum [206, 437], aluminum-silicon based alloys [205, 217, 438, 439, 440], and austenitic steels, e.g., 304L [315, 441, 452] and 316L [357, 367, 412, 443, 444, 445, 446], can be used to produce defect-free oxide-reinforced parts. High strength ferritic ODS steels, such as PM2000 [13, 325, 447, 448, 449, 450], MA956 [451], 18Cr-2W-0.5Ti-0.3Y_2O_3 [79] and 14Cr-1W-0.3Mn-0.3Si-0.2Ni-0.3TiH_2-0.3Y_2O_3 [452] exhibit higher crack susceptibilities, increasing the probability for crack formation during manufacturing, which is frequently observed in PM2000 material. [447, 448]

However, effective dispersion on nano-scaled oxide particles (Fig. 16a-c), typically enriched in Y and O (Fig. 16d-j) is achieved in PBF-processed ODS alloys.

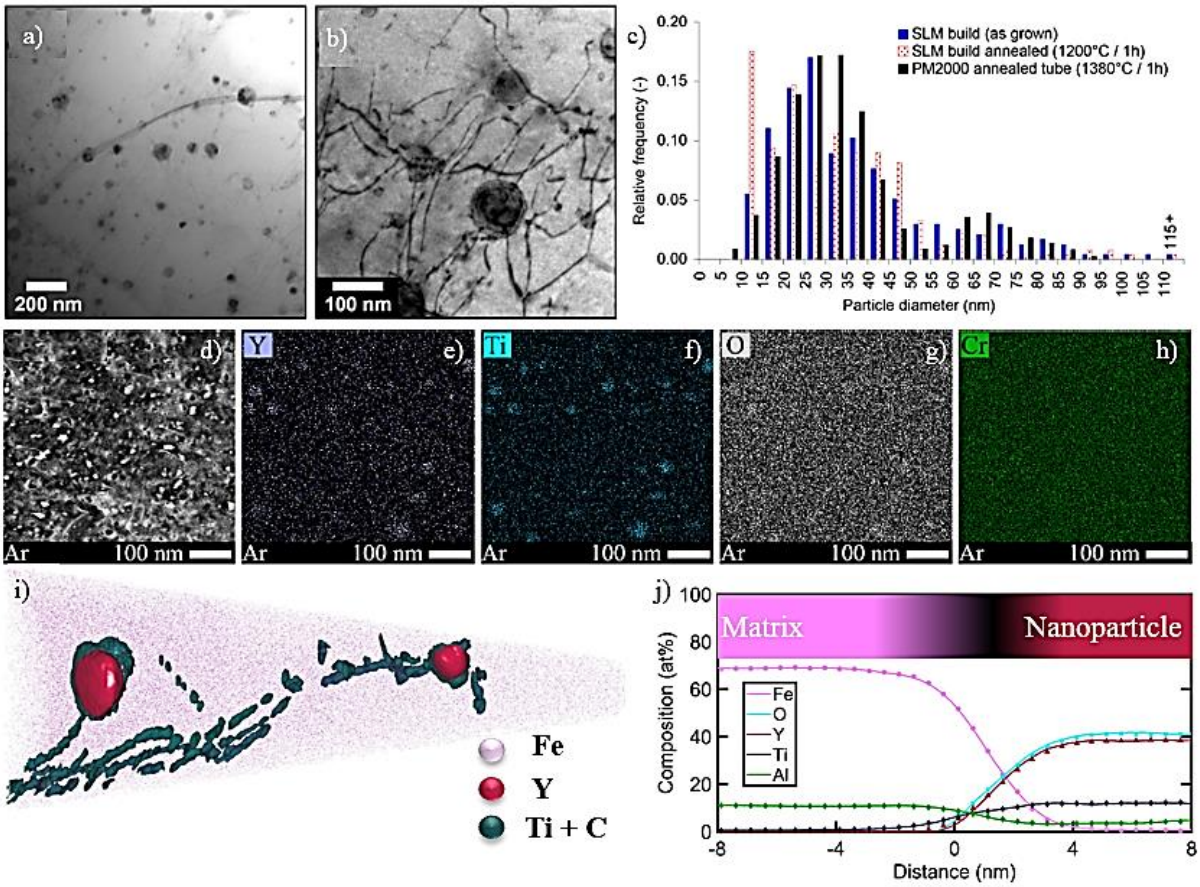

Fig. 16: a) TEM bright field images of the L-PBF processed ODS steel PM2000 showing nano-scaled dispersed nanoparticles. b) High magnification TEM bright field image exhibiting dislocation networks interacting with nanoparticles. c) Corresponding size distribution of nanoparticles in as grown- and annealed state with the reference size distribution of a conventionally manufactured PM2000 annealed tube. a-c) Reprinted with permission from [448]. d) HAADF TEM image and corresponding EDS maps e-h) of a L-PBF processed ODS steel in argon atmosphere using GARS powder material. Reprinted with permission from [321]. i) Reconstructed volume from atom probe tomography (APT) measurements of L-PBF processed PM2000 ODS steel with highlighted yttrium-rich nanoparticles and dislocations covered with titanium and carbon. j) Corresponding proximity diagram shows enrichments of Y, Ti and O in the nanoparticles. Reprinted with permission from [13].

In Table 6 an overview of studies on PBF-based AM of ferrous ODS alloys is shown, proving that dispersed oxide nanoparticles the formation of sub-100 nm sized nanoparticles is possible using PBF-based AM processes.

Table 6: Overview of ferrous ODS alloys manufactured via PBF-based AM processes with the used and resulting oxide size and type.

Base alloy	Process	Oxide phase	Oxide loading	Oxide size	Resulting Oxide type	Reference
Austenitic steels						
304L	L-PBF	Y_2O_3	5 wt.%	10 – 150 nm	n.r.	441
304L	L-PBF	Y_2O_3	0.5 wt.%	10 – 80 nm	Y-Si-O	315
316L	L-PBF	CeO_2	5 vol.%	< 100 nm	n.r.	443
316L	L-PBF	Y_2O_3	1 - 2 wt.%	10 – 140 nm	Y-Si-O	412
316L	L-PBF	Y_2O_3	0.3; 1 wt.%	n.r.	n.r.	357
316L	L-PBF	Y_2O_3	0.25 – 1 wt.%	~ 100 nm	Y-Si-(Mn-)-O	467
316L	L-PBF	OH-Apatite	5 - 15 vol.%	n.r.	n.r.	444
Ferritic steels						
PM2000	L-PBF	Y_2O_3	0.5 wt.%	~25 – 150 nm	n.r.	447
PM2000	L-PBF	Y_2O_3	0.5 wt.%	~5 – 160 nm	Y-Al-O	315, 448
PM2000	L-PBF	Y_2O_3	0.5 wt.%	10 – 100 nm	Y-Al-O	449
PM2000	L-PBF	Y_2O_3	0.08 wt.%	~ 30 nm	Y-Al-Si-O	13
PM2000	L-PBF	Y_2O_3	0.5 wt.%	< 100 nm	n.r.	450
PM2000	L-PBF	Y_2O_3	0.08 wt.%	n.r.	n.r.	363
MA956	L-PBF	Y_2O_3	0.3 – 0.7 wt.%	n.r.	Y-Al-O	451
14Cr-1W-0.3Mn-0.3Si-0.3Ni	L-PBF	Y_2O_3	0.3 wt.%	10 – 60 nm	Y-Ti-O	462
15Cr-0.15Y-0.10Ti	L-PBF	Y_2O_3	0.08 wt.%	10 – 35 nm	Y-Ti-O	321
14YWT	L-PBF	Y_2O_3	981 ppm	17 – 57 nm	Y-Ti-O	319
18Cr-2W-0.5Ti	EB-PBF	Y_2O_3	0.3 wt.%	10 – 45 nm	Y-Cr-O	79
Fe	EB-PBF	CeO_2	0.031 wt.%	n.r.	n.r.	453
Fe	EB-PBF	Fe_2O_3	0.045 wt.%	n.r.	n.r.	453

The dispersion of nano-scaled oxides also alters the solidification morphology by grain refinement (Fig. 17e-h), which is frequently observed in oxide-reinforced steels [13, 315, 441, 448] and particularly in nickel-based materials [46, 316, 454]. The introduction of nano-scaled oxide particles is believed to reduce hot crack formation at large-angle grain boundaries (LAGB), typically observed in additively manufactured γ'-reinforced nickel-base alloys [46, 454, 455] and high-strength aluminum alloys [42],

allowing the production of crack-free parts (Fig. 17a-d). The mechanism has not been studied in detail; however, it can be hypothesized that grain refinement suppresses the formation of large-angle grain boundaries by eliminating of the characteristic strong texture of additively manufactured materials. It is also noted, that the degree of grain refining varies with the oxide species added (Fig. 17e-h). [238] An overview of studies on AM of non-ferrous ODS alloys is shown in Table 7.

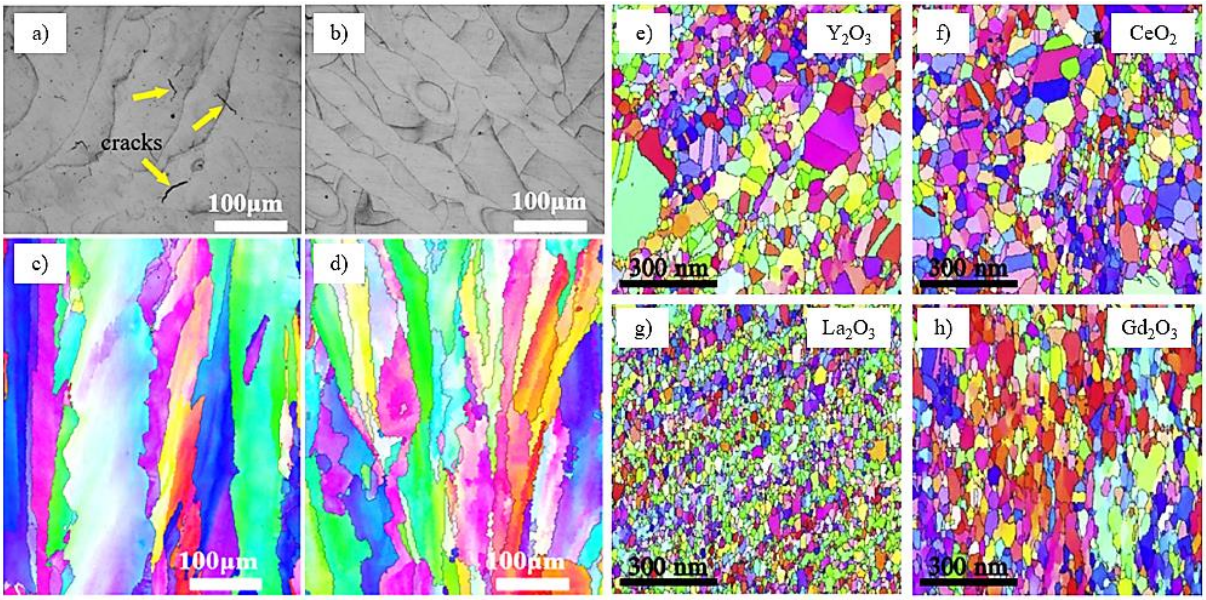

Fig. 17: LOM images of L-PBF manufactured undoped Hastelloy X with cracks (a) and the reinforced counterpart with 1 wt.% Y_2O_3 (b). c-d) Corresponding EBSD inverse pole figures showing the grain refinement induced by the yttrium oxide nanoparticles. a-d) are reprinted with permission from [46]. e-h) EBSD inverse pole figures of Y_2O_3, CeO_2, La_2O_3 and Gd_2O_3 added nickel-based alloy 690 (Ni-31Cr-11Fe (wt.%)) prepared by MA and HIP consolidation. Reprinted with permission from [238].

The dispersion of nano-scaled oxides in brittle materials, e.g., refractory metals [456, 457] and intermetallic alloys (e.g., γ-TiAl) [244] is typically accompanied by severe crack formation, which is typically tackled with higher process temperatures by utilization of preheating systems or additional irradiation exposure cycles. [245]

Table 7: Overview of non-ferrous ODS alloys manufactured via PBF-based processes with the used and resulting oxide size and type.

Base alloy	Process	Oxide phase	Oxide loading	Oxide size	Oxide type	Reference
Ni-8Cr-5.5Al-1Ti	L-PBF	Y_2O_3	0.5 wt.%	~ 100 nm	Y-O-S, Y-Al-O	316, 458
IN®625	L-PBF	Y_2O_3	0 - 2 wt.%	30 – 500 nm	Nb-Cr-Y-Al-O	454
IN®625	L-PBF	YSZ	1 wt.%	n.r.	n.r.	459
IN®625	L-PBF	Y_2O_3	0.48 wt.%	~ 42 nm	Y-Al-(Ti)-O	460
IN®718	L-PBF	Y_2O_3	1 wt.%	n.r.	Y-O	461
IN®718	L-PBF	Y_2O_3	0.3 wt.%	80 – 100 nm	Y-Ti-O	462
IN®718	L-PBF	Y_2O_3	0 – 1.5 wt.%	45 – 95 nm	Y-Ti-O-Nb-N	320
IN®738LC	L-PBF	Y_2O_3	0.05 wt.%	n.r.	Y-Al-Zr-O	463
Hastelloy X	L-PBF	Y_2O_3	1 wt.%	n.r.	n.r.	318
Hastelloy X	L-PBF	Y_2O_3	1 wt.%	~ 20 nm	Y-O	46
Ni-21Cr-0.85Fe-0.57Ti-0.25Al	L-PBF	n.r.	n.r.	n.r.	n.r.	464
Al	L-PBF	Al_2O_3	4 vol.%	350 nm	Al-O	205
Al	L-PBF	Al_2O_3	4 vol.%	n.r	Al-O	206
Al-1.7Zr	L-PBF	Al_2O_3	1 wt.%	80 – 100 nm	Al-O	465
Al-7Si-Mg	L-PBF	Al_2O_3	0.5 – 1 wt.%	n.r.	Al-O	207
Al-10Si-1Mg	L-PBF	$MgAl_2O_4$	0.5 wt.%	n.r.	n.r.	466
Al-10Si-1Mg	L-PBF	ZrO_2	0.45 wt.%	< 100 nm	Zr-O	440
Al-10Si-1Mg	L-PBF	Al_2O_3	15 wt.%	n.r.	n.r.	467
Al-10Si-1Mg	L-PBF	Al_2O_3	2; 5 wt.%	n.r.	Al-O	439
Cu	EB-PBF	Al_2O_3	5 vol.%	n.r.	Al-O, Cu-O	468
Ti-6Al-4V	L-PBF	ZrO_2-Y_2O_3	1; 2.5 wt.%	n.r.	n.r.	469
Ti-45Al-3Nb	L-PBF	Y_2O_3	> 0.2 at.%	30 – 120 nm	Y-O	244
W	L-PBF	Y_2O_3	1 wt.%	n.r.	W-Y-O	457
W	L-PBF	La_2O_3	0.5 - 2 wt.%	n.r.	n.r.	470

However, the use of preheating systems is associated with reductions in the solidification kinetics by inhibiting heat dissipation by heat conduction processes. The resulting increase in the melt-pool lifetime enhances agglomeration and flotation tendencies and promotes the formation of slag layers on the molten pool surfaces, which leads to a significant loss of dispersed oxide phases. [244, 442] Yet, the successful dispersion of nanoparticles is typically associated with increases in hardness and strength at the room temperature up to 30% [315] and 20% [443], as demonstrated by Ghayoor et al. and Salman et al., respectively. Additionally, the strength in high-temperature regimes is significantly increased by

approx. 20% [13] and creep rates up to several orders of magnitude lower [442, 458] compared to non-reinforced counterparts. There has only been limited reports comparing mechanical properties of conventionally (e.g. hot extruded) and printed ODS materials. Boegelein et al. [325] demonstrated a reduced tensile strength of L-PBF printed PM2000 ODS steel at room temperature, which is in agreement with findings of compressive strength determination of L-PBF-printed PM2000 ODS steel [13] and conventional PM2000 steel, described by Schneibel et al. [471]. One reason for the reduced mechanical strength might be attributed to the significantly smaller oxide nanoparticle size and the strong texture of additively manufactured ODS materials. Surprisingly, the compression yield strength of additively manufactured PM2000 material shows superior strength in high temperature environments (600°C) [13] compared to extruded counterparts [471]. Because of the limited data available on tensile or compressive strength of additively manufactured ODS alloys in high-temperature environments, more work is required to verify these results and explain this behavior. Furthermore, additional work is needed to characterize the creep properties of additively manufactured ODS materials in order to allow a tenable comparison with conventionally manufactured material. It is noted that additional heat treatment after the build process may enhance the strength by precipitation of additional nano-scaled oxide particles from the supersaturated microstructure formed during PBF processes. [448] Additionally, an increase of the ductility by approx. 16% by the dispersion of nanoparticles has been reported by Hu et al. [367].

In addition to the careful selection of matrix alloy and reinforcement phase, more factors influence the successful production of ODS alloys when using powder bed-based AM processes. Spherical powder materials with good flowability enhance the process stability and prevent the deterioration of the process parameter window for the fabrication of dense and defect-free components. [354] Process parameter sets including high energy intensities promote the formation of spatters during L-PBF, which originate from tearing of the turbulent molten metal [467, 472], particularly by recoil pressure, shown by Ly et al. [473]. Additionally, non-molten powder particles blown away by the instantaneous expansion of heated gas in the vicinity of the high-energy laser beam. [474] The ejected spatters are characterized by high temperatures [475] and large surface areas [476], which allows spatters to act as getter for residual oxygen in atmosphere of the build chamber in L-PBF and oxygen from the powder material, promoting the loss of oxygen in addition to slag formation due to flotation mechanisms. [316, 317, 477, 478, 479, 480, 481] The used gas atmosphere in L-PBF processes, may additionally have crucial influence on spatter formation. As shown by Amano et al. [474], the utilization of a helium atmosphere significantly reduced the amount of spatter produced compared to argon atmospheres, which may be attributed to the higher heat conductivity effectively cooling the melt pool and thus attenuating its turbulence and the lower density of helium compared to argon gas damping the expansion of the gas atmosphere close to the laser beam. However, due to the high solidification kinetics, powder-bed additive manufacturing processes are capable of dispersing a high number density of nano-scaled oxide particles down to a few nanometers. (Table 6, 7)

4.2.2 Directed energy deposition processes of ODS alloys

Directed energy deposition (DED) AM processes are characterized by a powder material feeding system, injecting powder material into a melt pool formed on a substrate surface by an energy source. Laser sources (L-DED), as well as electric arcs and plasma torches (WAAM) [482], are typically employed as the energy sources for the consolidation of composited powder materials. DED processes are characterized by significantly lower cooling rates than powder bed-based AM processes (L-DED: 10^3-10^4 K/s [13], WAAM: 10^2-10^3 K/s [483]), which is generally associated with lower solidification kinetics [483], which is due to the utilization of large beam diameters up to several millimeters [484, 485, 486]. Consequently, the time period of dispersed nanoparticles exposed to the complex flow conditions (e.g., Marangoni flow) in the melt pool is longer compared to powder bed-based processes, resulting in the pronounced agglomeration and aggregation tendencies of dispersed nanoparticles during the melting stage [197, 361] and thus smaller number densities and larger nanoparticle sizes in manufactured components. As shown by Wilms et al., limiting the dimensions and existence duration of formed melt pools in DED processes either by the selection of small beam diameters or high deposition velocities allows the reduction of the nanoparticle's residence time before capture by the advancing solidification front and consequently shifting number density and size distribution of nanoparticles towards powder-bed based processes. The process of high speed laser cladding (HSLC), a high-speed variant of the L-DED process, principally allows the application of high deposition velocitites and is characterized by cooling rates close to PBF-based processes (~10^6 K/s). [487] However, bimodal distributions of agglomerated nanoparticle clusters and non-agglomerated nanoparticles (Fig. 18a,b) are regularly observed in the solidified metallic matrix [197, 314, 347], which presumably stems from the successful incorporation of single nanoparticles by the solidification front by engulfment processes and the rejection of larger agglomerate clusters by the pushing mechanism and pronounced increased flotation tendencies due to higher buoyancy forces. [197, 347, 361, 411, 488, 489, 490, 491, 492] Multiple studies have been performed dealing with processing of ferrous (steels) and non-ferrous matrix alloys, summarized in Table 8 and 9, respectively. It is evident, that larger nanoparticles are encountered compared to PBF-based processes (cf. Table 6, 7) and the utilization of base plate preheating systems and large beam diameters (> 1 mm) result in large nanoparticle agglomerates (> 300 nm).

Table 8: Overview of ODS steels fabricated by directed energy deposition processes with the used beam diameter, oxide phase and loading. Resulting oxide size and type are also given.

Base alloy	Process (beam diameter)	Oxide phase	Oxide loading	Oxide size	Resulting oxide type	Reference
14Cr-0.2Si-0.4Ti	L-DED (250 µm)	Y_2O_3	0.3 wt.%	10 – 120 nm	Y-Ti-O	347
14Cr-2W-0.35Ti	L-DED (250 µm)	Y_2O_3 HfO_2	0.3 wt.% 0.3 wt.%	20 – 140 nm 120 – 300 nm	Y-Ti-O n.r.	197
14Cr-2W-0.35Ti-(0.2Te)	L-DED (250 µm)	Y_2O_3	0.4 wt.%	100 – 250 nm	Y-Ti-O, Ti-O	493
9Cr-2W-0.3Ti	L-DED (600 µm)	Y_2O_3	0; 1; 2; 5 wt.%	n.r.	Y-Ti-O	494
PM2000	L-DED (660 µm)	Y_2O_3	0.5 wt.%	100 – 200 nm	Y-Al-Ti-O	361
PM2000	L-DED (660 µm)	Y_2O_3	0.5 wt.%	n.r.	n.r.	450
PM2000	L-DED (660 µm)	Y_2O_3	0.08 wt.%	~ 50 nm	Y-Al-Si-O	13, 16
PM2000	HSLC (660 µm)	Y_2O_3	0.5 wt.%	50 – 150 nm	Y-Ti-O	487
9Cr-1.5W-0.3Ti	L-DED (n.r.)	Y_2O_3	0.3 wt.%	7 – 55 nm	Y-Ti-O	411
15Cr-2W-4.5Al-0.3Ti-0.3Zr	L-DED (n.r.)	Y_2O_3	0.2 wt.%	2 – 8 nm	Y-Zr-O, Al-O	488
17Cr2NiSi	L-DED (1600 µm)	Y_2O_3	0 – 1 wt.%	n.r.	Y-Si-O	495
16Cr2NiSiMo	L-DED (1200 µm)	Y_2O_3	0.25 – 1 wt.%	n.r.	Y-Si-O	496
316L	L-DED (n.r.)	Y_2O_3	0.5 wt.%	n.r.	n.r.	497
9Cr-1.5W-0.8Mn-0.5Ti-0.2Si	GMAW (n.r.)	Y_2O_3	0.5 wt.%	2 – 10 nm; ~ 200 nm	Y-Ti-O, Ti-O	314

Only little research has been performed on WAAM of ODS steels, which may be due to slower solidification kinetics compared to powder bed-based and the difficulty of manufacturing feasible oxide reinforced rod material. However, Zhou et al. [314] used canned steel tubes, filled with nano-scaled Y_2O_3 and prealloyed powders for manufacturing wall structures with the WAAM process of gas metal arc welding (GMAW), resulting in a bimodal distribution of large oxide nanoparticle agglomerates with sizes of approx. 200 nm as well as extremely fine oxide nanoparticles (2 – 10 nm). The printed material shows promising mechanical properties and demonstrates the potential of WAAM technologies for additive manufacturing of ODS materials with much higher throughput, but at the expenses of less resolution.

Table 9: Overview of non-ferrous alloys fabricated by directed energy deposition processes with the used beam diameter, oxide phase and loading. Resulting oxide size and type are also given. (* Base plate preheating devices used during L-DED processing)

Base alloy	Process	Oxide phase	Oxide loading	Oxide size	Resulting oxide type	Reference
Ni-19Cr-2.6Co-3.3Al-0.55C	L-DED (2000 µm)	Al_2O_3	0.5 – 1.5 wt.%	~ 100-500 nm	n.r.	502
Ni-21Cr-0.85Fe-0.57Ti-0.25Al	L-DED (n.r.)	Y_2O_3	0.6 wt.%	~ 40 – 250 nm	Y-Cr-O, Al-O	508
Ni-20Cr-5Al-3W	L-DED (n.r.)	Y_2O_3	1.5 wt.%	n.r.	n.r.	509
Co-27Cr-2.3Ni-4.5Mo-0.9Si-0.3C	L-DED (4500 µm)	Y_2O_3	0.2 - 1 wt.%	150 – 400 nm	n.r.	204
Co-27Cr-2.3Ni-4.5Mo-0.9Si-0.3C	L-DED (5000 µm)	Al_2O_3	0.2 – 1 wt.%	150 – 400 nm	Co-Al-O	216
Ti-45Al-3Nb	L-DED* (1300 µm)	Y_2O_3	< 0.2 mol.%	50 – 400 nm	n.r.	249
Ti-48Al-2Cr-2Nb	L-DED* (600 µm)	Y_2O_3	0.5 wt.%	~ 500 – 1000 nm	n.r.	251
Mo-13.5Si-7.5B	L-DED* (600 µm)	Y_2O_3	0.5 wt.%	n.r.	n.r.	500
V-9Si-5B	L-DED* (600 µm)	Y_2O_3	0.5 wt.%	n.r.	n.r.	500
$Al_{0.5}$CoCrCuFeNiSi	L-DED (n.r.)	Y_2O_3	1 wt.%	n.r.	n.r.	510

Incorporated nanoparticle agglomerates are typically found in the vicinity of grain boundaries [16, 314, 348], which are likely to trap agglomerated nanoparticle clusters during solidification. (Fig. 18a) The strong flotation or tendencies of agglomerated and aggregated nanoparticle clusters may ultimately lead to the formation of large-scaled agglomerates of oxide nanoparticles on the melt pool surface, which macroscopically appear as slag layers (Fig. 18c,d,e) [410, 488, 501], impeding the deposition of subsequent layers in WAAM processes. [410]

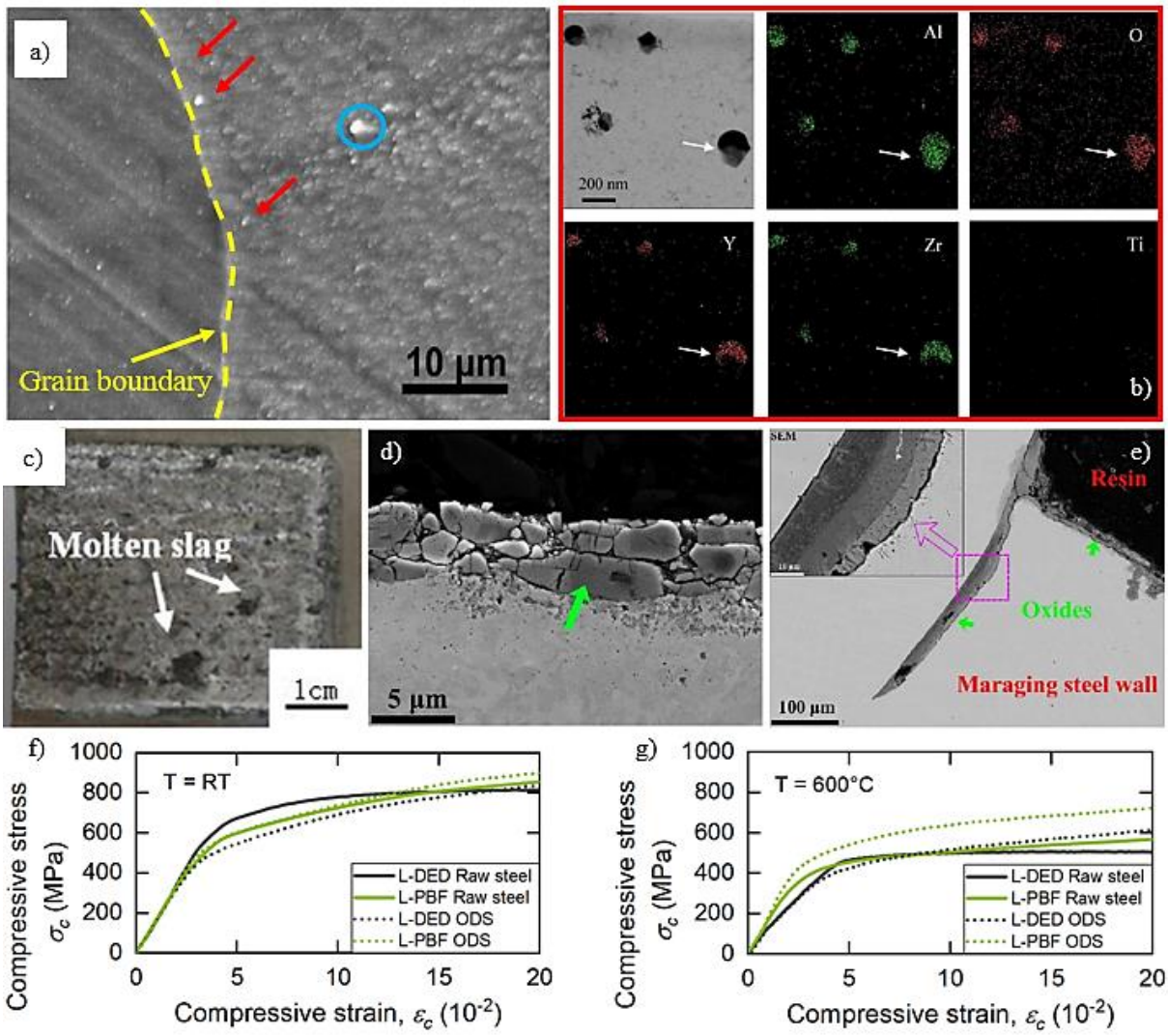

Fig. 18: a) SEM image of a L-DED processed Fe-20Cr-4.5Al-0.5Ti-0.3Y_2O_3 (wt.%) alloy showing dispersed nanoparticles in the ferritic stainless steel matrix and few smaller agglomerates (indicated by red arrows) close to the grain boundary (dashed yellow line) and a larger agglomerate (blue circle). Reprinted with permission from [16]. b) STEM and corresponding EDS mapping images of nano-scaled oxide particles in L-DED processed Fe-15Cr-2W-4.5Al-0.3Ti-0.3Zr-0.2Y_2O_3 (wt.%) showing enrichments in yttrium, aluminium and zirconium. Reprinted with permission from [488]. c) Slag islands on the surface of L-DED processed Fe-Cr-Mo steel dispersed with Al_2O_3 microparticles. Reprinted with permission from [198]. d) Slag formation (indicated by green arrow) on a five layered maraging steel manufactured by WAAM. e) Slag layer entrapped between layers in a maraging steel manufactured by WAAM. d-h) are reprinted with permission from [410]. f-g) Compressive stress of L-DED and L-PBF processed Fe-20Cr-4.5Al-0.5Ti (wt.%) ("Raw steel") and additions of 0.3 wt.% Y_2O_3 ("ODS") at room temperature (RT) and 600°C. Reprinted with permission from [13].

Depending on the matrix alloy selected, the incorporated nano-scaled oxide particles in DED processes may initiate grain refinement [13] by acting as heterogeneous nucleation sites and modifying the solidification structure towards equiaxed solidification structures [491, 492]. The mechanical properties of DED processed ODS alloys are typically characterized by higher strengths both at room temperature [13, 197, 246, 488, 489, 490] but especially in high-temperature environments [13, 17, 492] compared to their non-reinforced counterparts (Fig. 16f-g). However, the mechanical properties of PBF-processed

and conventionally manufactured ODS alloys are superior to DED-processed ODS alloys due to higher nanoparticle number densities and correspondingly smaller nanoparticle sizes. (Fig. 18f-g) [13]

4.2.3 Athermal synthesis of ODS alloys by AM

Athermal consolidation allows the additive synthesis without the creation of a liquid phase and therefore reduces the risk of nanoparticle agglomeration significantly. The cold spray (CS) deposition technique is characterized by composite powder materials directed onto a metallic substrate material with high kinetic energies. [502] Upon impact, the composite powder particles are cold-welded onto the substrate material allowing the deposition of claddings with low porosity [503]; however, high surface roughnesses are observed. In Table 10 studies using cold spray deposition for manufacturing claddings of ODS materials are presented.

Table 10: Overview of ODS alloy manufactured via the athermal AM process of cold spray (CS) and laser-assisted cold spray (LACS) deposition processes with the used and resulting oxide size as well as the resulting oxide type.

Base alloy	Process	Oxide phase	Oxide loading	Oxide size	Resulting oxide type	Reference
14YWT	CS	Y_2O_3	0.25 wt.%	n.r.	n.r.	502
14YWT	CS	Y_2O_3	0.2 wt.%	50 – 100 nm	Ti-O, Y-O	503
Fe-8Ni-1Zr	LACS	ZrO_2	n.r.	< 100 nm	Zr-O	504
Fe-8Ni-1Zr	LACS	ZrO_2	n.r.	< 100 nm	Zr-O	505

Because this process is based on cold welding mechanisms, the utilization of metallic powder particles covered with nano-scaled oxides or ceramic nanocoatings is likely to deteriorate the cold-welding process; only mechanically alloyed or GARS processed composite powder materials may be considered for CS-based deposition. The implementation of a laser beam directed at the substrate material (LACS) allows increased deposition efficiency at the expense of local grain and nanoparticle coarsening. [504, 505] However, equiaxed microstructures and large fractions of nano-scaled oxygen-rich nanoparticles can formed during deposition using the LACS process. (Fig.19a-c)

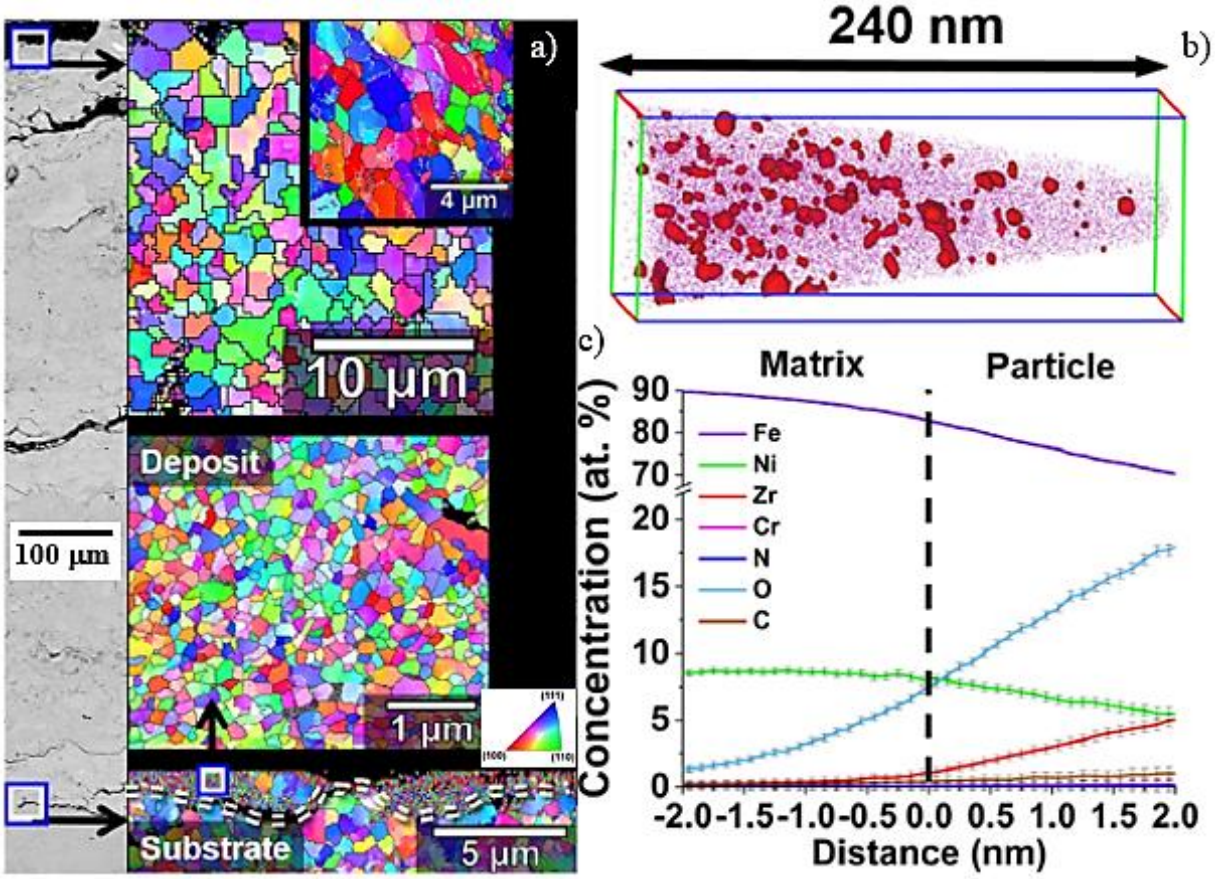

Fig. 19: a) BSE and EBSD inverse pole figures of LACS deposited Fe-8Ni-1Zr alloy at a substrate temperature of 650°C. b) Volume reconstruction from atom probe tomography (APT) measurements showing nano-scaled oxide particles. c) Corresponding proximity diagram showing enrichment of zirconium and oxygen in the nanoparticles. Reprinted with permission from [504].

Based on the assessment in this chapter, Table 11 presents a comparison of the AM techniques used for manufacturing ODS material and displays characteristic process properties, usable composite powder feedstocks and achievable nanoparticle sizes together with the degree of slag layer formation.

Table 11: Comparison of the assessed AM techniques feasible for the manufacturing of ODS materials. Abbrevations in the column "Composite powder feedstock applicable" are taken from Table 5.

	Method	Resolution	Productivity	Cooling rate	Composite powder feedstock applicable	Maximum resulting nano-particle size	Degree of slag layer formation
Power bed-based processes	L-PBF	µm	Low	10^4 - 10^7 K/s	M, MA, AAMA, RAM, DD, ED, CLD, GARS, STARS, FBD, PVD, RFMS	~ 150 nm	Low
	EB-PBF	µm	Low	10^4 – 10^6 K/s	M, MA, AAMA, RAM, DD, ED, CLD, GARS, STARS, FBD, PVD, RFMS	~ 150 nm	Low
Directed energy deposition processes	L-DED	µm-mm	Medium	10^3 - 10^4 K/s	M, MA, AAMA, RAM, DD, ED, CLD, GARS, STARS, FBD, PVD, RFMS	~ 300 nm	Medium
	HSLC	µm-mm	High	~ 10^6 K/s	M, MA, AAMA, RAM, DD, ED, CLD, GARS, STARS, FBD, PVD, RFMS	~ 150 nm	Low
	WAAM	mm	High	10^2 - 10^3 K/s	MA, AAMA, GARS	n.r.	High
Cold spray deposition processes	CS	µm-mm	High	n.a.	MA, AAMA, GARS	~ 100 nm	None
	LACS	µm-mm	High	n.r.	MA, AAMA, GARS	100 nm	Low

4.3 AM of ODS alloys using internal oxidation approaches

The success of AM of ODS alloys heavily depends on the provision of suitable composite powder materials. The complex and costly fabrication process of composite powder materials is considered a major drawback for manufacturing of ODS materials. A practical solution is offered by the in-situ fabrication of ODS alloys, in which chemical oxidation processes lead to nano-scaled oxide particles during processing in AM processes. Accordingly, oxygen can be provided to the melt pool by interaction with an oxygen-containing atmosphere or by introducing solid oxidizing agents that react chemically with alloying elements of the matrix alloy. The formation of oxide compounds by chemical oxidation reaction is governed by the selective oxidation of alloy components with highest affinity to oxygen and a negative enthalpy of formation altering the chemical composition of the matrix alloy. [506, 507] Therefore, preventing the formation of oxide species, e.g., manganese-, silicon- or chromium-rich oxides

in steels [370, 409, 445, 446, 508, 509, 510, 511, 512] or high-entropy alloys [513, 514], requires the adaption of the chemical composition of the matrix alloy, i.e., by the addition of yttrium to form typically desired yttrium-based oxide compounds. (Fig. 20) [128, 506, 513, 514, 515]

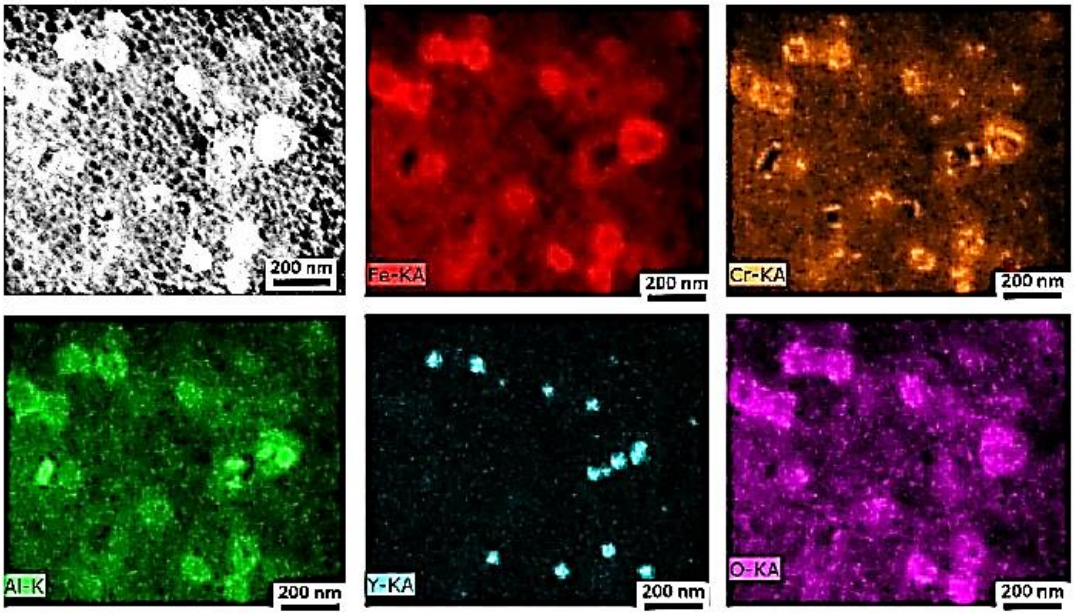

Fig. 20: HAADF STEM micrographs and corresponding EDS elemental maps of in-situ formed nano-scaled oxide nanoparticles enriched in aluminium and chromium in a Fe-24Cr-8Al-0.5Y steel. Reprinted with permission from [506].

4.3.1 Formation of nano-scaled oxides by interaction with gaseous atmospheres

An efficient methodology for manufacturing oxide-dispersion strengthened materials using AM technologies is the in-situ manufacturing by the active participation of oxygen-containing gas atmospheres in AM processes, allowing the dispersion of nano-scaled oxides without the addition of solid nanoparticles (Table 12). Small quantities of oxygen [321, 446, 507, 509, 510, 511, 512, 514, 515, 516, 517] or oxygen-containing gases, e.g., CO_2 [477], already allow the formation of nano-scaled oxides when added to inert gas atmospheres. Controlling the amount of oxygen introduced into the melt pool by the interaction of the active gas atmospheres with the surface of the highly turbulent melt pool in AM processes is challenging. As shown by Babu and coworkers, it depends not only on the partial pressure of the active component in the gas atmosphere, i.e., oxygen, but also on the dimensions, flow velocities as well as the solidification rate of the melt pool, which is typically governed by the process parameters selected. [518] While Sievert's law describes a direct proportionality between the concentration of a diatomic gas in a melt pool and its respective partial pressure in the surrounding gas atmosphere, the vicinity of a high-energy beam leads to the enforced incorporation of oxygen into the melt pool. [519] However, the underlying mechanism is not entirely understood. It may include the dissociation of gas molecules at the melt pools surface [506, 518] and the selective formation of oxide particles at the interface between melt and gas atmosphere and subsequent introduction into the melt pool by melt flows. (Fig. 21)

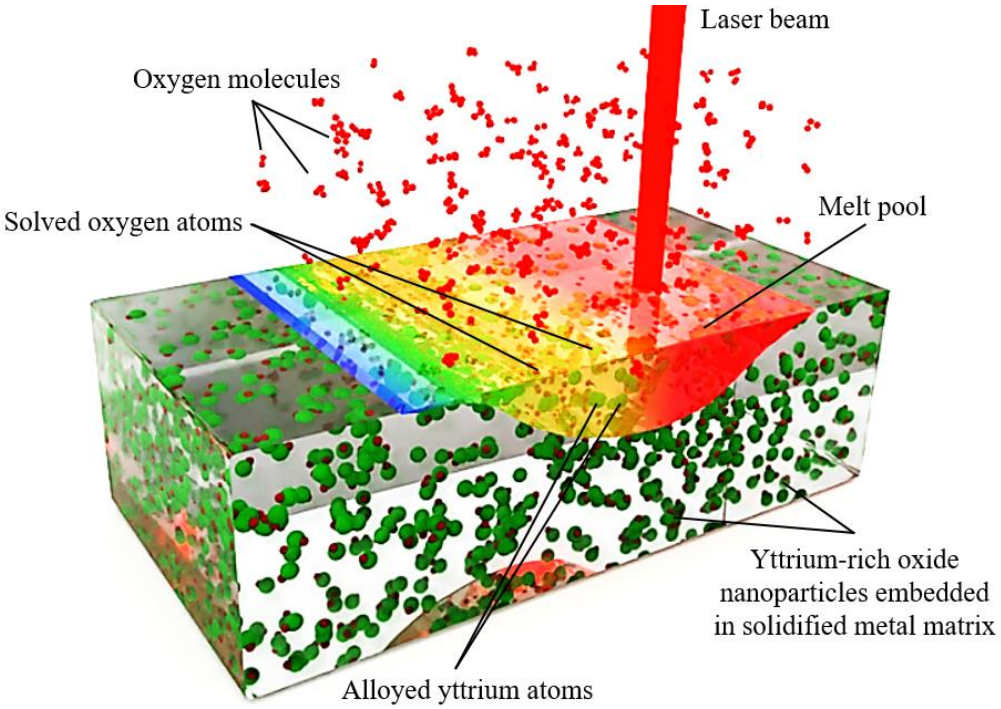

Fig. 21: Formation mechanism of oxide nanoparticles during AM in an oxygen-containing gas atmosphere including the dissociation of oxygen molecules (double red spheres) on the melt pool surface and solution of oxygen atoms (single red spheres) in the melt pool, reacting with solved yttrium atoms (green spheres) to form yttrium oxide (green and red spheres attached to each other) in the melt pool. The yttrium oxide is dispersed in the solidified metal matrix. This is a 3D depiction of the schematic shown in [506].

Severe oxide formation upon insufficient shielding of the melt pool [409, 484, 509] or contamination of the atmosphere [514, 520], may also lead to the undesired formation of nano-scaled dispersoids. However, the utility of atmospheric air [521] or nitrogen-containing atmospheres [522, 523, 524, 525] promotes the formation of nitrides in addition to oxides. (Table 12)

Table 12: Overview of ODS alloys manufactured by internal oxidation approaches using a reactive gaseous atmosphere during different AM processes with the oxide compound and oxide size formed in consolidated specimen.

Alloy	Process	Gas atmosphere	Oxide compound formed	Oxide size	Reference
PM2000	L-PBF	O_2 / CO_2	Ti-Al-O	< 100 nm	477
316L	L-PBF	Ar / 0.1 vol.% O_2	Si-O	> 100 nm	446
316L	L-PBF	n.r.	Mn-Si-Cr-O	60 – 100 nm	508
316L	L-PBF	Ar / 0.026 vol.% O_2	Mn-Cr-O	30 – 200 nm	509
316L	L-PBF	Ar / 50 – 1200 ppm O	Si-Cr-O	50 – 100 nm	510
316L	L-PBF	Ar / 0 – 1 vol.% O_2	Mn-Si-O	40 – 120 nm	370
Fe-15Cr-4.5Ni-4Cu-0.4Si-0.2Ti-0.15Y	L-PBF	Ar / 3500 ppm O	Y-Al-O, Ti-O	5 – 50 nm	514
Fe-15Cr-0.15Y-0.11Ti	L-PBF	1 vol.%; 5 vol.% O_2	Y-Ti-O	10 – 45 nm	321
Fe-15Cr-0.15Y-0.11Ti	L-PBF	Air	Y-Ti(-Cr)-O	20 – 50 nm	321
Fe-24Cr-8Al-0.5Y	L-PBF	Ar / 400 ppm O	Y-Al(-Cr)-O	10 – 100 nm	506
Fe-22Cr-5.1Al-0.5Ti-0.26Y	L-PBF	Ar / O	Y-(Al)-O	n.r.	526
17-4 PH	L-PBF	Ar / 500 ppm O	Mn-Si-O	50 nm	511
CoCrFeNiMn	L-PBF	Ar / 2000 ppm O	Mn-O	100 nm	512
W-Ta	L-PBF	Ar / 100 ppm O	Ta-O	~ 100 nm	517
Ni-20Cr-1Fe-0.5Y	L-PBF	Ar / < 0.35 vol.% O_2	Y-O	50 nm	527
Co-28Cr-9W-1.5Si	L-PBF	n.r.	Si-O	20 – 120 nm	528
Y-alloyed Ti alloy	EB-PBF	Vacuum / 7 ppm O	Y-O	50 – 250 nm	515
316L	L-DED	Air	Mn-Cr-O	400 nm	521
316L	L-DED	Air	n.r.	100 nm	507
316L	L-DED	Ar / 1000 ppm O	n.r.	300 – 500 nm	409
AISI 420	L-DED	Ar / 10^{-1}-10^{-5} atm O_2	Mn-Si-Cr-O	> 1000 nm	529
17-4 PH	L-DED	Air	Mn-Si-O	~ 500 nm	530, 531
X30Mn23	L-DED	Insufficient shielding	Mn-O	Slag layer formation	484
316L	WAAM	Insufficient shielding	Mn-Si-O	Slag layer formation	532

However it is observed, that nanoparticles formed by active gas atmospheres exhibit large sizes up to micrometer scale. This is considerably larger than nanoparticles formed by direct addition of nanoparticles to gas atomized powder particles and thus, may be attributed to the in-situ formation mechanism by exothermic oxidation reaction, posing a localized heat source, which may affect the melt pool behavior and facilitate coarsening of dispersed nanoparticles.

4.3.2 Formation of nano-scaled oxides by the introduction of solid oxidations agents

The introduction of oxygen into the melt pool for in-situ fabrication of ODS alloys can also be performed by the addition of solid oxide compounds, e.g., TiO_2 [98], V_2O_5 [533], Fe_2O_3 [534, 535], or Cr_2O_3 [536]. These oxide compounds decompose during the melting stage, liberating oxygen into the melt pool and subsequently forming oxide compounds with higher thermodynamical stability. This technique can be applied in fast solidifying manufacturing techniques like centrifugal casting [310, 537] or AM processes. [538, 539, 540] However, it must be considered that the metallic component of the oxidant is integrated into the matrix alloy as an additional alloying element and may alter the resulting mechanical properties of the ODS alloy. Thus, the approach of introducing solid oxidation agents for in-situ production of ODS materials in AM has not been explored in detailed studies.

5 Manufacturing of powder composites

5.1 Characterization of the educt micrometer-sized metal powder

Metallic powder material of the ferritic stainless steel is atomized by the process of Vacuum Inert Gas Atomization (VIGA) process using argon gas (Nanoval GmbH, Berlin, Germany). The chemical composition is given in Table 13, showing that the chemical composition of the received powder material is close to the nominal composition.

Table 13: Chemical composition of the gas atomized stainless steel powder material, determined by X-ray fluorescence spectroscopy (XRF).

	Fe	Cr	Al	Ti	Ni	Si	Cu	S	Zr
Unit	wt.%	wt.%	wt.%	wt.%	wt.%	ppm	ppm	ppm	ppm
Concentration	74.90	20.40	3.94	0.58	0.1	257	131	59.7	31.6
Stat. error (%)	0.05	0.09	0.80	0.73	1.91	12.7	7.76	15.70	14.00

The atomized powder material is sieved to two separate particle fractions (A and B) using analytical sieve analysis with mesh sizes of 45 µm and 90 µm, respectively. The powder fraction of < 45 µm (A) is used for L-PBF and HSLC processing, whereas the coarser powder fraction 45 – 90 µm (B) is processed via L-DED. In Fig. 22a,b, LOM and SEM images of powder fraction B after sieving are depicted showing a predominantly spherical morphology with few satellites attached to the powder particles. Cross-sections of the powder particles show the presence of occasional hollow powder particle structures (Fig. 22a), which are typical for gas atomization processes [541], but may result in higher porosities in printed parts. [542] Occasionally, irregular shaped powder particles are also observed (Fig. 22b). Correspondingly, LOM and SEM images of powder particles of fraction A are depicted in Fig. 22c,d.

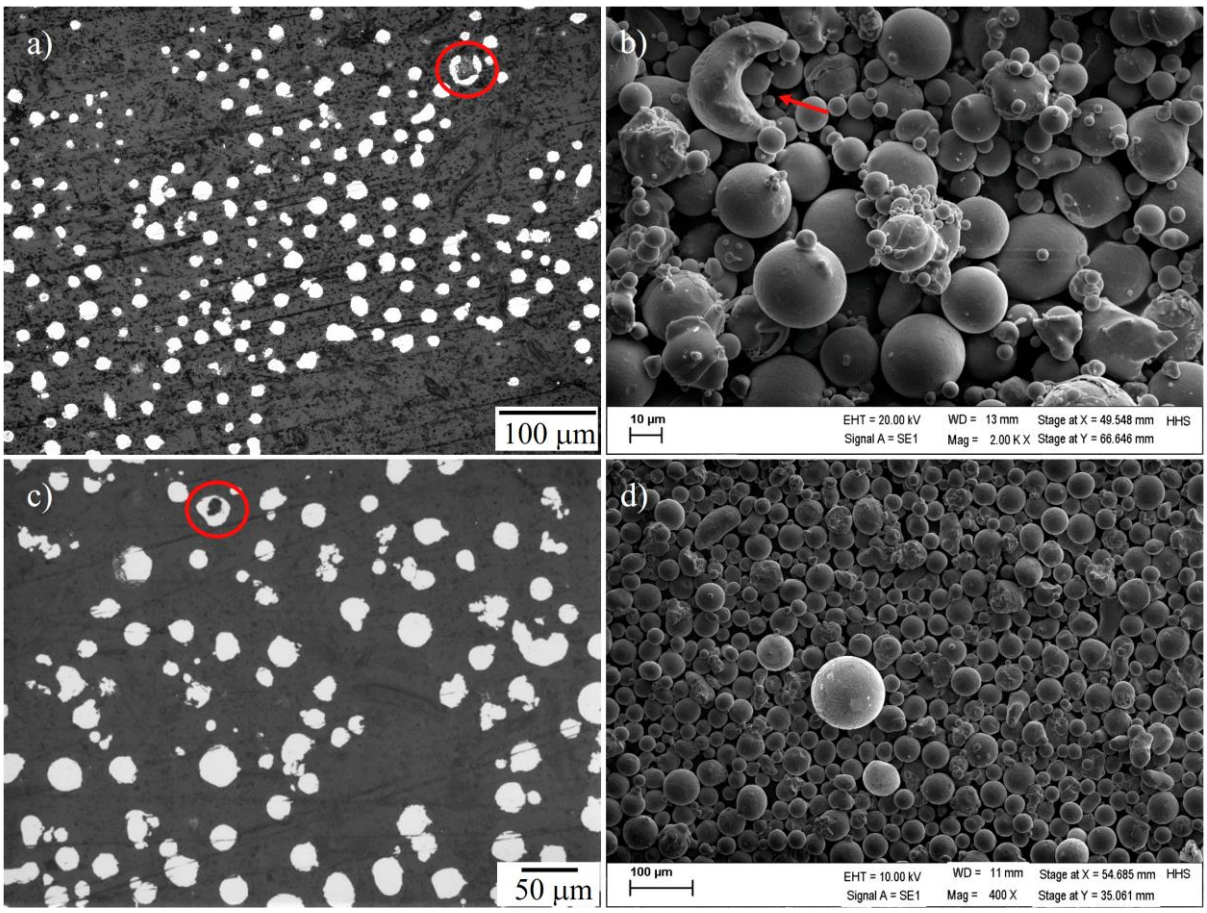

Fig. 22: a) LOM image of cross sections of powder particles (fraction B). b) Corresponding SEM image of powder particles of fraction B. c) LOM image of cross sections of powder particles (fraction A). d) Corresponding SEM image of powder particles of fraction A. Hollow particles are marked with circles and irregular shaped powder particles with red arrows.

In depth powder characterization is performed to capture the influence of further processing techniques on the powder properties. This includes the determination of the particles size distribution, represented by the percentiles d_{10}, d_{50} and d_{90}, the sphericity Ψ (often also referred as circularity [332]) and the flowability, represented by the avalanche angle α_A.

Particle size distribution and sphericity are determined using the Morphologi G3 (Malvern Panalytical, Malvern, UK) device measuring the size and shape of powder particles by static image analysis. The sphericity describes the deviation of the shape of a given object from a perfect sphere (Ψ=1) with identical volume and is calculated according to equation (5) [543]:

$$\Psi = \frac{4\pi A}{P^2} \qquad (5)$$

where A and P represent the perimeter of the projected object (here a single powder particle) determined by the static image analysis procedure.

The flowability is determined by a Revolution Powder Analyzer (RPA), where a tapped powder sample is rotated at a given speed in a drum [543]. The angle of repose α_A determines the rotation angle upon formation of a powder avalanche. An image of the RPA measurement of powder fraction A is shown in

Supplementary S1. UV-Vis measurements are conducted using a Silver-Nova Spectrometer (SI Scientific Instruments GmbH, Gilching bei München, Germany) and depicted in Supplementary S2. Results are depicted in Table 14.

Table 14: Gas atomized stainless steel powder material. Assessment of powder properties determined by particle size distribution measurement and RPA investigations for determination of the flowability.

Powder fraction	A	B
Particle size (sieved)	< 45 µm	45 – 90 µm
d_{10}	12.42 µm	19.95 µm
d_{50}	32.19 µm	56.69 µm
d_{90}	47.32 µm	88.10 µm
Sphericity Ψ	0.93	0.98
Flowability α_A	37.34° ± 0.04°	32.83° ± 0.07°

5.2 Nanometer-sized oxide powder material

Two commercial Y_2O_3 nanoparticle feedstocks are used to produce the ODS materials: Nanopowder 1 (NP1) provided by abcr GmbH (Karlsruhe, Germany) is used for production of composite powders via Mechanical Alloying in a ball milling process, described in detail in chapter 5.3. Nanopowder 2 (NP2) acquired from Sigma Aldrich/ Merck KGaA, (Darmstadt, Germany) is used for LSPC processing of composite powders, described in chapter 5.4.

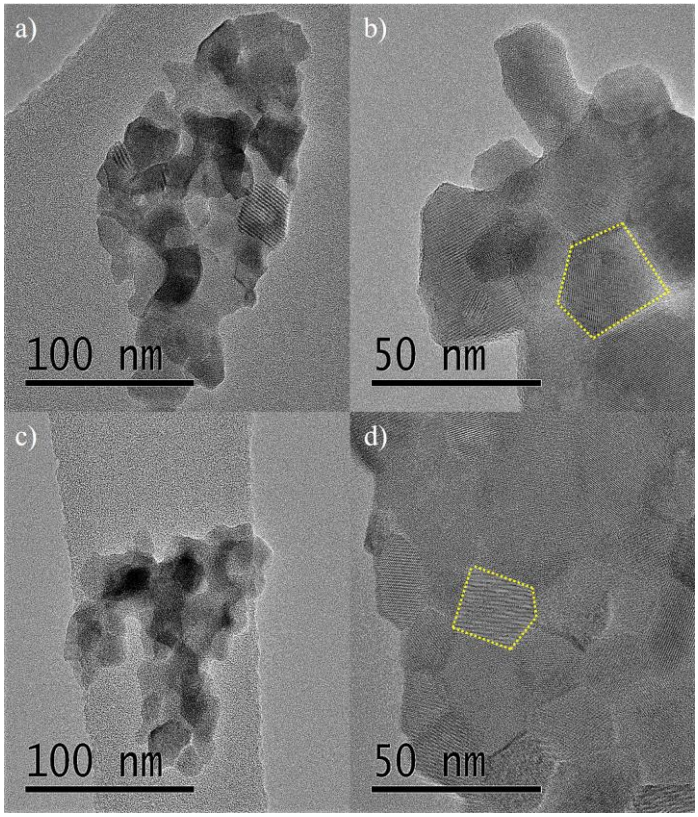

Fig. 23: BFTEM images of Y_2O_3 nanoparticles: a,b) NP1. c,d) NP2. Y_2O_3 crystallites are indicated by yellow dotted lines.

In Fig. 23 BFTEM images of both Y_2O_3 nanopowders are depicted, showing that both nanopowder materials have an approximate size of 100 nm and consist of aggregated Y_2O_3 crystallites. The crystallite size is determined indirectly via X-ray diffraction (XRD) measurements. Using Scherrer's equation (6) [544], which describes the inverse proportionality of peak width B and the crystallite size L, allows the approximation of the crystallite size.

Scherrer equation: $B(2\theta) = K \cdot \lambda / (L \cdot \cos\theta)$ (6)

Using the Scherrer equation, an average crystallite size L of approx. 15 nm is determined for the commercial Y_2O_3 powder material, which is consistent with observations from the BFTEM images (Fig. 23).

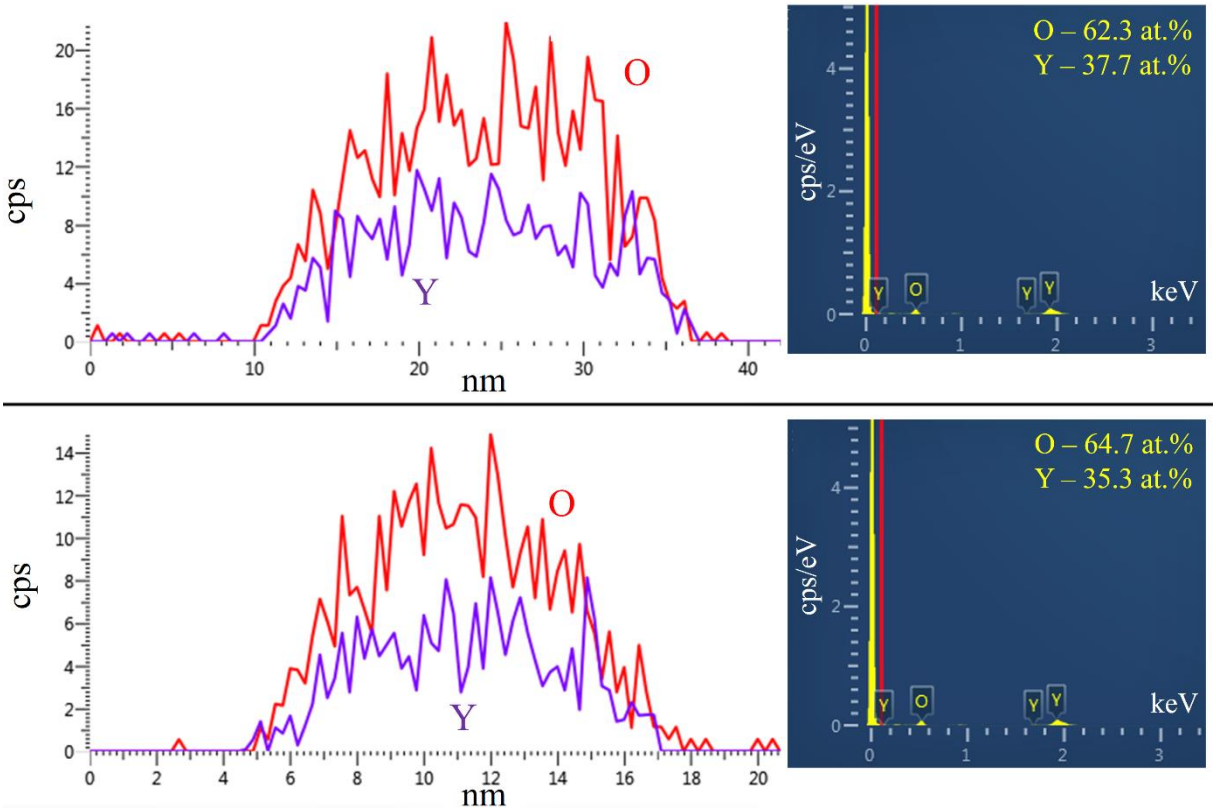

Fig. 24: EDS line scans of Y_2O_3 nanoparticles with EDS spectrum and quantification of the oxygen and yttrium content (in at.%) from point measurements: Upper panel: NP1. Lower panel: NP2.

The chemistry of the yttrium oxide nanoparticles is verified by EDS line scans and point measurements (Fig. 24), verifying that the powder material is pure Y_2O_3.

5.3 Composite powder manufacturing via Mechanical alloying (MA)

The mechanical alloying process is a widely established process for manufacturing of composite powder materials from micrometer-sized metallic powder and nano-scaled ceramic powder materials. The production of composite powder requires mechanical energy in order to achieve a solid bonding between metallic and ceramic powder components. The energy input into the powder material is largely determined by collision events of the grinding balls and the wall of the grinding container.

Macroscopically, the specific energy (E_i) introduced into the powder materials can be described assuming elastic impact processes according to (7): [545]

$$E_i = \frac{\sum_{j=1}^{n} SE_j \, \Delta SF_j}{m_p} t_M \qquad (7)$$

with SE_j as the energy per collision event in a time interval j, SF_j denoting the frequency of collision events in a time interval j, t_M the cumulative milling time and m_p the capacity of grinding container.

The frequency of the collision events SF_j depends approximately on the BPR and on the size of the grinding container used. Furthermore, the capacity per grinding container is not changed, so that the specific energy introduced is determined by the sum of the energies of all collision events and the cumulative grinding time.

$$\overline{SE_j} = \frac{v_j^2 m_1 m_2}{2(m_1+m_2)} \xrightarrow{m_1 = m_2 = m} \overline{SE_j} = \frac{v_j^2 m}{4} \qquad (8)$$

with v_j denoting the velocity of grinding balls and m_x the mass of grinding balls.

From equation (8) it can be deduced, that the specific energy introduced depends on the speed of the grinding balls, governed by the speeds of the main and planetary disks, their respective mass and the cumulative milling time. Thus, these process parameters are varied, while other process parameters are kept constant. (cf. Table 16)

Table 16: Overview of constant and varied process parameters of the mechanical alloying experiments.

Constant parameters	**Value**	**Varied parameters**	**Varied value range**
Milling time per cycle	20 min	Rotation speed (RS)	50 – 200 min^{-1}
Pause time per cycle	10 min	Number milling cycles	1 – 7
BPR	5	Grinding ball diameter	5; 10 mm

For the production of composite powders gas atomized (GA) Fe20Cr4.5Al0.5Ti (wt.%) and Y_2O_3 nanopowder (abcr GmbH, Karlsruhe, Germany) and the planetary mill "Pulverisette 4 Classic line" (Fritsch GmbH, Idar-Oberstein, Germany) is used (Fig. 24), capable of operating two individual grinding containers simultaneously. The grinding containers with a maximum capacity of 500 ml are made from abrasion-resistant yttrium-stabilized zirconium oxide (YSZ). The grinding balls used are made from YSZ with diameters of 5 mm and 10 mm, respectively.

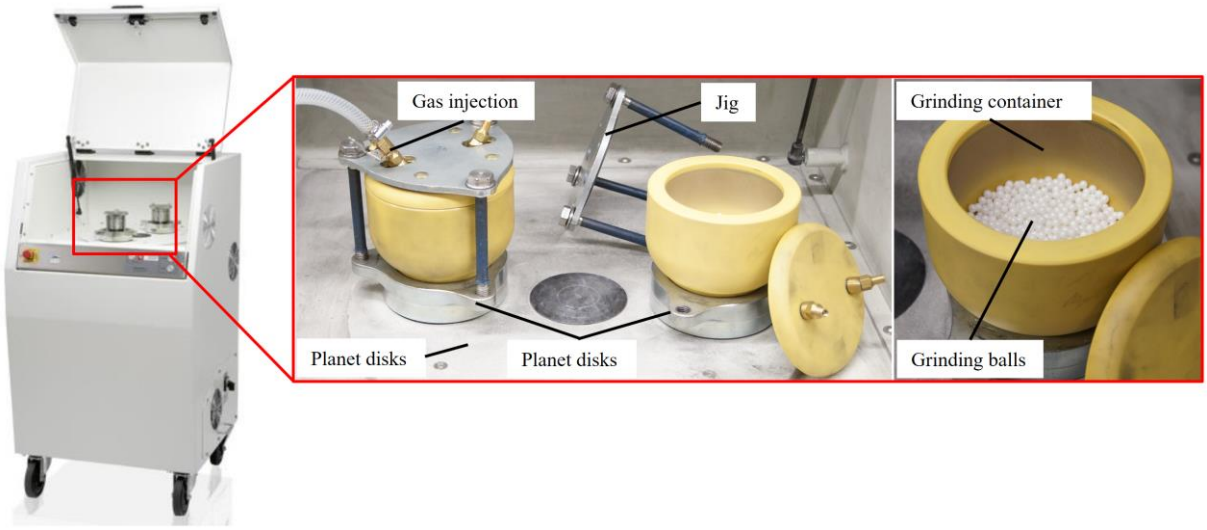

Fig. 24: Planetary mill "Pulverisette 4 classic line" with YSZ grinding containers and YSZ grinding balls (here: 5 mm diameter).

The speeds of the planetary disks located below the grinding containers and of the main disk can be adjusted independently of each other. A protective gas atmosphere of pure argon gas is established inside the grinding vessels by a valve system integrated into the lid of the grinding containers. According to equation 8 the grinding ball mass has a significant influence on the overall energy input in to the powder material. Since only grinding balls consisting of YSZ were available, grinding balls with diameters of m_1=5 mm and m_2=10 mm are used to determine the impact of the grinding ball mass on the final powder composite.

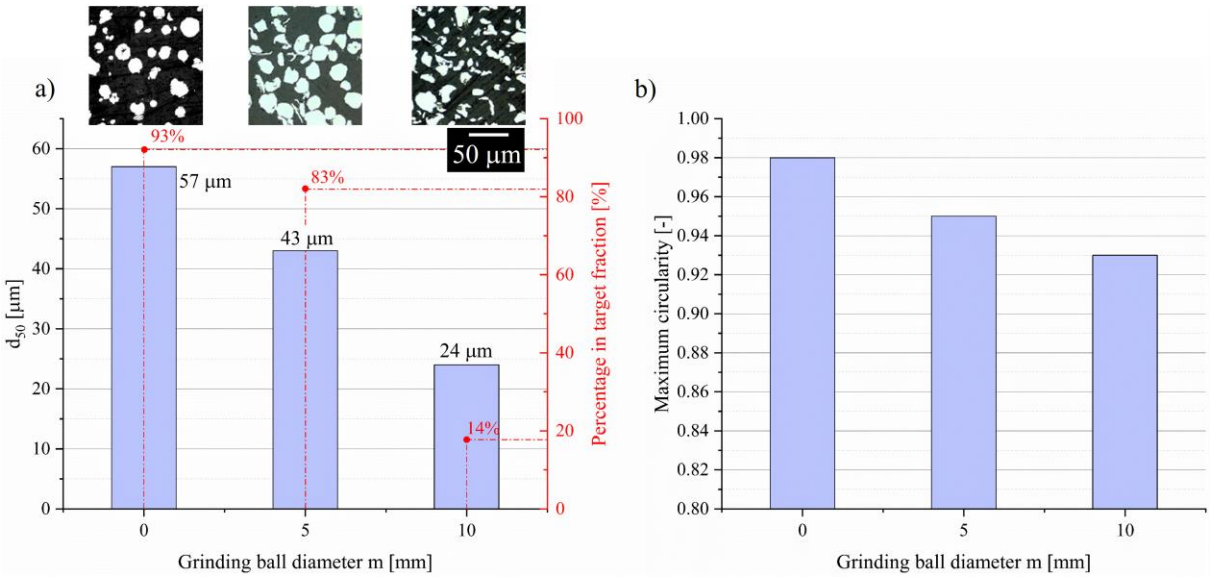

Fig 25: a) d_{50} value of mechanically alloyed (RS: 150 min^{-1}; t_M: 210 min) powder material from particle fraction A (45 – 90 µm) as a function of the grinding ball diameter ("0" corresponds to raw Fe20Cr4.5Al0.5Ti powder material) with corresponding LOM images of embedded powder particles. Additionally, the percentage of mechanically alloyed powder particles in the target particle distribution (45 – 90 µm) is indicated in red colour. b) Maximum circularity as a function of the used grinding ball diameter ("0" corresponds to raw Fe20Cr4.5Al0.5Ti powder material). Data is extracted from particle size and morphology measurements, depicted in Supplementary S3.

Whereas after mechanical alloying with small grinding balls (m_1=5 mm) the predominantly spherical particle morphology of the gas atomized powder material is retained and a large fraction (83%) of powder particles in the target particle size distribution (45 – 90 µm) is achieved. On the contrary, the utilization of larger grinding balls (m_2=10 mm) results in strong deformation, indicated by lower maximum circularity (Fig. 25b), and fracturing of the powder particles, as evident from the superimposed LOM images (Fig. 25a) and reflected by drastically decrease d_{50} values compared to raw powder material. Consequently, a reduced flowability of the resulting composite powder material can be expected. The strong deformation is due to the particularly high collision energies caused by increasing the grinding ball mass. By using grinding balls with a diameter of 5 mm, the predominantly spherical particle morphology of the starting powder material can be largely retained, so that these are used in the following.

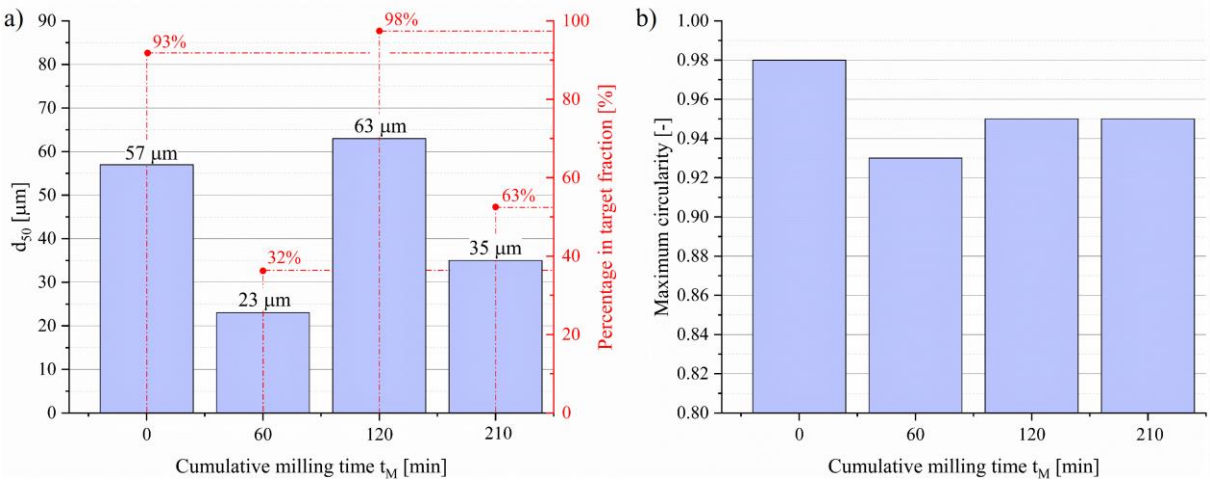

Fig. 26: a) d_{50} value of mechanically alloyed (m_1= 5 mm; RS: 150 min^{-1}) powder material from particle fraction A (45 – 90 µm) as a function of the cumulative milling time t_M ("0" corresponds to raw Fe20Cr4.5Al0.5Ti powder material). Additionally, the percentage of mechanically alloyed powder particles in the target particle distribution (45 – 90 µm) is indicated in red colour. b) Maximum circularity as a function of the cumulative milling time ("0" corresponds to raw Fe20Cr4.5Al0.5Ti powder material). Data is extracted from particle size and morphology measurements, depicted in Supplementary S4.

According to equation 8, the energy input into the composite powder material is governed by the number of collision events, in addition to the variation of the grinding conditions (rotational speed of the main and planetary discs and the diameter or mass of the grinding balls used). Consequently, by increasing the number of grinding cycles and cumulative milling time, the overall energy input into the powder material is increased. The results from the particle size distribution (Fig. 26a) indicate, that short milling times (60 min) are predominantly characterized by fracture of the stainless steel powder particles, as a high number of fine particles is formed, indicated by a low d_{50} value, with simultaneous decrease of the percentage of powder particles in the target fraction of 45 – 90 µm. Prolonged milling, i.e. by performing additional milling cycles, the fracturing processes are believed to be gradually replaced by cold-welding processes, leading to a progressing reduction of the fine particles' amount and simultaneous increase of the d_{50} value and the target fraction forming an equilibrium. The average collision energy is not

influenced here, so that strong deformation or fracturing of the powder material, which is observed with larger grinding ball diameters (Fig. 25a), can be limited. Accordingly, only moderate deformations of the powder particles are found, which is also expressed in high circularity of the powder material (Fig. 26b). Fig. 27 shows the influence of different rotational speeds (50, 100, 150 and 200 min^{-1}) on the resulting particle size distribution of the composite powder material after three grinding cycles (t_M = 120 min) using small grinding balls (5 mm).

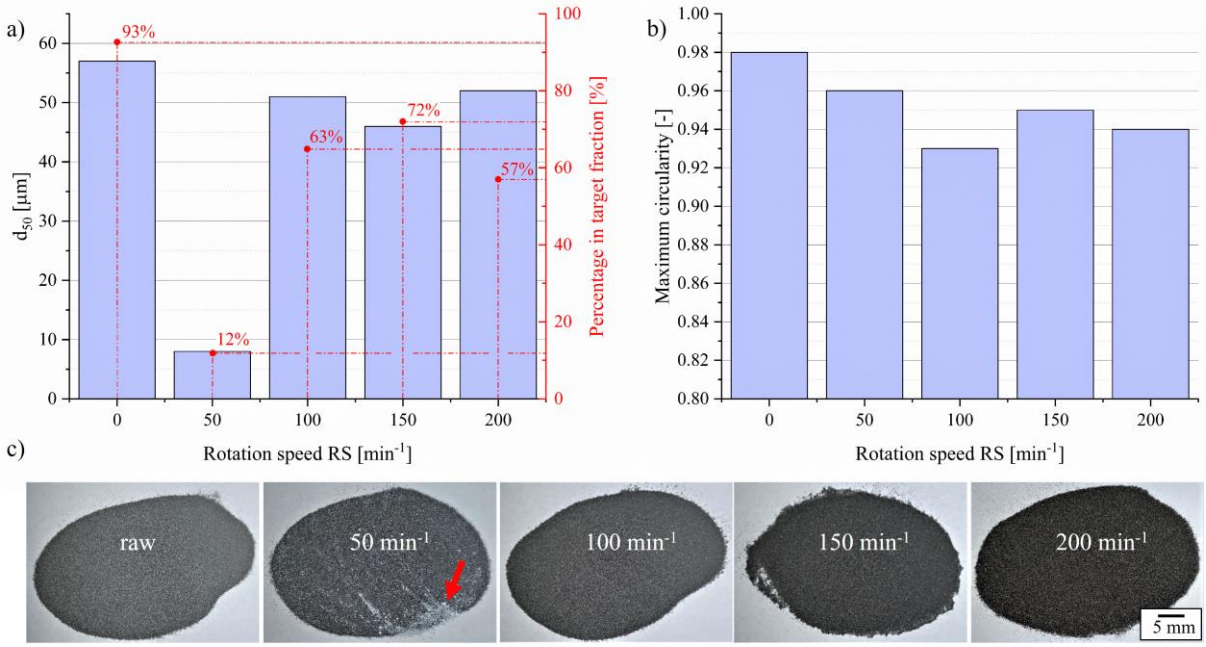

Fig. 27: a) d_{50} value of mechanically alloyed (m_1= 5 mm; t_M: 210 min) powder material from particle fraction A (45 – 90 µm) as a function of the rotation speed RS ("0" corresponds to raw Fe20Cr4.5Al0.5Ti powder material). Additionally, the percentage of mechanically alloyed powder particles in the target particle distribution (45 – 90 µm) is indicated in red colour. b) Maximum circularity as a function of the rotation speed (RS) ("0" corresponds to raw Fe20Cr4.5Al0.5Ti powder material). Data is extracted from particle size and morphology measurements, depicted in Supplementary S5. c) Photographic images of the gas atomized stainless steel powder ("raw") and composite powders after mechanical alloying procedure at different rotation speeds.

Irrespective of the used rotational speeds, a reduction of the particle fraction of the target fraction (45-90 µm) compared to the gas atomized powder material is observed (Fig. 27a). While a reduction of the finer particle fractions is additionally detected at medium and high rotation speeds, a massive increase of the fine fraction is detected at low rotation speeds, which is indicated by lower d_{50} values of the manufactured powder materials. Moreover, low rotation speeds result in metallic and oxide particles existing next to each other without formation of a composite powder, as evident from photographic images of the manufactured powder composites (Fig. 27c). This may also explain the remarkable drop of the d_{50} value at low rotation speeds (50 min^{-1}) as the used optical measuring system used is not capable to distinguish between ceramic and metallic powder particles. Thus, oxide nanoparticle agglomerates are falsely counted as powder particles. The utilization of medium (100 min^{-1}) or high rotation speeds (200 min^{-1}) is characterized by a high percentage of powder particles in the target grain fraction

indicating an equilibrium state of both fracturing processes of large powder particles and cold welding processes of small powder particles. However, homogeneous composite powder materials can be achieved for all tested rotation speeds between 100 and 200 min^{-1}. Increasing the rotational speed during MA reduces the particle circularity and consequently the flowability of the composite powder material (Fig.27b). In particular, high rotational speeds favour stronger deformation of the powder particles, which is attributed to the higher kinetic energy of the grinding balls and the consequently larger specific energy introduced into the powder particles on impact. The deformation can be detected quantitatively by determining the circularity and qualitatively by SEM images (SE mode) of the powder particles (Fig. 28).

Table 17: Process parameters used for mechanical alloying (MA) of ODS powder composites.

Milling time per cycle	20 min	Rotation speed (RS)	100 min^{-1}
Pause time per cycle	10 min	Number milling cycles	4
BPR	5	Grinding ball diameter	5 mm

Based on the experiments, the process parameter set shown in Table 17 is used for composite powder production. The developed mechanical alloying process using initial stainless steel powder with a particle size distribution of 45 – 90 µm is transferred to finer gas atomized powder material of fraction A (< 45 µm), intended for L-PBF and HSLC processing. LOM and SEM images (SE-mode) of mechanically alloyed composite powder particles for powder fraction A (Fig. 28a,b) and fraction B (Fig. 28c,d) are depicted in Fig. 28.

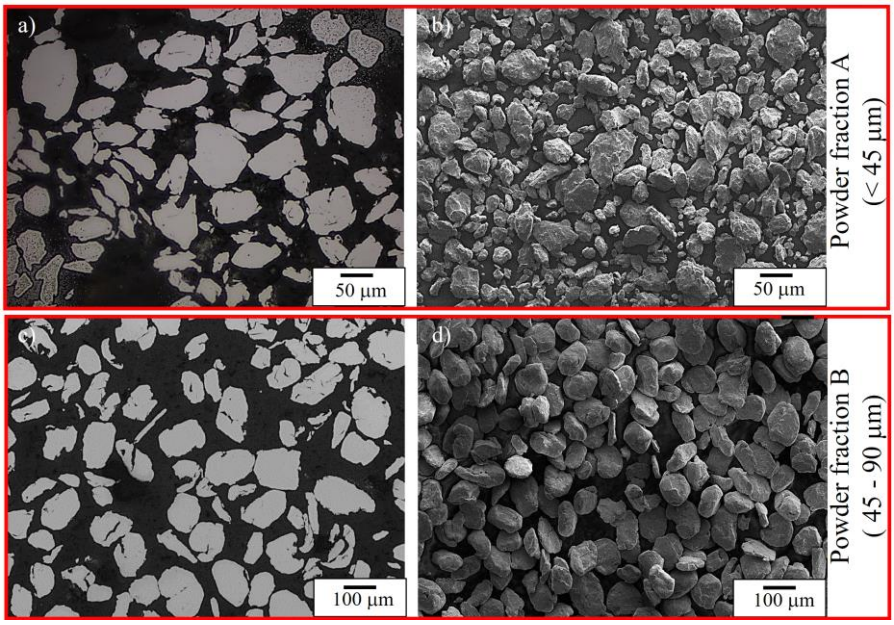

Fig. 28: a) LOM image of MA manufactured powder material (cross section) of the powder fraction A (< 45 µm). b) SEM image (SE-mode) of MA-manufactured powder material of the powder fraction A (< 45 µm). c) LOM image of MA-manufactured powder material (cross section) of the powder fraction B (45 – 90 µm). b) SEM image (SE-mode) of MA-manufactured powder material of the fraction B (45 – 90 µm).

In Table 18 the physical powder properties including the particle size distribution, the morphology represented by the circularity Ψ and the resulting flowability represented by the angle of repose α_A are summarized. Results from optical absorption measurement from UV-Vis spectrometry are shown in Supplementary S2, showing superior absorption for the laser wavelengths used in L-DED, HSLC and L-PBF processing compared to raw gas atomized stainless steel powder material and LSPC-generated powder material. The reason for the behaviour is presumably referred to the massive deformation of the powder particles during MA, as evident from Fig. 28. The high deformation of the powder particles may also result in the reduced flowability of the MA powder material, determined by flowability measurements using a Revolution Powder Analyzer (RPA), shown in the Supplementary S1.

Table 18: Overview of the physical powder properties of mechanically alloyed powder in fraction A and B.

Powder fraction	A	B
Particle size (sieved)	< 45 µm	45 – 90 µm
d_{10}	9.21 µm	59.09 µm
d_{50}	22.51 µm	72.57 µm
d_{90}	42.88 µm	88.91 µm
Max. Circularity Ψ	0.920 ± 0.12	0.953 ± 0.081
Flowability α_A	42.4° ± 0.11°	40.9° ± 0.06°

5.4 Composite powder manufacturing by Laser Synthesis and Processing of Colloids (LSPC)

Contains content from the following publication:

Depositing laser-generated nanoparticles on powders for additive manufacturing of oxide dispersed strengthened alloy parts via laser metal deposition

R. Streubel[a], M. B. Wilms[b], C. Doñate-Buendia[a], A. Weisheit[a], S. Barcikowski[a], J. H. Schleifenbaum[b], B. Gökce[a,*]

[a]Technical Chemistry I and Center for Nanointegration Duisburg-Essen (CENIDE), University of Duisburg-Essen, 45141 Essen, Germany
[b]Chair for Digital Additive Production, RWTH Aachen University & Fraunhofer Institute for Laser Technology, 52074 Aachen, Germany

Article Information

Article history:
Received 19 January 2018
Accepted 7 February 2018
Available online 6 March 2018

DOI: 10.7567/JJAP.57.040310
Japanese Journal of Applied Physics

**Corresponding author*
bilal.goekce@uni-due.de

Abstract

We present a novel route for the adsorption of pulsed laser-dispersed nanoparticles onto metal powders in aqueous solution without using any binders or surfactants. By electrostatic interaction, we deposit Y_2O_3 nanoparticles onto iron–chromium based powders and obtain a high dispersion of nano-sized particles on the metallic powders. Within the additively manufactured component, we show that the particle spacing of the oxide inclusion can be adjusted by the initial mass fraction of the adsorbed Y_2O_3 particles on the micropowder. Thus, our procedure constitutes a robust route for additive manufacturing of oxide dispersion-strengthened alloys via oxide nanoparticles supported on steel micropowders.

Own contribution: Sample preparation, contributing to writing and editing of the original draft and revised manuscript.

The production of composite powder materials by the Laser Synthesis and Processing of Colloids (LSPC) process is performed for both powder fractions A (< 45 µm) and B (45 – 90 µm). Commercial Y_2O_3 (Sigma Aldrich, St. Louis, MO, USA) nanopowder (NP2) is dispersed by ultrasonification for 30 min in deionized water. The nanoparticle-decoration, which is also referred to as “supporting”, is achieved by stirring the nanoparticle colloid with the stainless steel powder (Fe20Cr4.5Al0.5Ti (wt.%)) for 120 min in a pH-controlled environment. To achieve different mass concentrations of Y_2O_3 on the stainless steel powder particles, the pH value of the suspension is shifted at the beginning of the dispersion step by addition of either NaOH solution (for higher pH values) or HCl solution (for lower pH values). Due to the high charge and the resulting repulsive forces [546] of the Y_2O_3 nanoparticles at high pH values, only a small amount of nanoparticles can be absorbed by the stainless steel powder as exemplary shown for a pH of 9.5 (Fig. 29a). The superimposed photographic images depict the mixed suspensions where the supernatant (aqueous solution) still contains nanoparticles as indicated by the darker colour and thus higher absorption ratio in the UV-Vis extinction spectroscopy measurement, performed for the whole spectral range (200–1000 nm) (Fig. 29b). In contrast, almost all of the

nanoparticles are fixed on the powder particle as indicated by the clear supernatant for the suspension at a pH of 7 (Fig. 29a). Hence, the y-axis of Fig. 29a shows the degree of colloidal nanoparticles that are not deposited on the stainless steel powder. The pH-dependence of the supernatants' absorption ratio in the UV-Vis is given by the red line and is further referred as "absorption curve" (Fig. 29b). From Fig. 29c it becomes also evident, that the fraction of adsorbed oxide nanoparticles can be further increased by a laser fragmentation ("Laser dispersed") of the oxide nanoparticles prior to supporting onto the stainless steel powder particles. The laser fragmentation will be discussed in the following chapter (chapter 5.4.1). [361]

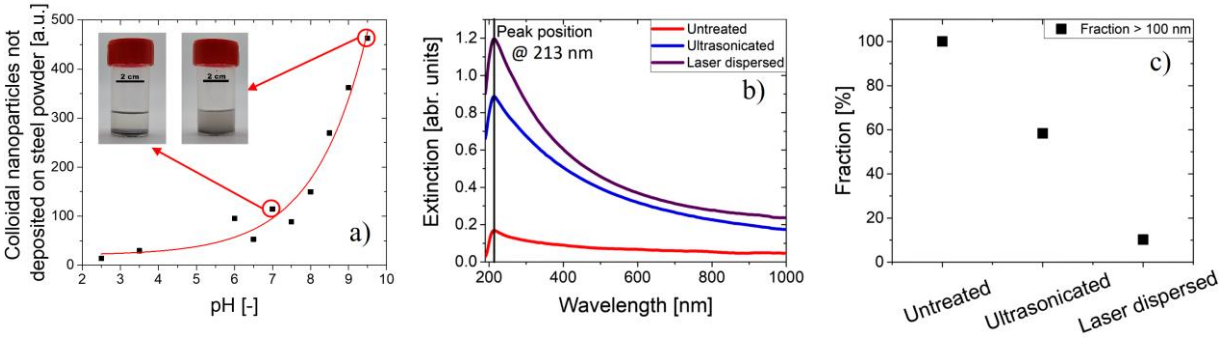

Fig. 29: a) The diagram indicates the efficiency of the supporting process by showing the degree of colloidal nanoparticles that are not deposited on the stainless steel powder. This data is extracted from the area integral of the UV–Vis spectra (integrated extinction) of the supernatant for different pH values. Lower values indicate greater adsorption efficiency. [361] b) Exemplary UV-Vis extinction spectra for untreated, ultrasonificated and laser fragmented nanoparticles. (Nanoparticle fragmentation will be discussed in the following chapter). [450] c) Measurement of the fraction of Y_2O_3 nanoparticles with hydrodynamic diameters >100 nm is performed by Dynamic Light Scattering (DLS). [450]

The absorption curve clearly shows an exponential trend. Accordingly, by lowering the pH value, the presence of nanoparticles in the supernatant is drastically decreased, and hence the supporting efficiency is increased. The isoelectric point (IEP) for Y_2O_3 is at a pH value of 7.5 (Supplementary S6) [547], whereas the IEP of stainless steel lies at pH 3 [548]. Hence, in the range of pH 3–7.5, the steel powder is negatively charged, and the Y_2O_3 is positively charged leading to an electrostatic or dielectrophoretic deposition. [549] Above pH 7.5, the Y_2O_3 nanoparticles, as well as the micrometer-sized metal particles, are negatively charged. Here, adsorption of oxide nanoparticles onto stainless steel microparticles is only diffusion-controlled, whereas a higher pH-value leads to a higher surface potential of the particle, which makes the adsorption process less efficient. At the IEP of Y_2O_3, the Y_2O_3 nanoparticles lose their electrostatic charge and adsorb on the surface of the microparticles by a sedimentation-driven co-deposition process leading to agglomeration and multilayers of nanoparticles. [361] After colloidal mixing, the powder sediments and the supernatant are removed. The composite powder material was obtained after drying the sludge in an oven for 2 days at 50°C. Prolonged drying procedures and higher drying temperatures of the sludge do not result is significant relative mass loss, as evident from measurements, shown in the Supplementary S7. In Fig. 30, SEM images (SE-mode) of raw stainless

steel and Y_2O_3 decorated powder particles (0.3 wt.% loading) are depicted, showing the homogeneous decoration of the powder stainless steel powder particles with Y_2O_3 nanoparticles. [16]

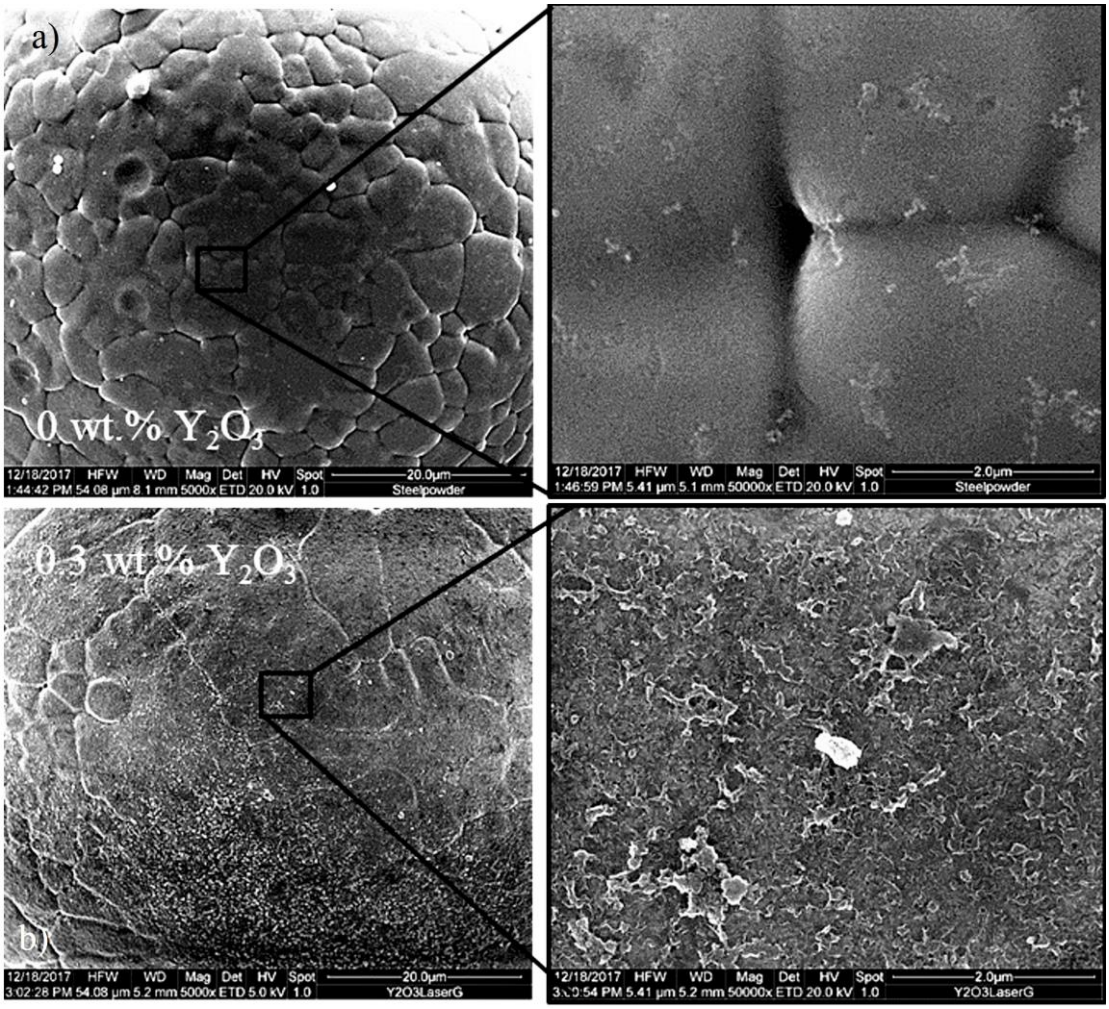

Fig. 30: SEM images (SE-mode) of the stainless steel micropowders with different loadings of Y_2O_3 nanoparticles: a) Gas atomized stainless steel powder particle. b) Decorated stainless steel powder particle with a loading of approx. 0.3 wt.% Y_2O_3 nanoparticles. [361]

Elemental analysis of the decorated powder materials by X-ray fluorescence analysis (XRF) show the efficiency of the decoration process lays between 20 and 90% for the materials used (Table 19). SEM-EDS measurements confirm, that no oxidation of the stainless steel powder has occurred during its transient immersion time in water, as evident from measurements shown in the Supplementary S8. [16]

Table 19: Elemental composition of Y_2O_3 decorated stainless steel powder material (manufactured by LSPC), determined by XRF.

	Fe	Cr	Al	Ti	Ni	Y	Si	Cu	S	Zr
Unit	wt.%	wt.%	wt.%	wt.%	wt.%	wt.%	ppm	ppm	ppm	ppm
Concentration	76.13	19.85	3.31	0.56	0.07	0.28	200	141	43.1	32.5
Stat. error (%)	0.05	0.19	0.83	0.7	2.31	3.55	14.3	6.84	12.44	13.65

The physical powder properties, including d_{10}, d_{50} and d_{90} values from the particle size distribution, circularity Ψ, flowability are summarized in Table 20. Results from optical absorption measurement from UV-Vis spectrometry are shown in Supplementary S2, showing lower absorption for the laser wavelengths used in L-PBF, L-DED and HSLC compared to MA-generated composite powder material, presumably due to the lower degree of particle deformation, as evident from Fig. 30. Moreover, the predominantly spherical morphology of LSPC processed powder particles allows flowabilities close to the GA powder material (Supplementary S1). However, the absorption is slightly higher than the raw GA powder material, proving that the deposition of oxide nanoparticles on the spherical stainless steel powder particles affect the absorption properties.

Table 20: Physical powder properties of powder composites manufactured by LSPC technique.

Powder fraction	A	B
Particle size (sieved)	< 45 µm	45 – 90 µm
d_{10}	11.95 µm	43.25 µm
d_{50}	22.53 µm	77.51 µm
d_{90}	33.49 µm	93.14 µm
Max. Circularity Ψ	0.930 ± 0.077	0.953 ± 0.058
Flowability α_A	34.83° ± 0.07°	33.17° ± 0.03°

5.4.1 Laser-based nanoparticle fragmentation process

As pointed out in chapter 3, the agglomeration of nanoparticles during additive manufacturing is considered an unavoidable mechanism, deteriorating the mechanical performance of printed oxide-dispersion strengthened materials. However, one way to compensate the agglomeration of nanoparticles during the melting stage is the utility of extremely small nanoparticles (< 10 nm). The laser-based process of nanoparticle fragmentation [13, 16, 361] is capable of significantly reduce the size of commercially available nanoparticles by ultra-short pulsed (USP) laser irradiation. The nanoparticle fragmentation process of commercial Y_2O_3 nano-sized powder material is performed in an aqueous solution with highly dispersed oxide nanoparticles. Prior to USP-laser irradiation, the aqueous solution with Y_2O_3 nanoparticles is ultrasonificated for 30 min to disrupt spontaneously formed nanoparticle agglomerates in the aqueous solution, with an ultrasonicator UP200S (Hielscher Ultrasonics GmbH, Teltow, Germany). In order to avoid prompt re-agglomeration a pH value of 9.5 and an environment with ionic strength of pH 0.1 mmol/L is established before entering the passage reactor, which is designed in a flow jet configuration (Fig. 31). In total, five passage cycles are performed using a 20 W laser (PX400-3-GH, EdgeWave GmbH, Würselen, Germany) working at a wavelength 355 nm (third harmonic of Nd:YAG laser), a pulse duration of 10 picoseconds and repetition rate of 80 kHz, focused by a cylindrical lens (100 mm focal length).

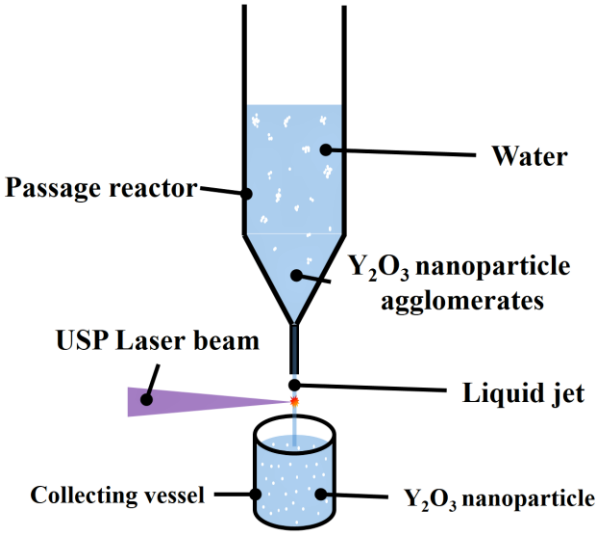

Fig. 31: Schematic depiction of the passage reactor. [13]

The fragmentation of the commercial Y_2O_3 nanopowder results in a typical bimodal nanoparticle population. As evident from Fig. 32a,b, heavily agglomerated educt oxide nanoparticles with a mean diameter of 27.5 ± 7.7 nm are de-agglomerated and a second mode of ultra-fine nanoparticles with a mean size of 3.2 ± 0.8 nm is generated, which is also evident from TEM-images (Fig. 32c,d).

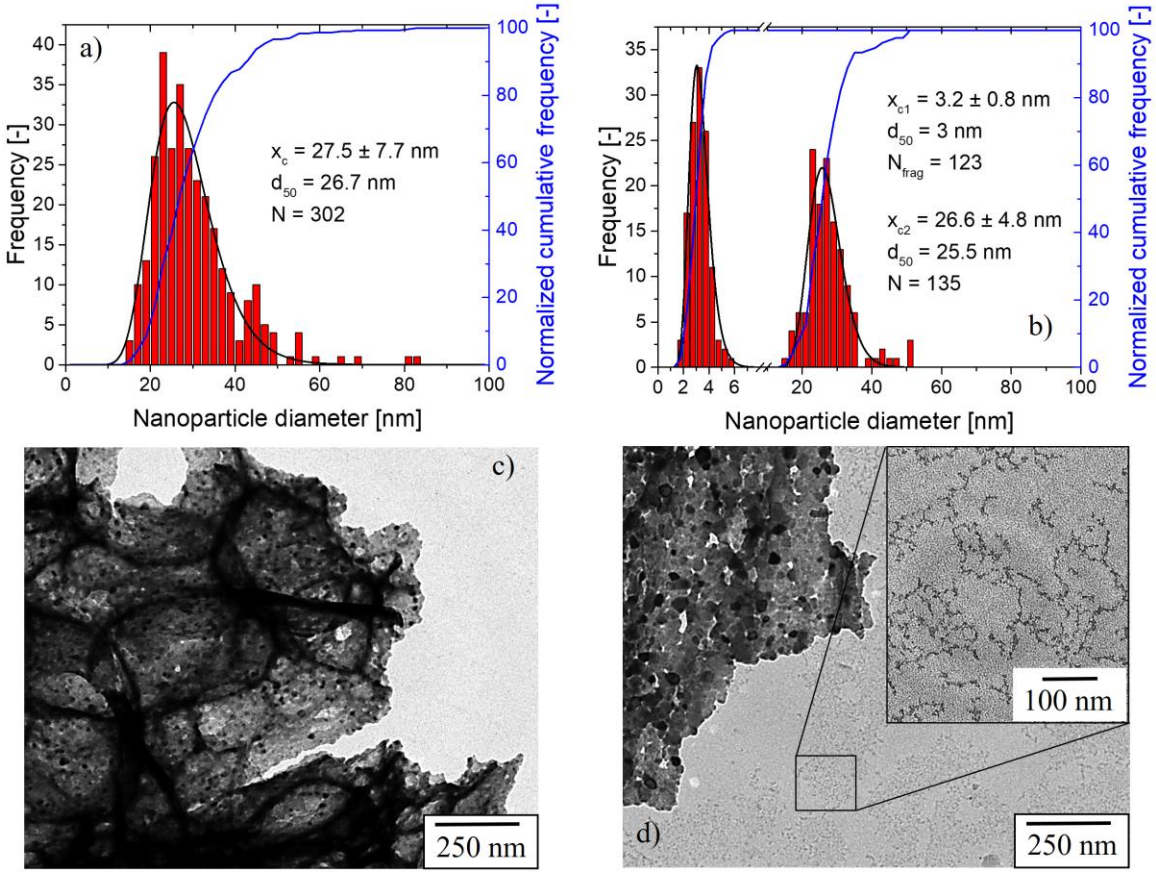

Fig. 32: Size histogram for Y_2O_3 nanoparticles before (a) and after (b) USP laser irradiation. A log-normal distribution is used as a fitting function. x_c denotes the centre of the function, N the number of counts and d_{50} the median diameter. c) and d) show corresponding TEM images of nanoparticles before (c) and after (d) laser fragmentation. Inset in (d) shows a magnification of the marked area that contains the small oxide nanoparticle fraction of approx. 3 nm. [361]

Y_2O_3 nanopowders, exposed to laser fragmentation are referred as laser irradiated nanoparticles. A measureable effect of stainless steel micropowders decorated with laser irradiated nanoparticles on powder properties (i.e. flowability) could not be detected.

6 Additive Manufacturing

6.1 Machine equipment for L-DED and L-PBF processing

6.1.1 L-DED machines

The used DED-machines are depicted schematically in Fig. 33 and Fig 34. L-DED machine 1 (Fig. 33) consists of a five-axis gantry system (SchulerHeld Lasertechnik GmbH & Co. KG, Dietzenbach, Germany) and is equipped with three translatory and two rotatory axes, controlled by a NC-based a Sinumeric 840D control software (Siemens AG, München, Germany). A fiber-coupled diode laser LDM 3000-60 (Laserline GmbH, Mülheim-Kärlich, Germany) with a maximum output power of 3 kW and a beam parameter product (BPP) of 60 mm·mrad. The laser system emits laser radiation with a specific wavelength of 976 nm, which is guided to the processing head by means of an optical fiber (HIGHYAG Lasertechnologie GmbH, Kleinmachnow, Germany) with a core diameter of 600 µm (NA = 0.2). The processing head consists of a collimating lens (f_{col} = 65 mm) and a focusing lens (f_{foc} = 210 mm), generating a circular TopHat-profiled focal spot with a diameter of 1.8 mm in the focal plane. The corresponding laser beam caustic is depicted in the Supplementary S9. For visual process observation a dichroitic glass, transparent for 976 nm, is integrated between the collimating and focusing lens, extracting light emitted from the melt pool and guided to a CMOS (Complementary metal-oxide-semiconductor) camera. Powder material is fed via a Twin-10C disc-based powder feeding system (OC Oerlikon AG, Pfäffikon, Switzerland), conveying powder material pneumatically with Argon gas via the diffusor unit into a continuous coaxial powder nozzle (type: D40, Fraunhofer ILT, Aachen, Germany). Powder material is focused by the cone-shaped powder nozzle at a working distance of 7 mm below the nozzle tip. The shielding of the molten bath formed during the process from atmospheric oxidation is ensured by a local inert gas atmosphere (Ar) provided by the powder nozzle.

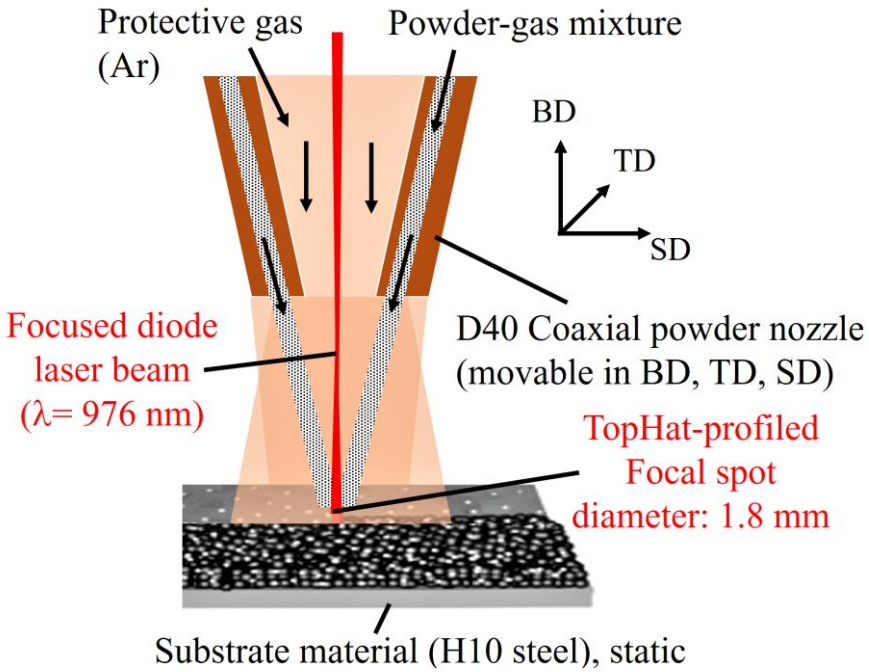

Fig. 33: Schematic depiction of the L-DED machine 1 setup, used for L-DED processing with a beam diameter of 1.8 mm. A photographic depiction is shown in Supplementary S10.

A three-axis handling system (Fig. 34) from Schuler Held Lasertechnik GmbH & Co. KG (SchulerHeld Lasertechnik GmbH & Co. KG, Dietzenbach, Germany) is used to create a smaller beam diameter of 0.6 mm (L-DED machine 2). The movement of the axis is controlled by NC using a MTX software (Bosch Rexroth AG, Stuttgart, Germany). The used laser system is a fiber-coupled diode laser system LDF 2000-30 (Laserline GmbH, Mülheim-Kärlich, Germany), emitting laser radiation (BPP: 30 mm·mrad) simultaneously with wavelengths of 1025 nm and 1064 nm up to a maximum output power of 2 kW. The emitted laser radiation is guided to the processing head via an optical fiber (HIGHYAG Lasertechnologie GmbH, Kleinmachnow, Germany) with a core diameter of 600 µm (NA = 0.2). The processing head is based on a processing optic "OTS2" (Laserline GmbH, Mülheim-Kärlich, Germany), including a collimation lens (f_{col} = 200 mm) and a focusing lens (f_{foc} = 200 mm), creating a TopHat profiled circular focal spots of 0.6 mm with homogeneous intensity distribution. The laser beam caustic is depicted in the Supplementary S11. Analogous to L-DED machine 1, a visual process monitoring system as well as a system for local shielding gas shielding with the inert gas argon are integrated. In addition, a powder nozzle of the same design as on L-DED machine 1 is used. The powder feeding system is also a disc-based powder conveying system PF 2/2 (GTV Verschleißschutz GmbH, Luckenbach, Germany). The corresponding calibration curve showing the correlation between the rotation speed of the disc and the resulting powder mass is depicted in the Supplementary S12.

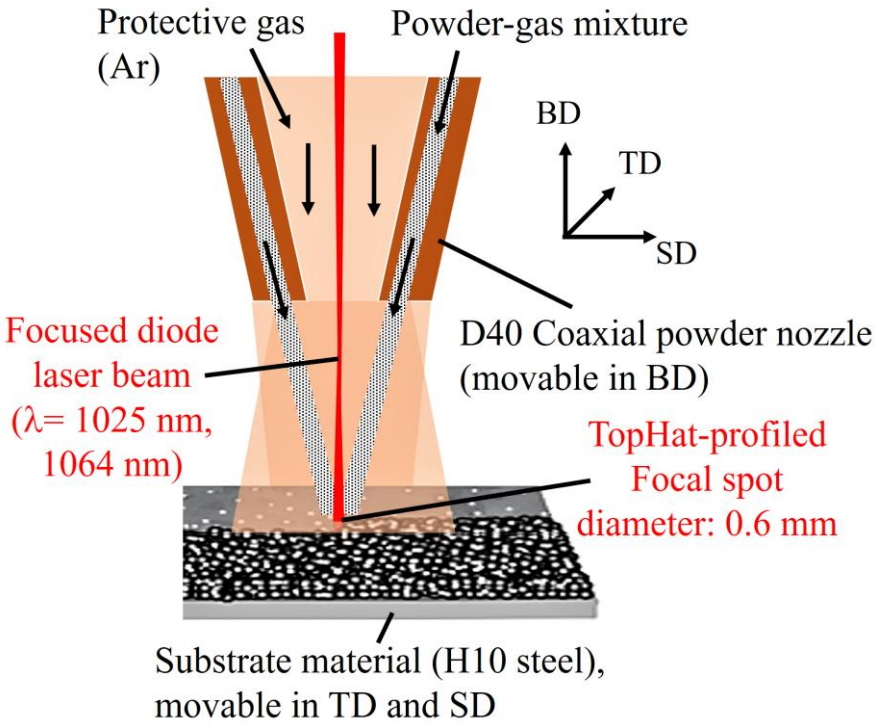

Fig.34: Schematic depiction of the L-DED machine 2 setup, used for L-DED processing with a beam diameter of 0.6 mm. A photographic depiction is shown in Supplementary S13.

The laser power calibration curve showing the correlation between the set voltage and the emitted laser powder (after leaving the optical alignment) is depicted in the Supplementary S14.

6.1.2 L-PBF machine

A laboratory L-PBF machine AconityMIDI (Aconity3D GmbH, Herzogenrath, Germany) is used for L-PBF processing of the composite powders. (Fig. 35). The machine is characterized by a circular build platform ($d_{platform}$= 170 mm), which can be reduced to 55 mm. Substrate preheating up to 1200°C is enabled by an integrated inductive heating system placed underneath the build platform. Both the build platform and the powder reservoir can be individually moved via vertically oriented axes. The recoating system consists of a crosshead mounted on two parallel linear axes, which is equipped with carbon fiber brush. A single-mode Yb-doped fiber laser YLC-1000-WC (IPG Photonics GmbH, Burbach, Germany) with a maximum output power of 1 kW (BPP: 0.37 mm·mrad) is used, emitting laser radiation with a wavelength of 1070 nm. Laser radiation is coupled into an optical fiber (core diameter: 200 µm) before entering the collimation lens (f_{col} = 40 mm). Further beam shaping and guidance is done by a subsequent arrangement of a varioScan40 dynamic focusing system and a galvanometer scanner intelliScan30 (both from Scanlab GmbH, Puchheim, Germany). With this setup a focal spot of approx. 80 µm in the focal plane is generated, whereby the dynamic focusing system ensures the field correction and the galvanometer scanner deflects the laser beam onto the powder bed. The corresponding laser beam caustic is depicted in the Supplementary S15. L-PBF processing is performed in a global protective gas atmosphere (Ar), whereby the entire installation space is operated with an overpressure of 80 mbar compared to normal atmosphere, ensuring a residual oxygen content in the process chamber below

100 ppm during processing. All components are controlled by the custom-made control software "SLM Machine" (Ortmann Digitaltechnik GmbH, Attendorn, Germany).

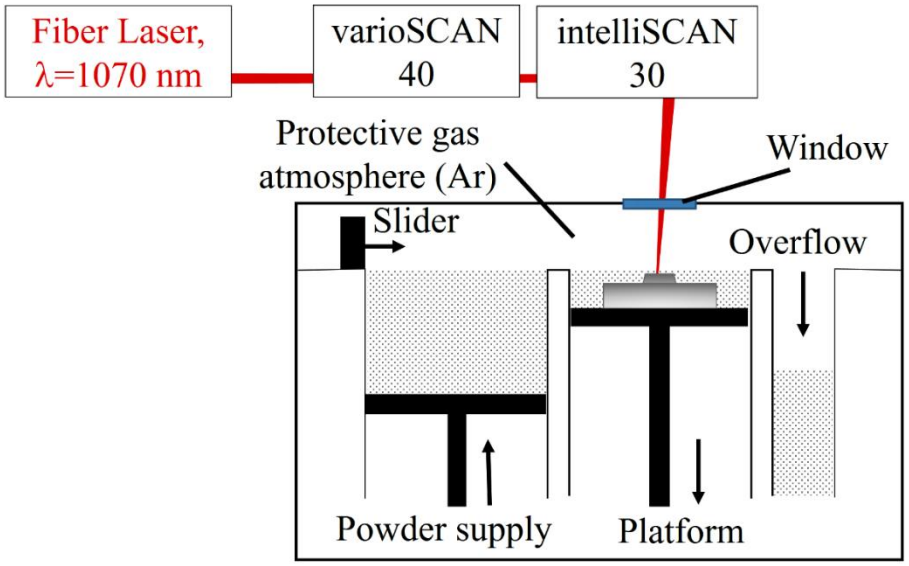

Fig. 35: Schematic depiction of the L-PBF machine AconityMIDI. A photographic depiction is shown in Supplementary S16.

6.1.3 High-speed laser cladding (HSLC) machine setup

For the HSLC setup L-DED machine 2 is used including a small beam diameter of 0.6 mm. The processing head is positioned above the stainless steel tube (AISI 304) with a wall thickness of 5 mm and an outer diameter of 50 mm, which is used as a substrate material. The substrate tube is mounted on a lathe machine Twister FU-180 (Neureiter Maschinen GmbH, Kuchl bei Salzburg, Austria), as shown in Fig. 36. The substrate material is sand-blasted and cleaned with ethanol before mounting to remove surface contaminations. [487]

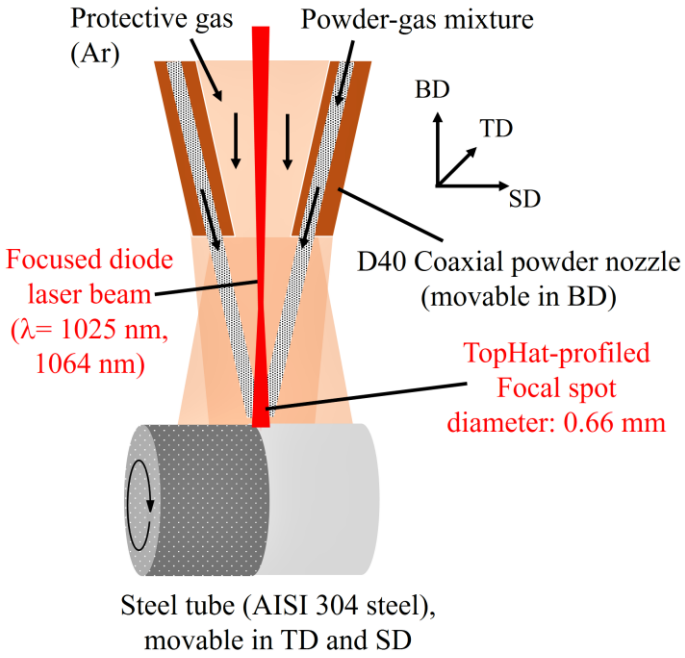

Fig. 36: Schematic depiction of the HSLC setup, integrated in L-DED machine 2. A photographic depiction is shown in Supplementary S17.

6.2 Printing of raw Fe20Cr4.5Al0.5Ti (wt.%) steel powder

In order to investigate the influence of yttrium oxide nanoparticle addition to the stainless steel alloy Fe20Cr4.5Al0.5Ti (wt.%) on microstructure development and mechanical properties, printing of the pure metallic phase with both additive manufacturing processes of L-DED and L-PBF is performed. Accordingly, the unreinforced powder material is used and processed on L-DED machine 1 (beam diameter: 1.8 mm) using the powder fraction B (45 – 90 µm). In parallel, powder fraction A is used for the production of L-PBF manufactured samples.

6.2.1 L-DED of raw Fe20Cr4.5Al0.5Ti (wt.%) steel powder

The iterative variation of the relevant process parameters of laser power (P_L), deposition velocity (v), powder feed rate (m_p), track offset (Δy) and height offset (Δz) a process parameter set is developed, which allows the deposition of crack-free specimen. It is aimed to adjust the process parameters towards a track width to track height ratio (C_R) of 3-4 in order to avoid geometrically caused defects, such as inter-run porosity (Fig. 37e) [550]. Thus, single tracks (Fig. 37a,b) with varied laser power and deposition velocity are manufactured resulting in different C_R values (Fig. 37a,b). Following a constant track offset (Δy) of single tracks is introduced to form single layers (Fig. 37c,d). The corresponding etched cross-section shows no crack formation and full metallurgical bonding between the layer manufactured and the substrate material (Fig. 37d). A double-layered specimen with low porosity and no cracks is depicted in Fig. 37f.

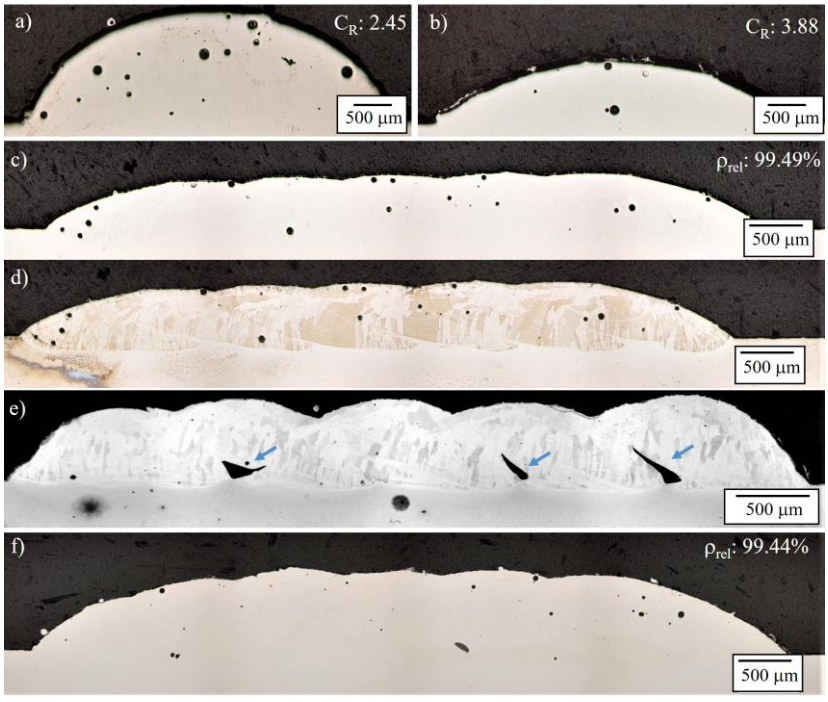

Fig. 37: Representative LOM images of the process parameter development of L-DED of the raw stainless steel material. a) Cross-section of a single track with high track width to track height ratio (C_R). b) Cross-section of a single track with track width to track height ratio (C_R) between 3 and 4. c) Cross-section of a single layer. d) Corresponding micrograph of the etched cross-section. e) Cross-section of a single layer manufactured with high C_R and inter-run porosity defect marked with blue arrows. f) Cross-section of a double-layered specimen with a C_R between 3 and 4 showing low porosity.

The optimized process parameter set for L-DED processing of specimen is shown in Table 21.

Table 21: Optimized process parameter set for L-DED processing of raw stainless steel and ODS specimens.

Process parameter	Laser power (P_L)	Deposition velocity (v)	Powder feed rate (m_p)	Track offset (Δy)	Height offset (Δz)	Beam diameter (d_B)
Unit	W	mm/min	g/min	µm	µm	mm
Value	750	600	3.7	940	520	1.8

Based on the process parameter study a four-layered specimen with ten adjacent weld tracks are manufactured with a beam diameter of 1.8 mm (Fig. 38a). The tool steel 32CrMoV12-28 (H10) is used as substrate material. A representative specimen is depicted in Fig. 38, showing no cracks and low relative porosity of 99.72%. Only spherical pores with maximum diameter of 30 µm can be observed, which are randomly distributed across the cross-section depicted. The microstructure, which is revealed by the etching procedure, is characterized by coarse grains growing with a small inclination from the build direction (Fig. 38b). Grain structures are not interrupted by the melt pool boundaries (yellow dotted lines), indicating epitaxial growth conditions (Fig. 38c).

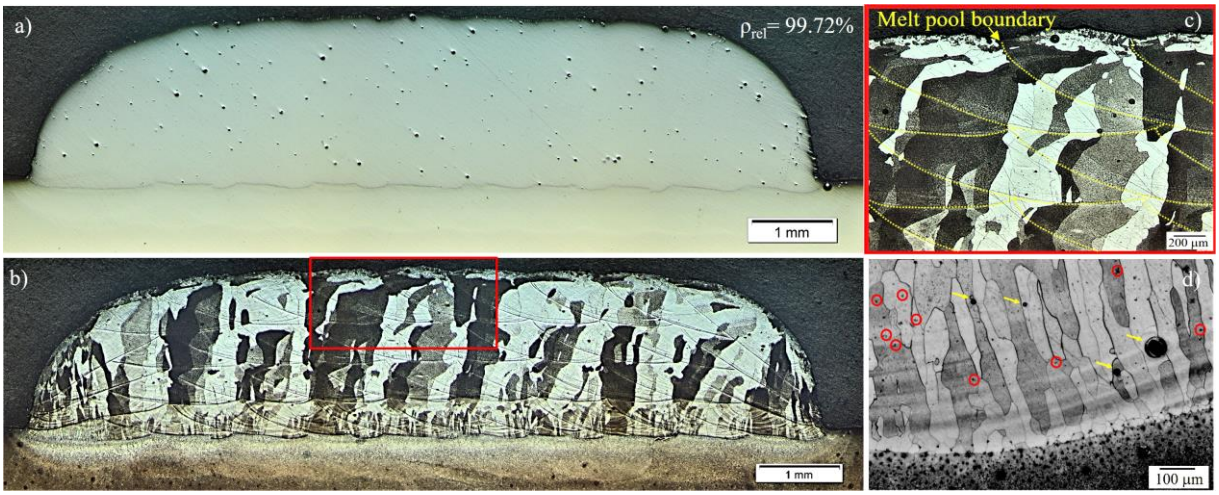

Fig. 38: LOM images of L-DED manufactured specimen made from pure stainless steel using the process parameters from Table 21. a) Polished cross-section. b) Corresponding etched cross-section. c) LOM images with higher magnification of the top region (red box in b). Melt pool boundaries are highlighted with yellow dotted lines. d) LOM images with higher magnification of the bottom region showing the refined grain structure with pores (yellow arrows) and carbide precipitates (red circles).

However, some abnormalities can be determined regarding the deposited layer close to the substrate material, exhibiting a significantly refined microstructure compared to subsequently deposited layers. On the one hand, this behaviour could be attributed to the higher cooling rates in this area due to deposition onto a cold substrate material (23°C). Further deposition of material is typically connected with continuous temperature increase [20], lowering the cooling rates and thus the solidification kinetics.

On the other hand, an explanation can also be found in the dilution of tool steel substrate material, containing significant amounts of carbon, promoting the formation of carbide particles acting as heterogeneous nucleation sites and thus enabling grain refining, frequently observed in additive manufacturing processes [264]. Accordingly, a large number of Ti-rich carbides are found in the area close to the substrate material, indicated by red circles (Fig. 38d). The top region of the last deposited layer exhibits a significant deviation from the slightly inclined growth direction of the observed coarse grains. The abrupt change of growth direction can be explained by the characteristically curved geometry of the solidification front in L-DED processes, changing the direction of the main thermal gradient and thus leading to the growth direction of the grains. This behaviour is only observed in the top layer, because this region is re-melted in lower layers upon subsequent deposition of additional layers.

6.2.2 L-PBF of raw stainless steel (Fe20Cr4.5Al0.5Ti (wt.%))

The production of Fe20Cr4.5Al0.5Ti (wt.%) material, processed by L-PBF, is performed by iterative process parameter development of relevant process parameters laser power (P_L), scan speed (v_s), hatch distance (h_s). The layer thickness is fixed at 30 µm. Cubic specimens with an edge length of 5 mm are fabricated on a stainless steel substrate material (316L stainless steel) at room temperature (Fig. 39a).

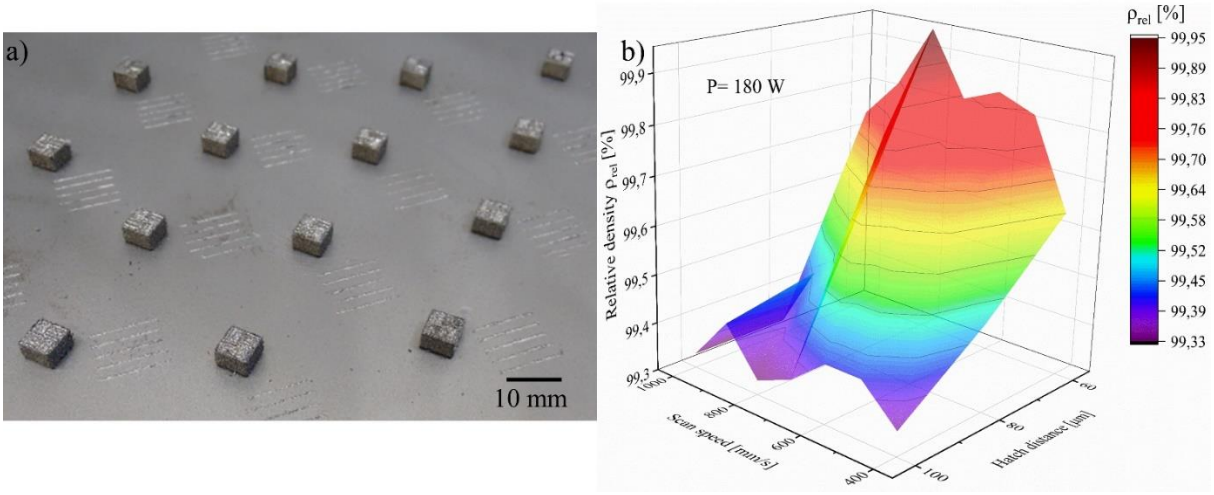

Fig. 39: a) Printed cube structures (5 mm) of Fe20Cr4.5Al0.5Ti (raw) stainless steel on 316L substrate material. b) Relative density as a function of scan speed (v_S) and hatch distance (h_S) at a constant laser power P of 180W.

It is found that samples manufactured with a hatch distance (h_s) of 60 µm show lowest porosities compared to larger hatch distances of 80 µm and 100 µm. (Fig. 39b) The optimized process parameter set is shown in Table 22 and corresponds to a volume energy density (VED) of 111.11 J/mm^3 for samples with maximum relative density of 99.99% (Fig. 39a,b). VED is calculated according to Caiazzo et al. [551] with (9).

$$VED = \frac{P_L}{h_s v_s l_s} \qquad (9)$$

where P_L is the laser power [W], v_s the scan speed [mm/s], h_s the hatch distance [µm] and l_s denotes the layer thickness [µm].

Comparable VED values are also used for L-PBF production of other stainless steel alloys (e.g. 316L stainless steel). [552] The optimized process parameter set is shown in Table 22.

Table 22: Optimized process parameter for production of raw stainless steel material using L-PBF.

Process parameter	Laser power (P_L)	Scan speed (v_S)	Hatch distance (h_S)	Layer thickness (l_S)	Layer-wise scan rotation	Scan strategy	VED
unit	W	mm/s	µm	µm	°	-	J/mm^3
Value	180	800	60	30	90	Stripes	111.11

The microstructure of L-PBF manufactured stainless steel is free of cracks (Fig. 40a,c) and characterized by elongated dendrites oriented parallel to the build direction (Fig. 40b,d). Hence a strong texture in [001] direction is observed for L-PBF processed material, which is considerably more pronounced compared to L-DED manufactured stainless steel material and characteristic for L-PBF printed steels. [553, 554] The stronger texture compared to L-DED manufactured specimen can be explained by the characteristic highly directional heat dissipation in L-PBF processes towards the substrate material and the higher cooling rates additionally enabling significant grain refining. [13]

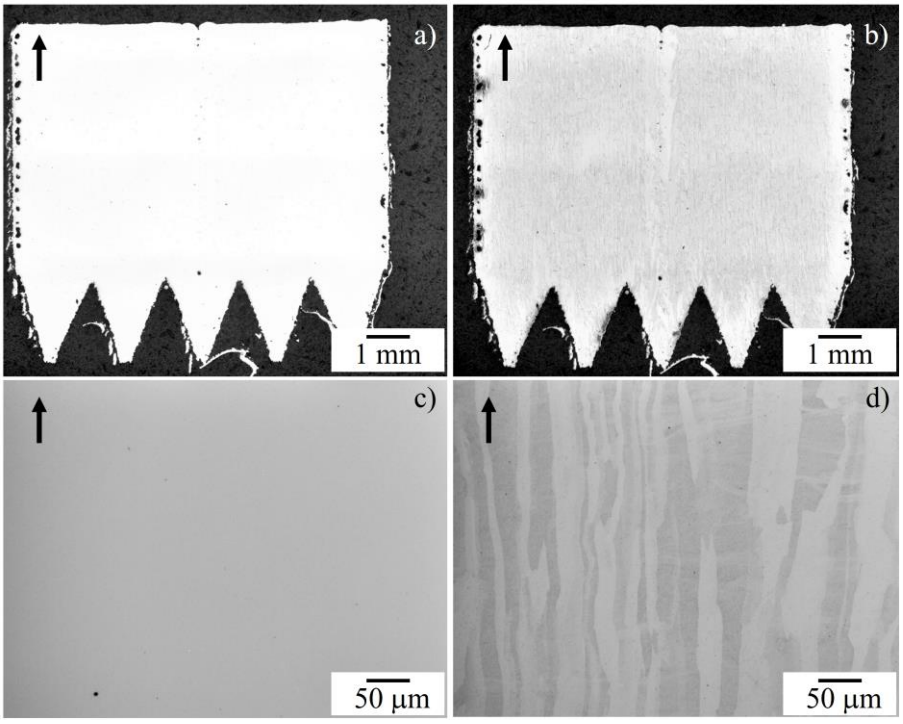

Fig. 40: a) Polished LOM images of cross-sections of L-PBF manufactured Fe20Cr4.5Al0.5Ti (wt.%) stainless steel manufactured with a VED of 111.11 J/mm^3. b) Corresponding etched cross-section of the specimen depicted in a). c) LOM image (polished state) with higher magnification showing the dense microstructure with a small pore in the bottom region (spherical black dot in the bottom left part of the image). d) LOM image (after etching) with higher magnification showing the fine-grained microstructure oriented along the build direction (marked with black arrows).

6.3 Additive manufacturing of oxide-dispersion strengthened Fe20Cr4.5Al0.5Ti (wt.%)

Contains content from the following publications:

Microstructure formation and mechanical properties of ODS steels built by laser additive manufacturing of nanoparticle coated iron-chromium powders

C. Doñate-Buendia[a], P. Kürnsteiner[b], F. Stern[c], M. B. Wilms[d], R. Steubel[a], I. M. Kusoglu[a], J. Tenkamp[c], E. Bruder[e], N. Pirch[d], S. Barcikowski[a], K. Durst[e], J. H. Schleifenbaum[d], F. Walther[c], B. Gault[b,f], B. Gökce[a,*]

[a]Technical Chemistry I and Center for Nanointegration Duisburg-Essen (CENIDE), University of Duisburg-Essen, 45141 Essen, Germany
[b]Department Microstructure Physics and Alloy Design, Max-Planck-Institut für Eisenforschung GmbH, 40237 Düsseldorf, Germany
[c]Department of Materials Test Engineering, TU Dortmund University, 44227 Dortmund, Germany
[d]Chair for Digital Additive Production, RWTH Aachen University & Fraunhofer Institute for Laser Technology, 52074 Aachen, Germany
[e]Physical Metallurgy, Materials Science Department, Technische Universität Darmstadt, 64287 Darmstadt, Germany
[f]Department of Materials, Royal School of Mines, Imperial College, Exhibition Road, London, SW7 2AZ, UK

Article Information

Article history:
Received 16 July 2020
Accepted 12 December 2020
Available online 17 December 2020

DOI: 10.1016/j.actamat.2020.116566
Acta Materialia

**Corresponding author*
bilal.goekce@uni-due.de

Abstract

Oxide dispersion strengthened (ODS) steels are known for their enhanced mechanical performance at high temperatures or under radiation exposure. Their microstructure depends on the manufacturing process, from the nanoparticle addition to the base steel powder, to the processing of the nanoparticle enriched powder. The optimization and control of the processing steps still represent a challenge to establish a clear methodology for the additive manufacturing of ODS steels. Here, we evaluate the microstructure, nanoparticle evolution, and mechanical properties of ODS steels prepared by dielectrophoretic controlled adsorption of 0.08 wt% laser-synthesized yttrium oxide (Y_2O_3) on an iron-chromium ferritic steel powder (PM2000). The influence of the ODS steel fabrication technique is studied for two standard additive manufacturing techniques, directed energy deposition (DED) and laser powder bed fusion (LPBF). The compressive strength of the ODS steels at 600 °C is increased by 21% and 29% for the DED and LPBF samples, respectively, compared to the DED and LPBF steels manufactured without Y_2O_3 nanoparticle addition. The Martens hardness is enhanced by 9% for the LPBF ODS steel while no significant change is observed in the DED ODS steel. The microstructure and nanoparticle composition and distribution are evaluated by electron backscatter diffraction, scanning electron microscopy–energy-dispersive X-ray spectroscopy, and atom probe tomography, to compare the microstructural features of DED and LPBF manufactured parts. Smaller grain size and more homogeneous distribution with lower agglomeration of Y-O nanoparticles in the LPBF sample are found to be key factors for enhanced mechanical response at 600°C. The enhanced mechanical properties of the LPBF-processed sample and the more homogeneous nanoparticle dispersion can be linked to results obtained by finite element methods simulations of the melt pool that show two orders of magnitude faster cooling rates for LPBF than for DED. Therefore, this work presents and validates a complete laser-based methodology for the preparation and processing of an ODS steel, proving the modification of the microstructure and enhancement of the high-temperature strength of the as-built parts.

Own contribution: Sample preparation, contributing to writing and editing of the original draft and revised manuscript.

Effect of nanoparticle additivation on the microstructure and microhardness of oxide dispersion strengthened steels produced by laser powder bed fusion and directed energy deposition

C. Doñate-Buendia[a], R. Steubel[a], P. Kürnsteiner[b], M. B. Wilms[c], F. Stern[d], J. Tenkamp[d], E. Bruder[e], S. Barcikowski[a], B. Gault[b], K. Durst[e], J. H. Schleifenbaum[c], F. Walther[d], B. Gökce[a,*]

[a]Technical Chemistry I and Center for Nanointegration Duisburg-Essen (CENIDE), University of Duisburg-Essen, 45141 Essen, Germany
[b]Department Microstructure Physics and Alloy Design, Max-Planck-Institut für Eisenforschung GmbH, 40237 Düsseldorf, Germany
[c]Chair for Digital Additive Production, RWTH Aachen University & Fraunhofer Institute for Laser Technology, 52074 Aachen, Germany
[d]Department of Materials Test Engineering, TU Dortmund University, 44227 Dortmund, Germany
[e]Physical Metallurgy, Materials Science Department, Technische Universität Darmstadt, 64287 Darmstadt, Germany

Article Information

DOI: 10.1016/j.procir.2020.09.009
Procedia CIRP

*Corresponding author
bilal.goekce@uni-due.de

Abstract

In this contribution, the effect of nanoparticle additivation on the microstructure and microhardness of oxide dispersion strengthened steels (ODS) manufactured by laser powder bed fusion (L-PBF) and directed energy deposition (DED) additive manufacturing (AM) is studied. The powder composites are made of micrometer-sized iron-chromium-alloy based powder which are homogenously decorated with Y_2O_3 nanoparticles synthesized by pulsed laser fragmentation in water. Consolidated by L-PBF and DED, an enhanced microhardness of the AM-built ODS sample is found. This increase is related to the significant microstructural differences found between the differently processed samples.

Own contribution: Sample preparation, contributing to writing and editing of the original draft and revised manuscript.

Depositing laser-generated nanoparticles on powders for additive manufacturing of oxide dispersed strengthened alloy parts via laser metal deposition

R. Streubel[a], M. B. Wilms[b], C. Doñate-Buendia[a], A. Weisheit[a], S. Barcikowski[a], J. H. Schleifenbaum[b], B. Gökce[a,*]

[a]Technical Chemistry I and Center for Nanointegration Duisburg-Essen (CENIDE), University of Duisburg-Essen, 45141 Essen, Germany
[b]Chair for Digital Additive Production, RWTH Aachen University & Fraunhofer Institute for Laser Technology, 52074 Aachen, Germany

Article Information

Article history:
Received 19 January 2018
Accepted 7 February 2018
Available online 6 March 2018

DOI: 10.7567/JJAP.57.040310
Japanese Journal of Applied Physics

**Corresponding author*
bilal.goekce@uni-due.de

The Japan Society of Applied Physics

Abstract

We present a novel route for the adsorption of pulsed laser-dispersed nanoparticles onto metal powders in aqueous solution without using any binders or surfactants. By electrostatic interaction, we deposit Y_2O_3 nanoparticles onto iron–chromium based powders and obtain a high dispersion of nano-sized particles on the metallic powders. Within the additively manufactured component, we show that the particle spacing of the oxide inclusion can be adjusted by the initial mass fraction of the adsorbed Y_2O_3 particles on the micropowder. Thus, our procedure constitutes a robust route for additive manufacturing of oxide dispersion-strengthened alloys via oxide nanoparticles supported on steel micropowders.

Own contribution: Sample preparation, contributing to writing and editing of the original draft and revised manuscript.

For the additive manufacturing of oxide-dispersion strengthened specimen the manufactured composite powder materials shown in chapter 5.3 and 5.4 are used. L-PBF is performed using the powder fraction A with a particle size distribution < 45 µm, whereas in L-DED experiments powder fraction B with a particle size distribution of 45 – 90 µm is used.

6.3.1 Laser directed energy deposition (L-DED)

The production of samples using mechanically alloyed and LSPC-manufactured Fe20Cr4.5Al0.5Ti+0.5 Y_2O_3 (wt.%) powder material is performed with an identical set of process parameters as shown in Table 21 in order to exclude the influence of process parameter variations on microstructural development. Dense specimen (Fig. 41a) can be manufactured, which are characterized by a slightly higher porosity (ρ_{rel}: 99.49%) compared to the raw steel specimen (ρ_{rel}: 99.72%). The grain structure is visualized by the etching of the cross-sections (Fig. 41b) and shows no visible difference of the grain structure to non-reinforced counterparts. Accordingly, no change of the grain size is detectable by light optical microscopy and the behaviour of the first layer close to the substrate material as well as the uppermost region of the last layer is comparable to the non-reinforced counterparts.

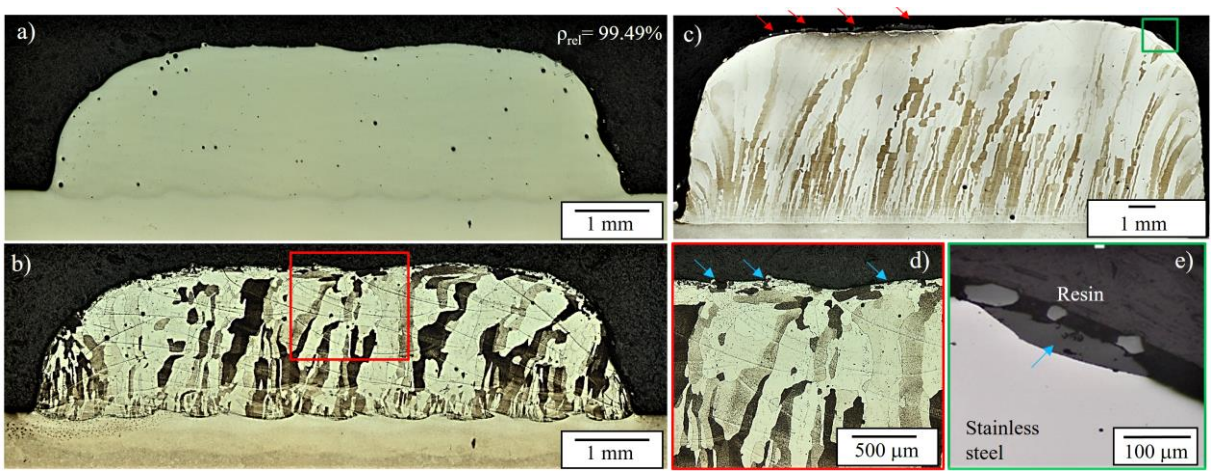

Fig. 41: Light optical micrographs of L-DED manufactured ODS specimen using mechanically alloyed powder material. a) LOM image of a polished cross-section showing randomly distributed pores. b) Corresponding image of the etched specimen showing the grain structure. c) L-DED printed large volume with visible discontinuous grey appearing layer on the upper surface indicated with red arrows. d) LOM images with higher magnification of the red box in (b), showing smallest inclusions of grey appearing ceramic material, marked with blue arrows. e) LOM images with higher magnification of the green box in (c), showing a larger agglomerate of grey appearing slag material (indicated with a blue arrow).

However, the production of larger specimen (20 layers), the formation of a ceramic layer, marked with red arrows (Fig. 41c) is observed. The ceramic layer is discontinuous (Fig. 41c-e) and spalls off the manufactured specimen during cooling after the building process. Elemental distribution maps prepared by EDS show that the discontinuous ceramic layer is enriched in in yttrium, aluminium and oxygen (Fig. 42). The formation of oxide layers on printed ODS specimen is frequently observed by other research groups [367, 484] and is referred as "slag layer formation" (c.f. chapter 3.2), which is caused by agglomeration and flotation processes of added oxide particles in the melt pool. The chemical composition of the formed slag layer indicates that the formation is due to the process schematically depicted in Fig. 13. Thus, a slag layer formation by atmospheric reaction due to insufficient shielding by inert of the melt pool from the atmosphere can be excluded.

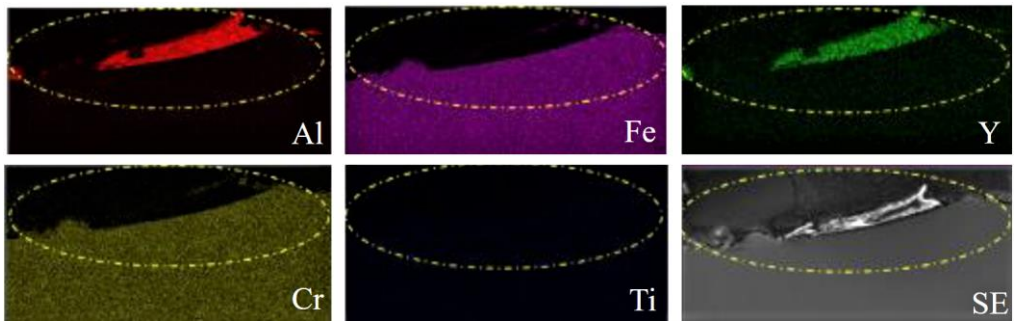

Fig. 42: EDS maps of the slag layer formed on the surface of L-DED manufactured ODS specimen. [554]

Spalling of the formed oxide layer can be explained by the concept of the Pilling-Bedworth-Ratio (PBR), which describes the ratio of the volumes of a metallic alloy and the oxide species formed upon atmospheric oxidation. PBR > 2 are found to spall off the metallic alloy due to increased volume. [555] According to this model the native Al_2O_3 layer, which is typically formed on pure Fe20Cr4.5Al0.5Ti

(wt.%) alloy [556], would not result in spalling. In contrast, yttrium-aluminium rich oxide compounds found in aluminium alloyed ODS steels ($Y_3Al_5O_{12}$, $Y_4Al_2O_9$, $YAlO_3$) as well as pure Y_2O_3 lead to high PBR (> 2) and therefore do not form a stable oxide layer. The PBR is calculated using (10): [555]

$$PBR = \frac{V_{oxide}}{V_{metal}} = \frac{M_{oxide} \cdot \rho_{metal}}{n \cdot M_{metal} \cdot \rho_{oxide}} \qquad (10)$$

where V_{oxide} relates to the volume of the elementary cell of the oxide compound and V_{metal} corresponds to the volume of the elementary cell of the corresponding metal. ρ denotes the density and M the atomic or molecular mass of the respective species, while n is the number of metal atoms in one molecule of the oxide compound. [555] The calculated PBR are shown in Table 23.

Table 23: Calculated PBR for aluminium oxide, yttrium oxide and different aluminium-rich yttrium oxides.

Alloy / Compound	Molar mass M [g/mol]	Density ρ [g/cm³]	n [-]	PBR [-]
Fe20Cr4.5Al0.5Ti (wt.%)	52.89	7.18 [557]	-	-
Al_2O_3	101.96	3.95	2	1.75
Y_2O_3	255.81	5.06	2	3.43
$Y_3Al_5O_{12}$	593.62	4.42	8	2.28
$Y_4Al_2O_9$	553.58	4.38	6	2.86
$YAlO_3$	163.89	5.19	2	2.14

Based on these observations, it can be explained that the process conditions selected in L-DED result in agglomeration and subsequent flotation of introduced oxide particles and, as a result, accumulate on the surface of the manufactured part. Accordingly, the metallic matrix is depleted of oxide nanoparticles, resulting in microstructural development comparable to non-reinforced specimen. However, single yttrium-enriched particles, predominantly located in the vicinity of grain boundaries between dendrites, are occasionally observed within the microstructure, as evident from EDS maps taken from the center of L-DED manufactured ODS samples (Fig. 43). It is hypothesized, that these micrometer-scaled particles are agglomerated yttrium-rich oxide nanoparticles and captured by the mechanism of entrapment, described in Fig. 15. Apart from titanium, where local enrichments on grain boundaries can be observed, no segregation of the alloying elements of chromium and aluminium can be detected. (Fig. 43)

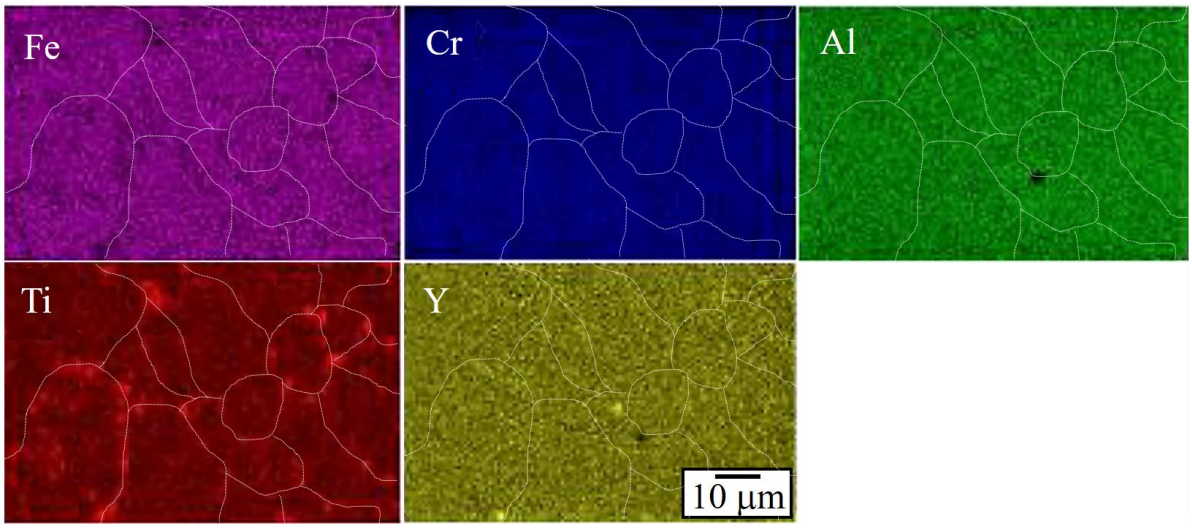

Fig. 43: EDS maps of L-DED manufactured ODS specimen using mechanically alloyed powder material showing local enrichments of titanium and two single yttrium-rich particles. [544] Grain boundaries are highlighted by white dotted lines.

As evident from the EDS maps (Fig. 43), a significant loss of oxide particles due to agglomeration and flotation occurred. The ability of nanoparticles to interact with each other to from agglomerates is principally based on their movement in the melting stage in L-DED. Thus, prolonged melt pool lifetimes and low melt movement would promote agglomeration tendencies. Consequently, the creation of smaller melt pools, which are typically characterized by higher cooling rates [558], may reduce the melt pools lifetime and thus effectively prevent agglomeration and flotation tendencies.

6.3.2 L-DED of ODS specimen with reduced beam diameter

The creation of small-scaled melt pools in L-DED is enabled by the utilization of a reduced laser beam diameter of 0.6 mm using laser processing system 2. Analogue process parameter development procedure is carried out to identify a suitable process parameter set for manufacturing of dense specimen. The optimized process parameter set is shown in Table 24.

Table 24: Optimized process parameters for L-DED manufacturing of ODS specimens with reduced beam diameter.

Process parameter	Laser power (P_L)	Deposition velocity (v)	Powder feed rate (m_p)	Track offset (Δy)	Height offset (Δz)	Beam diameter (d_B)
Unit	W	mm/min	g/min	µm	µm	mm
Value	370	2000	1.3	350	210	0.6

Based on these process parameters, crack-free specimen with high relative density (ρ_{rel}: 99.99%) are manufactured. The microstructure is characterized by large, darker appearing grains growing over multiple layers with a small inclination towards the building direction. (Fig. 44b) The inclination with approx. 10° ± 2° is found to be considerably lower than specimen manufactured with larger beam diameters (18° ± 6°) and may be influenced by different melt pool shape and solidification conditions. L-DED specimen manufactured with smaller beam diameter additionally exhibit significantly smaller

grain size compared to specimen manufactured with a large beam diameter, proving the effectiveness of beam diameter reduction to facilitate higher cooling rates (approx. $6 \cdot 10^3$ K/s for 1.8 mm beam diameter), which is also evident from finite element (FEM) simulations, shown in Supplementary S18 and using thermophysical data from [559] (Supplementary S19). Moreover, the surface of the manufactured specimen is found to be almost free of ceramic particles (Fig. 44a), indicating effective suppression of agglomeration and flotation processes of oxide nanoparticles during L-DED processing. However, a complete prevention of oxide nanoparticle agglomeration despite of using a small beam diameter of 0.6 mm could not be achieved.

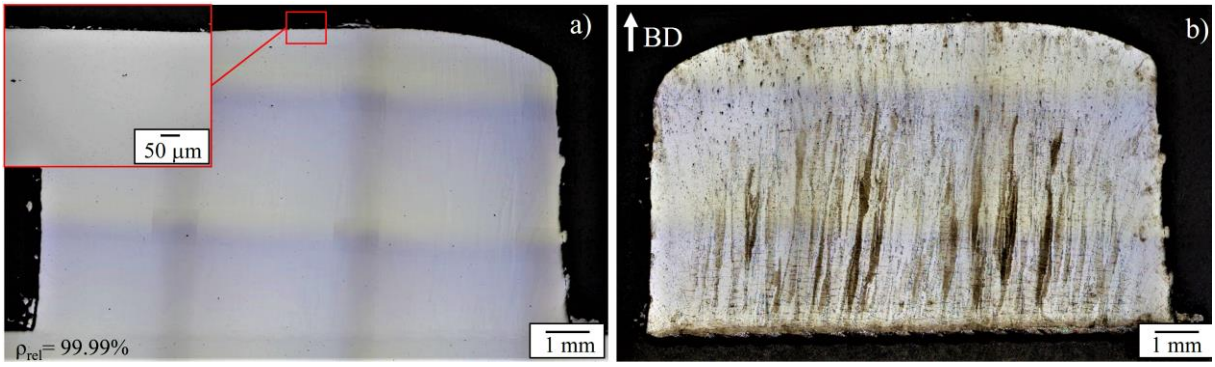

Fig. 44: Light optical micrographs (cross-sections) of L-DED manufactured ODS specimens using mechanically alloyed powder material and a reduced beam diameter of 0.6 mm. a) Polished state with superimposed micrograph with high magnification of the specimens' surface. b) Etched micrograph showing the presence of large grains with a small inclination towards the building direction (BD).

The cooling rate, temperature gradient and solidification front velocity cannot be determined experimentally in AM, thus FEM modelling is performed in order to calculate these values (Fig. 45). The calculations are based on a mathematical model integrating the time dependent heat equations, computation of the track geometry with the nonlinear Young-Laplace equation and subsequent solving using finite element methods. The calculated values of cooling rate and maximum melt pool temperature (Fig. 45) are in agreement with with results from other research groups [560, 561, 562]. Thus, it is demonstrated, that cooling rates up to $6 \cdot 10^4$ K/s in combination with melt pool temperatures (T_M) of approx. $3 \cdot 10^3$ K are not sufficient to completely prohibit agglomeration tendencies and provide sufficient time (approx. 50 ms) for agglomeration and flotation mechanism of oxide nanoparticles in the melt pool.

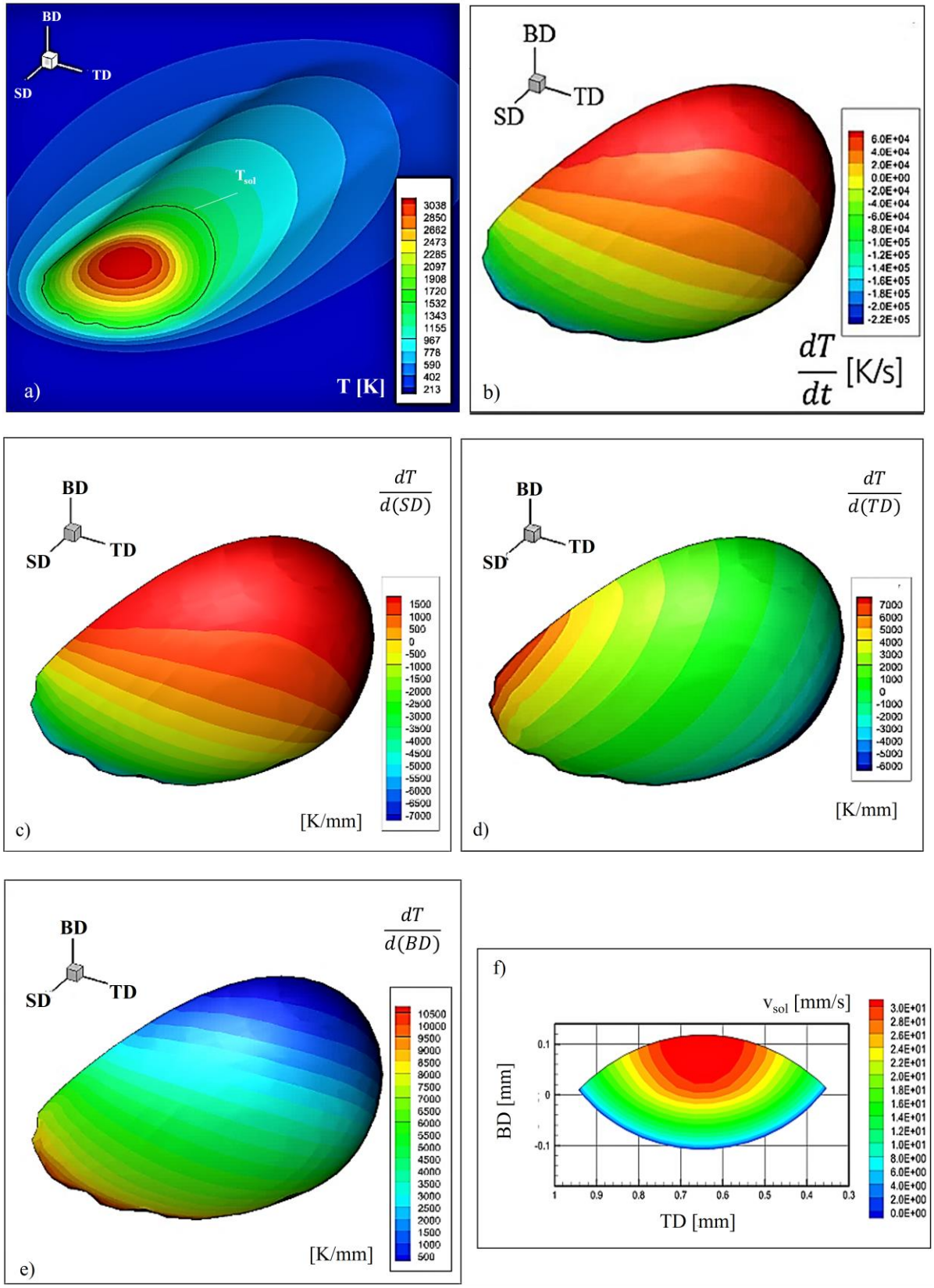

Fig. 45: FEM melt pool solidification simulations for L-DED manufactured material: a) Melt pool temperature with solidus line (T_{sol}). b) Cooling rate along the solidification front. Negative cooling rates can be considered as heating rates generated by the laser irradiation. c-e) The temperature gradients plotted in every direction in space $\frac{dT}{d(SD)}$ (d), $\frac{dT}{d(TD)}$ (e) and $\frac{dT}{d(BD)}$. f) Velocity of the solidification front v_{sol}. [13]

Despite some losses to slag layer formation, a significant number of nano-scaled oxide particles homogeneously dispersed in the stainless steel matrix can be detected as bright white spots in SEM imagery (Fig. 46c-f) after etching procedure of the specimen manufactured with MA- and LSPC-manufactured powder material, depicted in Fig 46a,b. Etching procedure before SEM examination is essential to remove the surrounding stainless steel matrix to expose the oxide particles. It is also evident that in all printed specimen the matrix material removal due to interaction with the etchant is not homogeneous and differs in adjacent grains. (Fig. 46c-f) This behaviour is frequently observed in wet chemical etching for various material systems and is related to the higher sensitivity of certain crystal orientations to etchants such as “Nital” (Nitric acid in water). [563, 564] No preferential accumulation of oxide nanoparticles on grain boundaries is observed throughout the microstructure. Rarely, larger agglomerates are detected, presumably formed as a result of agglomeration and captured by the solidification front by the entrapment processes (cf. chapter 3.2). An influence of the powder preparation method on the homogeneity of distribution of nanoparticles in the metallic matrix is not visible on this scale.

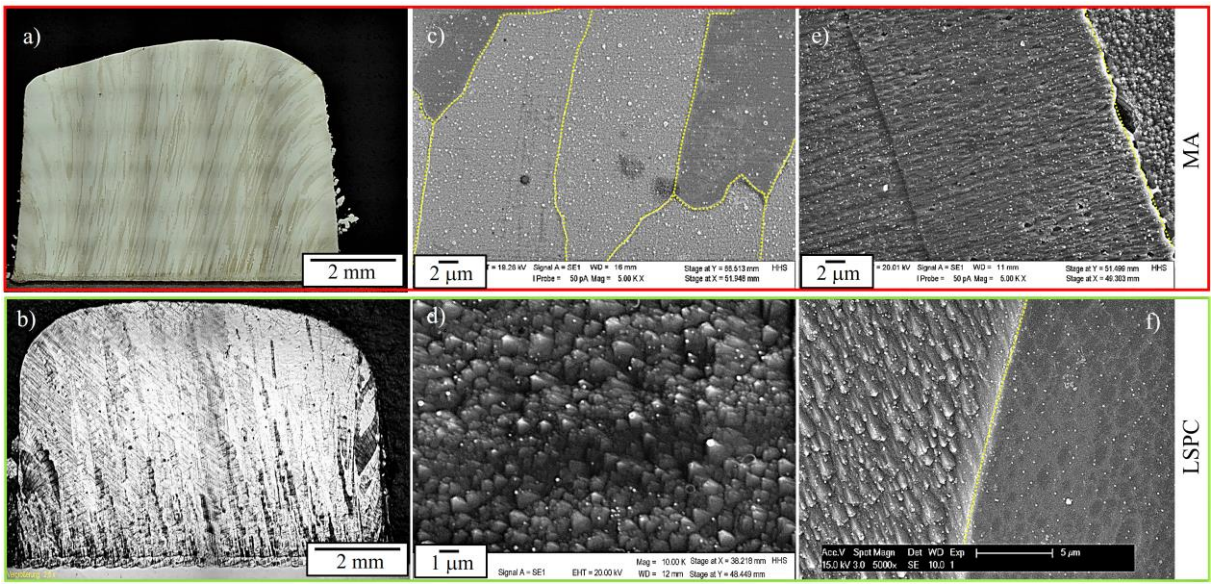

Fig. 46: a,b) LOM images of specimen manufactured (etched cross sections) with L-DED, utilizing a reduced beam diameter of 0.6 mm: Red box: Specimen manufactured from LSPC-manufactured powder material. Green box: Specimen manufactured from MA-manufactured powder material. c-f) SEM micrographs (SE-mode) after etching of specimen manufactured with L-DED, utilizing a reduced beam diameter. Green box: Specimen from MA-manufactured powder material. Red box: Specimen manufactured from LSPC-manufactured powder material.

In Fig. 47 the corresponding histograms showing the nanoparticle size distributions, captured from the respective SEM images in Fig. 46b using the image analysis software “ImageJ”, is depicted. It is evident, that the utilization of LSPC-manufactured powder material (Fig. 47b) results in slightly smaller oxide nanoparticles, by approx. 16% compared to MA-manufactured powder materials (Fig. 47a). However, both materials do contain significant amounts of nanoparticles below 100 nm.

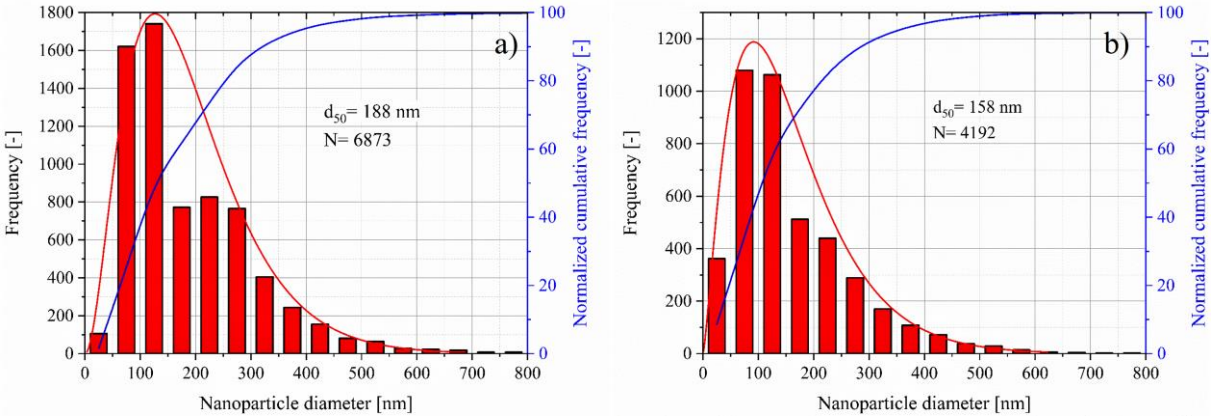

Fig. 47: Histograms of the nanoparticle size distribution of L-DED processed material with small beam diameter (0.6 mm): a) Specimen manufactured from MA-manufactured powder material. b) Specimen manufactured from LSPC-manufactured powder material.

The chemistry of these oxide nanoparticles is determined by EDS on larger agglomerates to minimize the signal from the surrounding matrix alloy. Nanoparticles (Fig. 48a) are found to be enriched in yttrium, oxygen, titanium and aluminium in materials printed with both powder feedstocks (Fig. 48b,c).

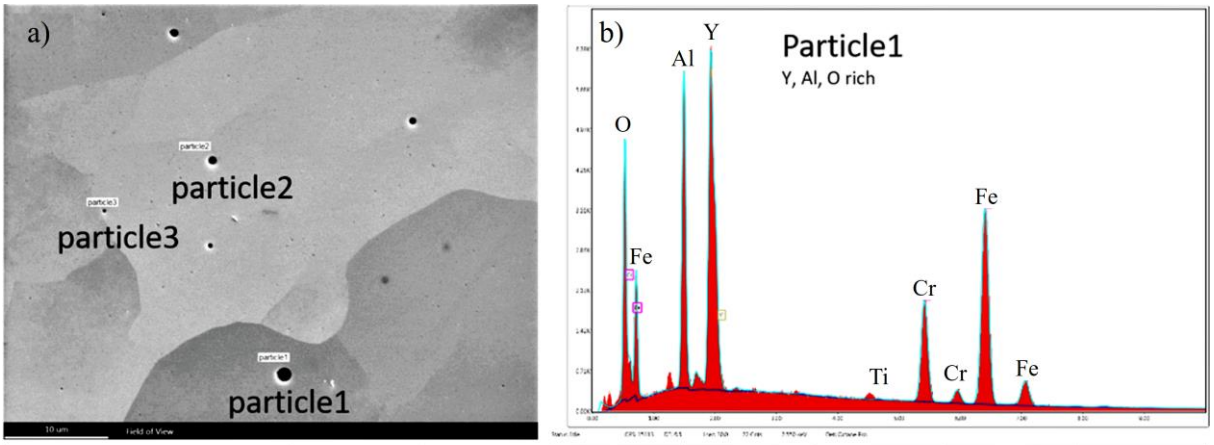

c)	Fe	Cr	Al	Ti	Y	O	Si
L-DED (MA)- Matrix	Bal.	14.82	2.98	0.82	-	-	-
L-DED (MA)- NP	Bal.	18.80	8.82	-	10.48	9.72	0.82
L-DED (LSPC)- Matrix	Bal.	14.85	3.50	-	-	-	-
L-DED (LSPC)- NP	Bal.	9.66	7.92	1.11	13.14	6.91	1.21

Fig. 48: Determination of the matrix and nanoparticles' chemical composition in L-DED manufactured ODS specimens. a) Exemplary SEM images (BSE mode) of an ODS specimen manufactured with LSPC-manufactured powder material. b) Corresponding spectrum from EDS measurement of particle 1 in (a). c) Table showing the chemical composition (in wt.%) for the matrix and nanoparticles (NP) in L-DED manufactures specimens, manufactured from MA- and LSPC-manufactured powder materials. [489]

Impurities such as silicon and carbon, which presumably stem from the stainless steel production, have a decisive impact on the nanoparticle formation. As pointed out in chapter 2.3.1, silicon can be incorporated into yttrium-based oxides to form complex oxides. Thus, Y-Al-Si-rich oxide nanoparticles are sporadically observed in L-DED manufactured specimens (Fig. 49a). The absence of titanium-

enriched oxide nanoparticles may be explained by the capture of titanium by residual carbon to form titanium carbides, which could be found in the volume reconstruction (Fig. 49b) from atom probe tomography (APT) examination and the corresponding proximity diagrams (Fig. 49c).

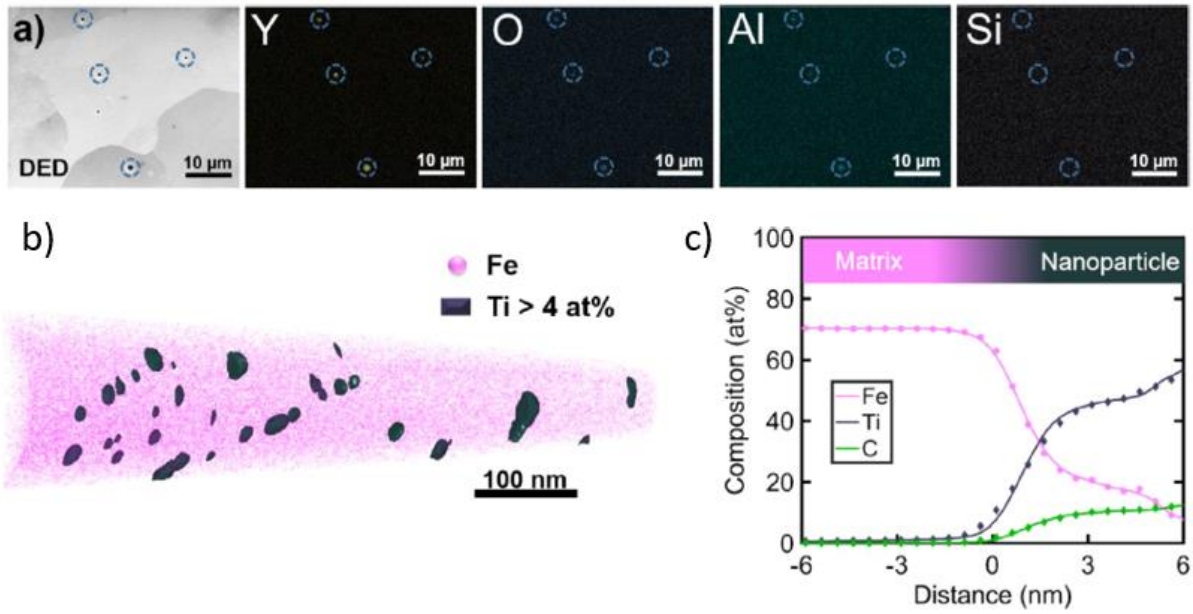

Fig. 49: a) SEM image (BSE mode) of a L-DED manufactured specimen with LSPC-manufactured powder material and corresponding EDS maps showing silicon enriched Y-Al-O nanoparticles dispersed in the Fe20Cr4.5Al0.5Ti (wt.%) matrix. Additional EDS maps can be found in Supplementary S20. b) APT volume reconstruction showing nano-scaled titanium-rich particles in the steel matrix. c) Proximity diagram identifies the titanium-rich particles as titanium carbides, presumably with Ti_2C composition. [13]

Scanning electron micrographs (BSE contrast) additionally show that the primary dendritic solidification microstructure (Fig. 50a) is characterized by an underlying substructure on the sub-micron scale, evident from different grey scales in the micrographs of the of the backscatter micrographs. (Fig. 50a,b) Higher magnification allows the direct observation of Y_2O_3-structured nanoparticles with a size of approx. 50-100 nm (Fig. 50c). The low volume density of observed nanoparticles may explain the difficulties to capture oxide nanoparticles in APT reconstructions using small tip sizes of approx. 600 x 200 nm (cf. Fig. 49b). The existence of substructures in the solidified primary dendritic microstructure is also evident in IPFs from EBSD-measurements conducted in parallel ("Longitudinal section") and perpendicular ("Cross section") to the build direction, showing that primary dendrites are separated by high angle grain boundaries (HAGB) with >15° misorientation and substructures, separated by low angle grain boundaries (LAGB) with >5° misorientation (classification of LAGB and HAGB according to ASTM E2627). The corresponding misorientation map is depicted in Fig. 50h. It becomes evident, that an increased amount of grain boundaries in L-DED manufactured ODS material is present than in raw stainless steel material. Correspondingly, the structure size is reduced from approx. > 260 µm for stainless steel material to > 100 µm for the ODS material. (Fig. 50d-g) Also, the impact of introducing oxide nanoparticles on crystallographic texture of printed specimen becomes evident. Strongest texture component is in any case the [001] direction, which is parallel to the build direction and typical for the

directional solidification in LAM techniques on polycrystalline substrates. [565] However, also other orientations are found, which may stem from the inclination also visible from Fig. 50i-j. Therefore, the predominant [001] texture is lowered. It should be noted that the grain statistics of both L-DED samples are insufficient for a reliable texture quantification due to their large grain size, which also explains the lack of rotational symmetry in the pole figures.

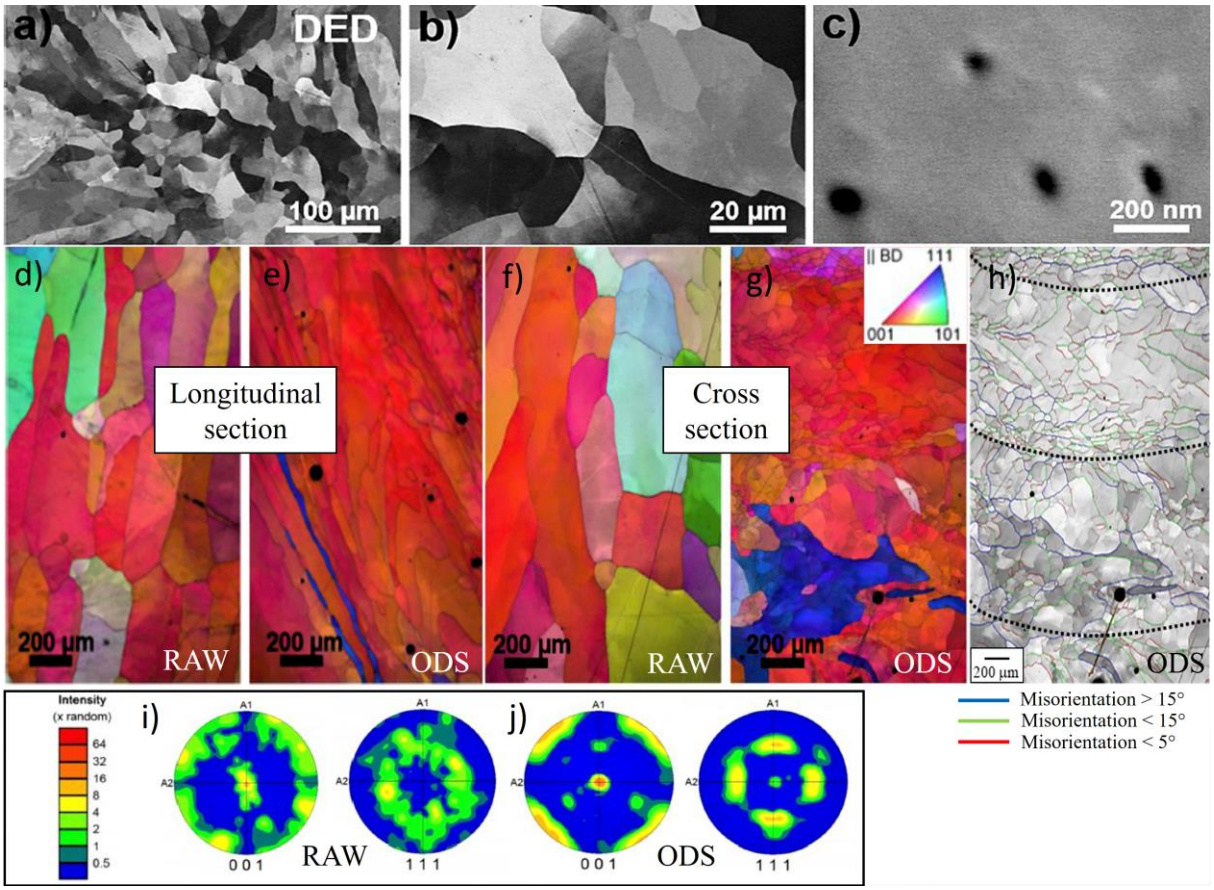

Fig. 50: a-c) SEM images (BSE mode) with different magnifications. d-g) Inverse pole figures (IPF) images from EBSD measurements in build direction (BD) for non-reinforced Fe20Cr4.5Al0.5Ti (wt.%) stainless steel ("raw") (d,f) and ODS stainless steel ("ODS") (e,g) in longitudinal and cross section from LSPC-manufactured powder material. h) Exemplary misorientation map of g) from EBSD measurements. i) Pole figures of raw stainless steel in [001] and [111] direction. j) Pole figures of ODS material in [001] and [111] direction. [13, 489]

As evident from the inverse pole figures and misorientation maps a clear impact of oxide nanoparticles on the grain size of the solidified microstructure can be observed. While raw stainless steel is characterized by large grains (Fig. 51a) the introduction of oxide nanoparticles results in pronounced reduction of the grain size of the ODS steel (Fig. 51b). The utilization of LSPC processed powder material for L-DED processing allows the formation of slightly smaller grains compared to MA-processed powder material (Fig. 51c), which might stem from more homogeneous dispersion of oxide nanoparticles on the metallic powder particles (Fig. 30) and furthermore in the consolidated metallic matrix (Fig. 47).

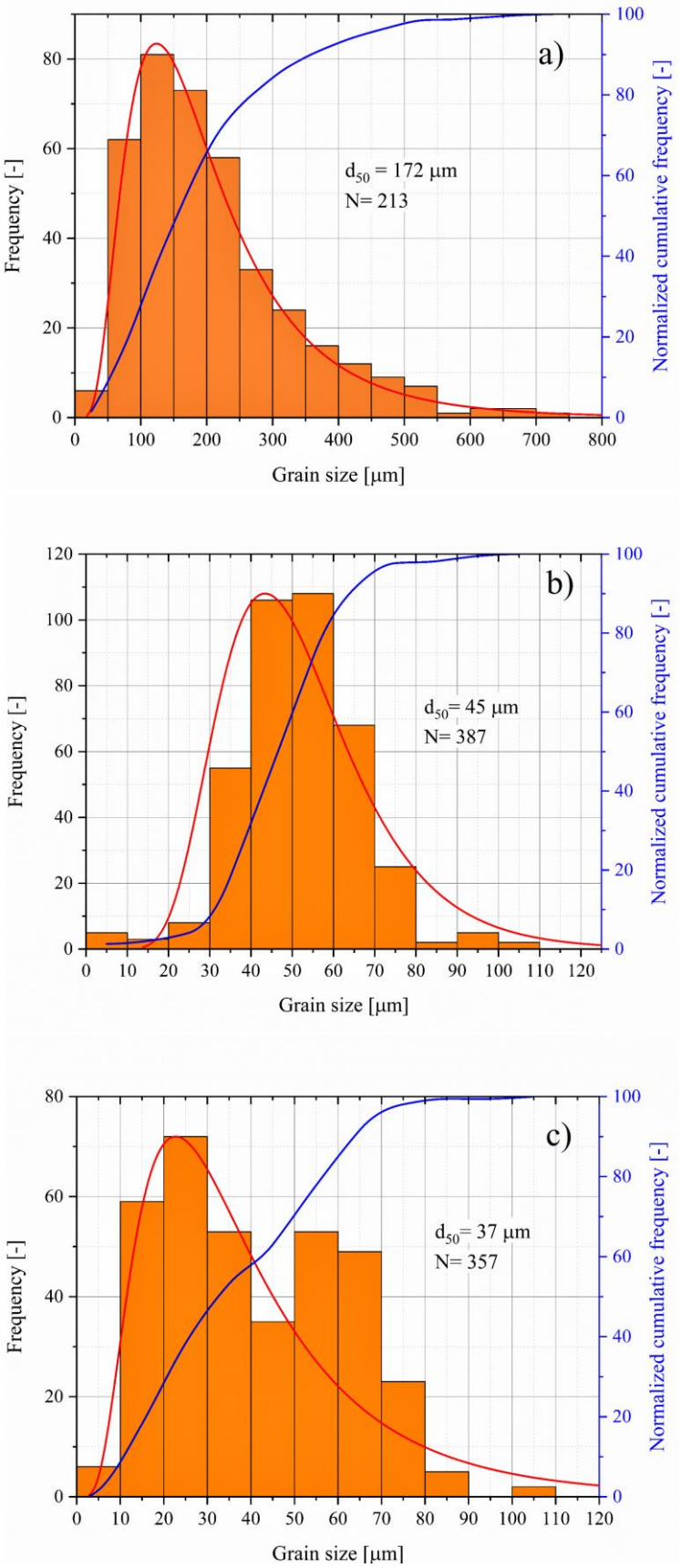

Fig. 51: Histograms of the grain size distribution of L-DED processed material with small beam diameter (0.6 mm): a) Specimen manufactured from raw stainless steel powder material. b) Specimen manufactured from MA-manufactured powder material. c) Specimen manufactured from LSPC-manufactured powder material.

6.3.3 HSLC processing of ODS specimen

Contains content from the following publication:

Manufacturing oxide-dispersion-strengthened steels using the advanced directed energy deposition process of high-speed laser cladding

M. B. Wilms[a,*], N. Pirch[b], B. Gökce[c]

[a]Material Science and Additive Manufacturing, School of Mechanical Engineering and Safety Engineering, University of Wuppertal, Gaußstr. 20, 42119 Wuppertal, Germany
[c]Fraunhofer Institute for Laser Technology, Steinbachstr. 15, 52074 Aachen, Germany
[c]Material Science and Additive Manufacturing, School of Mechanical Engineering and Safety Engineering, University of Wuppertal, Gaußstr. 20, 42119 Wuppertal, Germany

Article Information

Article history:
Received 8 December 2021
Accepted 10 June 2022
Available online 28 June 2022

DOI: 10.1007/s40964-022-00319-1
Progress in Additive Manufacturing

**Corresponding author*
mwilms@uni-wuppertal.de

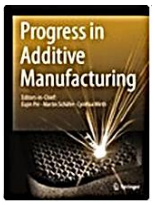

Abstract

In this work, we demonstrate the feasibility of manufacturing an iron-based oxide-dispersion-strengthened (ODS) PM2000 composite material with the chemical composition of Fe20Cr4.5Al0.5Ti + 0.5Y_2O_3 (in wt.%) via the advanced directed energy deposition (DED) process of high-speed laser cladding (HSLC). The characteristic high solidification rates of HSLC processes allow the successful dispersion of nano-scaled yttrium-based oxides in the ferritic stainless steel matrix. The effective suppression of nano-particle agglomeration during the melting stage, which is frequently observed in conventional DED processes of ODS materials, is reflected by smaller dispersoid sizes and corresponding higher hardness of manufactured specimen compared to DED-manufactured counterparts.

Own contribution: Sample preparation, writing and editing of the original draft and revised manuscript.

The high-speed laser cladding (HSLC) process is a novel, L-DED inspired additive manufacturing process, also known as EHLA [566], and characterized by increased process speeds compared to conventional L-DED processes. This enables significantly higher cooling rates, comparable to those in L-PBF processes. [567] and therefore offers the opportunity to improve the suppression of agglomeration of Y_2O_3 nanoparticles in the melting stage. Fig. 52 provides LOM images of cross-sections consisting of two subsequently manufactured layers for raw stainless steel (Fe20Cr4.5Al0.5Ti (wt.%)) (Fig. 51a) and oxide-dispersed stainless steel (Fig. 52b) using the process parameters in Table 25. The non-reinforced coating (Fig. 52a) features full metallurgical bonding to the substrate material without any sign of delamination or defects in the fusion zone. The full double-layered coatings are found to be almost defect-free, exhibiting no cracks and low porosity, resulting in a relative density of 99.94%.

Table 25: Process parameter set for manufacturing of double-layered specimen from raw stainless steel and oxide-dispersed Fe20Cr4.5Al0.5Ti (wt.%).

Process parameter	Laser power	Rotation speed	Traverse speed	Powder feed	Beam diameter	Shielding / Carrier gas
Unit	W	rpm	mm/min	g/min	mm	l/min
Value	1099	150	45	5.33	0.6	15/7

The curvature of the fusion zone proves that substantial melting of substrate material occurred, resulting in an effective layer height of approx. 100 µm. The fact that the upper layer exhibits a larger layer height indicates significant re-melting of the previously applied layer. A strong texture in build direction (BD) is observed, indicating that the main heat diffusion direction is perpendicular to the building direction. The inclination of the grain growth direction of grains starting at the substrate-cladding interface is caused by the curvature of the melt pool. [568, 569]

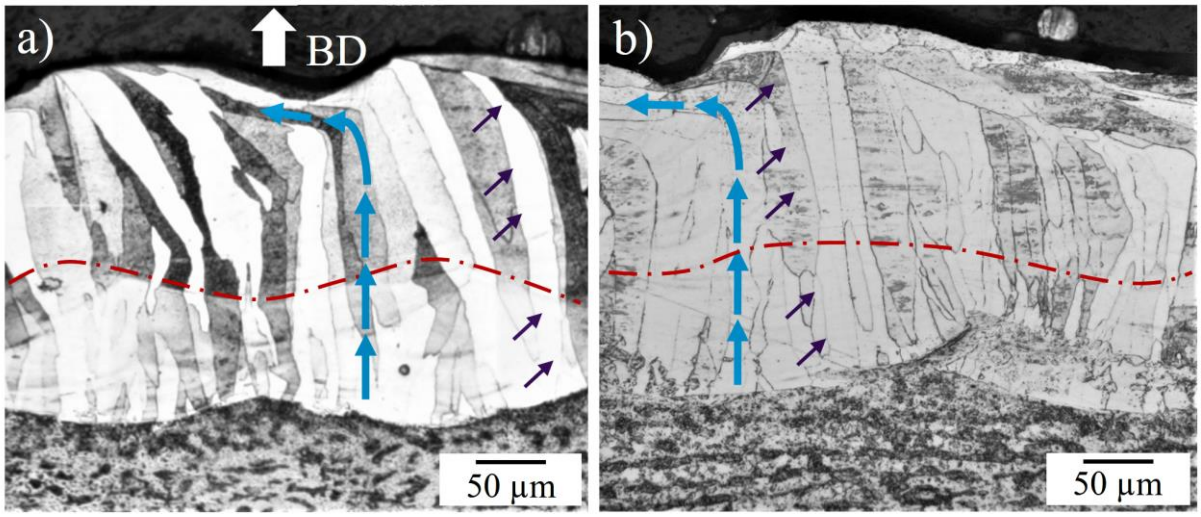

Fig. 52: LOM images of etched cross-sections of non-reinforced (a) and oxide reinforced double-layered coatings (b) manufactured by HSLC from MA-generated powder material. The red line indicates the boundaries between both subsequently deposited layers. Blue arrows mark the growth direction of the formed grains showing the abrupt change of growth direction in the top part of the deposited material. Purple arrows identify a single grain showing full epitaxy by growing from the substrate interface to the top of the specimen. [487]

The curvature of the melt pool is directly connected with the melt pool geometry and describes the solid-liquid interface from the bottom to the surface of the melt pool during the deposition process. [570] The grain growth direction is not altered by the layer boundary (indicated by the red line), and epitaxial grain growth (indicated by purple arrows) is observed regularly, comparable to L-DED manufactured specimen. However, the growth direction changes significantly parallel to the traverse direction in the top area of the cladding (indicated by blue arrows). The abrupt change of the grain growth orientation can be explained by the curvature of the melt pool boundary and the energetically preferred growth

direction, which is the smallest angle to the temperature gradient [571]. Because all these features can also be observed in the oxide reinforced stainless steel (Fig. 52b), thus it can be concluded that no apparent change between reinforced and non-reinforced cladding could be observed on LOM scale. However, SEM investigations allow the determination of the solidified grain structure, which shows a significant grain size reduction in oxide nanoparticle added material (Fig. 53b) compared to non reinforced material (Fig. 53a).

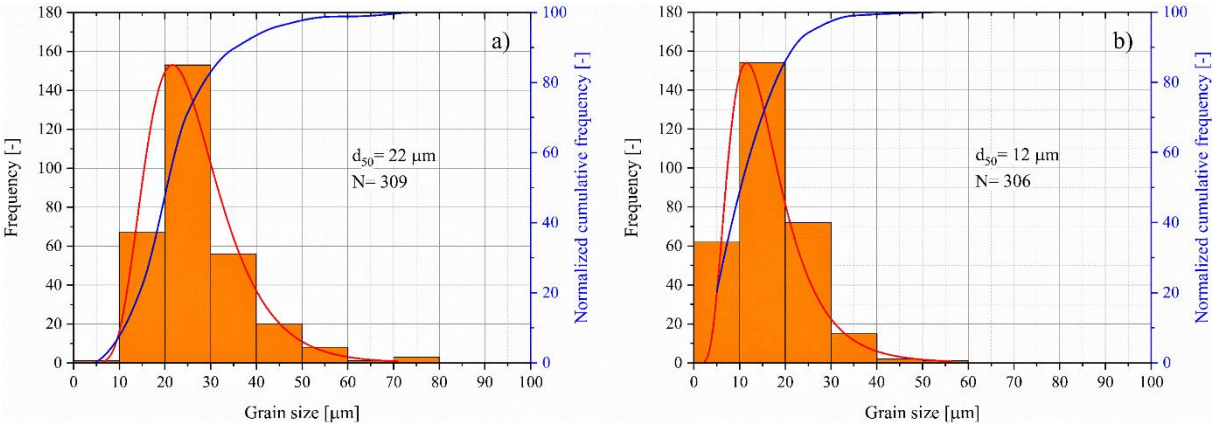

Fig. 53: Histograms of the grain size distribution of HSLC processed material: a) Specimen manufactured from raw stainless steel powder material. b) Specimen manufactured from MA-manufactured powder material.

Additional features of the microstructure of the raw stainless steel is shown in Fig. 54a,b and is characterized by grain boundaries (marked with yellow arrows) in the build direction and a predominantly dendritic solidification structure. Within the microstructure, no precipitations or dispersoids can be detected (Fig. 54b). The sporadically observed flakes (green circles) are identified as remnants of the etching process and are therefore discarded in the microstructure analysis.

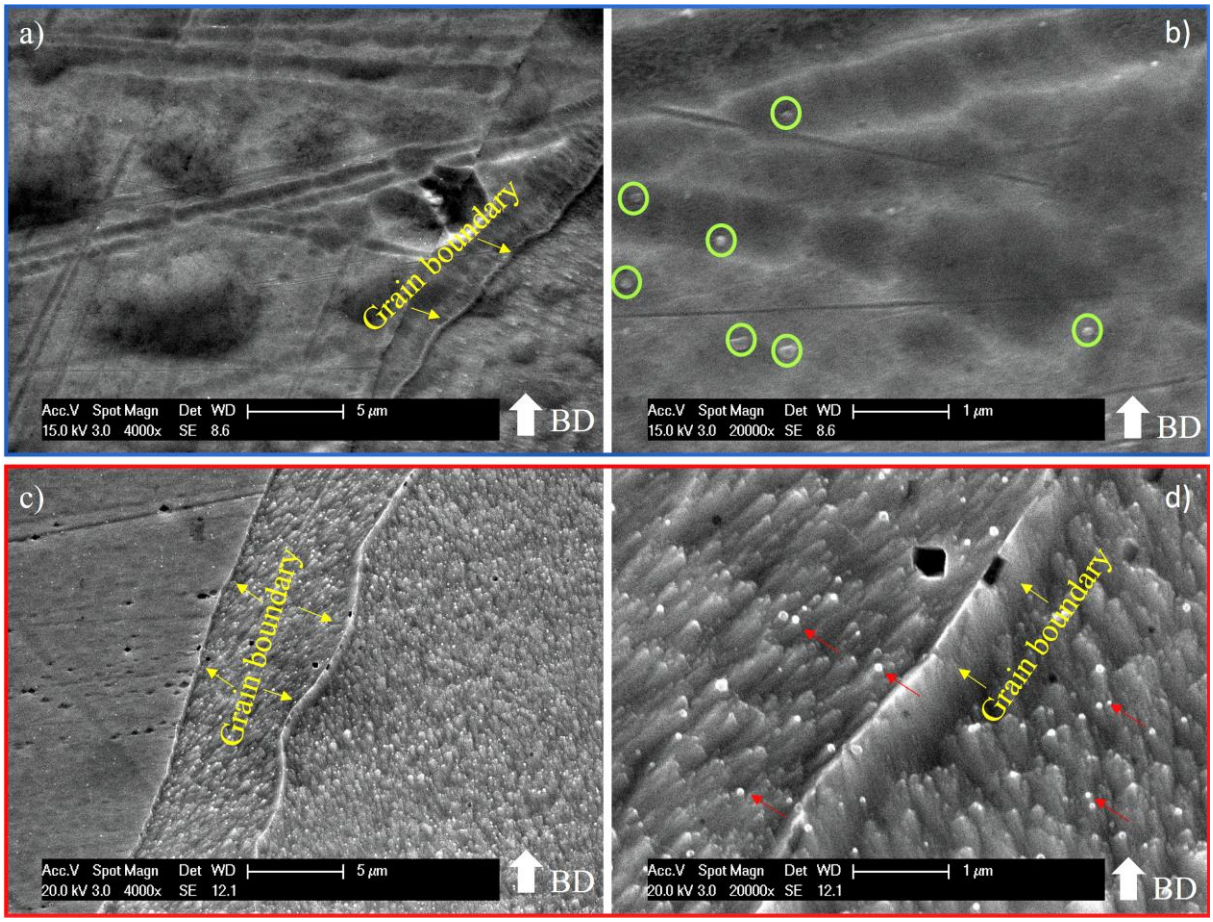

Fig. 54: SEM images (SE-mode) of the microstructures of HSLC manufactured raw stainless steel with different magnifications (a, b). Corresponding SEM images of oxide reinforced coatings (c,d) with indicated grain boundaries (yellow arrows) and dispersed oxide nanoparticles (red arrows). [497]

SEM images of oxide dispersed material (Fig. 54c,d) reveal the presence of sub-micrometer scaled oxide particles homogeneously distributed inside the grains, appearing as bright white spots throughout the microstructure. The microstructure evolution is not affected by the presence of the nanometer-scaled oxide particles, which do not appear to act as a site for heterogeneous nucleation of the ferritic stainless steel matrix. This may be attributed to the low wettability of Y_2O_3 by iron-chromium melts [132]. The size distribution of the dispersed oxide nanoparticles, shown in Fig. 55, confirms the reduction of the nanoparticles size of HSLC processed specimen (Fig. 55b) compared to L-DED manufactured specimen with identical beam diameter (Fig. 55a), proving the ability of high process speeds to suppress agglomeration of oxide nanoparticles.

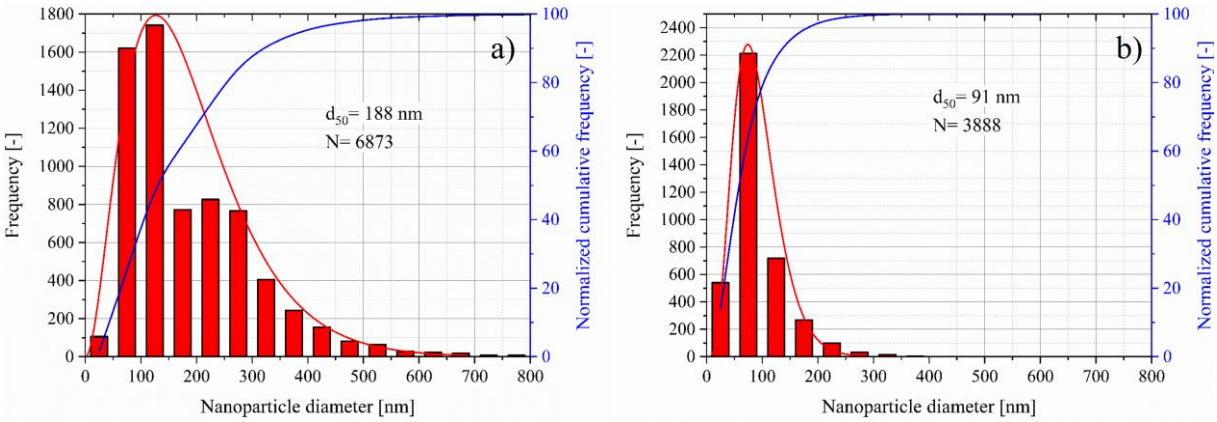

Fig. 55: Histograms showing the nanoparticle size distribution captured from SEM images of etched cross sections using the image analysis software "ImageJ". a) L-DED processed specimen using a reduced beam diameter (0.6 mm), b) HSLC processed specimen using an identical beam diameter of 0.6 mm.

However, smaller nanoparticles may also be present, which cannot be resolved with the used SEM system and thus are not captured by the image analysis software "ImageJ". However, the nanoparticles found in HSLC manufactured material are larger than nanoparticles found in conventionally manufactured PM2000 material with approx. 60 nm [157]. The process-related refinement of dispersed oxide particles in HSLC compared to L-DED are examined by modelling of the respective temperature distribution in the melt pool, the cooling rate, and the solidification rate encountered in the high-speed deposition process (Fig. 56a-c).

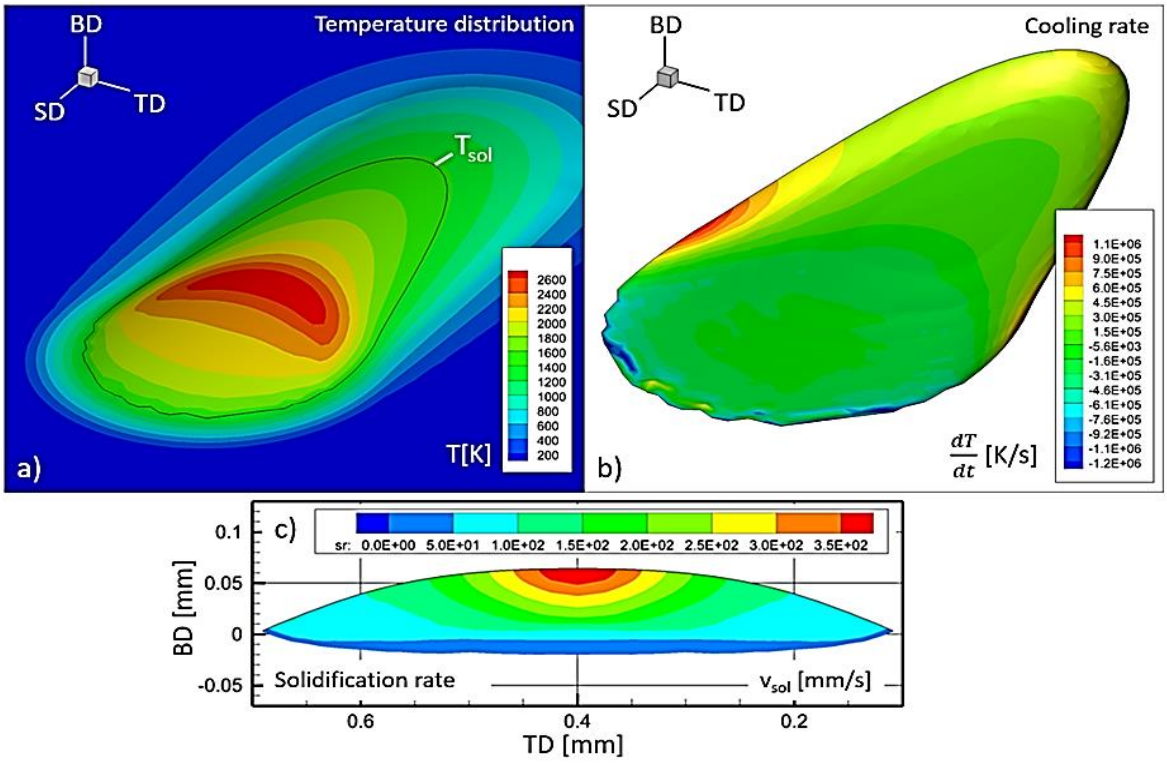

Fig. 56: Results of the FEM melt pool simulations. a) Temperature distribution of a single track with laser movement in positive scanning direction (SD). The melt pool dimensions are indicated by the solidus temperature (T_{sol}). b) Cooling rate in the

solidification zone. Negative cooling rates can be considered as heating rates by the laser irradiation. c) Solidification rate (v_{sol}) plotted in traverse (TD) vs. build direction (BD). [487]

Comparing the calculated process-related maximum values of melt pool temperature, cooling rate and solidification rate (Fig. 56) for HSLC with L-DED processing proves the higher solidification kinetics for HSLC processes and thus may explain the significant reduction of the formed nanoparticle diameters. (Table 26)

Table 26: Maximum process values of melt pool temperature, cooling rate and solidification rate, determined by FEM-based modelling for L-DED and HSLC processing of the stainless steel material. Data extracted from FEM modelling in Fig. 45 (L-DED) and Fig. 56 (HSLC).

Process value	Unit	L-DED	HSLC
Melt pool temperature	K	$3 \cdot 10^3$	$2.6 \cdot 10^3$
Cooling rate	K/s	$6 \cdot 10^4$	$1.1 \cdot 10^6$
Solidification rate	mm/s	$3 \cdot 10^1$	$3.5 \cdot 10^2$

The maximum melt pool temperature directly influences the melt viscosity and thus, enhances oxide nanoparticle mobility in the melt pool. Therefore, low melt pool temperatures are considered favourable for preventing nanoparticle agglomeration. In Fig. 56, high temperature gradients in HSLC-formed melt pools are observed, which are believed to cause severe melt pool dynamics induced by marangoni convection, effectively preventing particle agglomeration. It is hypothesized that even the disruption of occasionally formed agglomerates by marangoni-induced shear forces might occur. Another factor for successful dispersion of nanoparticles are high cooling and solidification rates limiting the existence time of the melt pool significantly inhibiting diffusion-controlled agglomeration mechanisms. Nanoparticles dispersed in the melt pool are instantaneously captured by the advancing solidification front and integrated in the mushy zone inhibiting the nanoparticles' mobility and therefore preventing agglomeration tendencies. Low solidification rates allow nanoparticles to agglomerate in the melt pool impeding capture by the mushy zone and are consequently being pushed in front of the solidification front [571] and ultimately forming slag layer, as observed in L-DED processed specimen with large beam diameters (Fig. 41c).

The chemical composition of the dispersoids in the ODS specimen are evaluated using EDS analysis on rarely observable agglomerates, revealing enrichments of yttrium, oxygen and titanium. This indicates the formation of $Y_2Ti_2O_7$ or Y_2TiO_5 compounds typically found in titanium-alloyed Fe-Cr-based ODS steels [130, 131]. The formation of Y-Al-O particles, found in Al-alloyed Fe-Cr-based ODS steels [572, 573], could not be observed, which is in contrast with L-DED processed specimen, where predominantly aluminium-rich yttrium oxide particles are found (Fig. 48). One possible explanation for this behaviour may lie in the susceptibility of aluminium to evaporate during additive manufacturing processes, particularly at higher laser energy intensities [574, 575, 576], in HSLC (3232 $W \cdot mm^{-2}$) compared to L-

DED (1088 $W \cdot mm^{-2}$). Consequently, the aluminium content of the alloy is lowered, increasing the probability for the formation of titanium-rich yttrium oxide nanoparticles.

6.3.4 L-PBF of ODS material

L-PBF of oxide-dispersion strengthened stainless steel is performed analogous to the non-reinforced material with the process parameter set, shown in Table 27. Both MA and LSPC manufactured powder materials are used for the production of cubic specimen (10 mm^3). As evident from Fig. 57a, b specimens with high relative densities ($\rho_{rel, MA}$= 99.98%, $\rho_{rel, LSPC}$= 99.99%) using the process parameter set shown in Table 27. Accordingly, no deteriorating effect of the less spherical composite powder particles of the MA manufactured powder material on processability can be observed. The microstructure is characterized by fine dendrites, significantly finer (approx. by 70 %) compared to dendrites observed in L-DED fabricated specimens.

Table 27: Process parameter set for manufacturing of specimen from raw stainless steel and oxide-dispersed Fe20Cr4.5Al0.5Ti (wt.%) using L-PBF. [13]

Process parameter	Laser power	Scan speed	Hatch distance	Layer thickness	Beam diameter	Hatch rotation	Scan strategy
Unit	W	mm/s	µm	µm	µm	°	-
Value	160	800	60	30	80	34	Stripes

Moreover the dendrites in L-PBF manufactured material are aligned strictly parallel to the build direction and the dendrite growth path is not interrupted by melt pool boundaries, showing that that epitaxial growth conditions are equally present during L-DED and L-PBF processing (Fig. 57c,d). Interestingly, horizontally aligned cracks are frequently observed during the fabrication of larger volumes, originating from the lateral edge of the printed material. (Fig. 57e-g)

Furthermore, the crack path is not affected by grain- or interlayer boundaries (Fig. 58), proving that transgranular crack mechanisms are dominant. Based on the crack path observations, the present crack structures are considered as cold cracks, which are frequently observed in L-PBF of high strength steels. [577, 578, 579, 580]

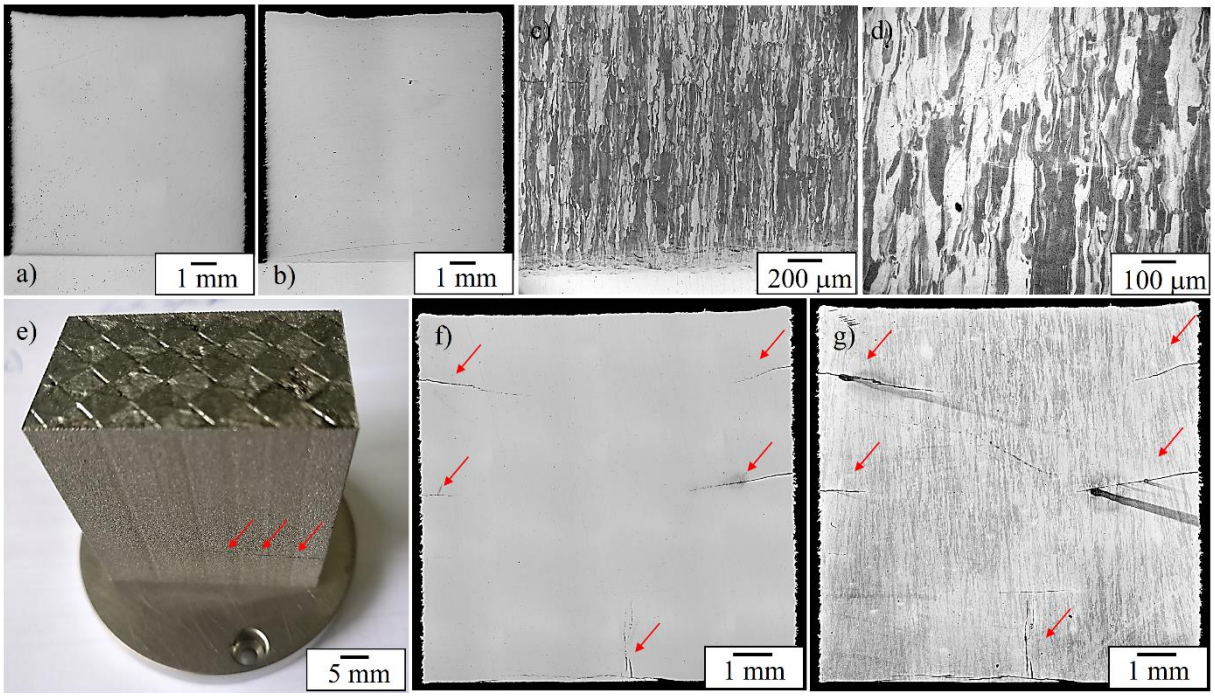

Fig. 57: a) LOM image of a cross-section of a specimen manufactured using MA-manufactured powder material. b) LOM image of a cross-section of a specimen manufactured using LSPC-manufactured powder material. c) Etched cross-section of the specimen depicted in a) showing the [001] oriented grain structure parallel to the build direction. d) Etched cross-section of the specimen depicted in b) showing the [001] oriented grain structure parallel to the build direction. e) Large bulk volume (approx. 28 x 16 x 20 mm^3), manufactured from MA-manufactured powder material, showing a horizontally grown crack (marked with red arrows). f) Cross section of a specimen manufactured from MA-manufactured powder material showing multiple horizontal cracks (marked with red arrows). The crack aligned in BD presumably stems from mechanical forces introduced during the separation process of the printed part from the substrate material. g) Etched cross section of the specimen depicted in f).

The increased cold crack susceptibility of nanoparticle dispersed stainless steel compared to raw stainless steel may be attributed on the one hand to the introduction of nano-scaled oxide particles, leading to significant strengthening, but also embrittlement of the material (cf. chapter 2.1) and consequently the proneness for cold cracking.

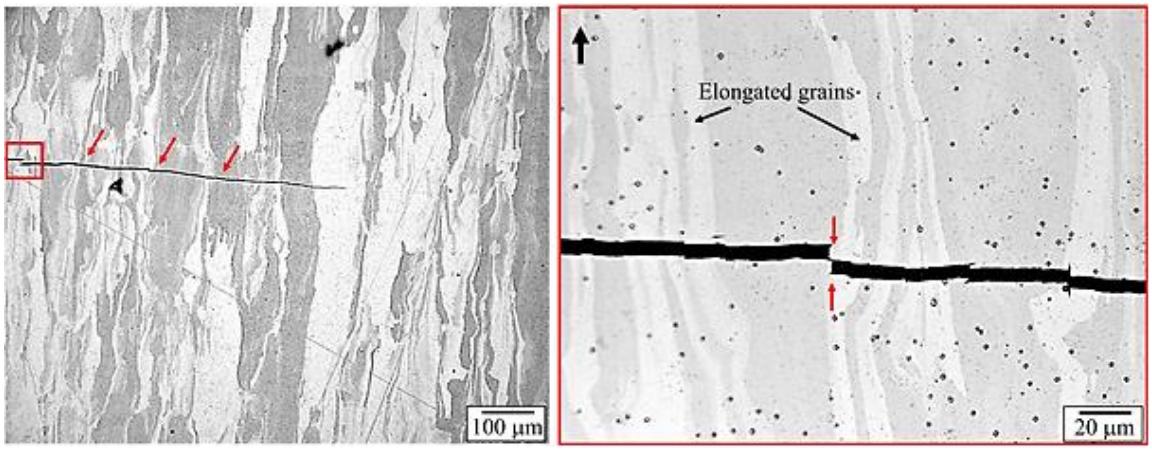

Fig. 58: High magnification LOM images of etched cross-sections showing the crack path and the elongated grain structure. The build direction is indicated by the black arrow in the upper left corner of the right image.

On the other hand, the solidification conditions in the L-PBF with high melt pool temperatures up to $2 \cdot 10^3$ K (Fig. 59a), high solidification front velocities (Fig. 59c) and high cooling rates of up to $2 \cdot 10^6$ K/s (Fig. 59b) in BD (cf. Fig. 59d-f) result in severe temperature gradients, ultimately leading to high residual stresses. Consequently, the probability of thermally induced cold cracking is significantly increased compared to L-DED processing, which is particularly the case in the production of complex or large-volume components due to local stress concentration on geometrical notches and progressing stress accumulation during the building process. [581] However, it should be noticed, that the observed cracks originate in the lateral region of the printed parts (Fig. 57e-g, Fig. 58), which might be explained by geometric notch effects stemming from the characteristic high surface roughness of L-PBF-produced specimen without contour exposure. [582, 583] Crack initiation in the vicinity of single nanoparticles, agglomerated clusters [584, 585] or pores [586] are not observed in L-PBF manufactured specimens.

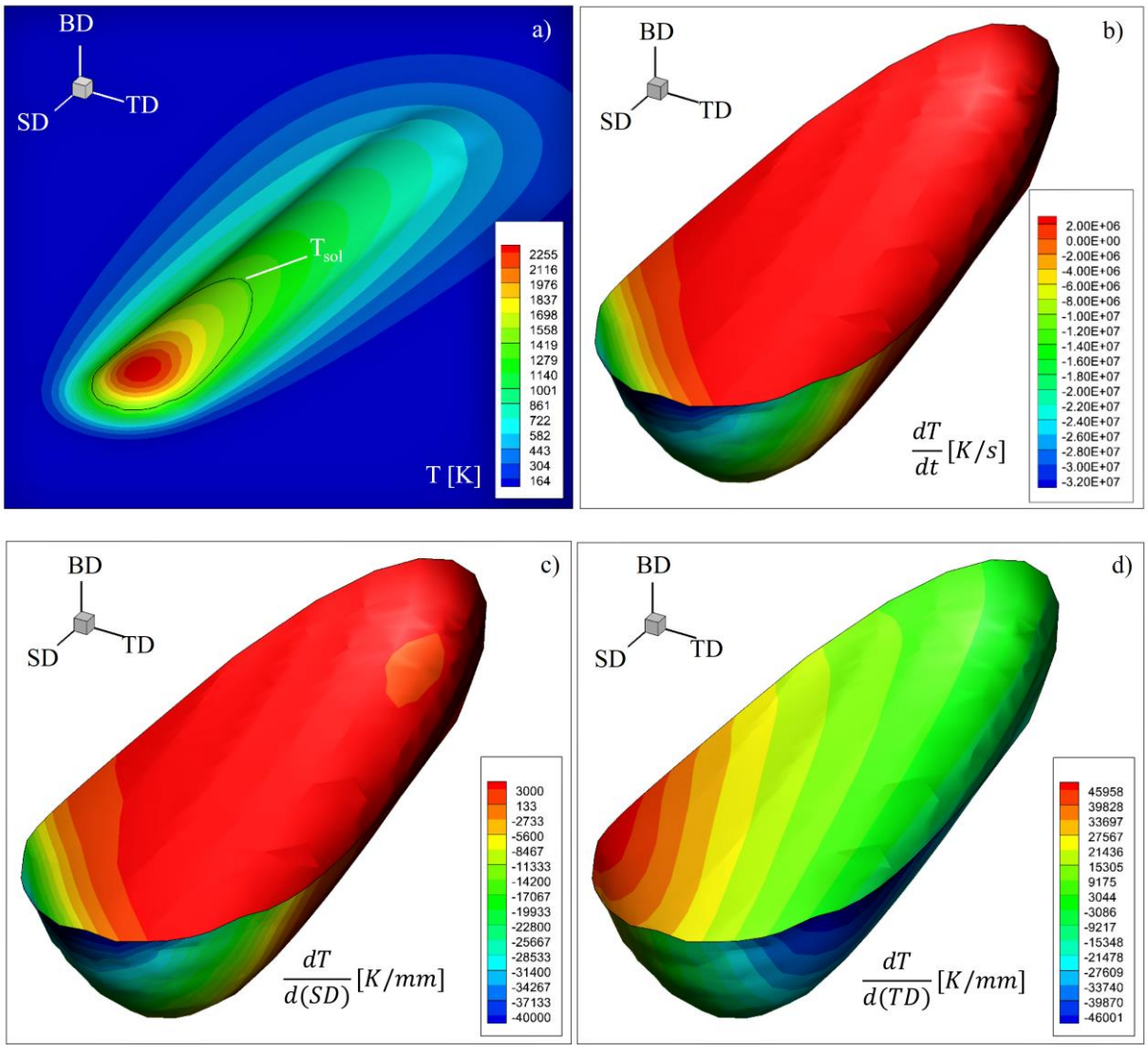

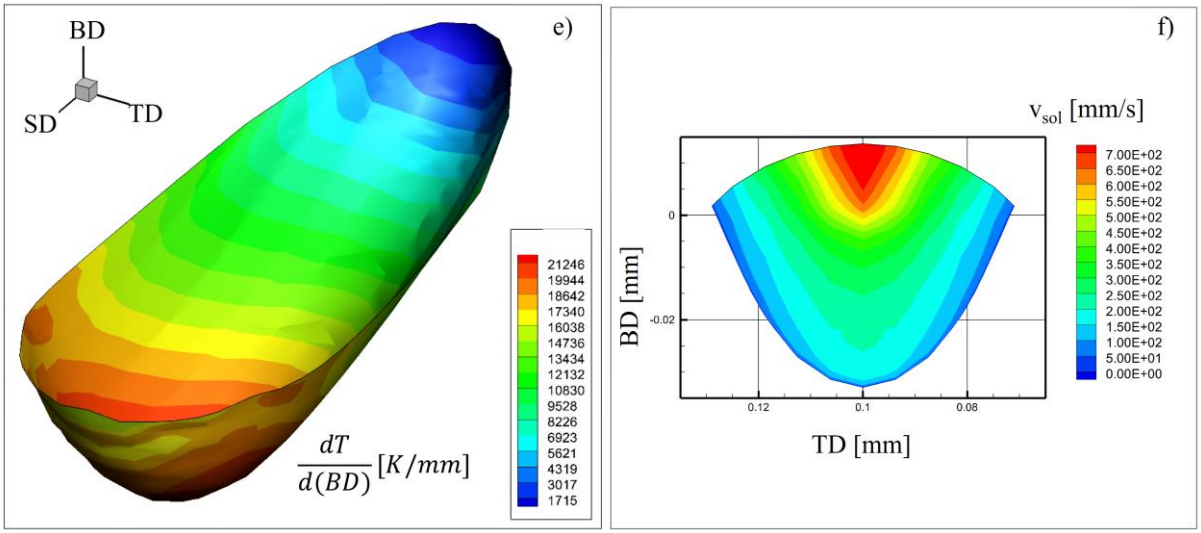

Fig. 59: FEM melt pool solidification simulations for L-PBF manufactured material: a) Melt pool temperature with solidus line (T_{sol}). b) Cooling rate along the solidification front. Negative cooling rates can be considered as heating rates generated by the laser irradiation. c-e) The temperature gradients plotted in every direction in space $\frac{dT}{d(SD)}$, $\frac{dT}{d(TD)}$ and $\frac{dT}{d(BD)}$. f) Velocity of the solidification front (v_{sol}), plotted in build direction (BD) over the traverse direction (TD). [13]

Based on the FEM simulations (Fig. 57) the maximum values of the maximum values for melt pool temperature, cooling rate and solidification rates can be deduced and compared with results from Table 28, confirming higher cooling and solidification rates in L-PBF manufactured specimens.

Table 28: Maximum process values of melt pool temperature, cooling rate and solidification rate, determined by FEM-based modelling for L-DED, HSLC and L-PBF processing of Fe20Cr4.5Al0.5Ti (wt.%) stainless steel. [13, 487]

Process value	Unit	L-DED	HSLC	L-PBF
Melt pool temperature	K	$3 \cdot 10^3$	$2.6 \cdot 10^3$	$2.3 \cdot 10^3$
Cooling rate	K/s	$6 \cdot 10^4$	$1.1 \cdot 10^6$	$2 \cdot 10^6$
Solidification rate	mm/s	$3 \cdot 10^1$	$3.5 \cdot 10^2$	$7 \cdot 10^2$

Thus, the microstructure is characterized by a high number of nano-scaled particles embedded in the stainless steel matrix, which are visualized by the etching of polished cross-sections prior to SEM examination. The oxide nanoparticles become visible as bright white spots (Fig. 60) in SE-mode. Both specimens produced from mechanically alloyed- and LSPC-manufactured powder materials are characterized by a large population of homogeneously dispersed nanoparticles. No enrichment at grain boundaries (marked with yellow dotted lines) or melt pool boundaries (marked with a blue dashed line in Fig. 60a) can be observed in parts manufactured from MA- and LSPC-processed powder materials (Fig. 60b). Occasionally larger agglomerates up to diameters of 200 nm are observed, which are significantly smaller than agglomerates found in L-DED processed material. It should also be noted, that small slag layer deposits are rarely observed on L-PBF manufactured specimen from MA-manufactured material (Supplementary S21).

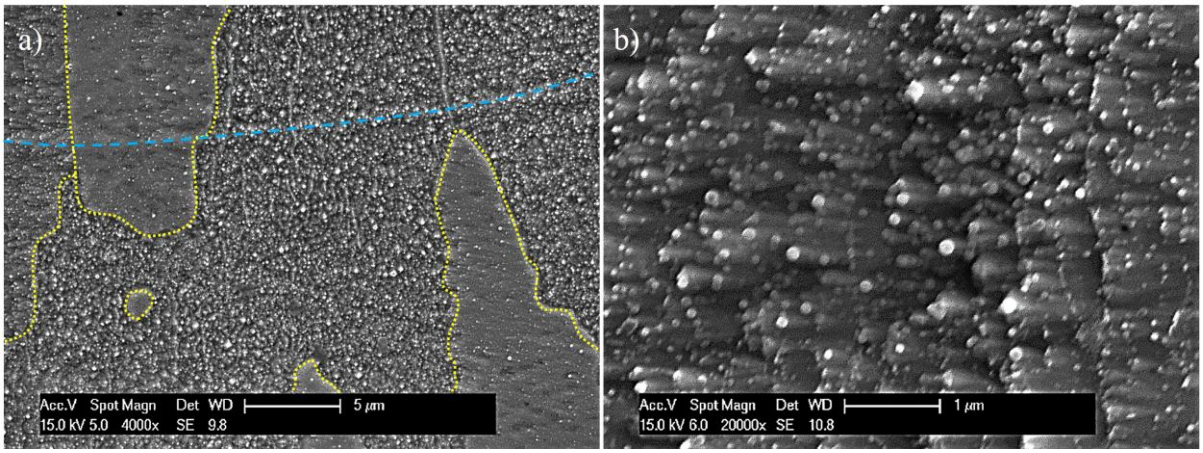

Fig. 60: SEM images (SE-mode) of etched cross-sections showing dispersed oxide nanoparticles (white spots) in the stainless steel matrix: a) Microstructure manufactured from MA-manufactured powder material. Grain boundaries are highlighted with yellow dotted lines. The melt pool boundary is indicated with the blue dashed line. b) Microstructure manufactured from LSPC-generated powder material.

In Fig. 61 the particle size distributions of oxide nanoparticles in L-PBF processed material using MA- and LSPC-manufactured powder feedstock is depicted. It is evident, that the utilization of LSPC-prepared powder materials result in a significantly larger fraction of ultra-fine nanoparticles (below 50 nm) compared to specimen, manufactured from MA processed powder materials (cf. Fig. 61a,b). Consequently, specimen manufactured from LSPC-generated powder materials are expected to result in superior mechanical properties of printed parts. However, the resulting nanoparticle population, consisting of smaller nanoparticles may also be attributed to the performed laser fragmentation process prior to supporting procedure of the nanoparticles on the surface of the micrometer stainless steel powder particles. It is hypothesized, that the inevitable agglomeration of the oxide nanoparticles during the melting stage in the L-PBF process is partly compensated by laser fragmentation of the nanoparticles prior to supporting, ultimately resulting in finer nanoparticles dispersed in the stainless steel matrix. This becomes evident when comparing the capturing frequency of nanoparticles below 50 and 100 nm in Fig. 61 in L-PBF manufactured specimen from both feedstocks and also evident from higher number density of dispersed nanoparticles in the stainless steel matrix, indicated by lower interparticle spacing of material manufactured from laser fragmentated nanoparticles compared to ultrasonificated nanoparticles in L-DED manufactured material (Supplementary S22). It should be noted, that the interparticle spacing is a decisive parameter for dispersion strengthening by the Orowan mechanism, as it defines the free path for dislocation motion between particles and thus controls the geometry of the dislocation bow. [592]

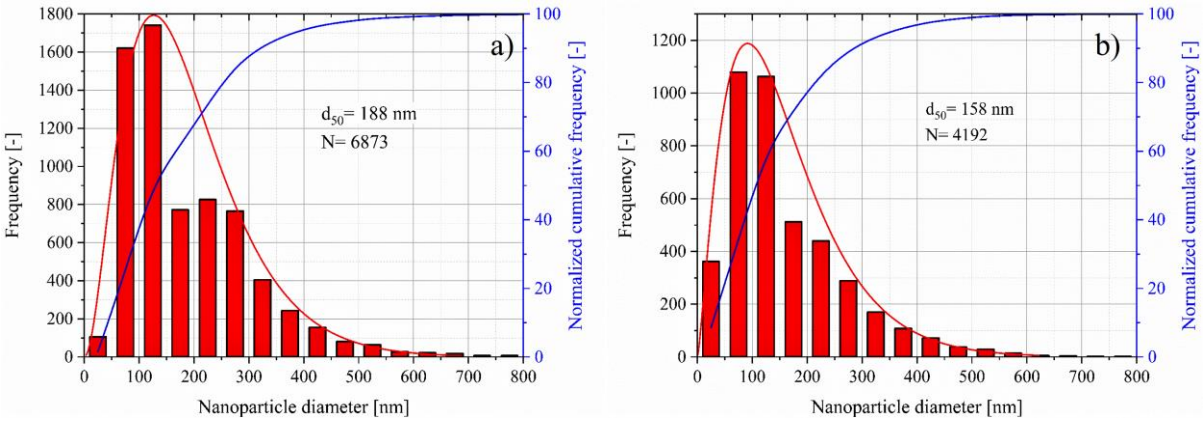

Fig. 61: Histograms showing the nanoparticle size distribution captured from SEM images of etched cross sections from L-PBF manufactured specimens using the image analysis software "ImageJ". a) Specimen manufactured from MA powder material. b) Specimen manufactured from LSPC-generated powder material.

However, L-PBF processed specimens show oxide particle populations with significantly smaller particle sizes, compared with the powder-blown additive manufacturing processes of L-DED and HSLC, which is evident from the summarized median particle diameters of the nanoparticle populations (Fig. 62).

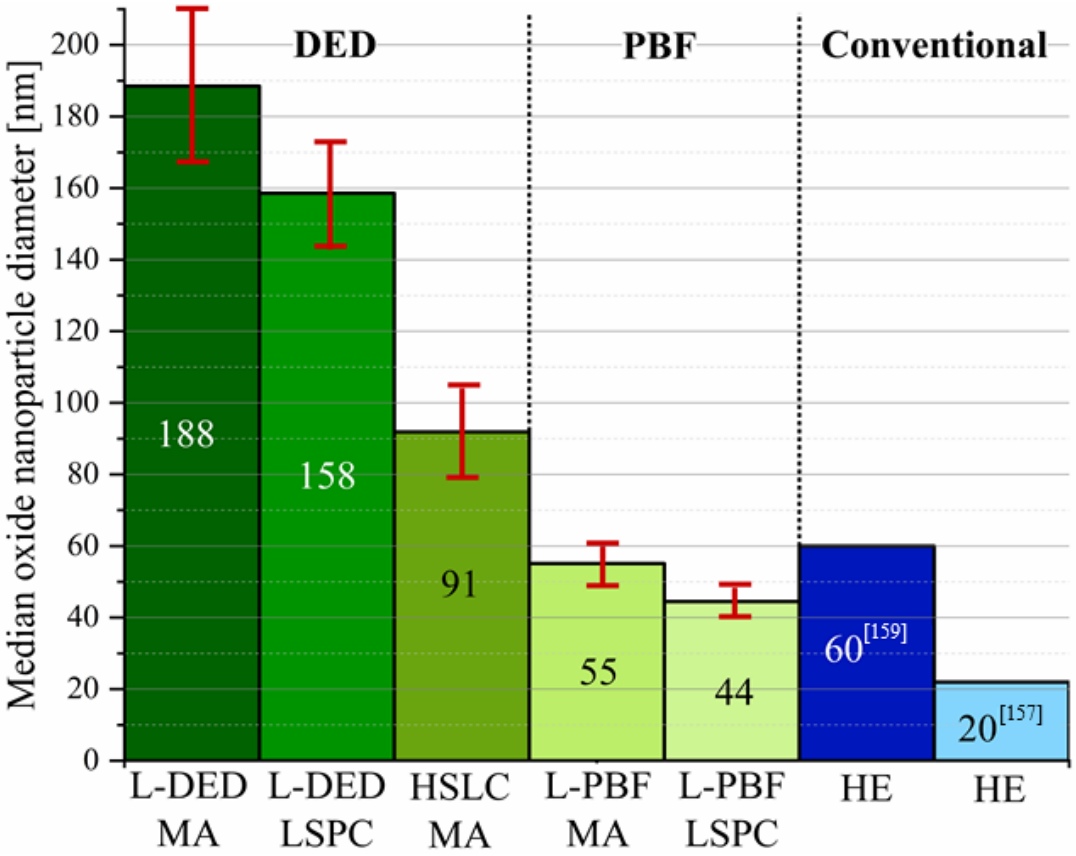

Fig. 62: Depiction of the median oxide nanoparticle size dispersed in stainless steel matrix for the AM processes L-DED, HSLC and L-PBF, manufactured from MA- and LSPC-generated composite powder materials (green bars) and hot-extruded material from [157] and [159] (blue bars).

These results are in accordance with results extracted from literature (cf. Table 7 and 9), where L-PBF processing of ODS alloys results in smallest nanoparticles of all examined AM processes. The reason for this behaviour are attributed to the higher cooling rates and solidification front velocities in L-PBF (Fig. 59b,c) increasing the efficiency of trapping and engulfment of oxide nanoparticles in the stainless steel matrix during solidification compared to L-DED. In addition to the highly efficient dispersion of fine oxide nanoparticles, the rapid solidification conditions in L-PBF processes moreover affect the microstructural evolution. High cooling rates typically result in high undercooling and thus promote a high rate of grain nucleation in front of the solidification interface during solidification resulting in significant grain refinement, as evident from Fig. 63. Due to higher cooling rates in L-PBF processes compared to L-DED processes, grain refining is more pronounced in L-PBF, which is also observed for other material systems [588]. A statistical analysis of etched traverse sections using the “ImageJ” image analysis software demonstrates, that the introduction of nanoparticles is also associated with strong grain refinement (Fig. 63b,c) compared to L-PBF printed raw stainless steel material (Fig. 63a). Analogue to L-DED manufactured ODS specimens, LSPC-manufactured powder materials result is slightly smaller grain sizes, presumably due to more homogeneous dispersion of oxide nanoparticles on the metallic powder particles (Fig. 30) and furthermore in the consolidated metallic matrix (Fig. 59).

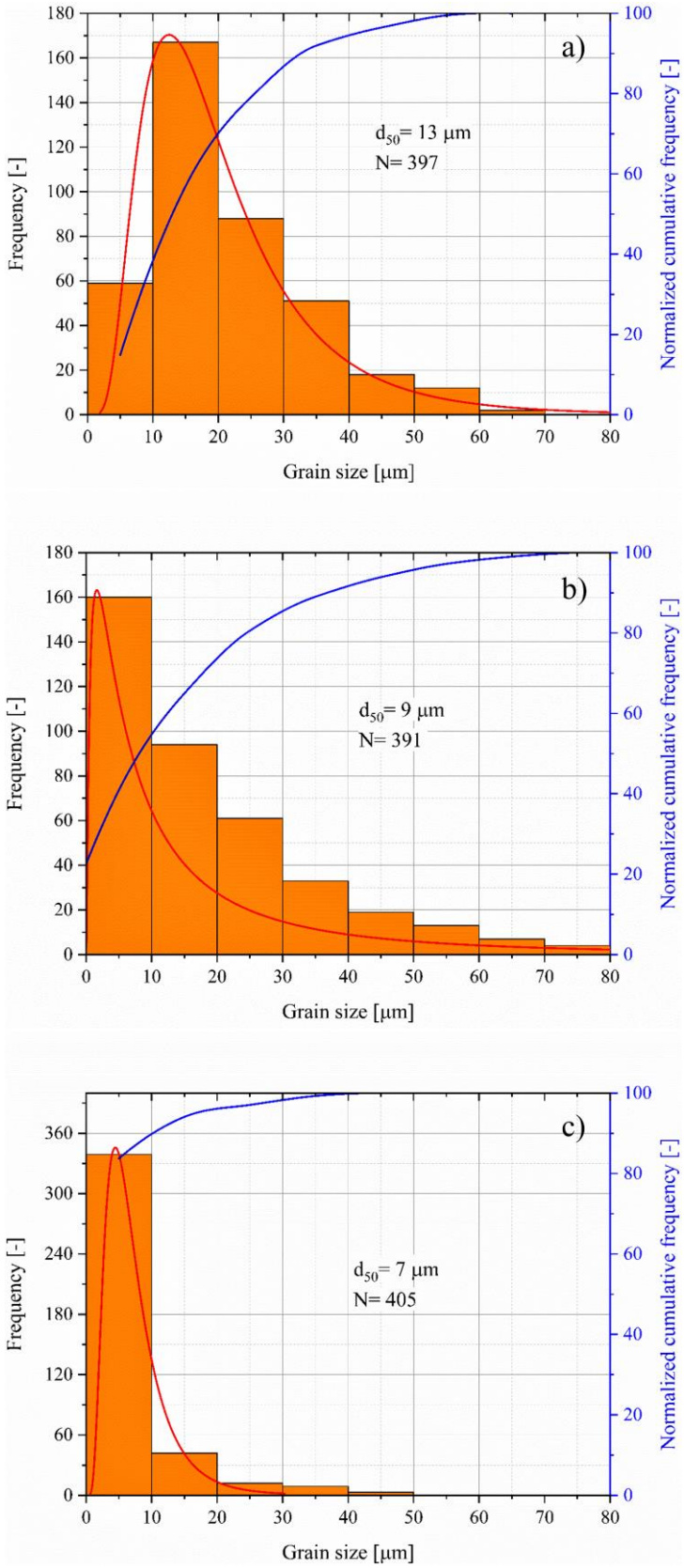

Fig. 63: Histograms of the grain size distribution of L-PBF processed material: a) Specimen manufactured from raw stainless steel powder material. b) Specimen manufactured from MA-manufactured powder material. c) Specimen manufactured from LSPC-manufactured powder material.

The grain structure is additionally characterized by an underlying substructure, which becomes evident from different grey-scales in the SEM images (Fig. 64a,b), which may stem from a high dislocation density forming a high number of low angle grain boundaries (LAGB) (Fig. 65e) during solidification. The introduction of oxide nanoparticles furthermore affects the orientation of formed grains, which is evident from EBSD measurements from longitudinal- (Fig. 65a,b) and cross section planes (Fig. 65c,d), showing a strong texture along the longitudinal direction. For L-PBF, there is only a small difference in the grain size distribution of the ODS, which differs from L-DED processed specimen, where the introduction of oxide nanoparticles leads to an intensification of the texture (Fig. 50).

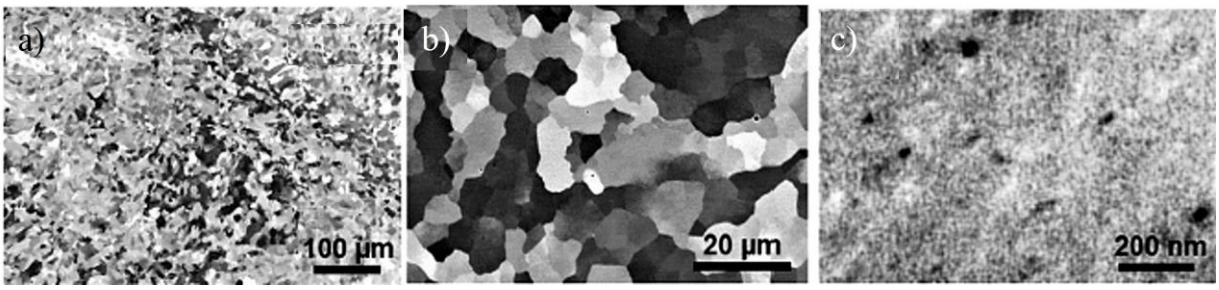

Fig. 64: a-c) SEM images (BSE-mode) with different magnifications, showing the grain structure and subgrain structure (indicated by different grey scales within single grains) and oxide nanoparticles (black dots in c)). [13]

Including the global texture measurement from XRD examinations and represented by the pole figures (Fig. 65f,g), it appears that the raw steel shows a sharper fiber texture in [001] direction as compared to the ODS steel. This is also observable in the inverse pole figure maps, which show more colour variations for the ODS steel. Interestingly the change of orientations (Fig. 65d) appears to be connected to the high density of HAGB (>15° misorientation between adjacent grains) as evident from the misorientation map and indicated by the black dotted line (Fig. 65e). One possible explanation might stem from higher undercooling in L-PBF compared to L-DED, favouring homogeneous nucleation of new grains over heterogeneous nucleation on oxide particles in L-DED. The high undercooling, stemming from the steep temperature gradient, might also result in high internal stress, which results in high dislocation densities across the microstructure.

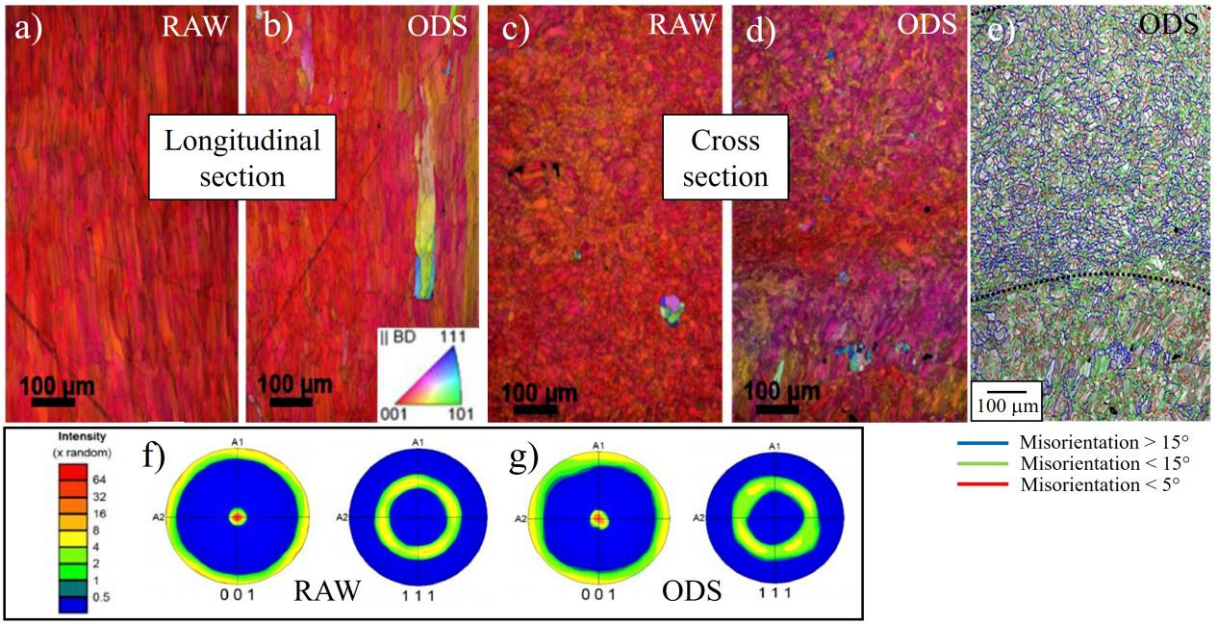

Fig. 65: Results from the EBSD analysis (a-e) and XRD examinations (f,g). a,c) Inverse pole figures (IPF) images for non-reinforced Fe20Cr4.5Al0.5Ti (wt.%) stainless steel ("raw") in longitudinal- (a) and cross section (c). Longitudinal direction is designated perpendicular to the build direction. Cross section plane is oriented parallel to the build direction. b,d) Inverse pole figures (IPF) images for oxide dispersion strengthened Fe20Cr4.5Al0.5Ti stainless steel ("ODS") in longitudinal- (b) and cross section (d). e) Misorientation map of (d). [499] f) Pole figure of "raw" stainless steel in [001] and [111] direction. g) Pole figure of oxide dispersion strengthened stainless steel ("ODS") in [001] and [111] direction. [13]

It becomes evident from the EDS measurements, that enrichments of yttrium and oxygen can only be roughly determined in larger agglomerates (Fig. 66a) as significant amounts of Fe and Cr are detected (Fig. 66b). However, significant enrichments of aluminium in yttrium oxide particles are determined. Moreover, significant incorporation of silicon is observed by EDS measurements of nanoparticle clusters (Fig. 66c). Silicon is believed to originate from the stainless steel powder material, as it is detected by XRF measurements of the used powder material (Table 19).

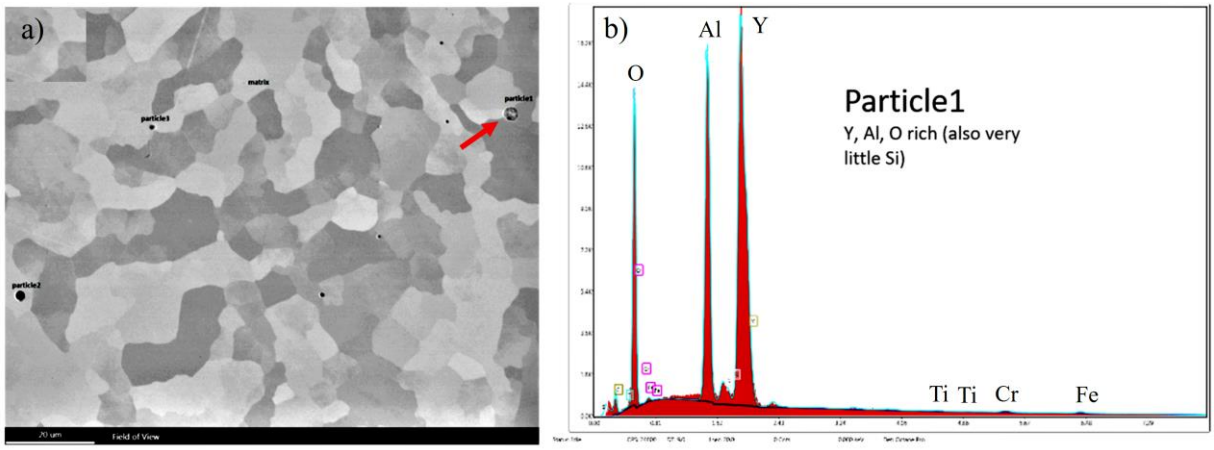

c)	Fe	Cr	Al	Ti	Y	O	Si
L-PBF (MA)- Matrix	Bal.	21.03	4.77	0.38	-	-	-
L-PBF (MA)- NP	Bal.	19.33	8.82	-	18.44	12.44	0.82
L-PBF (LSPC)- Matrix	Bal.	18.76	4.03	-	-	-	-
L-PBF (LSPC)- NP	Bal.	4.71	16.72	0.24	22.42	16.38	1.21

Fig. 66: Determination of the chemistry of dispersed nanoparticle agglomerates (a) in L-PBF manufactured ODS specimen by EDS. The exemplary specimen depicted is manufactured from LSPC generated powder material. b) EDS spectrum of the particle indicated with red arrow in (a). c) Chemical composition of the matrix and nanoparticle agglomerates of L-PBF manufactured specimen, manufactured from MA and LSPC-generated powder materials. [499]

The characterization of the observed particles by SEM-EDS gives a general view of the distribution and spatial homogeneity of the larger particles present in the microstructure. To analyse the nanometer-sized particles, APT measurements are performed, as shown in Fig. 67b-e. The APT volume reconstruction, shown in Fig. 67b, reveals the presence of both yttrium-rich oxide nanoparticles and titanium-rich carbides. These Ti-C structures surround the yttrium-rich nanoparticles, presumably marking low angle grain boundaries (LAGB), pinned by the two Y-Ti-O particles. This would prove the contribution of oxide nanoparticles additional to the determined grain refinement to increased material strength. On the other hand, strength contributions might also stem from the presence of Ti-C nanostructures, which are proven to increase the material strength in L-PBF manufactured steels [264]. The corresponding proximity histogram for the isocomposition surfaces in the APT volume reconstruction is shown in Fig. 67c. The proximity diagram plots the chemical composition as a function of the distance to the isocomposition surfaces. On the right side of the proximity diagram the particle composition can be found while the matrix composition is displayed on the left side of the graph, suggesting that the oxide nanoparticles contain equal amounts of Y and O. The exact stoichiometric composition of oxides is difficult to quantify by APT [589, 590]. Consequently, the description of the nanoparticle composition will be referred to as Y-O. The most similar stable Y-O phase to the one obtained by APT is the initial Y_2O_3 composition of the nanoparticles added. Nevertheless, the presence of different compositions cannot be discarded due to the complex precipitation processes occurring during the melting-solidification step of additive manufacturing [158]. The Y-rich nanoparticles found contain

approximately 10 – 15 at.% titanium, suggesting a complex scenario where the nanoparticles can be formed of Y-Ti-O composites as $Y_2Ti_2O_7$ or Y_2TiO_5, commonly found in ODS steels (cf. Table 1). Moreover, co-nucleation of carbides and oxides is occasionally observed, as evident from an APT volume reconstruction shown in the Supplementary S23.

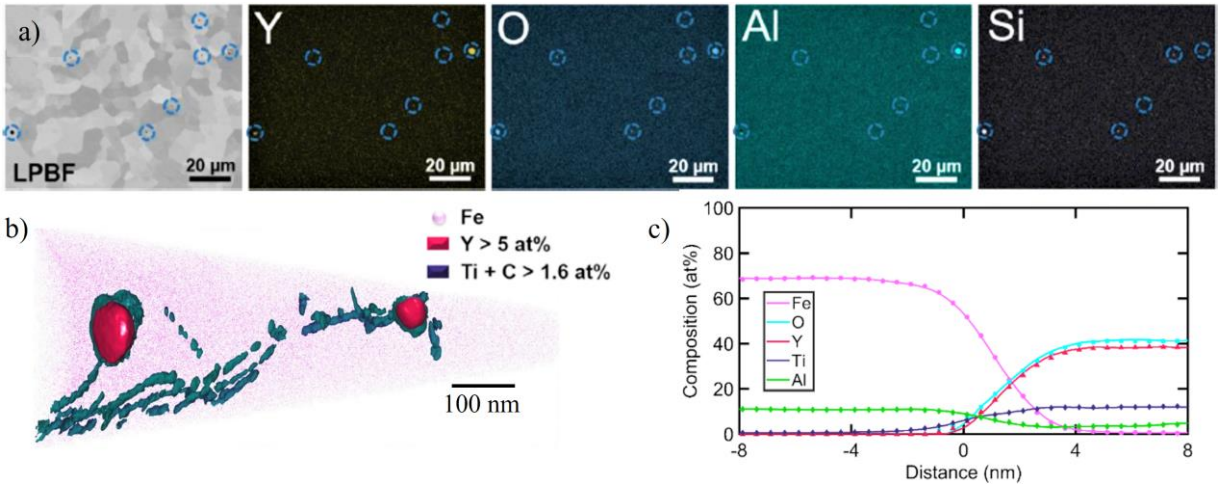

Fig. 67: a) SEM image (BSE mode) of a L-PBF manufactured specimen with LSPC-manufactured powder material and corresponding EDS maps showing silicon enriched Y-Al-O nanoparticles dispersed in the Fe20Cr4.5Al0.5Ti (wt.%) matrix. Additional EDS maps are shown in the Supplementary S24. b) APT volume reconstruction showing nano-scaled yttrium-rich particles in the steel matrix entangled with Ti-C structures. c) Proximity diagram showing titanium and slight aluminium content of the yttrium-rich oxide particles. [13]

However, also minor contents of aluminium are present in oxide nanoparticles, as evident from the proximity diagram (Fig. 67c) and TEM investigations also indicate the existence of aluminium-rich nanoparticles (Supplementary S25). Fig. 65 shows an example of an oxide nanoparticle embedded into the stainless steel matrix with a diameter of approx. 15 nm.

The diffraction pattern and lattice distance of the nanoparticles' crystal structure is determined by Fast Fourier Transformation (FFT) analysis (Fig. 68b) and inverse FFT analysis (Fig. 68c) from BF-STEM imaging (Fig. 68a), identifying the marked nanoparticle as YAG phase, $Y_3Al_5O_{12}$ (reflection (422), space group $la\bar{3}d$ (230) [158], which is regularly observed in conventionally manufactured PM2000 material [157] and other aluminium alloyed ODS steels [158] together with various other aluminium-rich Y-O compounds (cf. Table 1). It should be noted, that ODS steels typically do not contain a single Y-O species but consists of various species of titanium or aluminium-containing oxide species [159, 591].

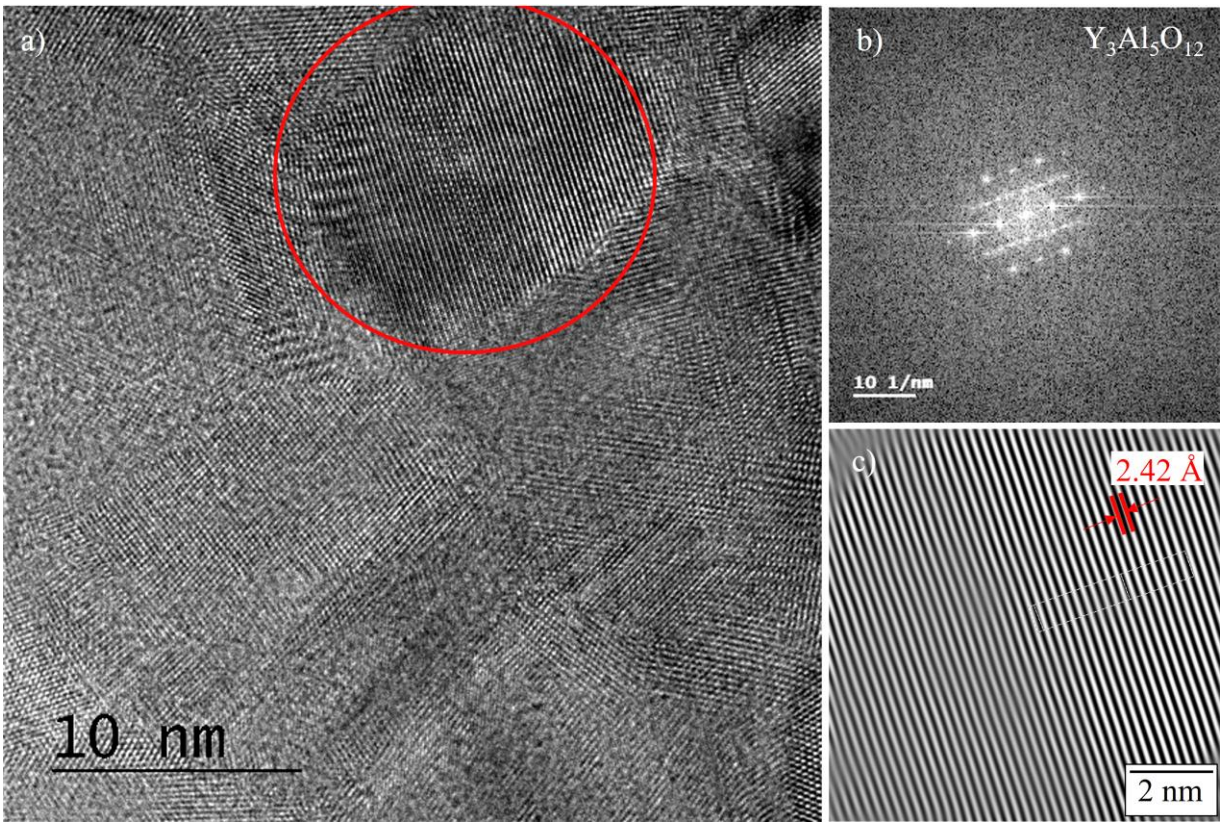

Fig. 68: a) High resolution-BF-STEM image of a L-PBF manufactured specimen, generated from LSPC generated powder materials. An embedded nanoparticle with a diameter of approx. 15 nm is highlighted by the red circle. b) Image after FFT showing the diffraction pattern of the nanoparticles' crystal structure. c) Inverse FFT showing the lattice distance of the nanoparticles' crystal structure with the determined lattice distance of approx. 2.42 Å, likely corresponding to the cubic $Y_3Al_5O_{12}$ (YAG) phase.

7 Mechanical properties of the additively manufactured material

Contains content from the following publications:

Microstructure formation and mechanical properties of ODS steels built by laser additive manufacturing of nanoparticle coated iron-chromium powders

C. Doñate-Buendia[a], P. Kürnsteiner[b], F. Stern[c], M. B. Wilms[d], R. Steubel[a], I. M. Kusoglu[a], J. Tenkamp[c], E. Bruder[e], N. Pirch[d], S. Barcikowski[a], K. Durst[e], J. H. Schleifenbaum[d], F. Walther[c], B. Gault[b,f], B. Gökce[a,*]

[a]Technical Chemistry I and Center for Nanointegration Duisburg-Essen (CENIDE), University of Duisburg-Essen, 45141 Essen, Germany
[b]Department Microstructure Physics and Alloy Design, Max-Planck-Institut für Eisenforschung GmbH, 40237 Düsseldorf, Germany
[c]Department of Materials Test Engineering, TU Dortmund University, 44227 Dortmund, Germany
[d]Chair for Digital Additive Production, RWTH Aachen University & Fraunhofer Institute for Laser Technology, 52074 Aachen, Germany
[e]Physical Metallurgy, Materials Science Department, Technische Universität Darmstadt, 64287 Darmstadt, Germany
[f]Department of Materials, Royal School of Mines, Imperial College, Exhibition Road, London, SW7 2AZ, UK

Article Information

Article history:
Received 16 July 2020
Accepted 12 December 2020
Available online 17 December 2020

DOI: 10.1016/j.actamat.2020.116566
Acta Materialia

**Corresponding author*
bilal.goekce@uni-due.de

Abstract

Oxide dispersion strengthened (ODS) steels are known for their enhanced mechanical performance at high temperatures or under radiation exposure. Their microstructure depends on the manufacturing process, from the nanoparticle addition to the base steel powder, to the processing of the nanoparticle enriched powder. The optimization and control of the processing steps still represent a challenge to establish a clear methodology for the additive manufacturing of ODS steels. Here, we evaluate the microstructure, nanoparticle evolution, and mechanical properties of ODS steels prepared by dielectrophoretic controlled adsorption of 0.08 wt% laser-synthesized yttrium oxide (Y_2O_3) on an iron-chromium ferritic steel powder (PM2000). The influence of the ODS steel fabrication technique is studied for two standard additive manufacturing techniques, directed energy deposition (DED) and laser powder bed fusion (LPBF). The compressive strength of the ODS steels at 600 °C is increased by 21% and 29% for the DED and LPBF samples, respectively, compared to the DED and LPBF steels manufactured without Y_2O_3 nanoparticle addition. The Martens hardness is enhanced by 9% for the LPBF ODS steel while no significant change is observed in the DED ODS steel. The microstructure and nanoparticle composition and distribution are evaluated by electron backscatter diffraction, scanning electron microscopy–energy-dispersive X-ray spectroscopy, and atom probe tomography, to compare the microstructural features of DED and LPBF manufactured parts. Smaller grain size and more homogeneous distribution with lower agglomeration of Y-O nanoparticles in the LPBF sample are found to be key factors for enhanced mechanical response at 600°C. The enhanced mechanical properties of the LPBF-processed sample and the more homogeneous nanoparticle dispersion can be linked to results obtained by finite element methods simulations of the melt pool that show two orders of magnitude faster cooling rates for LPBF than for DED. Therefore, this work presents and validates a complete laser-based methodology for the preparation and processing of an ODS steel, proving the modification of the microstructure and enhancement of the high-temperature strength of the as-built parts.

Own contribution: Sample preparation, contributing to writing and editing of the original draft and revised manuscript.

Oxide-dispersion-strengthened alloys generated by laser metal deposition of laser-generated nanoparticle-metal powder composites

C. Doñate-Buendia[a], F. Frömel[b], M. B. Wilms[c], R. Steubel[a], J. Tenkamp[b], T. Hupfeld[a], M. Nachev[d], E. Gökce[e], A. Weisheit[c], S. Barcikowski[a], F. Walther[b], J. H. Schleifenbaum[c], B. Gökce[a,*]

[a]Technical Chemistry I and Center for Nanointegration Duisburg-Essen (CENIDE), University of Duisburg-Essen, 45141 Essen, Germany
[b]Department of Materials Test Engineering, TU Dortmund University, 44227 Dortmund, Germany
[c]Chair for Digital Additive Production, RWTH Aachen University & Fraunhofer Institute for Laser Technology, 52074 Aachen, Germany
[d]Department of Aquatic Ecology and Centre for Water and Environmental Research, University of Duisburg-Essen, 45141 Essen, Germany
[e]Analytical Laboratory, Eurofins Umwelt West GmbH, 50398 Wesseling, Germany

Article Information

Article history:
Received 27 February 2018
Accepted 19 May 2018
Available online 21 May 2018

DOI: 10.1016/j.matdes.2018.05.044
Materials & Design

**Corresponding author*
bilal.goekce@uni-due.de

Abstract

A new method is proposed for producing nanoparticle-metal composite powders for laser additive manufacturing of oxide-dispersion strengthened (ODS) alloys. Different composite powders containing laser-generated Y_2O_3 and yttrium iron garnet (YIG) nanoparticles were produced and consolidated by Laser Metal Deposition (LMD). The structural properties of the manufactured ODS alloys were analyzed, and their hardness, remnant porosity, and temperature-dependent compression behavior were characterized to study the effect of the composition and size of the nanoparticles on the structural and mechanical properties. While the structural analyses did not show significant differences between the processed samples within the limits of the characterization methods that were used, the temperature-dependent compression behavior showed an increase of up to 22 ± 11% in the high-temperature strength of the specimens that contained only 0.08 wt% of laser-generated nanoparticles. This increase is attributed to the dispersed and deagglomerated nature of the nanoparticles that were used during the powder-preparation step.

Own contribution: Sample preparation, contributing to writing and editing of the original draft and revised manuscript.

Laser additive manufacturing of oxide dispersion strengthened steels using laser-generated nanoparticle-metal composite powders

M. B. Wilms[a], R. Steubel[b], F. Frömel[c], A. Weisheit[a], J. Tenkamp[c], F. Walther[c], S. Barcikowski[b], J. H. Schleifenbaum[a], B. Gökce[b,*]

[a]Chair for Digital Additive Production, RWTH Aachen University & Fraunhofer Institute for Laser Technology, 52074 Aachen, Germany
[b]Technical Chemistry I and Center for Nanointegration Duisburg-Essen (CENIDE), University of Duisburg-Essen, 45141 Essen, Germany
[c]Department of Materials Test Engineering, TU Dortmund University, 44227 Dortmund, Germany

Article Information

DOI: 10.1016/j.procir.2018.08.093
Procedia CIRP

*Corresponding author
bilal.goekce@uni-due.de

Abstract

A new route for the synthesis of powder composites suitable for processing with laser additive manufacturing is demonstrated. The powder composites, consisting of micrometer-sized stainless steel powder, homogenously decorated with nano-scaled Y_2O_3 powder particles, are manufactured by laser processing of colloids and electrostatic deposition. Consolidated by laser metal deposition and selective laser melting, the resulting specimens show superior mechanical properties at elevated temperatures, caused by the nano-sized, homogenously distributed dispersoids.

Own contribution: Sample preparation, writing and editing of the original draft and revised manuscript.

In this chapter, the mechanical properties of L-DED and L-PBF manufactured raw stainless steel and ODS material are comparatively presented. For the production of test specimens, large cubic or rectangular structures are manufactured using L-DED (reduced beam diameter 0.6 mm) and L-PBF. From these large specimens, test geometries for compressive strength examinations in build direction are obtained by means of water cutting procedure. [16] Fig. 69 shows examples of a large specimen, produced by L-PBF (Fig. 69a) and L-DED (Fig. 69b), respectively. Due to the limited amount of available material manufactured by HSLC, no test specimens could be manufactured in order to determine the compressive strength of HSLC processed material.

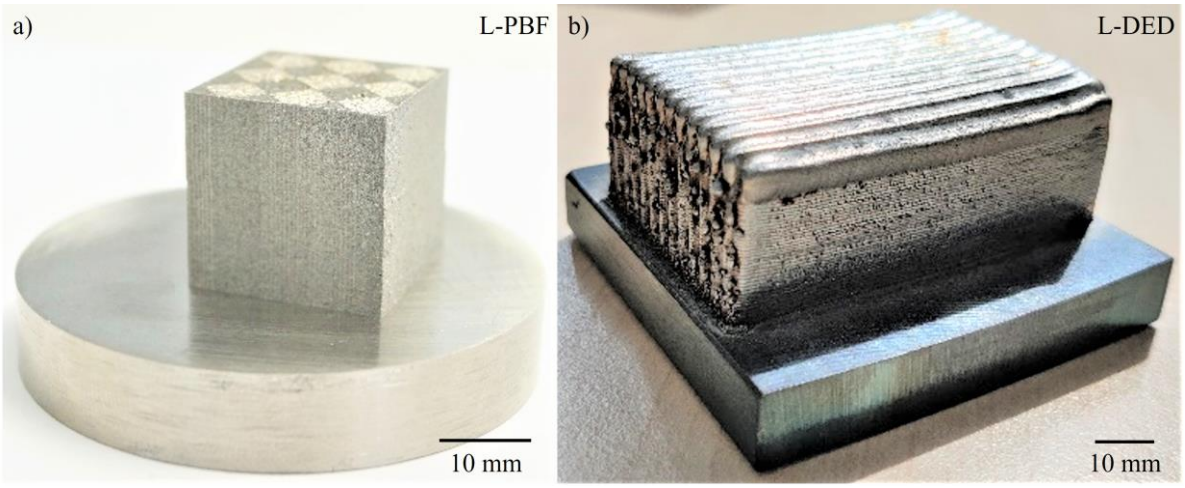

Fig. 69: Exemplary large specimens used for the generation of test specimens for compression tests. a) L-PBF. b) L-DED.

Furthermore, the characterization of the compressive strength of printed specimen is solely performed with material manufactured from LSPC-generated powder materials, as specimen manufactured from these powder feedstocks are characterized by finer nano-scale oxide structures (Fig. 62) and thus a more pronounced influence on the mechanical properties in room and high temperature range is expected.

7.1 Vickers microhardness

The specimens used for Vickers microhardness indentation are cold-embedded, ground and polished to a grit size of 0.3 µm using a colloidal SiO_2 polishing suspension. Microhardness of L-DED and L-PBF manufactured specimen are measured with a static load of 0.9807 N (HV0.1) with a Shimadzu DUH-211S (Shimadzu, Kyoto, Japan), under load-control (70 mN/s) up to a maximum test load of F_{max} = 980.7 mN according to DIN EN ISO 14577. The maximum force is kept constant for 13 seconds followed by unloading. Microhardness was determined for each batch, at the horizontal and vertical cross sections relative to the build direction. Five indentations are used for each cross section to determine the values of average hardness. Vickers microhardness of HSLC manufactured specimen is performed using a Qness Q30 A+ (ATM Qness GmbH, Mammelzen, Germany) with a load of 0.9807 N (HV0.1). Hardness values are calculated from six individual indents at every build height measured. Results from Vickers microhardness of raw and reinforced specimens manufactured by L-DED, HSLC and L-PBF are shown in Table 29. An increased hardness of L-PBF processed raw stainless steel material compared to L-DED processed specimen becomes evident, which is likely attributed to significant grain refining (cf. Fig. 50 and Fig. 61) but might also stem from high dislocation densities in L-PBF manufactured specimens, as evident from the misorientation maps generated from EBSD measurements (Fig. 65e).

Table 29: Results of the Vickers microhardness (HV0.1) measurements for raw stainless steel and ODS steel manufactured with L-DED (0.6 mm beam diameter), HSLC and L-PBF. [13, 497]

Material (Process)	Raw steel (L-DED)	ODS steel (L-DED)	Raw steel (HSLC)	ODS steel (HSLC)	Raw steel (L-PBF)	ODS steel (L-PBF)
Hardness (HV0.1)	233	222	244	258	238	249
Std. Dev. (HV0.1)	5	6	7	7	7	7

As evident from the microhardness values, shown in Table 29, slightly higher microhardnesses of ODS specimen can be determined for HSLC and L-PBF processed material compared to their non-reinforced counterparts. No hardening is observed for L-DED manufactured specimen, which may indicate, that the dispersion of large (> 150 nm) oxide nanoparticles does not lead to increased material strength. However, the determined microhardnesses for printed materials are lower compared to conventionally manufactured PM2000 material, exhibiting a microhardness of 270 ± 8 HV1 [592] and 300 HV1 [593], which is also confirmed for other Fe-based ODS steels, manufactured by AM. [451] The higher hardness of conventional manufactured material (Fig. 70) is believed to result from smaller oxide nanoparticle structures with approx. 20 nm [159, 231, 593] of conventionally manufactured PM2000 material compared to L-DED, HSLC or L-PBF printed material (cf. Fig. 62).

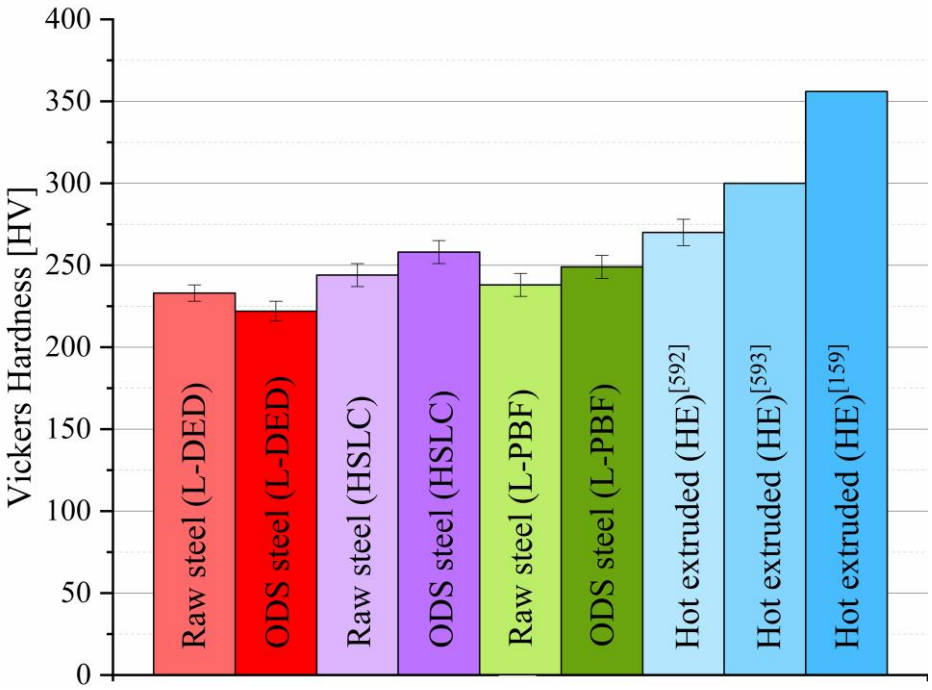

Fig. 70: Comparison of determined averaged Vickers hardness of raw Fe20Cr4.5Al0.5Ti (wt.%) stainless steel and ODS counterparts. Hardness values for hot extruded (HE) PM2000 material are taken from [159], [592] and [593].

7.2 Compression strength

The compression strength is determined by quasistatic compression tests at room temperature and at elevated temperatures (600°C) using a servohydraulic testing system Schenck PC63M, Instron 8800 controller (Instron®, Norwood, MA, USA) with a 50 kN load cell (Fig. 68a). The system is equipped with a high-temperature furnace MTS 653 (MTS Systems Corp., Eden Prairie, MN, USA) with two heating zones for temperatures up to 1100 °C. A micro water jet is used to cut the as-built samples into cylindrical specimens with diameters of 4 mm and heights of 5–6 mm (related to the as-built sample height). The front sides of the specimens were polished and lubricated with Molykote® to decrease friction between the specimens and the compression dies during the compression tests related to DIN 50106. The tests are conducted at a controlled speed (v_c= 0.0833 mm/min), and the displacements of the traverse and compression forces are recorded. For testing, the cylindrical specimens were placed on compression dies made of tungsten carbide-cobalt (WC-Co), which were used with water-cooled gripping jaws (Fig. 71a,b). Compressive strain ε_c was calculated using the measured displacement of the traverse. The applied load for all specimens is arranged parallel to the building direction. [16]

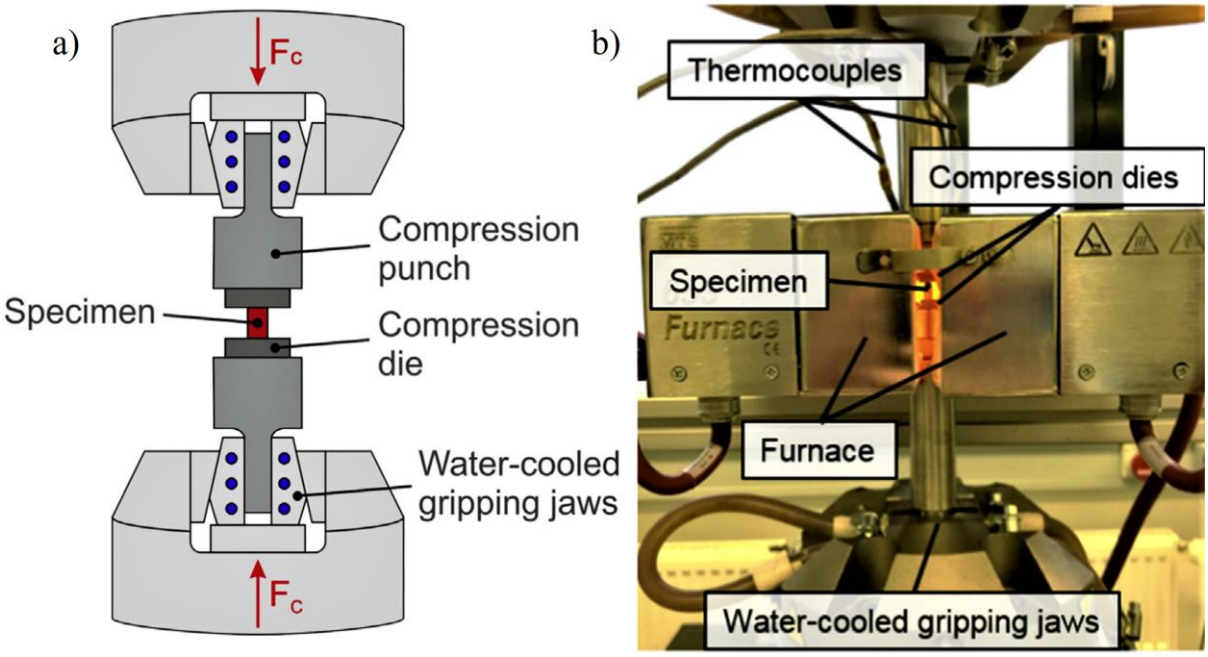

Fig. 71: a) Schematic depiction of the compression test setup for temperatures between RT and 600°C. b) Photographic image of the compression testing setup during compression testing. [16]

From the averaged compressive stress-strain curves at room temperature (Fig. 72a) it is evident, that L-PBF manufactured raw stainless steel specimen show higher compressive strength than L-DED processed specimen, which can be explained with smaller grain sizes and thus by Hall-Petch grain refining strengthening mechanism.

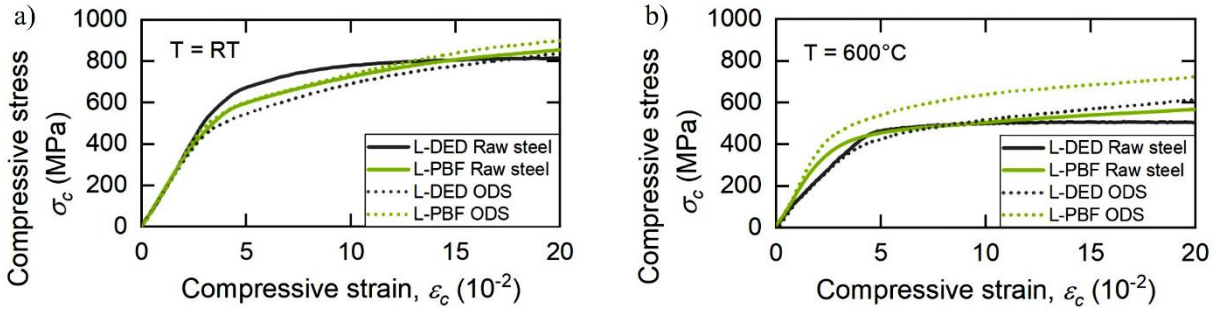

Fig. 72: Compressive stress σ_c of the as-built raw L-DED and L-PBF processed stainless steel and ODS steels as a function of the compressive strain ε_c for different temperatures, a) RT (23°C) and b) 600°C. Curves are averaged from three individual measurements depicted in the Supplementary S26 and S27. Data is taken from [13] and [16].

The introduction of nano-scaled nanoparticles leads to both higher strength in L-DED and L-PBF manufactured specimen at higher compressive strain ε_c. Interestingly, the L-DED manufactured ODS material shows lower compressive strength compared to its non-reinforced counterpart at lower compressive strain ε_c. This trend is also observed in the hardness measurements (Table 29). However, as evident from the determined compressive strength at different stains (Table 30) only moderate (approx. 13% in L-PBF processed specimens) effects on material strength by introduction of nanoparticles are found at room temperature (23°C), which is also observed by other research groups [186].

Table 30: Determined room temperature compression strength σ_c at compression strains ε_c=0.2; 5 and 15 for raw stainless steel and ODS material, manufactured by L-DED and L-PBF. [13]

Material	Raw steel (L-DED)	ODS steel (L-DED)	Raw steel (L-PBF)	ODS steel (L-PBF)
$\sigma_{c,\,p0.2}$ (MPa)	640 ± 30	452 ± 30	470 ± 30	538 ± 17
$\sigma_{c,\,p5}$ (MPa)	775 ± 5	674 ± 70	717 ± 1	720 ± 15
$\sigma_{c,\,p15}$ (MPa)	810 ± 40	844 ± 70	861 ± 7	900 ± 30

However, the determined values for $\sigma_{c,\,p0.2}$ of the additively manufactured specimen are found to be significantly lower than for conventionally manufactured PM2000 material by hot extrusion of mechanically alloyed composite powder material (Fig. 73). One reason for the reduced mechanical strength might be attributed to the significantly smaller oxide nanoparticle size of approx. 20 nm. [594, 595] compared to 45 nm in L-PBF and 158 nm in L-DED (Fig. 62).

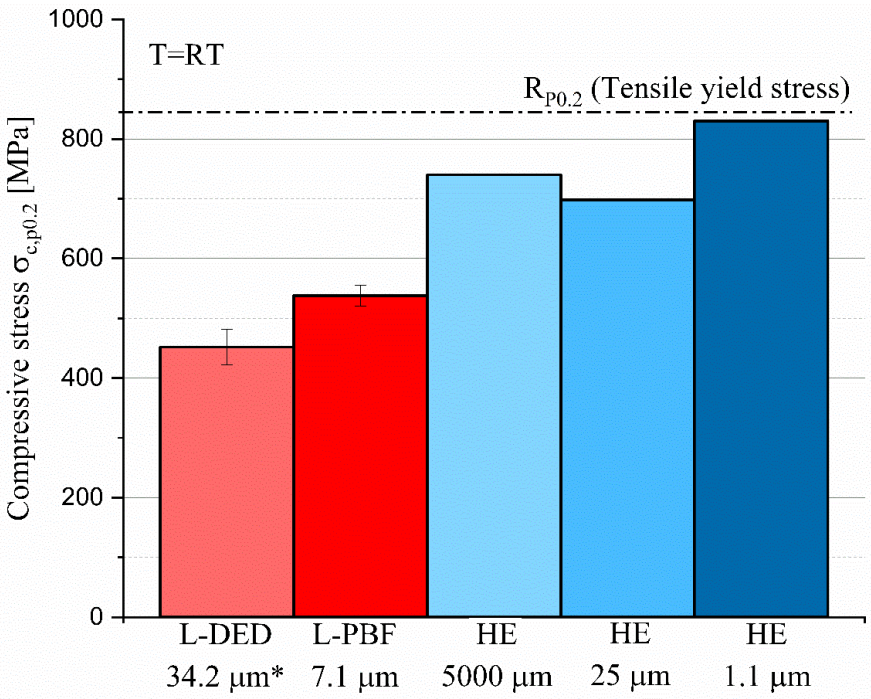

Fig. 73: Bar diagram of the determined room temperature (23°C) compression strength $\sigma_{c,\,p0.2}$ (compression strain ε_c=0.2) for L-DED (*grain size derived from BSE images) and L-PBF (red bars), as well as for hot-extruded (HE) PM2000 material (blue bars) with an average grain size 5000 µm, 25 µm [595] and 1.1 µm [594]. Additionally, the (tensile) yield strength ($R_{P0.2}$) of PM2000 material is indicated by the dashed line [596].

However, in high temperature testing conditions (600°C) pronounced strengthening by the introduction of oxide nanoparticles is encountered, as evident from Fig. 72b and the corresponding values, shown in Table 31. The increase in strength is particularly noticeable in L-PBF manufactured material, where strength increases of up to 30% (L-PBF) and 20% (L-DED) are observed.

Table 31: Determined elevated temperature (600°C) compression strength σ_c at compression strains ε_c=0.2; 5 and 15 for raw stainless steel and ODS material, manufactured by L-DED and L-PBF. [13]

Material	Raw steel (L-DED)	ODS steel (L-DED)	Raw steel (L-PBF)	ODS steel (L-PBF)
$\sigma_{c,\,p0.2}$ (MPa)	440 ± 5	360 ± 50	310 ± 30	430 ± 11
$\sigma_{c,\,p5}$ (MPa)	502 ± 4	510 ± 30	488 ± 17	620 ± 30
$\sigma_{c,\,p15}$ (MPa)	507 ± 15	620 ± 30	560 ± 20	720 ± 30

Comparing the results from compression testing with conventionally manufactured PM2000 material by hot-extrusion (HE), shows that additively manufactured material is superior to hot-extruded material (Fig. 74).

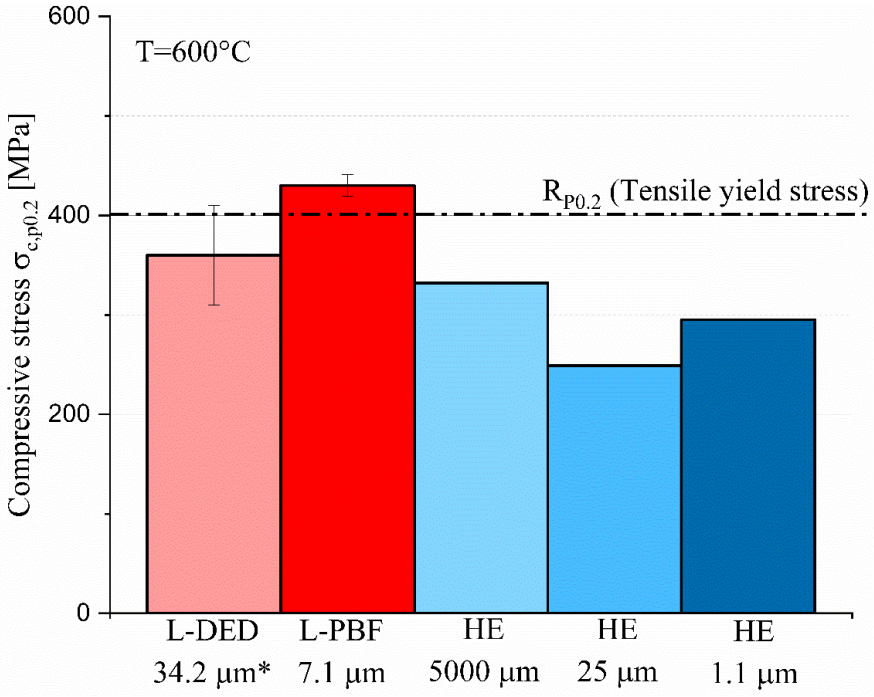

Fig. 74: Bar diagram of the determined elevated temperature (600°C) compression strength $\sigma_{c,\,p0.2}$ (compression strain ε_c=0.2) for L-DED (*grain size derived from BSE images) and L-PBF (red bars), as well as for hot-extruded (HE) PM2000 material (blue bars) with an average grain size 5000 µm, 25 µm [595] and 1.1 µm [594]. Additionally, the (tensile) yield strength ($R_{P0.2}$) of PM2000 material is indicated by the dashed line [596].

The results of the high-temperature compression tests indicate, that another strengthening mechanism is predominant in this temperature regime compared to room temperature. It is known from the literature that the strength contribution from grain refinement via Hall-Petch strengthening decreases with increasing temperature due to coarsening mechanisms [597, 598], while the Orowan mechanism shows an opposite trend and increases accordingly with higher temperature [599]. From BFTEM images (Fig. 75) it is evident, that in L-PBF manufactured material significant dislocation interaction with dispersed oxide nanoparticles is observed, comparable to conventionally manufactured material [73].

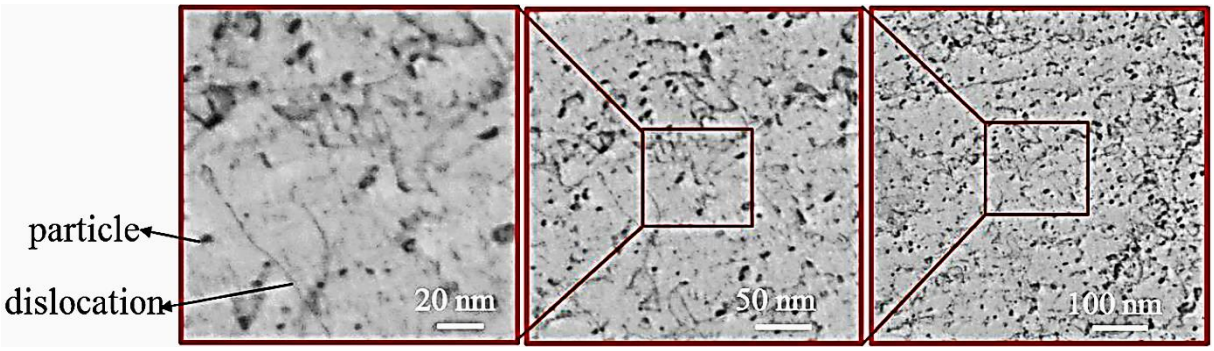

Fig. 75: BFTEM images showing dislocations interacting with oxide nanoparticles (black spots), dispersed in the L-PBF manufactured stainless steel matrix. Specimen was manufactured from MA powder material. [544]

8 Transfer of the methodology to alternative material systems

The methodology developed for manufacturing oxide-dispersion strengthened ferritic stainless steel Fe20Cr4.5Al0.5Ti (wt.%) allows the homogeneous dispersion of nano-scaled yttrium oxides in the metallic matrix by processing composite powder with the AM processes of L-DED, HSLC and L-PBF. In principle, this methodology can be extrapolated to alternative material systems, which is demonstrated in this chapter with two exemplary material systems, namely an intermetallic alloy based on the γ-TiAl alloy system processed by L-DED and a high-strength copper alloy based on the Cu-Cr-Nb alloys processed by L-PBF, which are prospective materials for aerospace applications. For both material systems, the composite powders are manufactured by MA, as both material classes are sensitive to oxygen and carbon contaminations, which may be introduced by exposure to water or organic solvents in the LSPC-based methodology.

8.1 L-DED of oxide dispersion-strengthened γ-TiAl alloy

Contains content from the following publication:

Oxide dispersion strengthening of γ-TiAl by laser additive manufacturing

S.-K. Rittinghaus*, M. B. Wilms

Fraunhofer Institute for Laser Technology ILT, Steinbachstr. 15, 52074 Aachen, Germany

Article Information

Article history:
Received 27 February 2019
Accepted 2 July 2019
Available online 3 July 2019

DOI: 10.1016/j.jallcom.2019.07.024
Journal of Alloys & Compounds

**Corresponding author*
siljakatharina.rittinghaus@ilt.fraunhofer.de

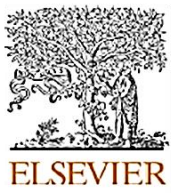

Abstract

γ-TiAl alloys, as a more and more frequently considered high-temperature material, face the challenge to meet increasingly high demands in property improvement. In the present work, the feasibility of laser additive manufacturing (LAM) of a short-milled powder compound consisting of gas atomized γ-TiAl powder and nano-scaled Y_2O_3 powder material materials via DED (direct energy deposition) process is demonstrated. Microstructure and hardness of the consolidated sample are presented. As a result, the suitability of the produced powder blend to achieve fully dense and crack free samples with homogenously dispersed Y_2O_3-particles with LAM is demonstrated.

Own contribution: Sample preparation, design of the study and editing and sample preparation.

Additive manufacturing of γ-titanium aluminides (γ-TiAl) is challenging, due to their characteristic brittleness at room temperature, typically resulting in severe crack formation during additive manufacturing [600]. One possible solution is the utilization of high-temperature substrate preheating systems to overcome the material-specific ductile-brittle transition temperature to allow some plasticity and thus prevention of thermally induced cracking. However, the application of high preheating temperatures may reduce the rapid solidification kinetics in L-DED and thus promote the agglomeration

of introduced oxide nanoparticles during the melting stage, as it impedes conductive heat dissipation of the melt pool towards the substrate material. In order to study the impact of substrate preheating on oxide nanoparticle evolution and distribution a composite powder material consisting of the commercial γ-TiAl alloy GE4822 (Ti-48Al-2Cr-2Nb (at.%)) and approx. 0.5 wt.% Y_2O_3 nanoparticles is manufactured by mechanical alloying analogue to the stainless steel, described in detail in chapter 5.3.

Table 32: Process parameter set for L-DED processing of raw GE4822 and GE4822-0.5Y_2O_3 specimens. Preheating is performed by a custom-made induction system, integrated into the L-DED machine.

Process parameter	Laser power (P_L)	Deposition velocity (v)	Powder feed rate (m_p)	Height offset (Δz)	Beam diameter (d_B)	Preheating temperature
Unit	W	mm/min	g/min	µm	mm	°C
Value	66	500	0.41	200	0.6	900

Fig. 76a presents the powder material after the mechanical alloying procedure. The composite powder particles are spherical with smooth surface and characterized by randomly distributed Y_2O_3-platelets on the surface, demonstrating the successful formation of a composite powder by deposition of nano-scaled Y_2O_3 on the intermetallic powder particles. Occasionally heavily deformed, flake-like particles are found, which do not show a detrimental effect on flowability during the consolidation via L-DED, using the process parameter set from Table 32. In Fig. 76b, the L-DED processed specimen is depicted, showing a crack-free microstructure. Some sintered particles are attached to the lateral surfaces. Measurements of the micrograph by light optical image analysis reveal a relative density of 99.9%.

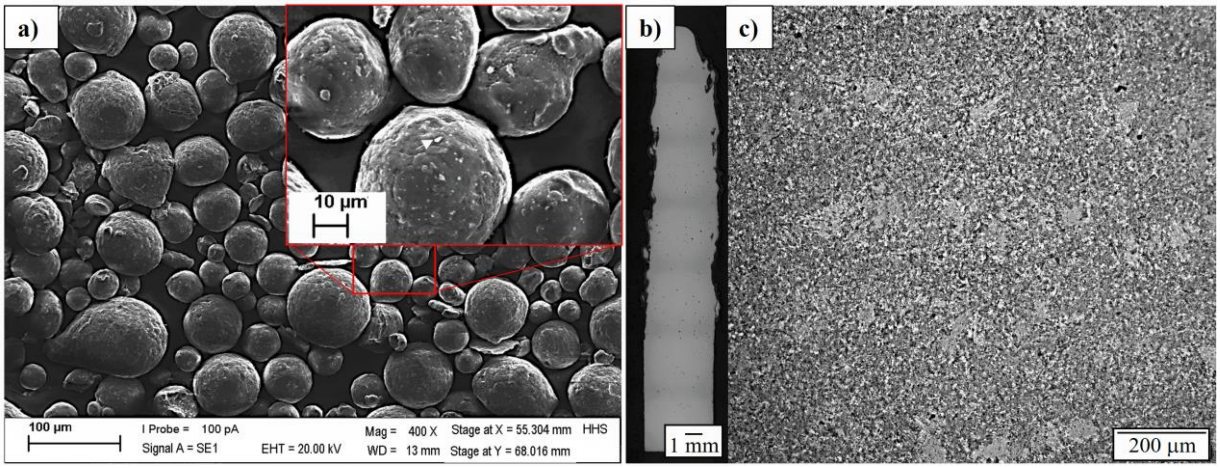

Fig. 76: a) SEM image (SE-mode) of GE4822 powder particles after mechanical alloying with a superimposed image showing the powder particles with higher magnification and randomly distributed Y_2O_3 particles on the intermetallic powder particles' surface. b) LOM image of a L-DED manufactured wall structure using the process parameters, shown in Table 31. c) LOM image of the microstructure of the wall structure depicted in b).

Pores form rarely in the low micrometer range with average diameters of 5 – 20 µm. Their globular appearance indicates the origin in gas entrapment. The microstructure is characterized by (Fig. 76c) both fine grained and lentil shaped coarser regions, which is believed to be attributed to the layer-wise

deposition of material, which includes partial re-melting of subsequent layers. Differences in the local solidification rate provide conditions for both grain nucleation at melt pool boundaries and directed grain growth in the slower cooling center of the welding track. Fig. 77a,b clearly presents the distribution of the Y_2O_3-particles (bright white) evolved during the L-DED process, whose identification was confirmed by EDS point measurements with high yttrium, aluminium and oxygen contents. The phases visible are mainly lamellar $a_2+\gamma$ colonies and γ-TiAl as well as remnants of α_2-phase at grain boundaries. The Y_2O_3-particles are homogenously distributed in the intermetallic matrix. No difference between center and melt pool boundary regions is observed. The size of the finely dispersed particles varies with the build height of the sample. LOM image analysis reveals, that particles in the top region are smaller in the range of approx. 200 nm and exist in a higher number density, while particles in the bottom section reach up to 1 µm with lower number density. Middle section particles range between 250 and 900 nm decreasing in size with increased build height. By the sequential re-heating caused by the layer-wise build-up and the high preheating temperature, the specimen experiences an in-situ heat treatment during the process. This heat treatment in combination with high pre-heating temperatures of 900°C and partial re-melting of already deposited material is believed to cause diffusion-controlled coarsening of the nano-scaled Y_2O_3-particles, gradually increasing with temperature and time.

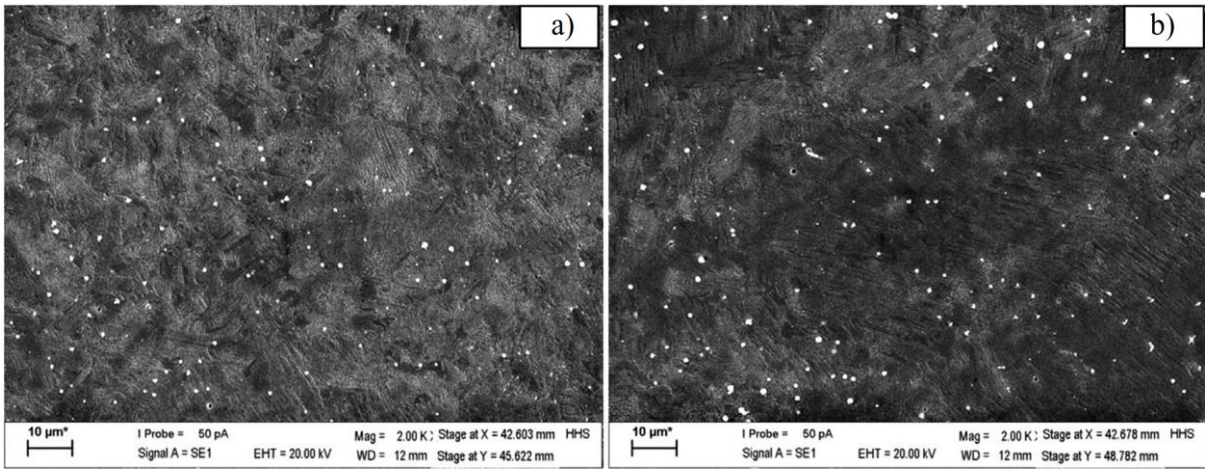

Fig. 77: SEM images (SE-mode) of L-DED manufactured oxide reinforced GE4822 γ-TiAl intermetallic alloy. a) Top region. b) Bottom region.

The hardness profiles over the build height is depicted in Fig. 78. Reference measurements are performed on a non-reinforced, L-DED manufactured Ti-48Al-2Cr-2Nb (at.%) sample. The average hardness of oxide reinforced GE4822 material is found to be 381 ± 24 HV0.3 and decreases slightly with increasing build height. The exceptional high hardness value (460 HV0.3) is measured in the top region of the specimens (blue circled point in Fig. 78), where no subsequent layers are applied. Hence, this region does not experience any re-heating effects, resulting in locally reduced grain size with finer oxide particles and thus higher hardness (Fig. 78).

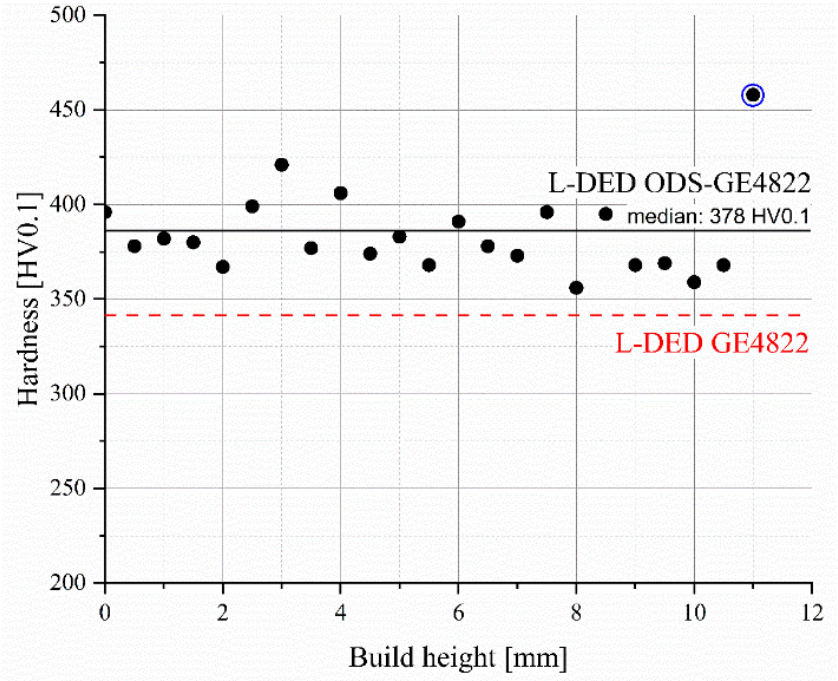

Fig. 78: Vickers hardness as a function of the built height of L-DED manufactured GE4822-0.5 wt.% Y_2O_3.

Compared to non-reinforced γ-TiAl material (L-DED GE4822) both built in this study and reported in literature with approx. 340 HV [601], the averaged hardness is approx. 40 HV0.3 higher. It can be concluded, that the utility of substrate preheating systems is affects the size distribution of dispersed nanoparticles, resulting in the formation of large nanoparticle agglomerates exceeding the nanometer scale. It is also apparent, that the partial re-melting of deposited oxide reinforced material during the build process affects the nanoparticle agglomerate size over the build height.

8.2 L-PBF of oxide dispersion-strengthened Cu-Cr-Nb alloys

Contains content from the following publication:

Laser additive manufacturing of oxide dispersion-strengthened copper–chromium–niobium alloys

M. B. Wilms*, S.-K. Rittinghaus

Chair of Materials Science and Additive Manufacturing, School of Mechanical Engineering and Safety Engineering, University of Wuppertal, Gaussstr. 20, 42119 Wuppertal, Germany

Article Information

Article history:
Received 19 July 2022
Accepted 8 September 2022
Available online 16 September 2022

DOI: 10.3390/jmmp6050102
Journal of Manufacturing & Materials Processing

*Corresponding author
mwilms@uni-wuppertal.de

Abstract

Copper is a key material for cooling of thermally stressed components in modern aerospace propulsion systems, due to its high thermal conductivity. The use of copper materials for such applications requires both high material strength and high stability at high temperatures, which can be achieved by the concept of oxide dispersion strengthening. In the present work, we demonstrate the oxide reinforcement of two highly conductive precipitation-strengthened Cu-Cr-Nb alloys using laser additive manufacturing. Gas-atomized Cu-3.3Cr-0.5Nb and Cu-3.3Cr-1.5Nb (wt.%) powder materials are decorated with Y_2O_3 nanoparticles by mechanical alloying in a planetary mill and followed by consolidation by the laser additive manufacturing process of laser powder bed fusion (LPBF). While dense specimens (>99.5%) of reinforced and non-reinforced alloys can be manufactured, oxide dispersion-strengthened alloys additionally exhibit homogeneously distributed oxide nanoparticles enriched in yttrium and chromium next to Cr_2Nb precipitates present in all alloys examined. Higher niobium contents result in moderate increase of the Vickers hardness of approx. 10 HV0.3, while the homogeneously dispersed nanometer-sized oxide particles lead to a pronounced increase of approx. 30 HV0.3 in material strength compared to their non-reinforced counterparts.

Own contribution: Conceptualization, writing and editing of the original draft and revised manuscript.

Laser additive manufacturing of copper and its alloys is challenging, due to the characteristic high reflectivity for the typically used near-infrared wavelength [399, 602]. Therefore, high laser powders and thus high energy densities are necessary for the production of dense parts from copper materials [603, 604], but inevitably lead to severly superheated melt pool temperatures and thus reduced solidification kinetics. It is evident from chapter 6.3, that the solidification kinetics govern the final nanoparticle size and their distribution within the metallic matrix. In order to study the impact of high energy densities an oxide nanoparticle evolution and distribution in a metallic matrix, two oxide dispersion-strengthened copper alloys are examined with L-PBF. The powder composites, consisting of two high-strength Cu-Cr-Nb copper alloys Cu-3.3Cr-0.5Nb and Cu-3.3Cr-1.5Nb (wt.%) and 0.5 wt.% Y_2O_3 nanopowder are manufactured by mechanical alloying analogue to the procedure, shown in chapter 5.3. The mechanically alloyed composite powders are depicted in Fig. 76.

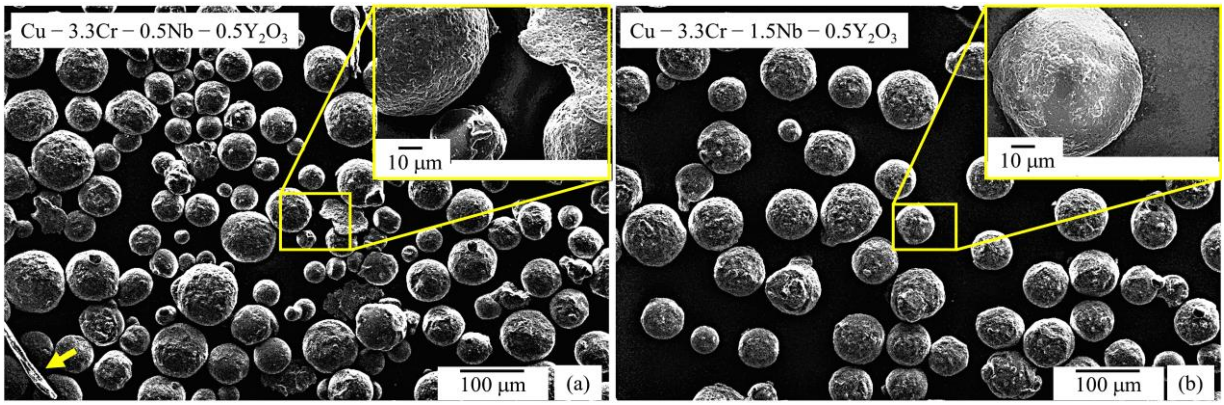

Fig. 79: SEM images (SE mode) of mechanically alloyed powder particles with superimposed SEM image with higher magnification: a) Cu-3.3Cr-0.5Nb alloy. b) Cu-3.3Cr-1.5Nb alloy.

After mechanical alloying, the circularity of the gas atomized powder particles decreases and flake-like powder particles (indicated by the yellow arrow in Fig. 79a) are observed occasionally, which are frequently found in mechanically alloyed powder materials [354, 605]. Additionally, the surface of the powder particles appears to be rougher, which presumably stems from the fracturing and cold welding events during mechanical alloying processes [341]. Mechanically alloyed powder particles are covered with white appearing particles (Fig. 79a,b). Using EDS measurements, enrichments of yttrium and oxygen can be detected, proving the successful deposition of Y_2O_3 or related compound nanoparticles on the surface of the Cu-Cr-Nb powder particles. (Table 33) Overall, a predominantly spherical particle morphology of both gas atomized powder materials could be retained after mechanical alloying (Fig. 79a,b) and thus the mechanically alloyed powder materials exhibit satisfactory flowability for L-PBF processing.

Table 33: Chemical composition (in wt.%) of the surface of the mechanically alloyed powder depicted in Fig. 79a,b. Averaged values from single point measurements on 15 randomly selected powder particles. GA: Gas atomized, MA: Mechanically alloyed.

Alloy	Powder state	Cu	Cr	Nb	Y	O
Cu-3.3Cr-0.5Nb	GA	Bal.	2.82	0.77	-	1.77
Cu-3.3Cr-0.5Nb-0.5Y_2O_3	MA	Bal.	3.73	1.15	4.91	3.18
Cu-3.3Cr-1.5Nb	GA	Bal.	3.55	1.86	-	2.58
Cu-3.3Cr-1.5Nb-0.5Y_2O_3	MA	Bal.	3.31	1.78	4.02	2.47

The presence of yttrium-rich oxide nanoparticles is believed to allow the utilization of substantially lower VED, compared to other studies 277.78 J/mm^3 [606], to produce dense specimen in this study (Table 34) by increasing the absorptivity for the used laser radiation [607] by multiple reflections [608]. EDS measurements on the powder particles surface additionally indicate an inhomogeneous distribution of chromium and niobium in the copper matrix of the gas atomized and mechanically alloyed powder particles, which is confirmed by EDS maps of the powder particles' cross-sections (Supplementary S28).

Table 34: Process parameter set for manufacturing the raw- and oxide-dispersed Cu-Cr-Nb alloys using L-PBF.

Process parameter	Laser power	Scan speed	Hatch distance	Layer thickness	Beam diameter	Hatch rotation	Scan strategy
Unit	W	mm/s	µm	µm	µm	°	-
Value	400	800	120	30	80	34	Stripes

Comparable inhomogeneities are also observed by Seltzman et al. [609, 610] but do not result in detrimental effects on the L-PBF printing process or homogeneous distribution of Cr_2Nb laves phase in the printed copper matrix [609]. In Fig. 77 SEM images of the microstructures of printed reinforced Cu-3.3Cr-0.5Nb-0.5Y_2O_3 (Fig. 80a,b) and Cu-3.3Cr-1.5Nb-0.5Y_2O_3 (Fig. 80c,d) specimen are shown using the process parameter set, shown in Table 33.

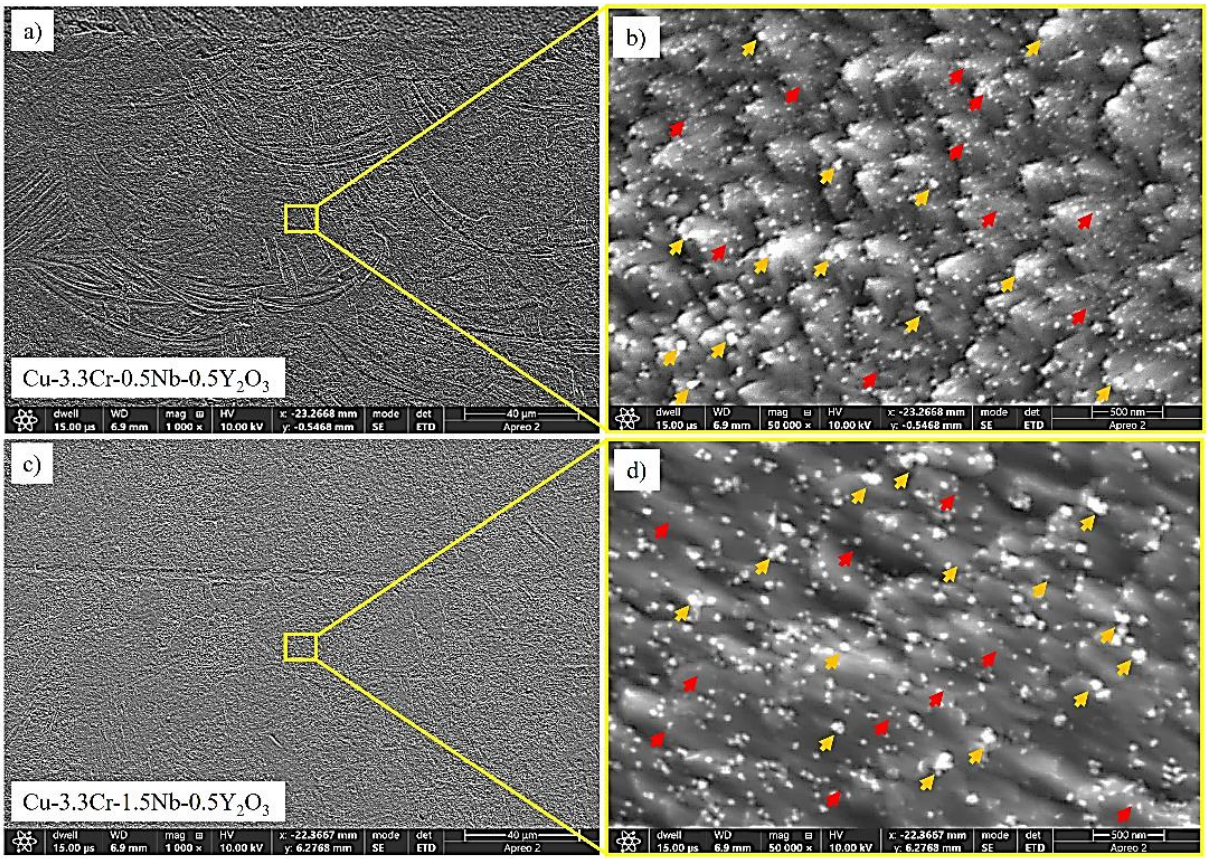

Fig. 80: SEM images (SE-mode) of oxide reinforced Cu-3.3Cr-0.5Nb alloy in low- (a) and high magnification (b) showing the presence of precipitates (red arrows) and dispersoids (yellow arrows). SEM images of oxide reinforced Cu-3.3Cr-1.5Nb alloy in low- (c) and high magnification (d) showing the presence of precipitates (red arrows) and dispersoids (yellow arrows).

No apparent differences, regarding grain morphology or size is observable compared to non-reinforced specimen in Fig. 80. However, on a lower scale significant differences in the microstructure evolution become apparent: A large number of sub-100 nm-sized nanoparticles are distributed within the metallic

matrix for both oxide reinforced copper alloys. However, EDS measurements of nanoparticle clusters (Table 34) reveal the presence of two nanoparticle species, marked with yellow and red arrows, respectively (Fig. 80b,d). Smaller particles are marked with red arrows and correspond to Cr-Nb-rich precipitates, which were observed in the non-reinforced specimen.

Interestingly, the larger nano-sized particles, which are marked with yellow arrows, are enriched in yttrium, chromium and oxygen. Thus, the addition of Y_2O_3 nanoparticles seem to promote the formation of complex oxide compounds. The found chromium-rich yttrium oxide nanoparticles may be attributed to the monoclinic-structured compound of $YCrO_3$, which is frequently observed in Cr-alloyed ODS steels [611, 612, 613] and nickel-based ODS alloys [498]. The formation reaction can be de-scribed according to (11) [152].

$$Cr_2O_3 + Y_2O_3 \rightarrow 2\ YCrO_3 \qquad (11)$$

Table 34. Chemical composition (in wt.%) of reinforced specimen determined by EDS. Values are averaged over 12 single point measurements on occasionally found clusters or larger particles of the respective nanoparticle species.

	Cu	Cr	Nb	Y	O
Cu-3.3Cr-0.5Nb-0.5Y_2O_3					
Red arrows	66.16	21.86	7.87	-	4.11
Yellow arrows	51.36	27.44	-	14.04	7.24
Cu-3.3Cr-1.5Nb-0.5Y_2O_3					
Red arrows	62.49	24.93	9.85	-	2.68
Yellow arrows	43.38	37.13	-	11.07	8.42

The proposed formation reaction of $YCrO_3$ implies the introduction of additional oxygen to the process zone. While the gas atmosphere during L-PBF processing only contains negligible amounts of oxygen (< 100 ppm), oxygen might be introduced into the printing process from the powder material. Copper powder handled in air is known to form an oxide layer, consisting of CuO [373, 468], and thus might carry oxygen into the printing process to provide oxygen to form $YCrO_3$. The EDS measurements performed on the powder particles' surface confirms the presence of oxygen, presumably bound as a thin oxide layer (Table 33).

The rather homogeneous nature of the hardness distribution is also reflected by the averaged hardness of the line profiles, showed in Fig. 81. Here, the superior hardness levels of oxide-dispersed material compared to the raw copper alloys becomes apparent.

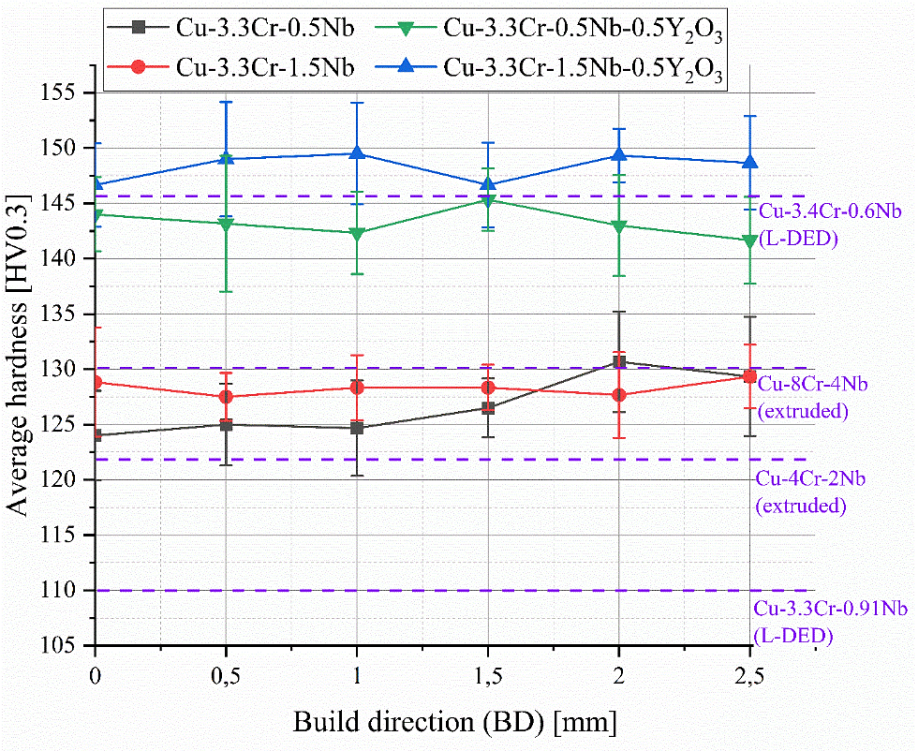

Fig. 81. Vickers hardness line profiles of manufactured specimen of Cu-3.3Cr-0.5Nb (black line), Cu-3.3Cr-1.5Nb (red line), Cu-3.3Cr-0.5Nb-0.5Y_2O_3 (green line), and Cu-3.3Cr-1.5Nb-0.5Y_2O_3 (blue line). Hardness values of Cu-Cr-Nb alloys manufactured by hot extrusion [614, 615] and laser directed energy deposition (L-DED) [616, 617] are shown in purple colour.

Additionally, higher niobium contents are also favourable for higher strength, presumably by higher fractions of nano-scaled precipitated Cr_2Nb laves phases, which cannot be resolved with the used SEM system. Considering the hardness values of extruded [614, 615] and L-DED [616, 617] processed Cu-Cr-Nb alloys, L-PBF manufactured material shows superior hardness despite lower chromium and niobium contents, which typically stems from smaller grain size due to higher cooling rates in L-PBF compared to L-DED or extrusion processes, as evident from chapter 6.3.3. However, Kini et al. [616] presents notably high hardness values (approx. 146 HV) for L-DED manufactured Cu-3.4Cr-0.6Nb (at.%) material, due to in-situ precipitation of Cr_2Nb laves particles by intrinsic heat treatment (IHT) mechanisms, frequently observed in L-DED processes [32, 33, 618, 619]. The higher fraction of precipitated Cr_2Nb and Cr-rich phases directly lead to an increased hardness. Thus, it is hypothesized, that a subsequent aging procedure of L-PBF manufactured ODS material will result in further increase of the hardness superior to L-DED manufactured counterparts. However, the resulting nanoparticle sizes with a d_{50} of approx. 58 nm (determined by ImageJ analysis from Fig. 80b) appear to by only slightly increased compared to PM2000 material (Fig. 62). Thus, it is deduced that the production of oxide dispersion-strengthened copper alloys using L-PBF is possible and higher volume energy densities show only moderate impact on the nanoparticle size and dispersion.

9 Conclusions

Additive manufacturing processes offer a promising alternative to the conventional manufacturing chain of ODS alloys. Due to the shorter process chain, i.e., by combining synthesis and shaping in a single process step, the economic production of ODS alloys by AM becomes feasible. However, the extensive literature research showed, that the current knowledge is still mainly based on singular mainly experimental studies, which are predominantely based on phenomenological and empirical research and focus on the feasibility of singular matrix alloy and oxide compound combinations using a single AM process. Only few studies exist, which include different AM processes utilizing identical powder feedstocks, allowing a comparative assessment of different AM technologies to identify critical factors regarding powder characteristics of the powder feedstock used and process-related conditions, including process parameters and solidification conditions. Thus, this thesis presents a comprehensive study including the conventional composite powder manufacturing process of Mechanical Alloying (MA) and the advanced laser-based methodology of Laser Synthesis and Processing of Colloids (LSPC) as well as the processing of the generated composite powders by the laser additive manufacturing technologies of Laser Directed Energy Deposition (L-DED), High-Speed Laser Cladding (HSLC) and Laser Powder Bed Fusion (L-PBF). The commercial ODS steel PM2000 with the chemical composition Fe20Cr4.5Al0.5Ti-0.5Y_2O_3 (wt.%) is used to demonstrate the impact of different composite powder manufacturing technologies and solidification conditions on oxide nanoparticle dispersion, size, and chemistry, determined by diverse microstructural chacterization techniques on different length scales. Additionally, the generated microstructures are correlated with mechanical properties from compression testing at room temperature and 600°C. Following conclusions can be drawn from this thesis:

In general, the preservation of the spherical morphology of composite powder materials and homogeneous distributions of nano-scaled oxides, which can be manufactured with the LSPC methodology appear to suit best for the examined AM processes regarding processability and final dispersion of nanoparticles in consolidated parts. In particular, the utilization of laser fragmentated oxide nanoparticles enhance the homogeneous dispersion of small oxide nanoparticles in the printed parts, as it compensates the inevitable agglomeration of oxide nanoparticles during the molten stage to a certain extend. L-PBF appears to be the most suitable process technique for ODS alloy manufacturing among the examined powder bed-based- and directed energy-based AM processes, as it offers the highest solidification rates compared to the powder blown-based L-DED process by utilizing significantly smaller beam diameters and consequently minimizing coarsening and flotation tendencies of dispersed nanoparticles during the melting stage. Consequently, L-PBF allows manufacturing dense microstructures with smallest oxide nanoparticle sizes of approx. 50 nm, whereas the utilization LSPC-generated composite powder materials results in a further reduction of the nanoparticle sizes by approx. 10% compared to MA-generated composite powders.

Considering the initial nanoparticle size, severe agglomeration of oxide nanoparticles is observed in L-DED manufactured specimens, particularly during processing with large beam diameters, leading to pronounced accumulation of oxide material on the surface of printed parts, which is referred as slag layer formation. It is however evident, that a high bandwidth oxide nanoparticles sizes are found in every consolidated part, regardless of the respective printing process. In this context, a need for more simulative studies disentangling influential factors on nanoparticle behavior in highly dynamic melt pools, which can be considered as almost unknown today, becomes evident. First studies, conducted by Xu and coworkers [413], show promising results and allow tracing of the nanoparticle pathways during the melting stage and after solidification. However, in order to guide simulative approaches deeper microstructural characterizations are required allowing the unequivocal identification of nanoparticle chemistries and the allocation of nanoparticles in the dispersed metallic matrix. Atom probe tomography (APT) is a suitable tool, but appears to be reliable only for features to be sufficiently small (> 100 nm) and present in high number densities, as no oxide nanoparticles in L-DED manufactured specimens could be captured. However, titanium-rich oxide nanoparticles could be identified in L-PBF manufactured specimen. Using additional TEM examinations, aluminium-rich nanoparticles with cubic-structured YAG-phase ($Y_3Al_5O_{12}$) are found proving that different species, namely titanium- and aluminum-rich oxide nanoparticles can be formed simultaneously during solidification in the titanium and aluminium alloyed ODS steel PM2000. In general, the additively manufactured ODS steels manufactured shows improved mechanical properties regarding compressive strength than the non-reinforced reference materials, particularly in high temperature environments. L-PBF manufactured material shows even higher compression strength at 600°C compared to conventionally manufactured PM2000 material from hot extrusion, showing the potential of AM for production of ODS materials. Moreover, the used methodology can be transferred to alternative material systems and the oxide reinforced variants of the exemplarily picked γ-TiAl intermetallic alloy and a Cu-Cr-Nb copper alloys are characterized by the homogeneous dispersion of nano-scaled oxide particles and higher mechanical strength.

However, further improvements of additively manufactured ODS materials still require a better understanding of the nanoparticle behavior in the melt pool, which may be determined by in-situ X-ray techniques [422, 423] allowing a direct observation of nanoparticle movement and agglomeration tendencies, which will directly affect the mechanical performance of ODS alloys. In order to demonstrate the potential of additively manufactured ODS alloys additional mechanical characterizations, including static and dynamic characterizations (e.g. creep examinations) over a broad temperature range are needed, which will allow to benchmark additvely manufactured ODS materials towards conventionally manufactured counterparts. This may allow the adjustment of the additive manufacturing process design towards homogeneous dispersions of extremely fine nanoparticles. Multiple approaches, based on the application of pulsed or short-termed energy introduction [621, 622], exposure of the melt pool by acoustic waves [623, 624, 625, 626, 627, 628, 629, 630], beam shaping

[631], and advanced scanning strategies [309] offer the potential to influence the melt pool behavior towards higher dynamics promoting the disruption of agglomerates formed during the melting stage in AM processes. Additional approaches, not involving tuning the AM process itself, may lie in tailoring the chemical composition of the matrix alloys. i.e., by adding specific elements, such as zirconium and hafnium, leading to the formation of chemically complex nano-scaled oxide compounds with extremely low solubility in metals and therefore enhancing the formation of smaller nanoparticles.

A. References

[1] Z. Stępień: A comprehensive overview of hydrogen-fueled internal combustion engines: Achievements and future challenges. Energies 14(20) (2021), 6504, https://doi.org/10.3390/en14206504

[2] A. A. Vasserman, M. A. Shutenko: Methods of increasing thermal efficiency of steam and gas turbine plants. IOP Conf. Ser. J. Phys. Ser. 891 (2017), 012248, https://doi.org/10.1088/1742-6596/891/1/012248

[3] M. M. Rahman, T. K. Ibrahim, A. N. Abdalla: Thermodynamic performance analysis of gas-turbine power-plant. Int. J. Phys. Sci. 6(14) (2011), 3539 – 3550, https://doi.org/10.5897/IJPS11.272

[4] X. Zhan, Z. Chen, C. Qin: Effect of hydrogen-blended natural gas on combustion stability and emission of water heater burner. Case Stud. Thermal Eng. 37 (2022), 102246, https://doi.org/10.1016/j.csite.2022.102246

[5] J. Gao, X. Wang, P. Song, G. Tian, C. Ma: Review of the backfire occurrences and control strategies for port hydrogen injection internal combustion engines. Fuel 307 (2022), 121553, https://doi.org/10.1016/j.fuel.2021.121553

[6] A. Onorati, R. Payri, B. M. Vaglieco, A. K. Agarwal, C. Bae, G. Bruneaux, M. Canakci, M. Gavaises, M. Günthner, C. Hasse, S. Kokjohn, S.-C. Kong, Y. Moriyoshi, R. Novella, A. Pesyridis, R. Reitz, T. Ryan, R. Wagner, H. Zhao: The role of hydrogen for future internal combustion engines. Int. J. Engine Res. 23(4) (2022), https://doi.org/10.1177/14680874221081947

[7] E. Stefan, B. Talic, Y. Larring, A. Gruber, T. A. Peters: Materials challenges in hydrogen-fuelled gas turbines. Int. Mater. Rev. 67(5) (2022), https://doi.org/10.1080/09506608.2021.1981706

[8] I. M. Kusoglu, B. Gökce, S. Barcikowski: Use of (nano-) additives in laser powder bed fusion of Al powder feedstocks: Research directions within the last decade. Proc. CIRP 94 (2020), 11 – 16, https://doi.org/10.1016/j.procir.2020.09.003

[9] X. P. Li, G. Ji, Z. Chen, A. Addad, Y. Wu, H. W. Wang, J. Vleugels, J. Van Humbeeck, J.-P. Kruth: Selective laser melting of nano-TiB_2 decorated AlSi10Mg alloy with high fracture strength and ductility. Acta Mater. 129 (2017), 183 – 193, https://doi.org/10.1016/j.actamat.2017.02.062

[10] X. Zhao, D. Gu, C. Ma, L. Xi, H. Zhang: Microstructure characteristics and its formation mechanism of selective laser melting SiC reinforced Al-based composites. Vacuum 160 (2019), 189 – 196, https://doi.org/10.1016/j.vacuum.2018.11.022

[11] P. Wang, C. Gammer, F. Brenne, T. Niendorf, J. Eckert, S. Scudino: A heat treatable TiB_2/Al-3.5Cu-1.5Mg-1Si composite fabricated by selective laser melting: Microstructure, heat treatment and mechanical properties. Comp. B 147 (2018), 162 – 168, https://doi.org/10.1016/j.compositesb.2018.04.026

[12] E. Gibney: Nuclear-fusion reactor smashes energy record. Nature 602 (2022), 371, https://doi.org/10.1038/d41586-022-00391-1

[13] C. Doñate-Buendia, P. Kürnsteiner, F. Stern, M. B. Wilms, R. Streubel, I. M. Kusoglu, J. Tenkamp, E. Bruder, N. Pirch, S. Barcikowski, K. Durst, J. H. Schleifenbaum, F. Walther, B. Gault, B. Gökce: Microstructure formation and mechanical properties of ODS steels built by laser additive manufacturing of nanoparticle coated iron- chromium powders. Acta Mater. 206 (2021), 116566, https://doi.org/10.1016/j.actamat.2020.116566

[14] J. R. Rieken, I. E. Anderson, M. J. Kramer, G. R. Odette, E. Stergar, E. Haney: Reactive gas atomization processing for Fe-based ODS alloys. J. Nucl. Mater. 428 (2012), 65 – 75, https://doi.org/10.1016/j.jnucmat.2011.08.015

[15] M. Letenneur, A. Kreitcberg, V. Brailovski: Optimization of laser powder bed fusion processing using a combination of melt pool modeling and design of experiment approaches: Density control. J. Manuf. & Mater. Proc. 3(1) (2019), 21, https://doi.org/10.3390/jmmp3010021

[16] C. Doñate-Buendia, F. Frömel, M. B. Wilms, R. Streubel, J. Tenkamp, T. Hupfeld, M. Nachev, E. Gökce, A. Weisheit, S. Barcikowski, F. Walther, J. H. Schleifenbaum, B. Gökce: Oxide dispersion-strengthened alloys generated by laser metal deposition of laser-generated nanoparticle-metal powder composites. Mater. & Des. 154 (2018), 360 – 369, https://doi.org/10.1016/j.matdes.2018.05.044

[17] M. K. Miller, D. T. Hoelzer, E. A. Kenik, K. F. Russell: Stability of ferritic MA/ODS alloys at high temperatures. Intermet. 13(3 – 4) (2005), 387 – 392, https://doi.org/10.1016/j.intermet.2004.07.036

[18] L. K. Mansur: Theory and experimental background on dimensional changes in irradiated alloys. J. Nucl. Mater. 216 (1994), 97 – 123, https://doi.org/10.1016/0022-3115(94)90009-4

[19] S.-K. Rittinghaus, E. A. Jägle, M. Schmid, B. Gökce: New frontiers in materials design for laser additive manufacturing. Mater. 15(17) (2022), 6172, https://doi.org/10.3390/ma15176172

[20] A. K. Singh, Y. Mundada, P. Bajaj, M. B. Wilms, J. P. Patil, S. K. Mishra, E. A. Jägle, A. Arora: Investigation of temperature distribution and solidification morphology in multilayered directed energy deposition of Al-0.5Sc-0.5Si alloy. Int. J. Heat & Mass Transf. 186 (2022), 122492, https://doi.org/10.1016/j.ijheatmasstransfer.2021.122492

[21] J. Berry, A. Perron, J.-L. Fattebert, J. D. Roehling, B. Vrancken, T. T. Roehling, D. L. Rosas, J. A. Turner, S. A. Khairallah, J. T. McKeown, M. J. Matthews: Toward multiscale simulations of tailored microstructure formation in metal additive manufacturing. Mater. Today 51 (2021), 65 – 86, https://doi.org/10.1016/j.mattod.2021.09.024

[22] S. A. Khairallah, A. T. Anderson, A. Rubenchik, W. E. King: Laser powder-bed fusion additive manufacturing: Physics of complex melt flow and formation mechanisms of pores, spatter, and denudation zones. Acta Mater. 108 (2016), 36 – 45, http://dx.doi.org/10.1016/j.actamat.2016.02.014

[23] F. Wirth, S. Arpagaus, K. Wegener: Analysis of melt pool dynamics in laser cladding and direct metal deposition by automated high-speed camera image evaluation. Addit. Manuf. 21 (2018), 369 – 382, https://doi.org/10.1016/j.addma.2018.03.025

[24] K. Schmidtke, F. Palm, A. Hawkins, C. Emmelmann: Process and mechanical properties: Applicability of a scandium modified Al-alloy for laser additive manufacturing. Phys. Proc. 12 A (2011), 369 – 374, https://doi.org/10.1016/j.phpro.2011.03.047

[25] A. B. Spierings, K. Dawson, T. Heeling, P. J. Uggowitzer, R. Schäublin, F. Palm, K. Wegener: Microstructural features of Sc- and Zr-modified Al-Mg alloys processed by selective laser melting. Mater. & Des. 115 (2017), 52 – 63, https://doi.org/10.1016/j.matdes.2016.11.040

[26] Q. Jia, P. Rometsch, P. Kürnsteiner, Q. Chao, A. Huang, M. Weyland, L. Bourgeois, X. Wu: Selective laser melting of a high strength Al-Mn-Sc alloy: Alloy design and strengthening mechanisms. Acta Mater. 171 (2019), 108 – 118, https://doi.org/10.1016/j.actamat.2019.04.014

[27] S. Griffiths, M. D. Rossell, J. Croteau, N. Q. Vo, D. C. Dunand, C. Leinenbach: Effect of laser rescanning on the grain microstructure of a selective laser melted Al-Mg-Zr alloy. Mater. Charact. 143 (2018), 34 – 42, https://doi.org/10.1016/j.matchar.2018.03.033

[28] J. R. Croteau, S. Griffiths, M. D. Rossell, C. Leinenbach, C. Kenel, V. Jansen, D. N. Seidman, D. C. Dunand, N. V. Vo: Microstructure and mechanical properties of Al-Mg-Zr alloys processed by selective laser melting. Acta Mater. 153 (2018), 35 – 44, https://doi.org/10.1016/j.actamat.2018.04.053

[29] M. Roscher, S. Balachandran, D. Mayweg, E. Jägle: Development of Al-Ti-based alloys for laser powder bed fusion. Addit. Manuf. 47 (2021), 102315, https://doi.org/10.1016/j.addma.2021.102315

[30] G. Rödler, F. G. Fischer, J. Preußner, V. Friedmann, C. Fischer, A. Weisheit, J. H. Schleifenbaum: Additive manufacturing of high-strength eutectic aluminium-nickel alloys – Processing and mechanical properties. J. Mater. Proc. Techn. 298 (2021), 117315, https://doi.org/10.1016/j.jmatprotec.2021.117315

[31] D. Knoop, A. Lutz, B. Mais, A. von Hehl: A tailored AlSi10Mg alloy for laser powder bed fusion. Metals 10(4) (2020), 514, https://doi.org/10.3390/met10040514

[32] P. Kürnsteiner, M. B. Wilms, A. Weisheit, P. Barriobero-Vila, E. A. Jägle, D. Raabe: Massive nanoprecipitation in an Fe-19Ni-xAl maraging steel triggered by the intrinsic heat treatment during laser metal deposition. Acta Mater. 129 (2017), 52 – 60, https://doi.org/10.1016/j.actamat.2017.02.069

[33] P. Kürnsteiner, M. B. Wilms, A. Weisheit, B. Gault, E. A. Jägle, D. Raabe: High-strength Damascus steel by additive manufacturing. Nature 582 (2020), 515 – 519, https://doi.org/10.1038/s41586-020-2409-3

[34] I. M. Kusoglu, F. Huber, C. Doñate-Buendia, A. R. Ziefuss, B. Gökce, J. T. Sehrt, A. Kwade, M. Schmidt, S. Barcikowski: Nanoparticle additivation effects on laser powder bed fusion of metals and polymers—A theoretical concept for an inter-laboratory study design all along the process chain, including research data management. Mater. 14(17) (2021), 4892, https://doi.org/10.3390/ma14174892

[35] S. D. Jadhav, P. P. Dhekne, E. Brodu, B. van Hooreweder, S. Dadbakhsh, J.-P. Kruth, J. van Humbeeck, K. Vanmeensel: Laser powder bed fusion additive manufacturing of highly conductive parts made of optically absorptive carburized CuCr1 powder. Mater. & Des. 198 (2021), 109369, https://doi.org/10.1016/j.matdes.2020.109369

[36] O. Pannitz, F. Großwendt, A. Lüddecke, A. Kwade, A. Röttger, J. T. Sehrt: Improved process efficiency in laser-based powder bed fusion of nanoparticle coated maraging tool steel powder. Mater. 14(13) (2021), 3465, https://doi.org/10.3390/ma14133465

[37] A. Lüddecke, O. Pannitz, H. Zetzener, J. T. Sehrt, A. Kwade: Powder properties and flowability measurements of tailored nanocomposites for powder bed fusion applications. Mater. & Des. 202 (2021), 109536, https://doi.org/10.1016/j.matdes.2021.109536

[38] E. Gärtner, H. Y. Jung, N. J. Peter, G. Dehm, E. A. Jägle, V. Uhlenwinkel, L. Mädler: Reducing cohesion of metal powders for additive manufacturing by nanoparticle dry-coating. Powder Techn. 379 (2021), 585 – 595, https://doi.org/10.1016/j.powtec.2020.10.065

[39] A. Mussatto, R. Groarke, A. A-Hameed, I. U. I. Ahad, R. K. Vijayaraghavan, A. O'Neill, P. McNally, Y. Delaure, D. Brabazon: Evaluation via powder metallurgy of nano-reinforced iron

powders developed for selective laser melting applications. Mater. & Des. 182, 108046, https://doi.org/10.1016/j.matdes.2019.108046

[40] C. Ma, L. Chen, C. Cao, X. Li: Nanoparticle-induced unusual melting and solidification behaviours of metals. Nature Comm. 8 (2017), 14178, https://doi.org/10.1038/ncomms14178

[41] M. Qu, Q. Guo, L. I. Escano, S. J. Clark, K. Fezzaa, L. Chen: Mitigating keyhole pore formation by nanoparticles during laser powder bed fusion additive manufacturing. Add. Manuf. Lett. 3 (2022), 100068, https://doi.org/10.1016/j.addlet.2022.100068

[42] J. H. Martin, B. D. Yahata, J. M. Hundley, J. A. Mayer, T. A. Schaedler, T. M. Pollock: 3D printing of high-strength aluminium alloys. Nature 549 (2017), 365 – 369, https://doi.org/10.1038/nature23894

[43] M. Opprecht, J.-P. Garandet, G. Roux, C. Flament, M. Soulier: A solution to the hot cracking problem for aluminium alloys manufactured by laser beam melting. Acta Mater. 197 (2020), 40 – 53, https://doi.org/10.1016/j.actamat.2020.07.015

[44] I. M. Kusoglu, B. Gökce, S. Barcikowski: Research trends in laser powder bed fusion of Al alloys within the last decade. Addit. Manuf. 36 (2020), 1014489, https://doi.org/10.1016/j.addma.2020.101489

[45] Q. Chao, S. Mateti, M. Annasamy, M. Imran, J. Joseph, Q. Cai, L. H. Li, P. Cizek, P. D. Hodgson, Y. Chen, D. Fabijanic, W. Xu: Nanoparticle-mediated ultra grain refinement and reinforcement in additively manufactured titanium alloys. Addit. Manuf. 46 (2021), 102173, https://doi.org/10.1016/j.addma.2021.102173

[46] X. Cheng, Y. Zhao, Z. Qian, J. Wu, J. Dong, Z. Ma, Y. Liu: Crack elimination and mechanical properties enhancement in additive manufactured Hastelloy X via in-situ chemical doping of Y_2O_3. Mater. Sci. & Eng. A 824 (2021), 141867, https://doi.org/10.1016/j.msea.2021.141867

[47] K. Li, D. Wang, L. Xing, Y. Wang, C. Yu, J. Chen, T. Zhang, J. Ma, W. Liu, Z. Shen: Crack suppression in additively manufactured tungsten by introducing secondary-phase nanoparticles into the matrix. Int. J. Refract. Met. & Hard Met. 79 (2019), 158 – 163, https://doi.org/10.1016/j.ijrmhm.2018.11.013

[48] S. A. M. Tofail, E. P. Koumoulos, A. Bandyopadhyay, S. Bose, L. O'Donoghue, C. Charitidis: Additive manufacturing: Scientific and technological challenges, market uptake and opportunities. Mater. Today 21(1) (2018), 22 – 37, https://doi.org/10.1016/j.mattod.2017.07.001

[49] D. Herzog, V. Seyda, E. Wycisk, C. Emmelmann: Additive manufacturing of metals. Acta Mater. 117 (2016), 371 – 392, https://doi.org/10.1016/j.actamat.2016.07.019

[50] D. D. Gu, W. Meiners, K. Wissenbach, R. Poprawe: Laser additive manufacturing of metallic components: materials, processes and mechanisms. Int. Mater. Rev. 57(3) (2012), 133 – 164, https://doi.org/10.1179/1743280411Y.0000000014

[51] T. DebRoy, T. Mukherjee, J. O. Milewski, J. W. Elmer, B. Ribic, J. J. Blecher, W. Zhang: Scientific, technological and economic issues in metal printing and their solutions. Nat. Mater. 18 (2019), 1026 – 1032, https://doi.org/10.1038/s41563-019-0408-2

[52] W. Bai, H. Fang, Y. Wang, Q. Zeng, G. Hu, G. Bao, Y. Wan: Academic insights and perspectives in 3D printing: A bibliometric review. Appl. Sci. 11 (2020), 8298, https://doi.org/10.3390/app11188298

[53] A. A. Ahmed, A. Musbah, A. Atiyah: 4D printing technology: A revolution across manufacturing. Int. J. Mech. & Industr. Techn. 7, (2020), 45 – 51, ISSN 2348-7593

[54] A. T. Clare, R. S. Mishra, M. Merklein, H. Tan, I. Todd, L. Chechik, J. Li, M. Bambach: Alloy design and adaptation for additive manufacturing. J. Mater. Proc. Techn. 299 (2022), 117358, https://doi.org/10.1016/j.jmatprotec.2021.117358

[55] C. Doñate-Buendia, D. Gu, M. Schmidt, S. Barcikowski, A. M. Korsunsky, B. Gökce: On the selection and design of powder materials for laser additive manufacturing. Mater. & Des. 204 (2021), 109653, https://doi.org/10.1016/j.matdes.2021.109653

[56] T. M. Pollock, A. J. Clarke, S. S. Babu: Design and tailoring of alloys for additive manufacturing. Met. & Mater. Trans. A 51 (2020), 6000 – 6019, https://doi.org/10.1007/s11661-020-06009-3

[57] G. Liu, X. Zhang, X. Chen, Y. He, L. Cheng, M. Huo, J. Yin, F. Hao, S. Chen, P. Wang, S. Yi, L. Wan, Z. Mao, Z. Chen, X. Wang, Z. Cao, J. Lu: Additive manufacturing of structural materials. Mater. Sci. & Eng. R 145 (2021), 100596, https://doi.org/10.1016/j.mser.2020.100596

[58] D. Bourell, J. P. Kruth, M. Leu, G. Levy, D. Rosen, A. M. Beese, A. Clare: Materials for additive manufacturing. CIRP Annals – Manuf. Techn. 66 (2017), 659 – 681, https://doi.org/10.1016/j.cirp.2017.05.009

[59] K. Mino: Development of ODS superalloy technology in Japan for turbine blade applications. J. Eng. Gas Turbines Power. 113(4) (1991), 568 – 573, https://doi.org/10.1115/1.2906279

[60] D. T. Hoelzer: History and outlook of ODS/NFA ferritic alloys for nuclear applications. Trans. American. Nucl. Soc. 118(1) (2018), 1587 – 1590, https://www.osti.gov/biblio/1464007

[61] M. E. Medhat, Y. Wang: Investigation on radiation shielding parameters of oxide dispersion strengthened steels used in high temperature nuclear reactor applications. Ann. Nucl. Ener. 80 (2015), 365 – 370, https://doi.org/10.1016/j.anucene.2015.01.044

[62] A. Czyrska-Filemonowicz, B. Dubiel: Mechanically alloyed, ferritic oxide dispersion strengthened alloys: Structure and properties. J. Mater. Proc. Techn. 64 (1997), 53 – 64, https://doi.org/10.1016/S0924-0136(96)02553-8

[63] S. Ukai, M. Fujiwara: Perspective of ODS alloys application in nuclear environments. J. Nucl. Mater. 307 – 311 (2002), 749 – 757, https://doi.org/10.1016/S0022-3115(02)01043-7

[64] T. Allen, J. Busby, M. Meyer, D. Petti: Materials challenges for nuclear systems. Mater. Today 13 (2010), 12, 14 – 23, https://doi.org/10.1016/S1369-7021(10)70220-0

[65] G. R. Odette: Recent progress in developing and qualifying nanostructured ferritic alloys for advanced fission and fusion applications. JOM 66 (2014), 12, https://doi.org/10.1007/s11837-014-1207-5

[66] M. K. Miller, D. T. Hoelzer, E. A. Kenik, K. F. Russell: Nanometer scale precipitation in ferritic MA/ODS alloy MA957. J. Nucl. Mater. 329 – 333 (2004), 338 – 341, https://doi.org/10.1016/j.jnucmat.2004.04.085

[67] M. Klimiankou, R. Lindau, A. Möslang: HRTEM study of yttrium oxide particles in ODS steels for fusion reactor application. J. Cryst. Growth 249 (2003), 381 – 387, https://doi.org/10.1016/S0022-0248(02)02134-6

[68] R. Schaeublin, T. Leguey, P. Spätig, N. Baluc, M. Victoria: Microstructure and mechanical properties of two ODS ferritic/martensitic steels. J. Nucl. Mater. 307 – 311 (2002), 778 - 782, https://doi.org/10.1016/S0022-3115(02)01193-5

[69] J. H. Schneibel, C. T. Liu, M. K. Miller, M. J. Mills, P. Sarosi, M. Heilmeier, D. Sturm: Ultrafine-grained nanocluster-strengthened alloys with unusually high creep strength. Scr. Mater. 61 (2009), 793 – 796, https://doi.org/10.1016/j.scriptamat.2009.06.034

[70] W. Xu, L. Li, J. A. Valdez, M. Saber, Y. Zhu, C. C. Koch, R. A. Scattergood: Effect of nano-oxide particle size on radiation resistance of iron-chromium alloys. J. Nucl. Mater. 469 (2016), 72 – 81, https://doi.org/10.1016/j.jnucmat.2015.11.044

[71] R. Casati, M. Vedani: Metal Matrix Composites reinforced by nano-particles- A Review. Metals 4(1) (2014), 65 – 83, https://doi.org/10.3390/met4010065

[72] P. Deng, M. Song, J. Yang, Q. Pan, S. McAllister, L. Li, B. C. Prorok, X. Lou: On the thermal coarsening and transformation of nanoscale oxide inclusions in 316L stainless steel manufactured by laser powder bed fusion and its influence on impact toughness. Mater. Sci. & Eng. A 835 (2022), 142690, https://doi.org/10.1016/j.msea.2022.142690

[73] M. Bartsch, A. Wasilkowska, A. Czyrska-Filemonowicz, U. Messerschmidt: Dislocation dynamics in the oxide dispersion strengthened alloy INCOLOY MA956. Mater. Sci. & Eng. A 272(1) (1999), 152 – 162, https://doi.org/10.1016/S0921-5093(99)00471-2

[74] P. Susila, D. Sturm, M. Heilmaier, B. S. Murty, V. Subramanya Sarma: Effect of yttria particle size on the microstructure and compression creep properties of nanostructured oxide dispersion strengthened ferritic (Fe–12Cr–2W–0.5Y_2O_3) alloy. Mater. Sci. & Eng. A 528 (2011), 4579 – 4584, https://doi.org/10.1016/j.msea.2011.02.078

[75] A. Ramar, N. Baluc, R. Schäublin: On the coherency of oxide particles dispersed in Eurofer97. J. Nucl. Mater. 386 – 388 (2009), 515 – 519, https://doi.org/10.1016/j.jnucmat.2008.12.137

[76] Y. Wu, J. Ciston, S. Kräemer, N. Bailey, G. R. Odette, P. Hosemann: The crystal structure, orientation relationships and interfaces of the nanoscale oxides in nanostructured ferritic alloys. Acta Mater. 111 (2016), 108 – 115, https://doi.org/10.1016/j.actamat.2016.03.031

[77] S. Ukai, S. Yamashita: Dislocation-climbing bypass over dispersoids with different lattice misfit in creep deformation of FeCrAl oxide dispersion-strengthened alloys. J. Mater. Res. & Techn. 16 (2022), 891 – 898, https://doi.org/10.1016/j.jmrt.2021.11.123

[78] Y.-K. Kim, J.-H. Yu, H. S. Kim, K.-A. Lee: In-situ carbid-reinforced CoCrFeMnNi high-entropy alloy matrix nanocomposites manufactured by selective laser melting: Carbon content effects on microstructure, mechanical properties, and deformation mechanism. Comp. B 210 (2021), 108638, https://doi.org/10.1016/j.compositesb.2021.108638

[79] R. Gao, L. Zeng, H. Ding, T. Zhang, X. Wang, Q. Fang: Characterization of oxide dispersion strengthened ferritic steel fabricated by electron beam selective melting. Mater. & Des. 89 (2016), 1171 – 1180, https://doi.org/10.1016/j.matdes.2015.10.073

[80] M. C. Brandes, L. Kovarik, M. K. Miller, G. S. Daehn, M. J. Mills: Creep behavior and deformation mechanisms in a nanocluster strengthened ferritic steel. Acta Mater. 60 (2012), 1827 – 1839, https://doi.org/10.1016/j.actamat.2011.11.057

[81] R. Jarugula, S. Channagiri, S. G. Sundara Raman, G. Sundararajan: Strengthening mechanism in nano oxide dispersion-strengthened Fe-18Cr ferritic steel at different temperatures. Metal. & Mater. Trans. A 52 (2021), 1901 – 1912, https://doi.org/10.1007/s11661-021-06200-0

[82] D. Häussler, B. Reppich, M. Bartsch, U. Messerschmidt: Interaction processes between dislocations and particles in the ODS nickel-base superalloy INCONEL MA 754 studied by means of in situ straining in an HVEM. Mater. Sci. & Eng. A 309 – 310 (2001), 500 – 504, https://doi.org/10.1016/S0921-5093(00)01642-7

[83] Y. Sugino, S. Ukai, B. Leng, N. Oono, S. Hayashi, T. Kaito, S. Ohtsuka: Grain boundary sliding at high temperature deformation in cold-rolled ODS ferritic steel. J. Nucl. Mater. 425(1-3) (2014), 628 – 632, https://doi.org/10.1016/j.jnucmat.2014.05.040

[84] H. Masuda, H. Tobe, E. Sato, Y. Sugino, S. Ukai: Diffusional mass flux accommodating two-dimensional grain boundary sliding in ODS ferritic steel. Acta Mater. 176 (2019), 63 – 72, https://doi.org/10.1016/j.actamat.2019.06.049

[85] R. Kamikawa, S. Ukai, S. Kasai, N. Oono, S. Zhang, Y. Sugino, H. Masuda, E. Sato: Cooperative grain boundary sliding in creep deformation of FeCrAl-ODS steels at high temperature and low strain rate. J. Nucl. Mater. 511 (2018), 591 – 597, https://doi.org/10.1016/j.jnucmat.2018.04.050

[86] H. Clemens, S. Mayer, C. Scheu: Microstructure and properties of engineering materials. In: Neutrons and synchrotron radiation in engineering materials science: From fundamentals to applications. (2017), https://doi.org/10.1002/9783527684489

[87] J.-H. Ahn, T. K. Kim, J. Ahn: The effect of additive element on the properties of mechanicalloy alloyed Fe-Y_2O_3 alloys. Arch. Met. Mater. 62(2B) (2017), 1043 – 1046, https://doi.org/10.1515/amm-2017-0150

[88] J. Malaplate, F. Mompiou, J.-L. Béchade, T. van den Berghe, M. Ratti: Creep behavior of ODS materials: A study of dislocations/precipitates interactions. J. Nucl. Mater. 417 (2011), 205 – 208, https://doi.org/10.1016/j.jnucmat.2010.12.059

[89] R. L. Klueh, P. J. Maziasz, I. S. Kim, L. Heatherly, D. T. Hoelzer, N. Hasimoto, E. A. Kenik, K. Miyahara: Tensile and creep properties of an oxide dispersion-strengthened ferritic steel. J. Nucl. Mater. 307 – 311 (2002), 773 – 777, https://doi.org/10.1016/S0022-3115(02)01046-2

[90] G. Yu, N. Nita, N. Baluc: Thermal creep behaviour of the EUROFER 97 RAFM steel and two European ODS EUROFER 97 steels. Fus. Eng. & Des. 75 – 79 (2005), 1037 – 1041, https://doi.org/10.1016/j.fusengdes.2005.06.311

[91] N. Oono, K. Nakamura, S. Ukai, T. Kaito, T. Torimaru, A. Kimura, S. Hayashi: Oxide particle coarsening at temperature over 1473 K in 9Cr ODS steel. Nucl. Mater. & Ener. 9 (2016), 342 – 345, https://doi.org/10.1016/j.nme.2016.06.008

[92] J. R. O. Leo, S. R. Moturu, M. E. Fitzpatrick: TEM study of the effect of high-temperature thermal cycles on the stability of the Y-Al-O oxides in MA956 ODS steel. J. Mater. Res. & Techn. 8(5) (2019), 3719 – 3725, https://doi.org/10.1016/j.jmrt.2019.06.027

[93] M. R. J. Sandim, I. R. Souza Filho, E. H. Bredda, A. Kostka, D. Raabe, H. R. Z. Sandim: Short Communication on "Coarsening of Y-rich oxide particles in 9% Cr-ODS Eurofer steel annealed at 1350°C". J. Nucl. Mater. 484 (2017), 283 – 287, https://doi.org/10.1016/j.jnucmat.2016.12.025

[94] J. Ribis, M.-L. Lescoat, S. Y. Zhong, M.-H. Mathon, Y. de Carlan: Influence of the low interfacial density energy on the coarsening resistivity of the nano-oxide particles in Ti-added ODS material. J. Nucl. Mater. 442(1 – 3) (2013), 101 – 105, https://doi.org/10.1016/j.jnucmat.2012.10.051

[95] N. V. Luzginova, H. S. Nolles, P. ten Pierick, T. Bakker, R. K. Mutnuru, M. Jong, D. T. Blagoeva: Irradiation response of ODS Eurofer97 steel. J. Nucl. Mater. 428 (2012), 192 – 196, https://doi.org/10.1016/j.jnucmat.2011.08.030

[96] F. D. Fisher, J. Svoboda, P. Fratzl: A thermodynamic approach to grain growth and coarsening. Phil. Mag. 83(9) (2003), 1075 – 1093, https://doi.org/10.1080/0141861031000068966

[97] V. S. M. Pereira, T. P. Davis, M. H. Mayoral, A. Kumar, H. Schut, J. Sietsma: Investigation of coarsening of oxide nanoparticles at 1400 K and its effect on the microstructure formation of an ODS Eurofer steel. Mater. Charact. 185 (2022), 111723, https://doi.org/10.1016/j.matchar.2022.111723

[98] M. A. Moghadasi, M. Nili-Ahmadabadi, F. Forghani, H. S. Kim: Development of an oxide-dispersion-strengthened steel by introducing oxygen carrier compound into the melt aided by a general thermodynamic model. Sci. Rep. 6 (2016), 38621, https://doi.org/10.1038/srep38621

[99] Z. Guo, Q. Liu, W. Yang, L. Guo: Densification and properties of ODS-iron based alloy. Rare Met. 31(4) (2012), 339 – 342, https://doi.org/10.1007/s12598-012-0517-4

[100] D. A. McClintock, M. A. Solokov, D. T. Hoelzer, R. K. Nanstad: Mechanical properties of irradiated ODS-EUROFER and nanocluster strengthened 14YWT. J. Nucl. Mater. 392 (2009), 353 – 359, https://doi.org/10.1016/j.jnucmat.2009.03.024

[101] A. Chauhan, F. Bergner, A. Etienne, J. Aktaa, Y. de Carlan, C. Heintze, D. Litvinov, M. Hernández-Mayoral, E. Oñorbe, B. Radiguet, A. Ulbricht: Microstructure characterization and strengthening mechanisms of oxide dispersion strengthened (ODS) Fe-9%Cr and Fe-14%Cr extruded bars. J. Nucl. Mater. 494 (2017), 6 – 19, https://doi.org/10.1016/j.jnucmat.2017.07.060

[102] T. Hayashi, P. M. Sarosi, J. H. Schneibel, M. J. Mills: Creep response and deformation processes in nanocluster-strengthened ferritic steels. Acta Mater. 56 (2008), 1407 – 1416, https://doi.org/10.1016/j.actamat.2007.11.038

[103] A. Bhadauria, L. K. Singh, A. R. Ballal, R. Vijay: Effect of yttria dispersion on creep properties of pure iron. Trans. Indian Inst. Met. 69(2) (2016), 253 – 259, https://doi.org/10.1007/s12666-015-0736-0

[104] A. Wasilkowska, M. Bartsch, U. Messerschmidt, R. Herzog, A. Czyrska-Filemonowicz: Creep mechanisms of ferritic oxide dispersion strengthened alloys. J. Mater. Proc. Techn. 133 (2003), 218 – 224, https://doi.org/10.1016/S0924-0136(02)00237-6

[105] B. N. Goshchitskii, V. V. Saragadze, V. I. Shalaev, V. L. Arbuzov, Y. Tian, W. Qun, S. Jiguang: Structure, radiation resistance and thermal creep of ODS ferritic steels. J. Nucl. Mater. 307 – 311(1) (2003), 783 – 787, https://doi.org/10.1016/S0022-3115(02)01047-4

[106] P. Dymáček, J. Svoboda, H. Jirková, L. Stratil, V. Hornik: Microstructure evolution and creep strength of new-generation oxide dispersion strengthened alloys with high volume fraction of nano-oxides. Proc. Struc. Integr. 17 (2019), 427 – 433, https://doi.org/10.1016/j.prostr.2019.08.056

[107] J. Rösler, E. Arzt: A new model-based creep equation for dispersion strengthened materials. Acta Metall. Mater. 38 (1990), 671 – 683, https://doi.org/10.1016/0956-7151(90)90223-4

[108] D. T. Hoelzer, J. Bentley, M. A. Sokolov, M. K. Miller. G. R. Odette, M. J. Alinger: Influence of particle dispersions on the high-temperature strength of ferritic alloys. J. Nucl. Mater. 367 – 370 (2007), 166 – 172, https://doi.org/10.1016/j.jnucmat.2007.03.151

[109] M. Dadé, J. Malaplate, J. Garnier, F. De Geuser, F. Barcelo, P. Wident, A. Dechamps: Influence of microstructural parameters on the mechanical properties of oxide dispersion strengthened Fe-14Cr steels. Acta Mater. 127 (2017), 165 – 177, https://doi.org/10.1016/j.actamat.2017.01.026

[110] J. Brodrick, D. J. Hepburn, G. J. Ackland: Mechanism for radiation damage resistance in yttrium oxide dispersion strengthened steels. J. Nucl. Mater. 445 (2014), 291 – 297, https://doi.org/10.1016/j.jnucmat.2013.10.045

[111] M. A. Auger, D. T. Hoelzer, K. G. Fields, M. P. Moody: Nanoscale analysis of ion irradiated ODS 14YWT ferritic alloy. J. Nucl. Mater. 528 (2020), 151852, https://doi.org/10.1016/j.jnucmat.2019.151852

[112] C. Lu, Z. Lu, X. Wang, R. Xie, Z. Li, M. Higgins, C. Liu, F. Gao, L. Wang: Enhanced radiation-tolerant oxide dispersion strengthened steel and its microstructure evolution under helium-implanation and heavy-ion irradiation. Sci. Rep. 7 (2017), 40343, https://doi.org/10.1038/srep40343

[113] M. P. Higgins, Q. Peng, L. Shao, F. Gao: Reduction of defect generation and development of sinks at nanocluster boundary in oxide dispersion-strengthened steel. J. Appl. Phys. 126 (2019), 084302, https://doi.org/10.1063/1.5102090

[114] P. Pareige, M. K. Miller, R. E. Stoller, D. T. Hoelzer, E. Cadel, B. Radiguet: Stability of nanometer-sized oxide clusters in mechanically-alloyed steel under ion-induced displacement cascade damage conditions. J. Nucl. Mater. 360 (2007), 136 – 142, https://doi.org/10.1016/j.jnucmat.2006.09.011

[115] S. J. Zinkle, L. L. Snead: Designing radiation resistance in materials for fusion energy. Annu. Rev. Mater. Res. 44 (2014), 241 – 267, https://doi.org/10.1146/annurev-matsci-070813-113627

[116] D. Sun, R. Li, J. Ding, S. Huang, P. Zhang, Z. Lu, J. Zhao: Helium behavior in oxide dispersion strengthened (ODS) steel: Insights from ab initio modeling. J. Nucl. Mater. 499 (2018), 71 – 78, https://doi.org/10.1016/j.jnucmat.2017.10.073

[117] V. Krsjak, T. Shen, J. Degmova, S. Sojak, E. Korpas, P. Noga, W. Egger, B. Li, V. Slugen, F. A. Garner: On the helium bubble swelling in nano-oxide dispersion-strengthened steels. J. Mater. Sci. & Techn. 105 (2022), 172 – 181, https://doi.org/10.1016/j.jmst.2021.08.004

[118] L. Yang, Y. Jiang, G. R. Odette, T. Yamamoto, Z. Liu, Y. Liu: Trapping helium in $Y_2Ti_2O_7$ compared to in matrix iron: A first principles study. J. Appl. Phys. 115 (2014), 143508, https://doi.org/10.1063/1.4871282

[119] K. Yutani, H. Kishimoto, R. Kasada, A. Kimura: Evaluation of helium effects on swelling behavior of oxide dispersion strengthened ferritic steels under ion irradiation. J. Nucl. Mater. 367 – 370 (2007), 423 – 427, https://doi.org/10.1016/j.jnucmat.2007.03.016

[120] Q. Li, C. M. Parish, K. A. Powers, M. K. Miller: Helium solubility and bubble formation in nanostructured ferritic alloy. J. Nucl. Mater. 445(1 – 3) (2014), 165 – 174, https://doi.org/10.1016/j.jnucmat.2013.10.048

[121] A. B. Sivak, P. A. Sivak, V. M. Chernov: Accelerated Monte Carlo method for calculation of sink strengths of absorbing surfaces for 3-D migrating particles in crystals of the cubic system. J. Nucl. Mater. 531 (2020), 152006, https://doi.org/10.1016/j.jnucmat.2020.152006

[122] P. D. Edmondson, A. London, A. Xu, D. E. J. Armstrong, S. G. Roberts: Small-scale characterisation of irradiated nuclear materials: Part I – Microstructure. J. Nucl. Mater. 462 (2015), 369 – 373, https://doi.org/10.1016/j.jnucmat.2014.11.067

[123] M. B. Toloczko, F. A. Garner, V. N. Voyevodin, V. V. Bryk, O. V. Borodin, V. V. Mel'nychenko, A. S. Kalchenko: Ion-induced swelling of ODS ferritic alloy MA957 tubing to 500 dpa. J. Nucl. Mater. 453 (2014), 323 – 333, https://doi.org/10.1016/j.jnucmat.2014.06.011

[124] F. A. Garner, M. B. Toloczko, B. H. Sencer: Comparison of swelling and irradiation creep behavior of fcc-austeinitic and bcc-ferritic/martensitic alloys at high neutron exposure. J. Nucl. Mater. 276 (2000), 123 – 142, https://doi.org/10.1016/S0022-3115(99)00225-1

[125] S. Xu, W. Zheng, L. Yang: A review of irradiation effects on mechanical properties of candidate SCWR fuel cladding alloys for design considerations. CNL Nucl. Rev. 5(2) (2016), https://doi.org/10.12943/CNR.2016.00036

[126] R. A. Robie, B. S. Hemingway, J. R. Fisher: Thermodynamic properties of minerals and related substances at 298.15 K and 1 bar (10^5 pascals) pressure and at higher temperatures. US Geolog. Surv. (1978), 1452, https://doi.org/10.3133/b2131

[127] S. G. Epstein, A. A. Bauer, R. F. Dickerson: Solubility limits of yttrium and the lanthanide rare-earth elements in chromium and chromium-iron alloys. US Rep. (1959), https://doi.org/10.2172/4194051

[128] S. Chung, B. Lee, S. Y. Lee, C. Do, H. J. Ryu: The effects of Y pre-alloying on the in-situ dispersoids of ODS CoCrFeMnNi high-entropy alloy. J. Mater. Sci. & Techn. 85 (2021), 62 – 75, https://doi.org/10.1016/j.jmst.2020.11.081

[129] L. L. Hsiung, M. J. Fluss, A. Kimura: Structure of oxide nanoparticles in Fe-16Cr MA/ODS ferritic steel. Mater. Let. 64(16) (2010), 1782 – 1785, https://doi.org/10.1016/j.matlet.2010.05.039

[130] A. J. London, S. Santra, S. Amirthapandian, B. K. Panigrahi, R. M. Sarguna, S. Balaji, R. Vijay, C. S. Sundar, S. Lozano-Perez, C. R. M. Grovenor: Effect of Ti and Cr on dispersion, structure and composition of oxide nano-particles in model ODS alloys. Acta Mater. 97 (2015), 223 – 233, https://doi.org/10.1016/j.actamat.2015.06.032

[131] M. Ratti, D. Leuvrey, M. H. Mathon, Y. de Carlan: Influence of titanium on nano cluster (Y, Ti, O) stability in ODS ferritic materials. J. Nucl. Mater. 386 – 388 (2009), 540 – 543, https://doi.org/10.1016/j.jnucmat.2008.12.171

[132] K. Verhiest, S. Mullens, J. Paul, I. De Graeve, N. De Wispelaere, S. Claessens, A. DeBremaecker, K. Verbeken: Experimental study on the contact angle formation of solidified iron-chromium droplets into yttria ceramic substrates for the yttria/ferrous alloy system with variable chromium content. Ceram. Int. 40 (2014), 2187 – 2200, https://doi.org/10.1016/j.ceramint.2013.07.137

[133] R. Rahmanifard, H. Farhangi, A. J. Novinrooz: Effect of zirconium and tantalum on the microstructural characteristics of 12YWT ODS steel nanocomposite. J. All. & Comp. 622 (2015), 948 – 952, https://doi.org/10.1016/j.jallcom.2018.07.047

[134] R. Gao, X. P. Wang, Q. F. Wang, C. S. Liu: Effect of zirconium addition on the microstructure and mechanical properties of ODS ferritic steels containing aluminum. J. Nucl. Mater. 444(1 – 3) (2014), 462 – 468, https://doi.org/10.1016/j.jnucmat.2013.10.038

[135] H. Yu, S. Kondo, R. Kasada, N. Oono, S. Hayashi, S. Ukai: Development of nano-oxide particles dispersed alumina scale formed on Zr-added FeCrAl ODS ferritic alloys. Nucl. Mater. & Ener. 25 (2020), 100798, https://doi.org/10.1016/j.nme.2020.100798

[136] P. Dou, A. Kimura, R. Kasada, T. Okuda, M. Inoue, S. Ukai, S. Ohnuki, T. Fujisawa, F. Abe, S. Jiang, Z. Yang: TEM and HRTEM study of oxide particles in an Al-alloyed high-Cr oxide

dispersion strengthened ferritic steel with Hf addition. J. Nucl. Mater. 485 (2017), 189 – 201, https://doi.org/10.1016/j.jnucmat.2016.12.001

[137] B. R. Sun, A. D. Zhou, Y. L. Li, Z. L. Zhang, C. C. Du, S. X. Y. Gu, Z. Chen, X. C. Cai, S. W. Xin, T. D. Shen: Ultrafine-grained oxide-dispersion-strengthened 9Cr steel with exceptional strength and thermal stability. Nucl. Mater. & Ener. 30 (2022), 101112, https://doi.org/10.1016/j.nme.2021.101112

[138] L. Song, X. Yang, Y. Zhao, W. Wang, X. Mao: Si-containing 9Cr ODS steel designed for high temperature application in lead-cooled fast reactor. J. Nucl. Mater. 519 (2019), 22 – 29, https://doi.org/10.1016/j.jnucmat.2019.03.029

[139] Z. Oksiuta, M. Lewandowska, K. J. Kurzydlowski, N. Baluc: Effect of vanadium addition on the microstructure and mechanical properties of the ODS ferritic steels. J. Nucl. Mater. 442 (2013), 84 – 88, https://doi.org/10.1016/j.jnucmat.2012.10.022

[140] J. Fu, T. P. Davis, A. Kumar, I. M. Richardson, M. J. M. Hermans: Characterisation of the influence of vanadium and tantalum on yttrium-based nano-oxides in ODS Eurofer steel. Mater. Charact. 175 (2020), 111072, https://doi.org/10.1016/j.matchar.2021.111072

[141] C. P. Massey, P. D. Edmondson, K. A. Unocic, Y. Yang, S. N. Dryepondt, A. Kini, B. Gault, K. A. Terrani, S. J. Zinkle: The effect of Zr on precipitation in oxide dispersion strengthened FeCrAl alloys. J. Nucl. Mater. 533 (2020), 152105, https://doi.org/10.1016/j.jnucmat.2020.152105

[142] L. Li, W. Xu, M. Saber, Y. Zhu, C. C. Koch, R. O. Scattergood: Influence of scandium addition on the high-temperature grain size stabilization of oxide-dispersion-strengthened (ODS) ferritic alloy. Mater. Sci. & Eng. A 636 (2015), 565 – 571, https://doi.org/10.1016/j.msea.2015.03.117

[143] P. Dou, S. Jiang, L. Qiu, A. Kimura: Effects of contents of Al, Zr, and Ti on oxide particles in Fe-15Cr-2W-0.35Y_2O_3 ODS steels. J. Nucl. Mater. 531 (2020), 152025, https://doi.org/10.1016/j.jnucmat.2020.152025

[144] P. Dou, L. Qiu, S. Jiang, A. Kimura: Crystal and metal/oxide interface structures of nanoparticles in Fe-16Cr-0.1Ti-0.35Y_2O_3 ODS steel. J. Nucl. Mater. 523 (2019), 320 – 332, https://doi.org/10.1016/j.jnucmat.2019.05.015

[145] P. Dou, Q. Ye, A. Kimura: Crystal and metal/oxide interface structures of nanoparticles in 15Cr-2W-0.1Ti-4Al-0.6Hf-0.35Y_2O_3 ODS steel. J. Nucl. Mater. 533 (2020), 152029, https://doi.org/10.1016/j.jnucmat.2020.152029

[146] P. Dou, A. Kimura, R. Kasada, T. Okuda, M. Inoue, S. Ukai, S. Ohnuki, T. Fujisawa, F. Abe: Effects of titanium concentration and tungsten addition on the nano-mesoscopic structure of high-Cr oxide dispersion strengthened (ODS) ferritic steels. J. Nucl. Mater. 442(1 – 3) (2013), 95 – 100, https://doi.org/10.1016/j.jnucmat.2013.04.090

[147] J. H. Lee: Development of oxide dispersion strengthened ferritic steels with and without aluminum. Front. Energy 6(1) (2012), 29 – 34, https://doi.org/10.1007/s11708-012-0178-x

[148] S. Mohan, G. Kaur, B. K. Panigrahi, C. David, G. Amarendra: Effect of Zr and Al addition on nanocluster formation in oxide dispersion strenghtened steel – An ab initio study. J. All. & Comp. 767 (2018), 122 – 130, https://doi.org/10.1016/j.jallcom.2018.07.047

[149] J. Isselin, R. Kasada, A. Kimura, T. Okuda, M. Inoue, S. Ukai, S. Ohnuki, T. Fujisawa, F. Abe: Effects of Zr addition on the microstructure of 14%Cr 4%Al ODS Ferritic Steels. Mater. Trans. 51(5) (2010), 1011 – 1015, https://doi.org/10.2320/matertrans.MBW200923

[150] Q. Qian, Y. Wang, Y. Jiang, C. He, T. Hu: Nucleation of Y-X-O (X=Al, Ti, or Zr) NCs in nano-structured ferritic alloys: A first principles comparative study. J. Nucl. Mater. 518 (2019), 140 – 148, https://doi.org/10.1016/j.jnucmat.2019.02.051

[151] M. Gong, Z. Zhou, H. Hu, G. Zhang, S. Li, M. Wang: Effects of aluminum on microstructure and mechanical behavior of 14Cr-ODS steels. J. Nucl. Mater. 462 (2015), 502 – 507, https://doi.org/10.1016/j.jnucmat.2014.12.079

[152] R. Chinnappan: Thermodynamic stability of oxide phases of Fe-Cr based ODS steels via quantum mechanical calculation. Calphad 45 (2014), 188 – 193, https://doi.org/10.1016/j.calphad.2013.12.008

[153] Y. Jiang, J. R. Smith, G. R. Odette: Prediction of structural, electronic and elastic properties of $Y_2Ti_2O_7$ and Y_2TiO_5. Acta Mater. 58 (2010), 1536 – 1543, https://doi.org/10.1016/j.actamat.2009.10.061

[154] P. Bhaskar, A. Dasgupta, M. Kamruddin, S. Saroja: Microstructural studies on Ti-Y_2O_3 interface reaction products. Trans. Ind. Inst. Met. 69(4) (2016), 901 – 905, https://doi.org/10.1007/s12666-015-0576-y

[155] M. J. Alinger, G. R. Odette, D. T. Hoelzer: On the role of alloy composition and processing parameters in nanocluster formation and dispersion strengthening in nanostructured ferritic alloys. Acta Mater. 57(2) (2009), 392 – 406, https://doi.org/10.1016/j.actamat.2008.09.025

[156] C. A. Williams, P. Unifantowicz, N. Baluc, G. D. W. Smith, E. A. Marquis: The formation and evolution of oxide particles in oxide-dispersion-strengthened ferritic steels during processing. Acta Mater. 61 (2013), 2219 – 2235, https://doi.org/10.1016/j.actamat.2012.12.042

[157] Y. Wang, J. Lin, B. Liu, Y. Chen, D. Li, H. Wang, Y. Shen: Nanosized oxide phases in oxide-dispersion-strengthened steel PM2000. Philos. Mag. (2021), https://doi.org/10.1080/14786435.2021.1979677

[158] K. A. Unocic, B. A. Pint, D. T. Hoelzer: Advanced TEM characterization of oxide nanoparticles in ODS Fe–12Cr–5Al alloys. J. Mater. Sci. 51 (2016), 9190 – 9206, https://doi.org/10.1007/s10853-016-0111-5

[159] Y.-Z. Shen, T. T. Zou, S. Zhang, L. Z. Shen: Identification of oxide phases in oxide dispersion strengthened PM2000 steel. ISIJ Int. 53(2) (2013), 304 – 310, https://doi.org/10.2355/isijinternational.53.304

[160] Z. Zhang, W. Pantleon: Oxide nanoparticles in an Al-alloyed oxide dispersion strengthened steel: Crystallographic structure and interface with ferrite matrix. Philos. Mag. (2017), https://doi.org/10.1080/14786435.2017.1316876

[161] H. Xu, Z. Lu, D. Wang, C. Liu: Microstructure refinement and strengthening mechanisms of a 9Cr oxide dispersion strengthened steel by zirconium addition. Nucl. Eng. & Techn. 49 (2017), 178 – 188, https://doi.org/10.1016/j.net.2017.01.002

[162] G. Zhang, Z. Zhou, K. Mo, Y. Miao, S. Li, X. Liu, M. Wang, J.-S. Park, J. Almer, J. F. Stubbins: The comparison of microstructures and mechanical properties between 14Cr-Al and 14Cr-Ti ferritic ODS alloys. Mater. & Des. 98 (2016), 61 – 67, https://doi.org/10.1016/j.matdes.2016.02.117

[163] O. Fabrichnaja, H. J. Seifert, R. Weiland, T. Ludwig, F. Aldinger, A. Navrotsky: Phase equilibria and thermodynamics in the Y_2O_3-Al_2O_3-SiO_2 system. Zeitschrift f. Metallkunde / Mater. Res. & Adv. Techn. 92(9) (2001), 1083 – 1097, https://doi.org/10.3139/ijmr-2001-0197

[164] J. Ren, L. Yu, Y. Liu, C. Liu, H. Li, J. Wu: Effects of Zr addition on strengthening mechanisms of Al-alloyed high-Cr ODS steels. Mater. 11(1) (2018), 118, https://doi.org/10.3390/ma11010118

[165] W. Li, H. Xu, X. Sha, J. Meng, Z. Wang: Microstructure and mechanical properties of 12Cr-ODS steels with Zr addition. High. Temp. Mater. Proc. 38 (2019), 404 – 410, https://doi.org/10.1515/htmp-2018-0067

[166] L. Zhang, L. Yu, Y. Liu, C. Liu, H. Li, J. Wu: Influence of Zr addition on the microstructures and mechanical properties of 14Cr ODS steels. Mater. Sci. & Eng. A 695 (2017), 66 – 73, http://dx.doi.org/10.1016/j.msea.2017.04.020

[167] H. Jia, R. Zhang, D. Long, Y. Sun, Z. Zhou: Effect of zirconium content on the microstructure of ODS FeCrAl alloys. Int. J. Energy Res. 45 (2021), 10226 – 10234, https://doi.org/10.1002/er.6511

[168] B. M. Arkhurst, J. H. Kim: Evolution of microstructure and mechanical properties of oxide dispersion strengthened steels made from water-atomized ferritic powder. Met. & Mater. Int. 24 (2018), 464 – 480, https://doi.org/10.1007/s12540-018-0071-1

[169] Y. Huang, H. Zhang, M. A. Auger, Z. Hong, H. Ning, M. J. Gorley, P. S. Grant, M. J. Reece, H. Yan, S. G. Roberts: Microstructural comparison of effects of hafnium and titanium additions in spark-plasma-sintered Fe-based oxide-dispersion strengthened alloys. J. Nucl. Mater. 487 (2017), 433 – 442, https://doi.org/10.1016/j.jnucmat.2017.02.030

[170] H. Dong, L. Yu, Y. Liu, C. Liu, H. Li, J. Wu: Enhancement of tensile properties due to microstructure microstructure optimization in ODS steels by zirconium addition. Fus. Eng. & Des. 125 (2017), 402 – 406, https://doi.org/10.1016/j.fusengdes.2017.03.170

[171] P. Dou, A. Kimura, T. Okuda, M. Inoue, S. Ukai, S. Ohnuki, T. Fujisawa, F. Abe: Polymorphic and coherency transition of Y–Al complex oxide particles with extrusion temperature in an Al-alloyed high-Cr oxide dispersion strengthened ferritic steel. Acta Mater. 59 (2011), 992 – 1002, https://doi.org/10.1016/j.actamat.2010.10.026

[172] N. H. Oono, S. Ukai, K. Tominaga, N. Ebisawa, K. Tomura: Precipitation of various oxides in ODS ferritic steels. J. Mater. Sci. 54 (2019), 8786 – 8799, https://doi.org/10.1007/s10853-019-03516-6

[173] Y. Li, L. Zhang, D. Long, L. Yu, H. Li: The precipitated particle refinement in high-Cr ODS steels by microalloying element addition. Metals 14(24) (2021), 7767, https://doi.org/10.3390/ma14247767

[174] K. Dawson, G. J. Tatlock: Characterisation of nanosized oxides in ODM401 oxide dispersion strengthened steel. J. Nucl. Mater. 444 (2014), 252 – 260, https://doi.org/10.1016/j.jnucmat.2013.10.003

[175] Y. Jiang, J. R. Smith, G. R. Odette: Prediction of structural, electronic and elasticproperties of $Y_2Ti_2O_7$ and Y_2TiO_5. Acta Mater. 58 (2010), 1536 – 1543, https://doi.org/10.1016/j.actamat.2009.10.061

[176] J.-J. Liang, A. Navrotsky, T. Ludwig, H. J. Seifert, F. Aldinger: Enthalpy of formation of rare-earth silicates Y_2SiO_5 and Yb_2SiO_5 and N-containing silicate $Y_{10}(SiO_4)_6N_2$. J. Mater. Res. 14 (4) (1999), 1181 – 1185, https://doi.org/10.1557/JMR.1999.0158

[177] Y. Uchida, S. Ohnuki, N. Hashimoto, T .Suda, T. Nagai, T. Shibayama, K. Hamada, N. Akasaka, S. Yamashita, S. Ohstuka, T. Yoshitake: Effect of minor alloying elements on dispersing nano-

particles in ODS steel. MRS Online Proc. Libr. 981 (2006), 709, https://doi.org/10.1557/PROC-981-0981-JJ07-09

[178] K. Dawson, S. J. Haigh, G. J. Tatlock, A. R. Jones: Nano-particle precipitation in mechanically alloyed and annealed precursor powders of legacy PM2000 ODS alloy. J. Nucl. Mater. 464 (2015), 200 – 209, https://doi.org/10.1016/j.jnucmat.2015.04.039

[179] W. Li, T. Hao, R. Gao, X. Wang, T. Zhang, Q. Feng, C. Liu: The effect of Zr, Ti addition on the particle size and microstructure evolution of yttria nanoparticle in ODS steel. Powder Techn. 319 (2017), 172 – 182, https://doi.org/10.1016/j.powtec.2017.06.041

[180] Z. Li, Z. Lu, R. Xie, C. Lu, Y. Shi, C. Liu: Effects of Y_2O_3, La_2O_3 and CeO_2 additions on microstructure and mechanical properties of 14Cr-ODS ferrite alloys produced by spark plasma sintering. Fus. Eng. & Des. 121 (2017), 159 – 166, http://dx.doi.org/10.1016/j.fusengdes.2017.06.039

[181] H. Dong, L. Yu, Y. Liu, C. Liu, H. Li, J. Wu: Effect of hafnium addition on the microstructure and tensile properties of aluminum added high-Cr ODS steels. J. All. & Comp. 702 (2017), 538 – 545, https://doi.org/10.1016/j.jallcom.2017.01.298

[182] P. Yan, L. Yu, Y. Liu, C. Liu, H. Li, J. Wu: Effects of Hf addition on the thermal stability of 16Cr-ODS steels at elevated aging temperatures. J. All. & Comp. 739 (2018), 368 – 379, https://doi.org/10.1016/j.jallcom.2017.12.245

[183] Q. Tang, T. Hoshino, S. Ukai, B. Leng, S. Hayashi, Y. Wang: Refinement of oxide particles by addition of Hf in Ni-0.5 mass% Al- 1 mass% Y_2O_3 alloys. Mater. Trans. 51(11) (2010), 2019 – 2024, https://doi.org/10.2320/matertrans.M2010163

[184] L. Li, M. Saber, W. Xu, Y. Zhu, C. C. Koch, R. O. Scattergood: High-temperature grain size stabilization of nanocrystalline Fe–Cr alloys with Hf additions. Mater. Sci. & Eng. A 613 (2014), 289 – 295, https://doi.org/10.1016/j.msea.2014.06.099

[185] K. Takezawa, S. Ukai, S. Hayashi: Microstructure control of Co-base ODS alloys. Adv. Mater. Res. 239 – 242 (2011), 864 – 867, https://doi.org/10.4028/www.scientific.net/AMR.239-242.864

[186] D. J. Park, H. G. Kim, Y. I. Jung, J. H. Park, B. K. Choi, J. H. Yang, Y. H. Koo: Fabrication and mechanical properties of an oxide-dispersion-strengthened FeCrAl alloy. Fus. Eng. & Des. 139 (2019), 81 – 85, https://doi.org/10.1016/j.fusengdes.2019.01.001

[187] G. Yuling, W. Meiping, M. Xiaojin, C. Chen: Effect of CeO_2 on crack sensitivity and tribological properties of Ni60A coatings prepared by laser cladding. Adv. Mech. Eng. 13(4) (2021), 1 – 12, https://doi.org/10.1177/16878140211013125

[188] H. Shibata, S. Ukai, N. H. Oono, K. Sakamoto, M. Hirai: Development of accident tolerant FeCrAl-ODS steels utilizing Ce-oxide particles dispersion. J. Nucl. Mater. 502 (2018), 228 – 235, https://doi.org/10.1016/j.jnucmat.2018.02.020

[189] H. Liu, X. Yuan, L. Rao, S. Liu, Z. Shi, Y. Zhou, Q. Yang: Refinement mechanism of NbC by CeO_2 in hypereutectic Fe-Cr-C hardfacing coating. J. All. & Comp. 770 (2019), 1016 – 1028, https://doi.org/10.1016/j.jallcom.2018.08.162

[190] S. Pasebani, I. Charit, Y. Q. Wu, D. P. Butt, J. I. Cole: Mechanical alloying of lanthana-bearing nanostructured ferritic steels. Acta Mater. 61(15) (2013), 5605 – 5617, https://doi.org/10.1016/j.actamat.2013.06.002

[191] S. Pasebani, I. Charit, D. P. Butt, J. I. Cole, Y. Wu, J. Burns: Sintering behavior of lanthana-bearing nanostructured ferritic steel consolidated via spark plasma sintering. Adv. Eng. Mater. 18(2) (2016), 324 – 332, https://doi.org/10.1002/adem.201500294

[192] T. Sakamoto, S. Kukeya, H. Ohfuji: Microstructure and room and high temperature mechanical properties of ultrafine structured Al-5 wt% Y_2O_3 and Al-5 wt% La_2O_3 nanocomposites fabricated by mechanical alloying and hot pressing. Mater. Sci. & Eng. A 748 (2019), 428 – 433, https://doi.org/10.1016/j.msea.2019.01.091

[193] S. Ahda, R. Salam, A. Sujatno, D. Hairani, N. Shabrina, S. Giat, Bandriyana: Microstructure and oxidation behavior of the oxide dispersion strengthened stainless steel 316L with zirconia dispersion. M.I.P.I. 15 (2021), 115 – 120, https://doi.org/10.29122/mipi.v15i2.4775

[194] P. K. Kumar, N. V. Sai, A. G. Krihna: Effect of Y_2O_3 and ZrO_2 on the microstructure and mechanical properties of nano-ODS 21Cr-9Mn-6Ni steels. MTAEC9 52(4) (2018), 493, https://doi.org/10.17222/mit.2017.199

[195] M. Galatanu, M. Enculescu, A. Galatanu: Thermophysical properties of Cu-ZrO_2 composites as potential thermal barrier materials for a DEMO W-monoblock divertor. Fus. Eng. & Des. 127 (2018), 179 – 184, https://doi.org/10.1016/j.fusengdes.2018.01.011

[196] K. G. Raghavendra, A. Dasgupta, C. Ghosh, K. Jayasankar, V. Srihari, S. Saroja: Development of a novel ZrO_2 dispersion strengthened 9Cr ferritic steel: Characterization of milled powder and subsequent annealing behavior. Powder Techn. 327 (2018), 267 – 274, https://doi.org/10.1016/j.powtec.2017.12.076

[197] B. A. Arkhurst, J.-J. Park, C.-H. Lee, J. H. Kim: Direct laser deposition of 14Cr oxide dispersion strengthened steel powders using Y_2O_3 and HfO_2 dispersoids. Kor. J. Met. Mater. 55(8) (2017), 550 – 558, https://doi.org/10.3365/KJMM.2017.55.8.550

[198] X. Duan, S. Gao, Q. Dong, Y. Zhou, M. Xi, X. Xian, B. Wang: Reinforcement mechanism and wear resistance of Al_2O_3/Fe-Cr-Mo steel composite coating produced by laser cladding. Surf. & Coat. Techn. 291 (2016), 230 – 238, https://doi.org/10.1016/j.surfcoat.2016.02.045

[199] J. T. Sehrt, S. Kleszczynski, C. Notthoff: Nanoparticle improved metal materials for additive manufacturing. Prog. Addit. Manuf. 2 (2017), 179 – 191, https://doi.org/10.1007/s40964-017-0028-9

[200] A. Reinhart, T. Ansell, W. Smith, A. Nieto: Oxide reinforced Ti64 composites processed by selective laser melting. JMEPEG 30 (2021), 6949 – 6960, https://doi.org/10.1007/s11665-021-06077-5

[201] M. Li, Y. He, X. Yuan, S. Zhang: Microstructure of Al_2O_3 nanocrystalline/cobalt-based alloy composite coatings by laser deposition. Mater. & Des. 27 (2006), 1114 – 1119, https://doi.org/10.1016/j.matdes.2005.03.018

[202] M. P. Phaniraj, D.-I. Kim, J.-H- Shim, Y. W. Cho: Microstructure development in mechanically alloyed yttria dispersed austenitic steels. Acta Mater. 57 (2009), 1856 – 1864, https://doi.org/10.1016/j.actamat.2008.12.026

[203] B. Q. Han, D. C. Dunand: Creep of magnesium strengthened with high volume fractions of yttria dispersoids. Mater. Sci. & Eng. A 300 (2001), 235 – 240, https://doi.org/10.1016/S0921-5093(00)01781-0

[204] A. M. Redsten, E. M. Klier, A. M. Brown, D. C. Dunand: Mechanical properties and microstructure of cast oxide-dispersion strengthened aluminum. Mater. Sci. & Eng. A 201(1-2) (1995), 88 – 102, https://doi.org/10.1016/0921-5093(94)09741-0

[205] J. Jue, D. Gu, K. Chang, D. Dai: Microstructure evolution and mechanical properties of Al-Al_2O_3 composites fabricated by selective laser melting. Powder Techn. 310 (2017), 80 – 91, https://doi.org/10.1016/j.powtec.2016.12.079

[206] Q. Han, Y. Geng, R. Setchi, F. Lacan, D. Gu, S. L. Evans: Macro and nanoscale wear behaviour of Al-Al_2O_3 nanocomposites fabricated by selective laser melting. Comp. Part B 127 (2017), 26 – 35, http://dx.doi.org/10.1016/j.compositesb.2017.06.026

[207] R. Sorci, O. Tassa, A. Colaneri, A. Astri, D. Mirabile, S. Iwnicki, A. G. Demir: Design of an innovative oxide dispersion strengthened Al alloy for selective laser melting to produce lighter components for the railway sector. J. Mater. Eng. & Perf. 30 (2021), 5184 – 5194, https://doi.org/10.1007/s11665-021-05693-5

[208] T. Yoshimura, T. Thrirujirapaphong, H. Imai, K. Kondoh: Mechanical properties of oxide dispersion strengthened pure titanium produced by powder metallurgy method. Mater. Sci. Forum 654 – 656 (2010), 815 – 818, https://doi.org/10.4028/www.scientific.net/MSF.654-656.815

[209] L. Huang, L. Jiang, T. D. Topping, C. Dai, X. Wang, R. Carpenter, C. Haines, J. M. Schoenung: In situ oxide dispersion strengthened tungsten alloys with high compressive strength and high strain-to-failure. Acta Mater. 122 (2017), 19 – 31, https://doi.org/10.1016/j.actamat.2016.09.034

[210] S.-Y. Wei, L.-N. Ji, W.-J. Wu, H.-L. Ma: Selective laser melting of lanthanum oxide-reinforced tungsten composites: Microstructure and mechanical properties. Tungsten 4 (2022), 67 – 78, https://doi.org/10.1007/s42864-021-00127-0

[211] Z. Dong, S. Chen, S. Liu, Z. Ma, L. Yu: Low-temperature accelerated sintering of high-performance oxide dispersion strengthened ultrafine grained Mo alloy. J. All. & Comp. 903 (2022), 163982, https://doi.org/10.1016/j.jallcom.2022.163982

[212] G.-D. Sun, G.-H. Zhang, K.-C. Chou: Nanostructured oxide dispersion strengthened Mo alloys from Mo nanopowder doping with oxide nanoparticles. J. Mater. Res. & Techn. 8(6) (2019), 5753 – 5762, https://doi.org/10.1016/j.jmrt.2019.09.044

[213] L. Mingxi, H. Yizhu, Y. Xiaomin: Effect of nano-Y_2O_3 on microstructure of laser cladding cobalt-based alloy coatings. Appl. Surf. Sci. 252 (2006), 2882 – 2887, https://doi.org/10.1016/j.apsusc.2005.04.038

[214] L. Zhang, S. Ukai, T. Hoshino, S. Hayashi, X. Qu: Y_2O_3 evolution and dispersion refinement in Co-base ODS alloys. Acta Mater. 57(12) (2009), 3671 – 3682, https://doi.org/10.1016/j.actamat.2009.04.033

[215] J. Naser, W. Riehemann, H. Ferkel: Dispersion hardening of metals by nanoscaled ceramic powders. Mater. Sci. & Eng. A 234 – 236 (1997), 467 – 469, https://doi.org/10.1016/S0921-5093(97)00269-4

[216] A. Daoud, J.-B. Vogt, E. Charkaluk, L. Zhang, J.-C. Biasci: Effect of temperature on the low cycle fatigue behavior of Glidcop Al-15. Proc. Eng. 2(1) (2010), 1487 – 1495, https://doi.org/10.1016/j.proeng.2010.03.160

[217] Y. Shimada, M. Mizumoto, Y. Hishinuma, K.-I. Ikeda, K. Yoshida, H. Noto, B. Ma, T. Muroga, Y. Nagai, T. J. Konno: Microstructural changes of oxide dispersion strengthened copper powders fabricated by mechanical alloying. Fus. Eng. & Des. 173 (2021), 112804, https://doi.org/10.1016/j.fusengdes.2021.112804

[218] Z. Cheng, L. Yang, W. Mao, Z. Huang, D. Liang, B. He, F. Ren: Achieving high strength and high ductility in a high-entropy alloy by a combination of a heterogeneous grain structure and oxide-dispersion strengthening. Mater. Sci. & Eng. A 805 (2021), 140544, https://doi.org/10.1016/j.msea.2020.140544

[219] T. Kong, B. Kang, H. J. Ryu, S. H. Hong: Microstructures and enhanced mechanical properties of an oxide dispersion-strengthened Ni-rich high entropy superalloy fabricated by a powder metallurgical process. J. All. & Comp. 839 (2020), 155724, https://doi.org/10.1016/j.jallcom.2020.155724

[220] Y. Guo, M. Li, P. Li, C. Chen, Q. Zhan, Y. Chang, Y. Zhang: Microstructure and mechanical properties of oxide dispersion strengthened FeCoNi concentrated solid solution alloys. J. All. & Comp. 820 (2020), 153104, https://doi.org/10.1016/j.jallcom.2019.153104

[221] H. Tanigawa, E. Gaganidze, T. Hirose, M. Ando, S. J. Zinkle, R. Lindau, E. Diegele: Development of benchmark reduced activation ferritic/martensitic steels for fusion energy applications. Nucl. Fus. 57 (2017), 092004, https://doi.org/10.1088/1741-4326/57/9/092004

[222] S. J. Zinkle, J. T. Busby: Structural materials for fission and fusion energy. Mater. Today 12(11) (2009), 12 – 19, https://doi.org/10.1016/S1369-7021(09)70294-9

[223] L. Raman, K. Gothandapani, B. S. Murty: Austenitic oxide dispersion strengthened steels: A review. Def. Sci. J. 66(4) (2016), 316 – 322, https://doi.org/10.14429/dsj.66.10205

[224] S. Ganesh, P. Sai Karthik, M. Ramakrishna, A. V. Reddy, S. B. Chandrasekhar, R. Vijay: Ultra–high strength oxide dispersion strengthened austenitic steel. Mater. Sci. & Eng. A 814 (2021), 141192, https://doi.org/10.1016/j.msea.2021.141192

[225] J. H. Kim, T. S. Byun, D. T. Hoelzer: Tensile fracture characteristics of nanostructured ferritic alloy 14YWT. J. Nucl. Mater. 407 (2010), 143 – 150, https://doi.org/10.1016/j.jnucmat.2010.09.054

[226] M. S. El-Genk, J.-M. Tournier: A review of refractory metal alloys and mechanically alloyed-oxide dispersion strengthened steels for space nuclear power systems. J. Nucl. Mater. 340(1) (2005), 93 – 112, https://doi.org/10.1016/j.jnucmat.2004.10.118

[227] M. Klimiankou, R. Lindau, A. Möslang, J. Schröder: TEM study of PM 2000 steel. Powder Met. 48(3) (2005), 227 – 287, https://doi.org/10.1179/174329005X64171

[228] C. H. Zhang, A. Kimura, R. Kasada, J. Jang, H. Kishimoto, Y. T. Yang: Characterization of the oxide particles in Al-added high-Cr ferritic steels. J. Nucl. Mater. 417 (2011), 221 – 224, https://doi.org/10.1016/j.jnucmat.2010.12.063

[229] A. Kimura, R. Kasada, N. Iwata, H. Kishimoto, C. H. Zhang, J. Isselin, P. Dou, J. H. Lee, N. Muthukumar, T. Okuda, M. Inoue, S. Ukai, S. Ohnuki, T. Fujisawa, T. F. Abe: Development of Al added high-Cr ODS steels for fuel cladding of next generation nuclear systems. J. Nucl. Mater. 417 (2011), 176 – 179, https://doi.org/10.1016/j.jnucmat.2010.12.300

[230] L. Stratil, V. Hornik, P. Dymáček, P. Roupcová, J. Svoboda: The influence of aluminum content on oxidation resistance of new-generation ODS alloys at 1200°C. Metals 10(11) (2020), 1478, https://doi.org/10.3390/met10111478

[231] T. Liu, L. Wang, C. Wang, H. Shen: Effect of Al content on the oxidation behavior of $Y_2Ti_2O_7$-dispersed Fe-14Cr ferritic alloys. Corr. Sci. 104 (2016), 17 – 25, https://doi.org/10.1016/j.corsci.2015.11.025

[232] S. N. Dryepondt, K. A. Unocic, D. T. Hoelzer, C. P. Massey, B. A. Pint: Development of low-Cr ODS FeCrAl alloys for accident-tolerant fuel cladding. J. Nucl. Mater. 501 (2018), 59 – 71, https://doi.org/10.1016/j.jnucmat.2017.12.035

[233] A. A. Ferreira, R. L. Amaral, P. C. Romio, J. M. Cruz, A. R. Reis, M. F. Vieira: Deposition of nickel-based superalloy claddings on low alloy structural steel by direct laser deposition. Metals 11(8) (2021), 1326, https://doi.org/10.3390/met11081326

[234] M. S. Dhanya, A. K. Shukla, S. Dineshraj, R. R. Kumar, K. Prabhakaran, S. V. S. Narayana Murty, P. Ramesh Narayanan: Processing and characterization of yttria-dispersed INCONEL 718 ODS alloy. Trans. Ind. Inst. Met. 72 (2019), 1395 – 1398, https://doi.org/10.1007/s12666-019-01649-5

[235] N. Oono, Q. X. Tang, S. Ukai: Oxide particle refinement in Ni-based ODS alloy. Mater. Sci. & Eng. A 649 (2016), 250 – 253, http://dx.doi.org/10.1016/j.msea.2015.09.094

[236] M. Nganbe, M. Heilmaier: High temperature strength and failure of the Ni-base superalloy PM 3030. Int. J. Plast. 25 (2009), 822 – 837, https://doi.org/10.1016/j.ijplas.2008.06.005

[237] G. Noh, Y. D. Kim, K.-A. Lee, H.-J. Kim: Effects of precipitates and oxide dispersion in the high-temperature mechanical properties of ODS Ni-based superalloys. J. Kor. Powder. Met. Inst. 27(1) (2020), 8 – 13, https://doi.org/10.4150/KPMI.2020.27.1.8

[238] Y. Oh, C. H. Han, M. Wang, Y.-B. Chun, H. N. Ham: Effect of rare earth oxide addition on microstructure and mechanical properties of Ni-based alloy. J. All. & Comp. 853 (2021), 156980, https://doi.org/10.1016/j.jallcom.2020.156980

[239] C. W. Park, J. M. Byun, W. J. Choi, S. Y. Lee, Y. D. Kim: Improvement of high temperature mechanical properties of Ni-based oxide dispersion strengthened alloys by preferential formation of Y-Ti-O complex oxide. Mater. Sci. & Eng. A 740 – 741 (2019), 363 – 367, https://doi.org/10.1016/j.msea.2018.10.004

[240] M. Wang, H. N. Han, H.-S. Chung, Y.-B. Chun, J. Jiang: Microstructural evolution of oxide and nitride dispersed nickel-based alloy powders. Met. & Mater. Int. 25 (2019), 140 – 146, https://doi.org/10.1007/s12540-018-0176-6

[241] T. Xia, C. Yang, W. Zeng, Y. Xie, Y. Zhang, D. Zhang, G. Zhu, D. Shu, E. J. Lavernia: Dispersoids and γ′ precipitates in an ultrafine grained René 88DT – 5 vol.% Y_2O_3 alloy with outstanding thermal stability. Mater. Charact. 141 (2018), 139 – 147, https://doi.org/10.1016/j.matchar.2018.04.027

[242] Q. Tang, S. Ukai, N. Oono, S. Hayashi, B. Leng, Y. Sugino, W. Han, T. Okuda: Oxide particle refinement in 4.5 mass% Al Ni-based ODS superalloys. Mater. Trans. 53(4) (2012), 645 – 651, https://doi.org/10.2320/matertrans.M2011251

[243] A. Knaislová, P. Novák, M. Cabibbo, L. Jarowska, D. Vojtěch: Development of TiAl–Si alloys—A review. Mater. 14(4) (2021), 1030, https://doi.org/10.3390/ma14041030

[244] C. Kenel, K. Dawson, J. Barras, C. Hauser, G. Dasagyri, T. Bauer, A. Colella, A. B. Spierings, G. J. Tatlock, C. Leinenbach, K. Wegener: Microstructure and oxide particle stability in a novel ODS γ-TiAl alloy processed by spark plasma sintering and laser additive manufacturing. Intermet. 90 (2017), 63 – 73, https://doi.org/10.1016/j.intermet.2017.07.004

[245] C. Kenel, G. Dasagyri, T. Bauer, A. Colella, A. B. Spierings, C. Leinenbach, K. Wegener: Selective laser melting of an oxide dispersion strengthened (ODS) γ-TiAl alloy towards production of complex structures. Mater. & Des. 134 (2017), 81 – 90, https://doi.org/10.1016/j.matdes.2017.08.034

[246] S.-K. Rittinghaus, M. B. Wilms: Oxide dispersion strengthening of γ-TiAl by laser additive manufacturing. J. All. & Comp. 804 (2019), 457 – 460, https://doi.org/10.1016/j.jallcom.2019.07.024

[247] P. V. Durga, K. Satya Prasad, S. B. Chandrasekhar, A. V. Reddy, S. R. Bakshi, R. Vijay: Microstructural and mechanical properties of oxide dispersion strengthened iron aluminides produced by mechanical milling and hot extrusion. J. All. & Comp. 834 (2020), 155218, https://doi.org/10.1016/j.jallcom.2020.155218

[248] H. Saage, M. Krüger, D. Sturm, M. Heilmaier, J. H. Schneibel, E. George, L. Heatherly, C. Somsen, G. Eggeler, Y. Yang: Ductilization of Mo-Si solid solutions manufactured by powder metallurgy. Acta Mater. 57(13) (2009), 3895 – 3901, https://doi.org/10.1016/j.actamat.2009.04.040

[249] J. Becker, M. Giese, M. Krüger: The effects of Zr and La_2O_3 additions on the microstructural and mechanical properties of a Mo-6Si-5B alloy. IOP Conf. Ser.: Mater. Sci. & Eng. 882 (2020), 012001, https://doi.org/10.1088/1757-899X/882/1/012001

[250] M. Krüger, O. Kauss, K. Naumenko, C. Burmeister, E. Wessel, J. Schmelzer: The potential of mechanical alloying to improve the strength and ductility of Mo-9Si-8B-1Zr alloys – experiments and simulation. Intermet. 113 (2019), 106558, https://doi.org/10.1016/j.intermet.2019.106558

[251] D. S. Schwartz, P. Fraundorf, S. M .L. Sastry: TEM study of B- and Er- containing dispersoids in rapidly solidified dispersion-strengthened titanium and titanium aluminide alloys. Ultramicros. 37(1 – 4) (1991), 310 – 317, https://doi.org/10.1016/0304-3991(91)90028-5

[252] K. Ueda, S. Nakaoka, T. Narushima: β-grain refinement of α+β-type Ti-4.5Al-6Nb-2Fe-2Mo alloy by using rare-earth-oxide precipitates. Mater. Trans. 54(2) (2013), 161 – 168, https://doi.org/10.2320/matertrans.MC201207

[253] P. B. Trivedi, S. N. Patankar, F. H. Froes, E. G. Baburaj, A. Genç, L. Ovecoglu: Grain-size control in Ti-48Al-2Cr-2Nb with yttrium additions. Met. & Mater. Trans. A 33 (2002), 2729 – 2736, https://doi.org/10.1007/s11661-002-0395-8

[254] D. G. Morris, M. A. Muñoz-Morris: Nanoprecipitation of oxide particles and related high strength in oxide-dispersion-strengthened iron–aluminium–chromium intermetallics. Acta Mater. 61(12) (2013), 4636 – 4647, https://doi.org/10.1016/j.actamat.2013.04.034

[255] T. D. Ngo, A. Kashani, G. Imbalzano, K. T. Q. Nguyen, D. Hui: Additive manufacturing (3D printing): A review of materials, methods, applications and challenges. Comp. B 143 (2018), 172 – 196, https://doi.org/10.1016/j.compositesb.2018.02.012

[256] A. Mussatto, R. Groarke, R. K. Vijayaraghavan, M. A. Obeidi, P. J. McNally, V. Nicolisi, Y. Delaure, D. Brabazon: Laser-powder bed fusion of silicon carbide reinforced 316L stainless steel using a sinusoidal laser scanning strategy. J. Mater. Res. & Techn. 18 (2022), 2672 – 298, https://doi.org/10.1016/j.jmrt.2022.03.170

[257] F. Chang, D. Gu, D. Dai, P. Yuan: Selective laser melting of in-situ Al_2SiC_4 + SiC hybrid reinforced Al matrix composites: Influence of starting SiC particle size. Surf. & Coat. Techn. 272 (2015), 15 – 24, https://doi.org/10.1016/j.surfcoat.2015.04.029

[258] X. Xi, B. Chen, C. Tan, X. Song, J. Feng: Microstructure and mechanical properties of SiC reinforced AlSi10Mg composites fabricated by laser metal deposition. J. Manuf. Proc. 58 (2020), 763 – 774, https://doi.org/10.1016/j.jmapro.2020.08.073

[259] D. Dai, D. Gu: Tailoring surface quality through mass and momentum transfer modelling using a volume of fluid method in selective laser melting of TiC/AlSi10Mg powder. Int. J. Mach. Tools & Manuf. 88 (2015), 95 – 107, https://doi.org/10.1016/j.ijmachtools.2014.09.010

[260] Y. Zhou, L- Duan, S. Wen, Q. Wei, Y. Shi: Enhanced micro-hardness and wear resistance of Al-15Si/TiC fabricated by selective laser melting. Comp. Commun. 10 (2018), 64 – 67, https://doi.org/10.1016/j.coco.2018.06.009

[261] B. AlMangour, D. Grzesiak, J.-M. Yang: In-situ formation of novel TiC-particle-reinforced 316L stainless steel bulk-form composites by selective laser melting. J. All. & Comp. 706 (2017), 409 – 418, https://doi.org/10.1016/j.jallcom.2017.01.149

[262] B. AlMangour, D. Grzesiak, J.-M. Yang: In-situ TiC particle reinforced 316L stainless steel matrix nanocomposites powder preparation by mechanical alloying and selective laser melting behaviour. SFF2016, (2016), 26th Ann. Intern. Solid Freef. Fabr. Symp. 2016

[263] B. AlMangour, D. Grzesiak, J. M. Yang: In-situ TiC particle reinforced 316L stainless steel matrix nanocomposites: Powder preparation by mechanical alloying and selective laser melting behavior. Powder Techn. 326 (2017), 467 – 478, https://doi.org/10.1016/j.powtec.2017.11.064

[264] B. AlMangour, M.-S. Baek, D. Grzesiak, K.-A. Lee: Strengthening of stainless steel by titanium carbide addition and grain refinement during selective laser melting. Mater. Sci. & Eng. A 712 (2018), 812 – 818, https://doi.org/10.1016/j.msea.2017.11.126

[265] D. Gu, H. Wang, D. Dai, P. Yuan, W. Meiners, R. Poprawe: Rapid fabrication of Al-based bulk-form nanocomposites with novel reinforcement and enhanced performance by selective laser melting. Scr. Mater. 96 (2015), 25 – 28, https://doi.org/10.1016/j.scriptamat.2014.10.011

[266] D. Gu, H. Wang, G. Zhang: Selective laser melting additive manufacturing of Ti-based nanocomposites: The role of nanopowder. Met. & Mater. Trans. A 45 (2014), 464 – 476, https://doi.org/10.1007/s11661-013-1968-4

[267] D. Gu, G. Meng, C. Li, W. Meiners, R. Poprawe: Selective laser melting of TiC/Ti bulk nanocomposites: Influence of nanoscale reinforcement. Scr. Mater. 67(2) (2012), 185 – 188, https://doi.org/10.1016/j.scriptamat.2012.04.013

[268] D. Gu, H. Zhang, D. Dai, M. Xia, C. Hong, R. Poprawe: Laser additive manufacturing of nano-TiC reinforced Ni-based nanocomposites with tailored mirostructure and performance. Comp. B: Eng. 163 (2019), 585 – 597, https://doi.org/10.1016/j.compositesb.2018.12.146

[269] S. Dadbakhsh, R. Mertens, K. Vanmeensel, G. Ji, J.-P. Kruth: In situ transformations during SLM of an ultra-strong TiC reinforced Ti composite. Sci. Rep. 10 (2020), 10523, https://doi.org/10.1038/s41598-020-67434-3

[270] W. Wei, Q. Zhang, W. Wu, H. Cao, J. Shen, S. Fan, X. Duan. Agglomeration-free nanoscale TiC reinforced titanium matrix composites achieved by in-situ laser additive manufacturing. Scr. Mater. 187 (2020), 310 – 316, https://doi.org/10.1016/j.scriptamat.2020.06.057

[271] T.-C. Lin, C. Cao, M. Sokoluk, L. Jiang, X. Wang, J. M. Schoenung, E. J. Lavernia, X. Li: Aluminum with dispersed nanoparticles by laser additive manufacturing. Nature Comm. 10 (2019), 4124, https://doi.org/10.1038/s41467-019-12047-2

[272] P. Yuan, D. Gu, D. Dai: Particulate migration behavior and its mechanism during selective laser melting of TiC reinforced Al matrix nanocomposites. Mater. & Des. 82 (2015), 45 – 55, http://dx.doi.org/10.1016/j.matdes.2015.05.041

[273] H. Ouyang, G. Wang, Z. Li, Q. Guo: Additively manufactured copper matrix composites: Heterogeneous microstructures and combined strengthening effects. J. Mater. Res. 35(15) (2020), 1913 – 1921, https://doi.org/10.1557/jmr.2020.62

[274] X. Li, S. Shi, S. Han, X. Hu, Q. Zhu, H. Lu, W. Li, Y. Shi, H. Ding: Microstructure, solidification behavior and mechanical properties of Al-Si-Mg-Ti/TiC fabricated by selective laser melting. Addit. Manuf. 35 (2020), 101326, https://doi.org/10.1016/j.addma.2020.101326

[275] O. Ertugrul, T. M. Enrici, H. Paydas, E. Sagionetto, F. Boschini, A. Mertens: Laser cladding of TiC reinforced 316L stainless steel composites: Feedstock powder preparation and microstructural evaluation. Powder Techn. 375 (2020), 384 – 396, https://doi.org/10.1016/j.powtec.2020.07.100

[276] S. Cao, D. Gu: Laser metal deposition additive manufacturing of TiC/Inconel 625 nanocomposites: Relation of densification, microstructures and performance. J. Mater. Res. 30 (2015), 3616 – 3628, https://doi.org/10.1557/jmr.2015.358

[277] C. Hong, D. Gu, D. Dai, A. Gasser, A. Weisheit, I. Kelbassa, M. Zhong, R. Poprawe: Laser metal deposition of TiC/Inconel 718 composites with tailored interfacial microstructures. Opt. & Laser Techn. 54 (2013), 98 – 109, https://doi.org/10.1016/j.optlastec.2013.05.011

[278] N. Kang, W. Ma, L. Heraud, M. El Masori, F. Li, M. Liu, H. Liao: Selective laser melting of tungsten carbide reinforced maraging steel composite. Addit. Manuf. 22 (2018), 104 – 110, https://doi.org/10.1016/j.addma.2018.04.031

[279] J. H. Martin, B. D. Yahata, E. C. Clough, J. A. Mayer, J. M. Hundley: Additive manufacturing of metal matrix composites via nanofunctionalization. MRS Comm. 8(2) (2018), 297 – 302, https://doi.org/10.1557/mrc.2018.95

[280] Q. Han, Y. Gu, H. Gu, Y. Yin, J. Song, Z. Zhang, S. Soe: Laser powder bed fusion of WC-reinforced Hastelloy-X composite: microstructure and mechanical properties. J. Mater. Sci. 56 (2021), 1768 – 1782, https://doi.org/10.1007/s10853-020-05327-6

[281] H. Shen, H. Qi: Laser powder deposition of WC particle reinforced metal matrix composites. J. Laser Appl. (ICALEO) (2015), 913, https://doi.org/10.2351/1.5063240

[282] E. Fereiduni, A. Ghasemi, M. Elbestawi: Selective laser melting of hybrid ex-situ/in-situ reinforced titanium matrix composites: Laser/powder interaction, reinforcement formation mechanism, and non-equilibrium microstructural evolutions. Mater. & Des. 184 (2019), 108185, https://doi.org/10.1016/j.matdes.2019.108185

[283] Z. Xu, Y. Xie, M. Ebrahimnia, H. Dang: Effect of B_4C nanoparticles on microstructure and properties of laser cladded IN625 coating. Surf. & Coat. Techn. 416 (2021), 127154, https://doi.org/10.1016/j.surfcoat.2021.127154

[284] Y.-K. Kim, J.-H. Yu, H. S. Kim, K.-A. Lee: In-situ carbide-reinforced CoCrFeMnNi high-entropy alloy matrix nanocomposites manufactured by selective laser melting: Carbon content effects on microstructure, mechanical properties, and deformation mechanism. Comp. B Eng. 210 (2021), 108638, https://doi.org/10.1016/j.compositesb.2021.108638

[285] W. Li, Y. Yang, J. Liu, Y. Zhou, M. Li, S. Wen, Q. Wie, C. Yan, Y. Shi: Enhanced nanohardness and new insights into texture evolution and phase transformation of TiAl/TiB_2 in-situ metal matrix composites prepared via selective laser melting. Acta Mater. 136 (2017), 90 – 104, https://doi.org/10.1016/j.actamat.2017.07.003

[286] Y. Li, D. Gu, H. Zhang, L. Xi: Effect of trace addition of ceramic on microstructure development and mechanical properties of selective laser melted AlSi10Mg alloy. Chin. J. Mech. Eng. 33 (2020), https://doi.org/10.1186/s10033-020-00448-0

[287] L. X. Xi, H. Zhang, P. Wang, H. C. Li, K. G. Prashanth, K. J. Lin, I. Kaban, D. D. Gu: Comparative investigation of microstructure, mechanical properties and strengthening mechanisms of Al-12Si/TiB_2 fabricated by selective laser melting and hot pressing. Ceram. Int. 44(15) (2018), 17635 – 17642, https://doi.org/10.1016/j.ceramint.2018.06.225

[288] L. Xi, D. Gu, K. Lin, S. Guo, Y. Liu, Y. Li, M. Guo: Effect of ceramic particle size on densification behavior, microstructure formation, and performance of TiB_2-reinforced Al-based composites prepared by selective laser melting. J. Mater. Res. 35(6) (2020), 559 – 570, https://doi.org/10.1557/jmr.2019.392

[289] H. Attar, M. Bönisch, M. Calin, L.-C. Zhang, S. Scudino, J. Eckert: Selective laser melting of in situ titanium-titanium boride composites: Processing, microstructure and mechanical properties. Acta Mater. 76 (2014), 13 – 22, http://dx.doi.org/10.1016/j.actamat.2014.05.022

[290] Y. L. Wang, L. Zhao, S. Guan, K. C. Chan: Additive manufacturing of TiB_2-containing CoCrFeNiMn high-entropy alloy matrix composites with high density and enhanced mechanical properties. Mater. Sci. & Eng. A 825 (2021), 141871, https://doi.org/10.1016/j.msea.2021.141871

[291] E. Fereiduni, M. Elbestawi: Process-structure-property relationships in additively manufactured metal matrix composites. In: Additive Manufacturing of emerging materials, https://doi.org/10.1007/978-3-319-91713-9_4

[292] P. Mair, V. S. Goettgens, T. Rainer, N. Weinberger, I. Letofsky-Papst, S. Mitsche, G. Leichtfried: Laser powder bed fusion of nano-CaB_6 decorated 2024 aluminum alloy. J. All. & Comp. 863 (2021), 158714, https://doi.org/10.1016/j.jallcom.2021.158714

[293] P. Mair, L. Kaserer, J. Braun, J. Stajkovic, C. Klein, D. Schimbäck, L. Perfler, E. Zhuravlev, O. Kessler, G. Leichtfried: Dependence of mechanical properties andmicrostructure on solidification onset temperature for Al2024–CaB_6 alloys processed using laser powder bed fusion. Mater. Sci. & Eng. A 833 (2022), 142552, https://doi.org/10.1016/j.msea.2021.142552

[294] Q. Tan, J. Zhang, N. Mo, Z. Fan, Y. Yin, M. Bermingham, Y. Liu, H. Huang, M.-X. Zhang: A novel method to 3D-print fine grained AlSi10Mg alloy with isotropic properties via inoculation with LaB_6 nanoparticles. Addit. Manuf. 32 (2020), 101034, https://doi.org/10.1016/j.addma.2019.101034

[295] Q. Tan, Y. Yin, Z. Fan, J. Zhang, Y. Liu, M.-X. Zhang: Uncovering the roles of LaB_6-nanoparticle inoculant in the AlSi10Mg alloy fabricated via selective laser melting. Mater. Sci. & Eng. A 800 (2021), 140365, https://doi.org/10.1016/j.msea.2020.140365

[296] M. P. Behera, T. Dougherty, S. Singamneni: Selective laser melting of stainless steel and silicon nitride fibre metal matrix composites. Proc. Inst. Mech. Eng. B: J. Eng. Manuf. 234(12) (2020), 1513 – 1525, https://doi.org/10.1177/0954405420928684

[297] T. Minasyan, L. Liu, S. Aydinyan, M. Antonov, I. Hussainova: Selective laser melting of Ti/cBN composite. Key Eng. Mater. 799 (2019), 257 – 262, https://doi.org/10.4028/www.scientific.net/KEM.799.257

[298] S. H. Kim, G.-H. Shin, B.-K. Kim, K. T. Kim, D.-Y. Yang, C. Aranas Jr., J.-P. Choi, J.-H. Yu: Thermo-mechanical improvement of Inconel 718 using ex situ boron nitride-reinforced

composites processed by laser powder bed fusion. Sci. Rep. 7 (2017), 14359, https://doi.org/10.1038/s41598-017-14713-1

[299] D. Dai, D. Gu, M. Xia, C. Ma, H. Chen, T. Zhao, C. Hong, A. Gasser, R. Poprawe: Melt spreading behavior, microstructure evolution and wear resistance of selective laser melting additive manufactured AlN/AlSi10Mg nanocomposite. Surf. & Coat. Techn. 349 (2018), 279 – 288, https://doi.org/10.1016/j.surfcoat.2018.05.072

[300] C. Wallis, B. Buchmayr, R. Bermejo, P. Supancic: Fabrication of 3D metal-ceramic (Al-AlN) architectures using laser-powder bed fusion process. Addit. Manuf. 38 (2021), 101799, https://doi.org/10.1016/j.addma.2020.101799

[301] A. Riquelme, P. Rodrigo, M. D. Escalera-Rodriguez, J. Rams: Effect of the process parameters in the additive manufacturing of in situ Al/AlN samples. J. Manuf. Proc. 46 (2019), 271 – 278, https://doi.org/10.1016/j.jmapro.2019.09.011

[302] C. Gao, Z. Wang, Z. Xiao, D. You, K. Wong, A. H. Akbarzadeh: Selective laser melting of TiN nanoparticle-reinforced AlSi10Mg composite: Microstructural, interfacial, and mechanical properties. J. Mater. Proc. Techn. 281 (2020), 116618, https://doi.org/10.1016/j.jmatprotec.2020.116618

[303] Y. Zhao, C. Wu, S. Zhou, J. Yang, W. Li, L.-C. Zhang: Selective laser melting of Ti-TiN composites: Formation mechanism and corrosion behaviour in H_2SO_4/HCl mixed solution. J. All. & Comp. 863 (2021), 158721, https://doi.org/10.1016/j.jallcom.2021.158721

[304] I. Hilger, X. Boulnat, J. Hoffmann, C. Testani, F. Bergner, Y. DeCarlan, F. Ferraro, A. Ulbricht: Fabrication and characterization of oxide dispersion strengthened (ODS) 14Cr steels consolidated by means of hot isostatic pressing, hot extrusion and spark plasma sintering. J. Nucl. Mater. 472 (2016), 206 – 214, https://doi.org/10.1016/j.jnucmat.2015.09.036

[305] X. Boulnat, M. Perez, D. Fabregue, T. Douillard, M.-H. Mathon, Y. DeCarlan: Microstructure evolution in nano-reinforced ferritic steel processed by mechanical alloying and spark plasma sintering. Met. & Mater. Trans. A 45 (2013), 1485 – 1497, https://doi.org/10.1007/s11661-013-2107-y

[306] S. Pasebani, A. K. Dutt, J. Burns, I. Charit, R. S. Mishra: Oxide dispersion strengthened nickel based alloys via spark plasma sintering. Mater. Sci. & Eng. A 630 (2015), 155 – 169, https://doi.org/10.1016/j.msea.2015.01.066

[307] C. Heintze, M. Hernández-Mayoral, A. Ulbricht, F. Bergner, A. Shariq, T. Weissgärber, H. Frielinghaus: Nanoscale characterization of ODS Fe 9%Cr model alloys compacted by spark plasma sintering. J. Nucl. Mater. 428 (2012), 139 – 146, https://doi.org/10.1016/j.jnucmat.2011.08.053

[308] B. Gwalani, R. M. Pohan, J. Lee, B. Lee, R. Banerjee, H. J. Ryu, S. H. Hong: High-entropy alloy strengthened by in-situ formation of entropy stabilized nano-dispersoids. Sci. Rep. 8 (2018), 14085, https://doi.org/10.1038/s41598-018-32552-6

[309] B. V. Ponraj, A. Dinesh Kumar, S. Kumaran: Rapid synthesis of oxide dispersion strengthened ferritic alloys through spark plasma sintering. Mater. Today: Proc. 27(3) (2020), https://doi.org/10.1016/j.matpr.2019.11.094

[310] D. Pilone, G. Pulci, L. Paglia, A. Mondal, F. Marra, F. Felli, A. Brotzu: Mechanical behaviour of an Al_2O_3 dispersion strengthened γ-TiAl alloy produced by centrifugal casting. Metals 10 (2020), 1457, https://doi.org/10.3390/met10111457

[311] M. Sarma, I. Grants, I. Kaldre, A. Bojarevics, G. Gerbeth: Casting technology for ODS steels-dispersion of nanoparticles in liquid metals. IOP Conf. Ser.: Mater. Sci. & Eng. 228 (2017), 012020, https://doi.org/10.1088/1757-899X/228/1/012020

[312] Z. Hong, A. P. C. Morrison, H. Zhang, S. G. Roberts, P. S. Grant: Development of a novel melt spinning-based processing route for oxide dispersion-strengthened steels. Met. & Mater. Trans. A 49 (2018), 604 – 612, https://doi.org/10.1007/s11661-017-4398-x

[313] H. Tang, X. Chen, M. Chen, L. Zuo, B. Hou, Z. Wang: Microstructure and mechanical property of in-situ nano-particle strengthened ferritic steel by novel internal oxidation. Mater. Sci. & Eng. A 609 (2014), 293 – 299, https://doi.org/10.1016/j.msea.2014.05.020

[314] Y. Zhou, S. Yin, Y. Jiang, Q. Zhou, J. Peng, Y. Yan: Wire and arc additive manufacturing fabrication of ODS-RAFM steels and preliminary evaluation on microstructures and mechanical preosperties, J. Nucl. Mater. 572 (2022), 154068, https://doi.org/10.1016/j.jnucmat.2022.154068

[315] M. Ghayoor, K. Lee, Y. He, C.-H. Chang, B. K. Paul, S. Pasebani: Selective laser melting of austenitic oxide dispersion strengthened steel: Processing, microstructural evolution and strengthening mechanisms. Mater. Sci. & Eng. A 788 (2020), 139532, https://doi.org/10.1016/j.msea.2020.139532

[316] C. Kenel, A. De Luca, S. S. Joglekar, C. Leinenbach, D. C. Dunand: Evolution of Y_2O_3 dispersoids during laser powder bed fusion of oxide dispersion strengthened Ni-Cr-Al-Ti γ/γ' superalloy. Addit. Manuf. 47 (2021), 102224, https://doi.org/10.1016/j.addma.2021.102224

[317] A. De Luca, C. Kenel, J. Pado, S. S. Joglekar, D. C. Dunand, C. Leinenbach: Thermal stability and influence of Y_2O_3 dispersoids on the heat treatment response of an additively manufactured ODS Ni-Cr-Al-Ti γ/γ‘ superalloy. J. Mater. Res. & Techn. 15 (2021), 2883 – 2898, https://doi.org/10.1016/j.jmrt.2021.09.076

[318] J. U. Rakhmonov, C. Kenel, A. De Luca, C. Leinenbach, D. C. Dunand: Effect of Y_2O_3 dispersoids on microstructure and creep properties of Hastelloy X processed by laser powder-bed fusion. Addit. Manuf. Lett. 3 (2022), 100069, https://doi.org/10.1016/j.addlet.2022.100069

[319] S. Saptarshi, M. deJong, C. Rock, I. Anderson, R. Napolitano, J. Forrester, S. Lapidus, D. Kaoumi, T. Horn: Laser powder bed fusion of ODS 14YWT from gas atomization reaction synthesis precursor powders. JOM 74 (2022), 3303 – 3315, https://doi.org/10.1007/s11837-022-05418-6

[320] D. N. Luu, W. Zhou, S. M. L. Nai: Influence of nano-Y_2O_3 addition on the mechanical properties of selective laser melted Inconel 718. Mater. Sci. & Eng. A 845 (2022), 143233, https://doi.org/10.1016/j.msea.2022.143233

[321] T. Horn, C. Rock, D. Kaoumi, I. Anderson, E. White, T. Prost, J. Rieken, S. Saptarshi, R. Schoell, M. DeJong, S. Timmins, J. Forrester, S. Lapidus, R. Napolitano, D. Zhang, J. Darsell: Laser powder bed fusion additive manufacturing of oxide dispersion strengthened steel using gas atomized reaction synthesis powder. Mater. & Des. 216 (2022), 110574, https://doi.org/10.1016/j.matdes.2022.110574

[322] J. Liu, Y. Guan, X. Xia, P. Peng, Q. Ding, X. Liu: Laser cladding of $Al_{0.5}$CoCrCuFeNiSi high entropy alloy coating without and with yttria addition H13 steel. Crystals 10(4) (2020), 320, https://doi.org/10.3390/cryst10040320

[323] A. van Teijlingen, S. A. Davis, S. R. Hall: Size-dependent melting point depression of nickel nanoparticles. Nanoscale Adv. 2(6) (2020), https://doi.org/10.1039/D0NA00153H

[324] D.-R. Eo, S.-G. Chung, J.-H. Yang, I.-H. Jung, J.-W. Cho: Numerical modeling of oxide particle evolution during additive manufacturing. Addit. Manuf. 51 (2022), 102631, https://doi.org/10.1016/j.addma.2022.102631

[325] T. Boegelein, S. N. Dryepondt, A. Pandey, K. Dawson, G. J. Tatlock: Mechanical response and deformation mechanisms of ferritic oxide dispersion strengthened steel structures produced by selective laser melting. Acta Mater. 87 (2015), 201 – 215, https://doi.org/10.1016/j.actamat.2014.12.047

[326] F. Bergner, I. Hilger, J. Virta, J. Lagerbom, G. Gerbeth, S. Connolly, Z. Hong, P. S. Grant, T. Weißgärber: Alternative fabrication routes toward oxide-dispersion-strengthened steels and model alloys. Met. & Mater. Trans. A 47 (2016), 5313 – 5324, https://doi.org/10.1007/s11661-016-3616-2

[327] M. Hofele, A. Roth, J. Schanz, D. K. Harrison, A. K. M. De Silva, H. Riegel: Laser polishing of laser powder be fusion AlSi10Mg parts – Influence of initial surface roughness on achievable surface quality. Mater. Sci. & Appl. 12(1) (2021), 15 – 41, https://doi.org/10.4236/msa.2021.121002

[328] A.du Plessis, E. Macdonald: Hot isostatic pressing in metal additive manufacturing: X-ray tomography reveals details of pore closure. Addit. Manuf. 34 (2020), 101191, https://doi.org/10.1016/j.addma.2020.101191

[329] I. S. Grech, J. H. Sullivan, R. J. Lancaster, J. Plummer, N. P. Lavery: The optimization of hot isostatic pressing treatments for enhanced mechanical and corrosion performance of stainless steel 316L produced by laser powder bed fusion. Addit. Manuf. 58 (2022), 103072, https://doi.org/10.1016/j.addma.2022.103072

[330] S. Ukai, M. Harada, H. Okada, M. Inoue, S. Nomura, S. Shikakura, T. Nishida, M. Fujiwara, K. Asabe: Tube manufacturing and mechanical properties of oxide dispersion strengthened ferritic steel. J. Nucl. Mater. 204 (1993), 74 – 80, https://doi.org/10.1016/0022-3115(93)90201-9

[331] A. B. Spierings, M. Voegtlin, T. Bauer, K. Wegener: Powder flowability characterisation methodology for powder-bed-based metal additive manufacturing. Prog. Addit. Manuf. 1 (2016), 9 – 20, https://doi.org/10.1007/s40964-015-0001-4

[332] L. Haferkamp, L. Haudenschild, A. Spierings, K. Wegener, K. Riener, S. Ziegelmeier, G. J. Leichtfried: The influence of particle shape, powder flowability, and powder layer density on part density in laser powder bed fusion. Metals 11(3) (2021), 418, https://doi.org/10.3390/met11030418

[333] N. T. Aboulkhair, I. Maskery, I. Ashcroft, C. Tuck, N. M. Everitt: The role of powder properties on the processability of aluminium alloys in selective laser melting. Proc. LIM 2015, Munich, Germany

[334] S. E. Brika, M. Letenneur, C. A. Dion, V. Brailovski: Influence of particle morphology and size distribution on the powder flowability and laser powder bed fusion manufacturability of Ti-6Al-4V alloy. Addit. Manuf. 31 (2020), 100929, https://doi.org/10.1016/j.addma.2019.100929

[335] J. J. Dunkley: Metal powder atomisation methods for modern manufacturing. Johnson Mattey Techn. Rev. 63(3) (2019), 226 – 232, https://doi.org/10.1595/205651319X15583434137356

[336] Y. Nie, J. Tang, B. Yang, Q. Lei, S. Yu, Y. Li: Comparison in characteristic and atomization behavior of metallic powders produced by plasma rotating electrode process. Adv. Powder Techn. 31(5) (2020), 2152 – 2160, https://doi.org/10.1016/j.apt.2020.03.006

[337] K. Riener, N. Albrecht, S. Ziegelmeier, R. Ramakrishnan, L. Haferkamp, A. B. Spierings, G. J. Leichtfried: Influence of particle size distribution and morphology on the properties of the powder feedstock as well as of AlSi10Mg parts produced by laser powder bed fusion (LPBF). Addit. Manuf. 34 (2020), 101286, https://doi.org/10.1016/j.addma.2020.101286

[338] R. Bidulsky, F. S. Gobber, J. Bidulska, M. Ceroni, T. Kvackaj, M. A. Grande: Coated metal powders for laser powder bed fusion (L-PBF) processing: A review. Metals 11(11) (2021), 1831, https://doi.org/10.3390/met11111831

[339] J. S. Benjamin: Dispersion strengthened superalloys by mechanical alloying. Met. Trans. 1 (1970), 2943 – 2951, https://doi.org/10.1007/BF03037835

[340] K. Jayasankar, A. Pandey, B. K. Mishra, S. Das: In-situ formation of complex oxide precipitates during processing of oxide dispersion strengthened ferritic steels. Fus. Eng. & Des. 102 (2016), 14 – 20, https://doi.org/10.1016/j.fusengdes.2015.11.004

[341] C. Suryanarayana: Mechanical alloying and milling. Progr. Mater. Sci. 46(1 – 2) (2001), 1-184, https://doi.org/10.1016/S0079-6425(99)00010-9

[342] D. K. Mukhopadhyay, F. H. Froes, D. S. Gelles: Development of oxide dispersion strengthened ferritic steels for fusion. J. Nucl. Mater. 258 – 263 (1998), 1209 – 1215, https://doi.org/10.1016/S0022-3115(98)00188-3

[343] Q. Zhao, L. Yu, Y. Liu, H. Li: Morphology and structure evolution of Y_2O_3 nanoparticles in ODS steel powders during mechanical alloying and annealing. Adv. Powder Techn. 26 (2015), 1578 – 1582, https://doi.org/10.1016/j.apt.2015.08.017

[344] M. Nagini, R. Vijay, K. V. Rajulapati, K. B. Sankara Rao, M. Ramakrishna, A. V. Reddy, G. Sundararajan: Effect of process parameters on microstructure and hardness of oxide dispersion strengthened 18Cr ferritic steel. Met. & Mater. Trans. A 47 (2016), 4197 – 4209, https://doi.org/10.1007/s11661-016-3583-7

[345] V. de Castro, T. Leguey, M. A. Monge, A. Muñoz, R. Pareja, D. R. Amador, J. M. Torralba, M. Victoria: Mechanical dispersion of Y2O3 nanoparticles in steel EUROFER 97: process and optimisation. J. Nucl. Mater. 322(2 – 3) (2003), 228 – 234, https://doi.org/10.1016/S0022-3115(03)00330-1

[346] S. K. Karak, T. Chudoba, Z. Witczak, W. Lojkowski, I. Manna: Development of ultra high strength nano-Y_2O_3 dispersed ferritic steel by mechanical alloying and hot isostatic pressing. Mater. Sci. & Eng. A 528 (2011), 7475 – 7483, https://doi.org/10.1016/j.msea.2011.06.039

[347] K. Euh, B. Arkhurst, I. H. Kim, H.-G. Kim, J. H. Kim: Stability of Y-Ti-O nanoparticles during laser deposition of oxide dispersion strengthened steel powder. Met. Mater. Int. 23(6) (2017), 1063 – 1074, https://doi.org/10.1007/s12540-017-6832-4

[348] H. Xu, Z. Lu, D. Wang, C. Liu: Microstructural evolution in a new Fe based ODS alloy processed by mechanical alloying. Nucl. Mater. & Ener. 7 (2016), 1 – 4, https://doi.org/10.1016/j.nme.2016.04.006

[349] J. Fu, J. C. Brouwer, I. M. Richardson, M. J. M. Hermans: Effect of mechanical alloying and spark plasma sintering on the microstructure and mechanical properties of ODS Eurofer. Mater. & Des. 177 (2019), 107849, https://doi.org/10.1016/j.matdes.2019.107849

[350] G. Ressel, D. Holec, A. Fian, F. Mendez-Martin, H. Leitner: Atomistic insights into milling mechanisms in an Fe-Y_2O_3 model alloy. Appl. Phys. A 115 (2014), 851 – 858, https://doi.org/10.1007/s00339-013-7877-y

[351] I. Hilger, M. Tegel, M. J. Gorley, P. S. Grant, T. Weißgärber, B. Kieback: The structural changes of Y_2O_3 in ferritic ODS alloys during milling. J. Nucl. Mater. 447(1 – 3) (2014), 242 – 247, https://doi.org/10.1016/j.jnucmat.2014.01.026

[352] A. Dechamps, F. De Geuser, J. Malaplate, D. Sornin: When do oxide precipitates form during consolidation of oxide dispersion strengthened steels? J. Nucl. Mater. 482 (2016), 83 – 87, https://doi.org/10.1016/j.jnucmat.2016.10.017

[353] G. Spartacus, J. Malaplate, F. De Geuser, D. Sornin, A. Gangloff, R. Guillou, A. Dechamps: Nano-oxide precipitation kinetics during the consolidation process of a ferritic oxide dispersion strengthened steel. Scr. Mater. 188 (2020), 10 – 15, https://doi.org/10.1016/j.scriptamat.2020.07.003

[354] J. H. Schneibel, C. T. Liu, D. T. Hoelzer, M. J. Mills, P. Sarosi, T. Hayashi, U. Wendt, H. Heyse: Development of porosity in an oxide dispersion-strengthened ferritic alloy containing nanoscale oxide particles. Scr. Mater. 57 (2004), 1040 – 1043, https://doi.org/10.1016/j.scriptamat.2007.07.029

[355] M. A. Auger, V. de Castro, T. Leguey, S. Lozano-Perez, P. A. J. Bagot, M. P. Moody, S. G. Roberts: Effect of the milling atmosphere on the microstructure and mechanical properties of a ODS Fe-14Cr model alloy. Mater. Sci. & Eng. A 671 (2016), 264 – 274, https://doi.org/10.1016/j.msea.2016.06.054

[356] S. Noh, B.-K. Choi, S. H. Kang, T. K. Kim: Influence of mechanical alloying atmospheres on the microstructures and mechanical properties of 15Cr ODS steels. Nucl. Eng. & Techn. 46(6) (2014), 857 – 862, https://doi.org/10.5516/NET.07.2013.096

[357] W. Zhai, W. Zhou, S. M. L. Nai, J. Wei: Characterization of nanoparticle mixed 316L powder for additive manufacturing. J. Mater. Sci. &. Techn. 47 (2020), 162 – 168, https://doi.org/10.1016/j.jmst.2020.02.019

[358] E. Vasquez, P.-F. Giroux, F. Lomello, M. Nussbaum, H. Maskrot, F. Schuster, P. Castany: Effect of powder characteristics on production of oxide dispersion strengthened Fe-14Cr steel by laser powder bed fusion. Powder Techn. 360 (2020), 998 – 1005, https://doi.org/10.1016/j.powtec.2019.11.022

[359] P. K. Farayibi, T. E. Abioye, A. Kennedy, A. T. Clare: Development of metal matrix composites by direct energy deposition of ‘satellited‘ powders. J. Manuf. Proc. 45 (2019), 429 – 437, https://doi.org/10.1016/j.jmapro.2019.07.029

[360] T. M. Smith, A. C. Thompson, T. P. Gabb, C. L. Bowman, C. A. Kantzos: Efficient production of a high-performance dispersion strengthened, multi-principal element alloy. Sci. Rep. 10 (2020), 9663, https://doi.org/10.1038/s41598-020-66436-5

[361] R. Streubel, M. B. Wilms, C. Doñate-Buendia, A. Weisheit, S. Barcikowski, J. H. Schleifenbaum, B. Gökce: Depositing laser-generated nanoparticles on powders for additive manufacturing of oxide dispersion strengthened alloy parts via laser metal deposition. Jap. J. Appl. Phys. 57 (2018), 040310, https://doi.org/10.7567/JJAP.57.040310

[362] S. Reichenberger, G. Marzun, M. Muhler, S. Barcikowski: Perspective of surfactant-free colloidal nanoparticles in heterogeneous catalysis. ChemCatChem 11(18) (2019), 4489 – 4518, https://doi.org/10.1002/cctc.201900666

[363] B. Gökce, R. Streubel, M. B. Wilms, J. H. Schleifenbaum, S. Barcikowski: Laser additive manufacturing of oxide dispersion strengthened steels. Proc. SPIE (2019), 10909, https://doi.org/10.1117/12.2507829

[364] A. M. Jasim, X. He, T. A. White, Y. Xing: Nano-layer deposition of metal oxides via a condensed water film. Comm. Mater. 1 (2020), 9, https://doi.org/10.1038/s43246-020-0010-9

[365] F. Xiao, Q. Miao, S. Wei, T. Barriere, G. Cheng, S. Zuo, L. Xu: Uniform nanosized oxide particles dispersion strengthened tungsten alloy fabricated involving hydrothermal method and hot isostatic pressing. J. All. & Comp. 824 (2020), 153894, https://doi.org/10.1016/j.jallcom.2020.153894

[366] Z. Dong, N. Liu, Z. Ma, C. Liu, Q. Guo, Y. Yamauchi, H. R. Alamri, Z. A. Alothman, M. S. A. Hossain, Y. Liu: Synthesis of nanosized composite powders via a wet chemical process for sintering high performance W-Y_2O_3 alloy. Int. J. Refract. Met. & Hard Met. 69 (2017), 266 – 272, https://doi.org/10.1016/j.ijrmhm.2017.09.001

[367] Z. Hu, K. Guan, Z. Qian, J. Dong, J. Wu, Z. Ma: Simultaneous enhancement of strength and ductility in selective laser melting manufactured 316L alloy by employing Y_2O_3 coated spherical powder as precursor. J. All. & Comp. 899 (2022), 163262, https://doi.org/10.1016/j.jallcom.2021.163262

[368] Y.-I. Lee, N.-Y- Kwon, S.-T. Oh: Fabrication of Fe-base superalloy powders with yttrium oxide dispersion by mechanical alloying and chemical route. Mater. Lett. 197 (2017), 135 – 138, https://doi.org/10.1016/j.matlet.2017.03.123

[369] D. Riabov, M. Rashidi, E. Hryha, S. Bengtsson: Effect of the powder feedstock on the oxide dispersion strengthening of 316L stainless steel produced by laser powder bed fusion. Mater. Charact. 169 (2020), 110582, https://doi.org/10.1016/j.matchar.2020.110582

[370] P. Deng, M. Karadge, R. B. Rebak, V. K. Gupta, B. C. Prorok, X. Lou: The origin and formation of oxygen inclusions in austenitic stainless steels manufactured by laser powder bed fusion. Addit. Manuf. 35 (2020), 101334, https://doi.org/10.1016/j.addma.2020.101334

[371] J. Yan, Y. Zhou, R. Gu, X. Zhang, W.-M. Quach, M. Yan: A comprehesive study of steel powders (316L, H13, P20 and 18Ni300) for their selective laser melting additive manufacturing. Metals 9(1) (2019), 86, https://doi.org/10.3390/met9010086

[372] H. Yu, S. Hayashi, K. Kakehi, Y.-L. Kuo: Study of formed oxides in IN718 alloy during the fabrication by selective laser melting and electron beam melting. Metals 9(1) (2019), 19, https://doi.org/10.3390/met9010019

[373] R. Guschlbauer, A. K. Burkhardt, Z. Fu, C. Körner: Effect of the oxygen content of pure copper powder on selective electron beam melting. Mater. Sci. & Eng. A 779 (2020), 139106, https://doi.org/10.1016/j.msea.2020.139106

[374] Z. Dong, H. Kang, Y. Xie, C. Chi, X. Peng: Effect of powder oxygen content on microstructure and mechanical properties of a laser additively-manufactured 12CrNi2 alloy steel. Mater. Let. 236 (2019), 214 – 217, https://doi.org/10.1016/j.matlet.2018.10.091

[375] D. Zhang, J. T. Darsell, J. Wang, X. Ma, G. J. Grant, I. E. Anderson, J. R. Rieken, D. J. Edwards, W. Setyawan, T. J. Horn, G. R. Odette: No ball milling needed: Alternative ODS steel manufacturing with gas atomization reaction synthesis (GARS) and friction-based processing. J. Nucl. Mater. 566 (2022), 153768, https://doi.org/10.1016/j.jnucmat.2022.153768

[376] H. Lee, J. E. Jung, D.-S. Kang, H. W. Jeong, D. W. Yun, J. Choe, Y. S. Yoo, S.-M. Seo: Oxide dispersion strengthened IN718 owing to powder reuse in selective laser melting. Mater. Sci. & Eng. A 832 (2022), 142369, https://doi.org/10.1016/j.msea.2021.142369

[377] C. Qiu: A new approach to synthesise high strength nano-oxide dispersion strengthened alloys. J. All. & Comp. 790 (2019), 1023 – 1033, https://doi.org/10.1016/j.jallcom.2019.03.221

[378] X. Yang, F. Gao, F. Tang, X. Hao, Z. Li: Effect of surface oxides on the melting and solidification of 316L stainless steel powder for additive manufacturing. Metall. & Mater. Trans. A 52 (2021), 4518 – 4532, https://doi.org/10.1007/s11661-021-06405-3

[379] Y. Sun, R. J. Herbert, M. Aindow: Non-metallic inclusions in 17-4PH stainless steel parts produced by selective laser melting. Mater. & Des. 140 (2018), 153 – 162, https://doi.org/10.1016/j.matdes.2017.11.063

[380] Y.-K. Kim, M.-C. Kim, K.-A. Lee: 1.45 GPa ultrastrong cryogenic strength with superior impact toughness in the in-situ nano oxide reinforced CrMnFeCoNi high-entropy alloy matrix nanocomposite manufactured by laser powder bed fusion. J. Mater. Sci. & Techn. 97 (2022), 10 – 19, https://doi.org/10.1016/j.jmst.2021.04.030

[381] D. Pazos, A. Cintins, V. de Castro, P. Fernández, J. Hoffmann, W. Garcia Vargas, T. Leguey, J. Purans, A. Anspoks, A. Kuzmin, I. Iturriza, N. Ordás: ODS ferritic steels obtained from gas atomized powders through the STARS processing route: Reactive synthesis as an alternative to mechanical alloying. Nucl. Mater. & Ener. 17 (2018), 1 – 8, https://doi.org/10.1016/j.nme.2018.06.014

[382] Y. Zhai, Y. Yan, Y. Chen, W. Qin, H. Che, T. Wang, R. Cao: Microstructure and tensile property analysis of 22Cr-3Al oxide dispersion strengthened steel obtained through the STARS route. J. Mater. Eng. & Perf. (2022), https://doi.org/10.1007/s11665-021-06528-z

[383] V. V. Sagaradze, A. V. Litvinov, K. A. Kozlov, V. A. Shabashov, N. F. Vil'danova, N. V. Kataeva: Manufacturing of oxide-dispersion-strengthened steels with the use of preliminary surface oxidation. Phys. Met. & Metallogr. 112 (2011), 1, 53 – 60, https://doi.org/10.1134/S0031918X11010327

[384] X. Yang, F. Tang, X. Hao, Z. Li: Oxide evolution during the solidification of 316L stainless steel from additive manufacturing powders with different oxygen contents. Metall. & Mater. B 52 (2021), 2253 – 2262, https://doi.org/10.1007/s11663-021-02191-w

[385] J. H. Schneibel, S. Shim: Nano-scale oxide dispersoids by internal oxidation of Fe–Ti–Y intermetallics. Mater. Sci. & Eng. A 488(1 – 2) (2008), 134 – 138, https://doi.org/10.1016/j.msea.2007.10.074

[386] A. S. Yadav, P. Kürnsteiner, E. A. Jägle, K. N. Sasidhar, S. R. Meka: Nitride dispersion strengthened steel development after sintering of nitrided Fe-4.6 at% Al alloy powder. Steel Res. Int. 92 (2021), 2100174, https://doi.org/10.1002/srin.202100174

[387] D. Powell, A. E. W. Rennie, L. Geekie, N. Burns: Understanding powder degradation in metal additive manufacturing to allow the upcycling of recycled powders. J. Clean. Product. 268 (2020), 122077, https://doi.org/10.1016/j.jclepro.2020.122077

[388] C. L. A. Leung, S. Marussi, M. Towrie, R. C. Atwood, P. J. Withers, P. D. Lee: The effect of powder oxidation on defect formation in laser additive manufacturing. Acta Mater. 166 (2019), 294 – 305, https://doi.org/10.1016/j.actamat.2018.12.027

[389] H. Gruber, C. Luchian, E. Hryha, L. Nyborg: Effect of powder recycling on defect formation in electron beam melted alloy 718. Metall. & Mater. Trans. A 51 (2020), 2430 – 2443, https://doi.org/10.1007/s11661-020-05674-8

[390] L. Cordova, M. Campos, T. Tinga: Revealing the effects of powder reuse for selective laser melting by powder characterization. JOM 71 (2019), 1062 – 1072, https://doi.org/10.1007/s11837-018-3305-2

[391] Y. Sun, M. Aindow, R. J. Herbert: The effect of recycling on the oxygen distribution in Ti-6Al-4V powder for additive manufacturing. Mater. High Temp. 35 (2018), 1 – 3, https://doi.org/10.1080/09603409.2017.1389133

[392] A. Saboori, A. Aversa, F. Bosio, E. Bassini, E. Librera, M. De Chirico, S. Biamino, D. Ugues, P. Fino, M. Lombardi: An investigation on the effect of powder recycling on the microstructure and mechanical properties of AISI 316L produced by directed energy deposition. Mater. Sci. & Eng. A 766 (2019), 138360, https://doi.org/10.1016/j.msea.2019.138360

[393] S. F. Li, K. Geng, R. D. K. Misra, J. Y. Cui, D. Ye, Y. Liu, Y. F. Yang: Commercial scale uniform powder coating for metal additive manufacturing. JOM 72 (2020), 12, https://doi.org/10.1007/s11837-020-04386-z

[394] S. Brust, A. Röttger, W. Theisen: CVD coating of oxide particles for the production of novel particle-reinforced iron-based metal matrix composites. Open J. Appl. Sci. 6 (2016), 260 – 269, http://dx.doi.org/10.4236/ojapps.2016.64026

[395] B.-L. Zhao, L. Wang, L.-F. Zhang, J.-G. Ke, Z.-M. Xie, J.-F. Yang, X.-P. Wang, T. Hao, C.-S. Liu, X.-B. Wu: Effect of nano-Y_2O_3 content on microstructure and mechanical properties of Fe18Cr films fabricated by RF magnetron sputtering. Nanomater. 11(7) (2021), 1754, https://doi.org/10.3390/nano11071754

[396] J. P. Kruth, X. Wang, T. Laoui, L. Froyen: Lasers and materials in selective laser sintering. Assembly Autom. 23(4) (2003), 357 – 371, https://doi.org/10.1108/01445150310698652

[397] J. Zhang, D. Gu, Y. Yang, H. Zhang, H. Chen, D. Dai, K. Lin: Influence of particle size on laser absorption and scanning track formation mechanisms of pure tungsten powder during selective laser melting. Eng. 5 (2019), 736 – 745, https://doi.org/10.1016/j.eng.2019.07.003

[398] O. A. Tertuliano, P. J. DePond, D. Doan, M. J. Matthews, X. W. Gu, W. Cai: Nanoparticle-enhanced absorptivity of copper during laser powder bed fusion. Addit. Manuf. 51 (2022), 10562, https://doi.org/10.1016/j.addma.2021.102562

[399] B. Brandau, A. Da Silva, C. Wilsnack, F. Brueckner, A. F. H. Kaplan: Absorbance study of powder conditions for laser additive manufacturing. Mater. & Des. 216 (2022), 110591, https://doi.org/10.1016/j.matdes.2022.110591

[400] V. I. Bogdanovich, M. G. Giorbelidze: Numerical investigation of the thermal transformation of composition powder particles in the technology of selective laser melting. IOP Conf. Ser.: Mater. Sci. & Eng. 510 (2019), 012005, https://doi.org/10.1088/1757-899X/510/1/012005

[401] P. A. Hooper: Melt pool temperature and cooling rates in laser powder bed fusion. Addit. Manuf. 22 (2018), 548 – 559, https://doi.org/10.1016/j.addma.2018.05.032

[402] P. Bidare, I. Bitharas, R. M. Ward, M. M. Attallah, A. J. Moore: Fluid and particle dynamics in laser powder bed fusion. Acta Mater. 142 (2018), 107 – 120, https://doi.org/10.1016/j.actamat.2017.09.051

[403] X. Xiao, C. Lu, Y. Fu, X. Ye, L. Song: Progress on experimental study of melt pool flow dynamics in laser material processing. In: Liquid metals (2021), https://doi.org/10.5772/intechopen.97205

[404] D. Gu, C. Ma, M. Xia, D. Dai, Q. Shi: A multiscale understanding of the thermodynamic and kinetic mechanisms of laser additive manufacturing. Eng. 3 (2017), 675 – 684, https://doi.org/10.1016/J.ENG.2017.05.011

[405] I. B. Ozsoy, G. Li, H. Choi, H. Zhao: Shape effects on nanoparticle engulfment for metal matrix nanocomposites. J. Cryst. Growth 442 (2015), 62 – 68, https://doi.org/10.1016/j.jcrysgro.2015.04.025

[406] H. J. Chang, H. Y. Cho, J. H. Kim: Stability of Y-Ti-O nanoparticles during laser melting of advanced oxide dispersion-strengthened steel powder. J. All. & Comp. 653 (2015), 528 – 533, https://doi.org/10.1016/j.jallcom.2015.08.273

[407] L. Barnard, G. R. Odette, I. Szlufarska, D. Morgan: An ab initio study of Ti-Y-O nanocluster energetics in nanostructured ferritic alloys. Acta Mater. 60(3) (2012), 935 – 347, https://doi.org/10.1016/j.actamat.2011.11.011

[408] A. De Luca, C. Kenel, S. Griffiths, S. S. Joglekar, C. Leinenbach, D. C. Dunand: Microstructure and defects in a Ni-Cr-Al-Ti γ/γ' model superalloy processed by laser powder bed fusion. Mater. & Des. 201 (2021), 109531, https://doi.org/10.1016/j.matdes.2021.109531

[409] D.-R. Eo, S.-H. Park, J.-W. Cho: Inclusion evolution in additive manufactured 316L stainless steel by laser metal deposition process. Mater. & Des. 155 (2018), 212 – 219, https://doi.org/10.1016/j.matdes.2018.06.001

[410] X. Xu, J. Ding, S. Ganguly, C. Diao, S. Williams: Oxide accumulation effects on wire + arc layer-by-layer additive manufacture process. J. Mater. Proc. Techn. 252 (2018), 739 – 750, https://doi.org/10.1016/j.jmatprotec.2017.10.030

[411] Y. Shi, Z. Lu, H. Xu, R. Xie, Y. Ren, G. Yang: Microstructure characterization and mechanical properties of laser additive manufactured oxide dispersion strengthened Fe-9Cr alloy. J. All. & Comp. 791 (2019), 121 – 133, https://doi.org/10.1016/j.jallcom.2019.03.284

[412] Y. Zhong, L. Liu, J. Zou, X. Li, D. Cui, Z. Shen: Oxide dispersion strengthened stainless steel 316L with superior strength and ductility by selective laser melting. J. Mater. Sci. & Techn. 42 (2020), 97 – 105, https://doi.org/10.1016/j.jmst.2019.11.004

[413] Y. Yang, C. Doñate-Buendia, T. D. Oyedeji, B. Gökce, B.-Y. Xu: Nanoparticle tracing during laser powder bed fusion of oxide dispersion strengthened steels. Mater. 14(13) (2021), 3463, https://doi.org/10.3390/ma14133463

[414] C. Meier, S. L. Fuchs, A. J. Hart, W. A. Wall: A novel smoothed particle hydrodynamics formulation for thermo-capillary phase change problems with focus on metal additive manufacturing melt pool modeling. Comp. Meth. Appl. Mech. & Eng. 381 (2021), 113812, https://doi.org/10.1016/j.cma.2021.113812

[415] C. L. A. Leung, S. Marussi, R. C. Atwood, M. Towrie, P. J. Withers, P. D. Lee: In situ X-ray imaging of defect and molten pool dynamics in laser additive manufacturing. Nature Comm. 9 (2018), 1355, https://doi.org/10.1038/s41467-018-03734-7

[416] C. Iantaffi, C. L. A. Leung, Y. Chen, S. Guan, R. C. Atwood, J. Lertthanasarn, M.-S. Pham, M. Meisnar, T. Rohr, P. D. Lee: Oxidation induced mechanisms during directed energy deposition additive manufactured titanium alloy builds. Addit. Manuf. Lett. 1 (2021), 100022, https://doi.org/10.1016/j.addlet.2021.100022

[417] T. Hibiya, S. Ozawa: Effect of oxygen partial pressure on the maragoni flow of molten metals. Cryst. Res. Techn. 48(4) (2013), 208 – 213, https://doi.org/10.1002/crat.201200514

[418] C. Ma, J. Zhao, C. Cao, T.-C. Lin, X. Li: Fundamental study on laser interactions with nanoparticles-reinforced metals-Part II: Effect of nanoparticles on surface tension, viscosity and laser melting. J. Manuf. Sci. & Eng. 138(12) (2016), 121001, https://doi.org/10.1115/1.4033392

[419] M. Le Dantec, L. Güniat, M. Leistner, R. Figi, D. Bleiner, M. Leparoux, P. Hoffmann: Impact of oxygen content in powders on the morphology of the laser molten tracks in preparation for additive manufacturing of silicon. Powder Techn. 361 (2020), 704 – 710, https://doi.org/10.1016/j.powtec.2019.11.052

[420] S. Lu, H. Fujii, K. Nogi: Sensitivity of maragoni convection and weld shape variations to welding parameters in O_2-Ar shielded GTA welding. Scr. Mater. 51 (2004), 271 – 277, https://doi.org/10.1016/j.scriptamat.2004.03.004

[421] T.-N. Le, Y.-L. Lo: Effects of sulfur concentration and Marangoni convection on melt-pool formation in transition mode of selective laser melting process. Mater. & Des. 179 (2019), 107866, https://doi.org/10.1016/j.matdes.2019.107866

[422] S. J. Wolff, S. Webster, N. D. Parab, B. Aronson, B. Gould, A. Greco, T. Sun: In-situ observations of directed energy deposition additive manufacuring using high-speed X-ray imaging. JOM 73 (2021), 1, https://doi.org/10.1007/s11837-020-04469-x

[423] A. A. Martin, N. P. Calta, J. A. Hammonds, S. A. Khairallah, M. H. Nielsen, R. M. Shuttlesworth, N. Sinclair, M. J. Matthews, J. R. Jeffries, T. M. Willey, J. R. I. Lee: Ultrafast dynamics of laser-metal interactions in additive manufacturing alloys captured by in situ X-ray imaging. Mater. Today Adv. 1 (2019), 100002, https://doi.org/10.1016/j.mtadv.2019.01.001

[424] S. M. H. Hojjatzadeh, N. D. Parab, W. Yan, Q. Guo, L. Xiong, C. Zhao, M. Qu, L. I. Escano, X. Xiao, K. Fezzaa, W. Everhardt, T. Sun, L. Chen: Pore elimination mechanisms during 3D printing of metals. Nature Comm. 10 (2019), 3088, https://doi.org/10.1038/s41467-019-10973-9

[425] Y. Huang, T. G. Fleming, S. J. Clark, S. Marussi, K. Fezzaa, J. Thiyagalingam, C. L. A. Leung, P. D. Lee: Keyhole fluctuation and pore formation mechanisms during laser powder bed fusion additive manufacturing. Nature Comm. 13 (2022), 1170, https://doi.org/10.1038/s41467-022-28694-x

[426] Y. Wang, J. Shi: Engulfment and distribution of second-phase nanoparticle during dendrite solidification of an Al-Si binary alloy: A simulation study. Appl. Phys. A 125 (2019), 449, https://doi.org/10.1007/s00339-019-2738-y

[427] D. Kalisz: Interaction of non-metallic inclusion particles with advancing solidification front. Arch. Metall. & Mater. 59 (2014), 493 – 500, https://doi.org/10.2478/amm-2014-0081

[428] D. M. Stefanescu, F. R. Juretzko, B. K. Dhindaw, S. Sen, P. A. Curreri: Particle engulfment and pushing by solidifying interfaces. Mater. Sci. Forum 77 (1991), 25 – 42, https://doi.org/10.4028/www.scientific.net/MSF.77.25

[429] R. Daudin, S. Terzi, P. Lhuissier, L. Salvo, E. Boller: Remelting and solidification of a 6082 Al alloy containing submicron yttria particles: 4D experimental study by in situ X-ray microtomography. Mater. & Des. 87 (2015), 313 – 317, https://doi.org/10.1016/j.matdes.2015.07.141

[430] X.-H. Chen, H. Yan: Solid–liquid interface dynamics during solidification of Al 7075–Al2O3np based metal matrix composites. Mater. & Des. 94 (2016), 148 – 158, https://doi.org/10.1016/j.matdes.2016.01.042

[431] G.-H. Kim, S.-M. Hong, M.-K. Lee, S.-H. Kim, I. Ioka, B.-S. Kim, I.-S. Kim: Effect of oxide dispersion on dendritic grain growth characterisitics of cast aluminum alloy. Mater. Trans. 51(10) (2010), 1951 – 1957, https://doi.org/10.2320/matertrans.M2010166

[432] L. Zhang: Nucleation, growth, transport, and entrapment of inclusions during steel casting. JOM 65(9) (2013), 1138 – 1144, https://doi.org/10.1007/s11837-013-0688-y

[433] U. S. Bertoli, G. Guss, S. Wu, M. J. Matthews, J. M. Schoenung: In-situ characterization of laser-powder interaction and cooling rates through high-speed imaging of powder bed fusion additive manufacturing. Mater. & Des. 135 (2017), 385 – 396, https://doi.org/10.1016/j.matdes.2017.09.044

[434] V. Thampy, A. Y. Fong, N. P. Calta, J. Wang, A. A. Martin, P. J. Depond, A. M. Kiss, G. Guss, Q. Xing, R. T. Ott, A. van Buuren, M. F. Toney, J. Nelson Weker, M. J. Kramer, M. J. Matthews, C. J. Tassone, K. H. Stone: Subsurface cooling rate and microstructural response during laser based metal additive manufacturing. Sci. Rep. 10 (2020), 1981, https://doi.org/10.1038/s41598-020-58598-z

[435] B. Cheng, Y. Kevin Chou: Thermal simulations for cooling rate mapping in electron beam additive manufacturing. Proc. ASME (IMECE2015) Houston, TX, USA, https://doi.org/10.1115/IMECE2015-52343

[436] N. Shen: Thermal modeling of electron beam additive manufacturing process: Powder sintering effects. Proc. ASME 2012, Notre Dame, IN, USA. https://doi.org/10.1115/MSEC2012-7253

[437] Q. Han, R. Setchi, S. L. Evans: Synthesis and characterisation of advanced ball-milled Al-Al_2O_3 nanocomposites for selective laser melting. Powder Techn. 297 (2016), 183 – 192, https://doi.org/10.1016/j.powtec.2016.04.015

[438] L. Wang, J. Jue, M. Xia, L. Guo, B. Yan, D. Gu: Effect of the thermodynamic behavior of selective laser melting on the formation of in situ oxide dispersion-strengthened aluminum-based composites. Metals 6 (2016), 286, https://doi.org/10.3390/met6110286

[439] Z. Du, H.-C. Chen, M. J. Tan, G. Bi, C. K. Chua: Effect of nAl_2O_3 on the part density and microstructure during the laser-based powder bed fusion of AlSi10Mg composite. Rapid Prototyp. J. 26(4) (2020), 727 – 734, https://doi.org/10.1108/RPJ-05-2019-0136

[440] S. Zhang, Z. Chen, P. Wei, K. Huang, Y. Zou, S. Yao, M. Li, B. Lu, J. Xing: Microstructure and properties of a nano-ZrO_2-reinforced AlSi10Mg matrix composite prepared by selective laser melting. Mater. Sci. & Eng. A 838 (2022), 142792, https://doi.org/10.1016/j.msea.2022.142792

[441] M. Ghayoor, S. Mirzababaei, K. Lee, Y. He, C.-H. Chang, B. K. Paul, S. Pasebani: Strengthening of 304L stainless steel by addition of yttrium oxide and grain refinement during selective laser melting. Int. Solid Freeform Fabr. Symp. (2019), TX, USA, http://dx.doi.org/10.26153/tsw/17332

[442] M. Ghayoor, S. Mirzababaei, A. Sittiho, I. Charit, B. K. Paul, S. Pasebani: Thermal stability of additively manufactured austenitic 304L ODS alloy. J. Mater. Sci. & Techn. 83 (2021), 208 – 218, https://doi.org/10.1016/j.jmst.2020.12.033

[443] O. O. Salman, A. Funk, A. Waske, J. Eckert, S. Scudino: Additive manufacturing of a 316L steel matrix composite reinforced with CeO_2 particles: Process optimization by adjusting the laser scanning speed. Techn. 6(1) (2018), 25, https://doi.org/10.3390/technologies6010025

[444] Q. Wei, S. Li, C. Han, W. Li, L. Cheng, L. Hao, Y. Shi: Selective laser melting of stainless-steel/nano- hydroxyapatite composites for medical applications: Microstructure, element distribution, crack and mechanical properties. J. Mater. Proc. Techn. 222 (2015), 444 – 453, https://doi.org/10.1016/j.jmatprotec.2015.02.010

[445] K. Saeidi, X. Gao, Y. Zhong, Z. J. Shen: Hardened austenite steel with columnar sub-grain structure formed by laser melting. Mater. Sci. & Eng. A 625 (2015), 221 – 229, https://doi.org/10.1016/j.msea.2014.12.018

[446] K. Saeidi, L. Kvetkova, F. Lofaj, Z. Shen: Austenitic stainless steel strengthened by the in situ formation of oxide nanoinclusions. RSC Adv. 5 (2015), 20747 – 20750, https://doi.org/10.1039/C4RA16721J

[447] J. C. Walker, K. M. Berggreen, A. R. Jones, C. J. Sutcliffe: Fabrication of Fe-Cr-Al oxide dispersion strengthened PM2000 alloy using selective laser melting. Adv. Eng. Mater. 11(7) (2009), 541 – 546, https://doi.org/10.1002/adem.200800407

[448] T. Boegelein, E. Louvis, K. Dawson, G. J. Tatlock, A. R. Jones: Characterisation of a complex thin walled structure fabrication by selective laser melting using a ferritic oxide dispersion strengthened steel. Mater. Charact. 112 (2016), 30 – 40, https://doi.org/10.1016/j.matchar.2015.11.021

[449] G. J. Tatlock, K. Dawson, T. Boegelein, K. Moustoukas, A. R. Jones: High resolution microstructural studies of the evolution of nano-scale, yttrium-rich oxides in ODS steels subjected to ball milling, selective laser melting or friction stir welding. Mater. Today Proc. 3(9, Part B) (2016), 3086 – 3093, https://doi.org/10.1016/j.matpr.2016.09.024

[450] M. B. Wilms, R. Streubel, F. Frömel, A. Weisheit, J. Tenkamp, F. Walther, S. Barcikowski, J. H. Schleifenbaum, B. Gökce: Laser additive manufacturing of oxide dispersion strengthened steels using laser-generated nanoparticle-metal composite powders. Proc. CIRP 74 (2018), 196 – 200, https://doi.org/10.1016/j.procir.2018.08.093

[451] R. M. Hunt, K. J. Kramer, B. El-Dasher: Selective laser melting of MA956 oxide dispersion strengthened steel. J. Nucl. Mater. 464 (2015), 80 – 85, https://doi.org/10.1016/j.jnucmat.2015.04.011

[452] E. Vasquez, P.-F. Giroux, F. Lomello, A. Chniouel, H. Maskrot, F. Schuster, P. Castany: Elaboration of oxide dispersion strengthened Fe-14Cr stainless steel by selective laser melting. J. Mater. Proc. Tech. 267 (2019), 403 – 413, https://doi.org/10.1016/j.jmatprotec.2018.12.034

[453] C. J. J. Torrent, P. Krooß, J. Huang, M. Voigt, C. Ebbert, S. Knust, G. Grundmeier, T. Niendorf: Oxide modified iron in electron beam powder bed fusion - From processability to corrosion properties. Alloys 1(1) (2022), 31 – 53, https://doi.org/10.3390/alloys1010004

[454] A. B. Spierings, T. Bauer, K. Dawson, A. Colella, K. Wegener: Processing ODS modified IN625 using selective laser melting. Proc. Ann. 25th Int. Solid. Freeform Symp. (2015), Austin, TX, USA, https://repositories.lib.utexas.edu/handle/2152/89379 Accessed: 03.02.2022

[455] J. K. Pancreious, J. P. Deepa, V. Jayan, U. S. Bill, T. P. D. Rajan, B. C. Pai: Nanoceria induced grain refinement in electroless Ni-B-CeO_2 composite coating for enhanced wear and corrosion resistance of aluminium alloy. Surf. & Coat. Techn. 356 (2018), 29 – 37, https://doi.org/10.1016/j.surfcoat.2018.09.046

[456] J. Braun, L. Kaserer, J. Stajkovic, K.-H. Leitz, B. Tabernig, P. Singer, P. Leibenguth, C. Gspan, H. Kestler, G. Leichtfried: Molybdenum and tungsten manufactured by selective laser melting: Analysis of defect structure and solidification mechanisms. Int. J. Refract. Met. & Hard Met. 84 (2019), 104999, https://doi.org/10.1016/j.ijrmhm.2019.104999

[457] Z. Hu, Y. Zhao, K. Guan, Z. Wang, Z. Ma: Pure tungsten and oxide dispersion strengthened tungsten manufactured by selective laser melting: Microstructure and cracking mechanism. Addit. Manuf. 36 (2020), 101579, https://doi.org/10.1016/j.addma.2020.101579

[458] C. Kenel, A. De Luca, C. Leinenbach, D. C. Dunand: High temperature creep properties of an additively manufactured Y_2O_3 oxide dispersion-strengthened Ni-Cr-Al-Ti γ/γ' superalloy. Adv. Eng. Mater. (2022), 2200753, https://doi.org/10.1002/adem.202200753

[459] M. Z. Ghodsi, S. Khademzadeh, E. Marzbanrad, M. H. Razmpooch, N. De Marchi, E. Toyserkani: Development of yttria-stabilized zirconia reinforced Inconel 625 metal matrix composite by laser powder bed fusion. Mater. Sci. & Eng. A 827 (2021), 142037, https://doi.org/10.1016/j.msea.2021.142037

[460] M. Li, L. Wang, H. Yang, S. Zhang, X. Lin, W. Huang: Microstructure and mechanical properties of Y_2O_3 strengthened Inconel 625 alloy fabricated by selective laser melting. Mater .Sci. & Eng. A 854 (2022), 143813, https://doi.org/10.1016/j.msea.2022.143813

[461] Q.-S. Song, Y. Zhang, Y.-F. Wei, X.-Y. Zhou, Y.-F. Shen, Y.-M. Zhou, X.-M. Feng: Microstructure and mechanical performance of ODS superalloys manufactured by selective laser melting. Optics & Laser Techn. 144 (2021), 107423, https://doi.org/10.1016/j.optlastec.2021.107423

[462] M. Y. Yalcin, B. Derin, E. Aydogan: Development and additive manufacturing of oxide dispersion strengthened Inconel 718: Thermomechanical and experimental studies. J. All. & Comp. 914 (2022), 165193, https://doi.org/10.1016/j.jallcom.2022.165193

[463] C. Guo, Z. Yu, X. Hu, G. Li, F. Zhou, Z. Xu, S. Han, Y. Zhou, R. M. Ward, Q. Zhu: Y_2O_3 nanoparticles decorated IN738LC superalloy manufactured by laser powder bed fusion: Cracking inhibition, microstructures and mechanical properties. Comp. B: Eng. 230 (2022), 109555, https://doi.org/10.1016/j.compositesb.2021.109555

[464] G. Wang, L. Huang, Z. Liu, Z. Qin, W. He, F. Liu, C. Chen, Y. Nie: Process optimization and mechanical properties of oxide dispersion strengthened nickel-based superalloy by selective laser melting. Mater. & Des. 188 (2020), 108418, https://doi.org/10.1016/j.matdes.2019.108418

[465] J. A. Glerum, A. De Luca, M. L. Schuster, C. Kenel, C. Leinenbach, D. C. Dunand: Effect of oxide dispersoids on precipitation-strengthened Al-1.7Zr (wt %) alloys produced by laser powder-bed fusion. Addit. Manuf. 56 (2022), 102933, https://doi.org/10.1016/j.addma.2022.102933

[466] G. Marchese, A. Aversa, M. Lorusso, D. Manfredi, F. Calignano, M. Lombardi, S. Biamino, M. Pavese: Development and characterisation of aluminium matrix nanocomposites AlSi10Mg/$MgAl_2O_4$ by laser powder bed fusion. Metals 8(3) (2018), 175, https://doi.org/10.3390/met8030175

[467] H. Liao, H. Zhu, G. Xue, X. Zeng: Alumina loss mechanism of Al_2O_3-AlSi10Mg composites during selective laser melting. J. All. Comp. 785 (2019), 286 – 295, https://doi.org/10.1016/j.jallcom.2019.01.116

[468] C. R. Pobel, M. A. Lodes, C. Körner: Selective electron beam melting of oxide dispersion strengthened copper. Adv. Mater. Eng. 20 (2018), 1800068, https://doi.org/10.1002/adem.201800068

[469] A. Hattal, T. Chaveau, M. Djemai, J. J. Fouchet, B. Bacroix, G. Dirras: Effect of nano-yttria stabilized zirconia addition on the microstructure and mechanical properties of Ti6Al4V parts manufactured by selective laser melting. Mater. & Des. 180 (2019), 107909, https://doi.org/10.1016/j.matdes.2019.107909

[470] S.-Y. Wei, L.-N. Ji, W.-J. Wu, H.-L. Ma: Selective laser melting of lanthanum oxide-reinforced tungsten composite: microstructure and mechanical properties. Tungsten 4 (2022), 67 – 78, https://doi.org/10.1007/s42864-021-00127-0

[471] J. H. Schneibel, M. Heilmaier, W. Blum, G. Hasemann, T. Shanmugasundaram: Temperature dependence of the strength of fine- and ultrafine-grained materials. Acta Mater. 59 (2011), 1300 – 1308, https://doi.org/10.1016/j.actamat.2010.10.062

[472] Y. Liu, Y. Yang, S. Mai, D. Wang, C. Song: Investigation into spatter behavior during selective laser melting of AISI 316L stainless steel powder. Mater. & Des. 87 (2015), 797 – 806, https://doi.org/10.1016/j.matdes.2015.08.086

[473] S. Ly, A. M. Rubenchik, S. A. Khairallah, G. Guss, M. J. Matthews: Metal vapor micro-jet controls material redistribution in laser powder bed fusion additive manufacturing. Sci. Rep. 7 (2017), 4085, https://doi.org/10.1038/s41598-017-04237-z

[474] H. Amano, Y. Yamaguchi, T. Ishimoto, T. Nakano: Reduction of spatter generation using atmospheric gas in laser powder bed fusion of Ti-6Al-4V. Mater. Trans. 62(8) (2021), 1225 – 1230, https://doi.org/10.2320/matertrans.MT-M2021059

[475] W. Zhang, H. Ma, Q. Zhang, S. Fan: Prediction of powder bed thickness by spatter detection from coaxial optical images in selective laser melting of 316L stainless steel. Mater. & Des. 213 (2022), 110301, https://doi.org/10.1016/j.matdes.2021.110301

[476] A. Raza, E. Hryha: Characterization of spatter and sublimation in Alloy 718 during electron beam melting. Mater. 14 (2021), 5953, https://doi.org/10.3390/ma14205953

[477] M. P. Haines, N. J. Peter, S. S. Babu, E. A. Jägle: In-situ synthesis of oxides by reactive process atmospheres during L-PBF of stainless steel. Addit. Manuf. 33 (2020), 101178, https://doi.org/10.1016/j.addma.2020.101178

[478] A. N. D. Gasper, D. Hickman, I. Ashcroft, S. Sharma, X. Wang, B. Szost, D. Johns, A. T. Clare: Oxide and spatter powder formation during laser powder bed fusion of Hastelloy X. Powder Techn. 354 (2019), 333 – 337, https://doi.org/10.1016/j.powtec.2019.06.004

[479] A. Noskov, T. K. Ervik, I. Tsivilskiy, A. Gilmutdinov, Y. Thomassen: Characterization of ultrafine particles emitted during laser-based additive manufacturing of metal parts. Sci. Rep. 10 (2020), 20989, https://doi.org/10.1038/s41598-020-78073-z

[480] A. R. Nassar, M. A. Gundermann, E. W. Reutzel, P. Guerrier, M. H. Krane, M. J. Weldon: Formation processes for large ejecta and interactions with melt pool formation in powder bed fusion additive manufacturing. Sci. Rep. 9 (2019), 5038, https://doi.org/10.1038/s41598-019-41415-7

[481] C. Lu, R. Zhang, X. Wei, M. Xiao, Y. Yin, Y. Qu, H. Li, P. Liu, X. Qiu, T. Guo: An investigation on the oxidation behavior of spatters generated during the laser powder bed fusion of 316L stainless steel. Appl. Surf. Sci. 586 (2022), 152796, https://doi.org/10.1016/j.apsusc.2022.152796

[482] D. Jafari, T. H. J. Vaneker, I. Gibson: Wire and arc additive manufacturing: Opportunities and challenges to control the quality and accuracy of manufactured parts. Mater. & Des. 202 (2021), 109471, https://doi.org/10.1016/j.matdes.2021.109471

[483] W. Ou, T. Mukherjee, G. L. Knapp, Y. Wie, T. DebRoy: Fusion zone geometries, cooling rates and solidification parameters during wire arc additive manufacturing. Int. J. Heat & Mass Transf. 127 (2018), 1084 – 1094, https://doi.org/10.1016/j.ijheatmasstransfer.2018.08.111

[484] F. Kies, M. B. Wilms, N. Pirch, K. G. Pradeep, J. H. Schleifenbaum, C. Haase: Defect formation and prevention in directed energy deposition of high-manganese steels and the effect on mechanical properties. Mater. Sci. & Eng. A 772 (2020), 138688, https://doi.org/10.1016/j.msea.2019.138688

[485] C. Halisch, T. Radel, D. Tyralla, T. Seefeld: Measuring the melt pool size in a wire arc additive manufacturing process using a high dynamic range two-colored pyrometric camera. Weld. In World 64 (2020), 1349 – 1356, https://doi.org/10.1007/s40194-020-00892-5

[486] A. Richter, T. Gehling, K. Treutler, V. Wesling, C. Rembe: Real-time measurement of temperature and volume of the weld pool in wire-arc additive manufacturing. Measurement: Sensors 17 (2021), 100060, https://doi.org/10.1016/j.measen.2021.100060

[487] M. B. Wilms, N. Pirch, B. Gökce: Manufacturing oxide dispersion strengthened steels using the advanced directed energy deposition process of high-speed laser cladding. Progr. Addit. Manuf. (2022), https://doi.org/10.1007/s40964-022-00319-1

[488] Y. Shi, Z. Lu, L. Yu, R. Xie, Y. Ren, G. Yang: Microstructure and tensile properties of Zr-containing ODS-FeCrAl alloy fabricated by laser additive manufacturing. Mater. Sci. & Eng. A 774 (2020), 138937, https://doi.org/10.1016/j.msea.2020.138937

[489] C. Doñate-Buendia, R. Streubel, P. Kürnsteiner, M. B. Wilms, F. Stern, J. Tenkamp, E. Bruder, S. Barcikowski, B. Gault, K. Durst, J. H. Schleifenbaum, F. Walther, B. Gökce.: Effect of nanoparticle additivation on the microstructure and microhardness of oxide dispersion strengthened steels produced by laser powder bed fusion and directed energy deposition. Proc. CIRP 94 (2020), 41 – 45, https://doi.org/10.1016/j.procir.2020.09.009

[490] J. Schmelzer, S.-K. Rittinghaus, M. B. Wilms, O. Michael, M. Krüger: Strengthening of additively manufactured Me-Si-B (Me = Mo, V) by Y_2O_3 particles. Int. J. Refract. Met. & Hard Mater. 101 (2021), 105623, https://doi.org/10.1016/j.ijrmhm.2021.105623

[491] M. Li, Y. He, X. Yuan: Effect of nano-Y_2O_3 on microstructure of laser cladding cobalt-based alloy coatings. Appl. Surf. Sci. 252 (2006), 2882 – 2887, https://doi.org/10.1016/j.apsusc.2005.04.038

[492] H.-Y. Wang, D.-W. Zuo, Y.-L. Sun, F. Xu, D. Zhang: Microstructure of nanometer Al_2O_3 dispersion strengthened Ni-based high-temperature protective coatings by laser cladding. Trans. Nonferrous Met. Soc. China 19 (2009), 586 – 591, https://doi.org/10.1016/S1003-6326(08)60317-9

[493] B. M. Arkhurst, J. H. Bae, M. Y. Na, H. J. Chang, H. G. Kim, I. H. Kim, H. J. Ryu, J. H. Kim: Effect of tellurium on the microstructure and mechanical properties of Fe-14Cr oxide-dispersion-strengthened steels produced by additive manufacturing. J. Mater. Sci. & Techn. 95 (2021), 114 – 126, https://doi.org/10.1016/j.jmst.2021.03.068

[494] X. Li, H. Chu, Y. Chen, P. Hua, G. Wang, W. Kong, J. Chen, Y. Wu, W. Zhou: Microstructure and properties of the laser cladding ODS layers on CLAM steel. Surf. & Coat. Techn. 357 (2019), 172 – 179, https://doi.org/10.1016/j.surfcoat.2018.10.006

[495] X.-Y. Liu, Y. Sui, J.-B. Li, J.-Y. Yue, X.–H. Sun, L.-F. Yang, C.-S. Liu: Dimension effect of Y_2O_3 nanomaterial on microstructure and tensile properties of laser metal deposited stainless steel coatings. Surf. & Coat. Techn. 419 (2021), 127259, https://doi.org/10.1016/j.surfcoat.2021.127259

[496] X.-Y. Liu, Y. Sui, J.-B. Li, Y.-M. Li, X.–H. Sun, C.-S. Liu: Laser metal deposited steel alloys with uniform microstructures and improved properties prepared by addition of small amounts

of dispersed Y_2O_3 nanoparticles. Mater. Sci. & Eng. A 806 (2021), 140827, https://doi.org/10.1016/j.msea.2021.140827

[497] M. Grandhi, C. Ma, Z. Liu, B. Kang: Microstructural characterization and properties of laser-DED built oxide dispersion strengthened SS 316 L. Manuf. Lett. 33 (2022), 758 – 764, https://doi.org/10.1016/j.mfglet.2022.07.094

[498] L. Tan, G. Wang, Y. Guo, Q. Fang, Z. Liu, X. Xiao, W. He, Z. Qin, Y. Zhang, F. Liu, L. Huang: Additively manufactured oxide dispersion strengthened nickel-based superalloy with superior high temperature properties. Virt. &. Phys. Prototyp. 15 (2020), 555 – 569, https://doi.org/10.1080/17452759.2020.1848283

[499] E. Chia, B. S. Kang, M. Zheng, Y. Li, M. Chyu: Development of ODS coating for high temperature turbine components using DED additive manufacturing. Proc. ASME (2018), https://doi.org/10.1115/GT2018-76274

[500] J. Liu, Y. Guan, X. Xia, P. Peng, Q. Ding, X. Liu: Laser cladding of $Al_{0.5}$CoCrCuFeNiSi high entropy alloy coating without and with yttria addition on H13 steel. Crystals 10(4) (2020), 320, https://doi.org/10.3390/cryst10040320

[501] S. N. El Moghazi, T. Wolfe, D. G. Ivey, H. Henein: Plasma transfer arc additive manufacturing of 17-4 PH: Assessment of defects. Int. J. Adv. Manuf. Techn. 108 (2020), 2301 – 2313, https://doi.org/10.1007/s00170-020-05540-2

[502] B. Maier, M. Lenling, H. Yeom, G. Johnson, S. Maloy, K. Sridharan: A novel approach for manufacturing oxide dispersion strengthened (ODS) steel cladding tubes using cold spray technology. Nucl. Eng. & Techn. 51 (2019), 1069 – 1074, https://doi.org/10.1016/j.net.2019.01.015

[503] M. Lenling, H. Yeom, B. Maier, G. Johnson, T. Dabney, J. Graham, P. Hosemann, D. Hoelzer, S. Maloy, K. Sridharan: Manufacturing oxide dispersion-strengthened (ODS) steel fuel cladding tubes using the cold spray process. JOM 71 (2019), 8, 2868 – 2873, https://doi.org/10.1007/s11837-019-03582-w

[504] D. J. Barton, B. C. Hornbuckle, K. A. Darling, L. N. Brewer, G. B. Thompson: Influence of surface temperature in the laser assisted cold spray deposition of sequential oxide dispersion strengthened layers: Microstructure and hardness. Mater. Sci. & Eng. A 811 (2021), 141027, https://doi.org/10.1016/j.msea.2021.141027

[505] W. A. Story, D. J. Barton, B. C. Hornbuckle, K. A. Darling, G. B. Thompson, L. N. Brewer: Laser assisted cold spray of Fe–Ni–Zr oxide dispersion strengthened steel. Mater. 3 (2018), 239 – 242, https://doi.org/10.1016/j.mtla.2018.08.028

[506] S. Mirzababaei, M. Ghayoor, R. P. Doyle, S. Pasebani: In-situ manufacturing of ODS FeCrAlY alloy via laser powder bed fusion. Mater. Let. 284 (2021), 129046, https://doi.org/10.1016/j.matlet.2020.129046

[507] N. Sridharan, S. Dryepondt, K. G. Field: Investigation of laser direct energy deposition for production of ODS alloys. ORNL Reports (2018)

[508] X. Lou, P. L. Andresen, R. B. Rebak: Oxide inclusions in laser additive manufactured stainless steel and their effects on impact toughness and stress corrosion cracking behavior. J. Nucl. Mater. 499 (2018), 182 – 190, https://doi.org/10.1016/j.jnucmat.2017.11.036

[509] F. Yan, W. Xiong, E. Faierson, G. B. Olson: Characterization of nano-scale oxides in austenitic stainless steel processed by powder bed fusion. Scr. Mater. 155 (2018), 104 – 108, https://doi.org/10.1016/j.scriptamat.2018.06.011

[510] X. Zhou, Z. An, Z. Shen, W. Liu, C. Yao: Particles control in selective laser melting in-situ oxide dispersion strengthened method. IOP Conf. Series: Mater. Sci. & Eng. 167 (2017), 012048, https://doi.org/10.1088/1757-899X/167/1/012048

[511] T.-H. Hsu, Y.-J. Chang, C.-Y. Huang, H.-W. Yen, C.-P. Chen, K.-K. Jen, A.-C. Yeh: Microstructure and property of a selective laser melting process induced oxide dispersion strengthened 17-4 PH stainless steel. J. All. & Comp. 803 (2019), 30 – 41, https://doi.org/10.1016/j.jallcom.2019.06.289

[512] P. Chen, C. Yang, S. Li, M. M. Attallah, M. Yan: In-situ alloyed, oxide-dispersion-strengthened CoCrFeMnNi high entropy alloy fabricated via laser powder bed fusion. Mater. & Des. 194 (2020), 108966, https://doi.org/10.1016/j.matdes.2020.108966

[513] Y.-K. Kim, M.-S. Baek, S. Yang, K.-A. Lee: In-situ formed oxide enables extraordinary high-cycle fatigue resistance in additively manufactured CoCrFeMnNi high-entropy alloy. Addit. Manuf. 38 (2021), 101832, https://doi.org/10.1016/j.addma.2020.101832

[514] H. Jia, Z. Zhou, S. Li: A new strategy for additive manufacturing ODS steel using Y-containing gas atomized powder. Mater. Charact. 187 (2022), 111876, https://doi.org/10.1016/j.matchar.2022.111876

[515] S. L. Lu, H.-P. Tang, M. Qian, Q. Hong, L.-Y. Zeng, D. H. StJohn: A yttrium-containing high-temperature titanium alloy additively manufactured by selective electron beam melting. J. Cent. South Univ. 22 (2015), 2857 – 2863, https://doi.org/10.1007/s11771-015-2818-x

[516] Y. Zhang, J. Zhang, Q. Yan, L. Zhang, M. Wang, B. Song, Y. Shi: Amorphous alloy strengthened stainless steel manufactured by selective laser melting: Enhanced strength and improved corrosion resistance. Scr. Mater. 148 (2018), 20 – 23, https://doi.org/10.1016/j.scriptamat.2018.01.016

[517] K. Li, G. Ma, L. Xing, Y. Wang, C. Yu, J. Chen, J. Ma, G. Wu, W. Liu, Z. Shen, X. Huang: Crack suppression via in-situ oxidation in additively manufactured W-Ta alloy. Mater. Let. 263 (2020), 127212, https://doi.org/10.1016/j.matlet.2019.127212

[518] S. S. Babu, S. A. David, J. M. Vitek, K. Mundra, T. DebRoy: Development of macro- and microstructures of carbon-manganese alloy low alloy steel welds: Inclusion formation. Mater. Sci. & Techn. 11(2) (1995), 186 – 199, https://doi.org/10.1179/mst.1995.11.2.186

[519] K. Mundra, T. DebRoy: A general model for partitioning of gases between a metal and its plasma environment. Met. & Mater. Trans. B 26 (1995), 149 – 157, https://doi.org/10.1007/BF02648987

[520] E. Sadeghi, P. Karimi, N. Israelsson, J. Shipley, T. Månsson, T. Hansson: Inclusion-induced fatigue crack initiation in powder bed fusion of Alloy 718. Addit. Manuf. 36 (2020), 101670, https://doi.org/10.1016/j.addma.2020.101670

[521] H. Springer, C. Baron, A. Szczepaniak, E. A. Jägle, M. B. Wilms, A. Weisheit, D. Raabe: Efficient additive manufacturing production of oxide- and nitride-dispersion-strengthened materials through atmospheric reactions in liquid metal deposition. Mater. & Des. 111 (2016), 60 – 69, https://doi.org/10.1016/j.matdes.2016.08.084

[522] W. Wei, W. Wu, S. Fan, X. Duan: In-situ laser additive manufacturing of Ti6Al4V matrix composites by gas-liquid reaction in dilute nitrogen gas atmospheres. Mater. & Des. 202 (2021), 109578, https://doi.org/10.1016/j.matdes.2021.109578

[523] D. Zhao, Q. Yang, D. Wang, M. Yan, P. Wang, M. Jiang: Ordered nitrogen complexes overcoming strength–ductility trade-off in an additively manufactured high-entropy alloy. Virt. Phys. Proto. 15 (2020), 532 – 542, https://doi.org/10.1080/17452759.2020.1840783

[524] L. Liu, C. Chen, R. Zhao, X. Wang, H. Tao, S. Shuai, J. Wang, H. Liao, Z. Ren: In-situ nitrogen strengthening of selective laser melted Ti6Al4V with superior mechanical performance. Addit. Manuf. 46 (2021), 102142, https://doi.org/10.1016/j.addma.2021.102142

[525] C. Chen, L. Liu, R. Zhao, T. Cao, T. Hu, S. Xu, S. Shuhai, S. Yin, J. Wang, H. Liao, Z. Ren: Microstructure evolution and mechanical properties of laser additive manufacturing Ti6Al4V alloy under nitrogen-argon reactive atmosphere. Mater. Sci. & Eng. A 841 (2022), 143076, https://doi.org/10.1016/j.msea.2022.143076

[526] Y. Wang, B. Wang, L. Luo, B. Li, T. Liu, J. Zhao, B. Xu, L. Wang, Y. Su, J. Guo, H. Fu: Laser-based powder bed fusion of pre-alloyed oxide dispersion strengthened steel containing yttrium. Addit. Manuf. 58 (2022), 103018, https://doi.org/10.1016/j.addma.2022.103018

[527] R. Xu, Z. Geng, Y. Wu, C. Chen, M. Ni, D. Li, T. Zhang, H. Huang, F. Liu, R. Li, K. Zhou: Microstructure and mechanical properties of in-situ oxide-dispersion-strengthened NiCrFeY alloy produced by laser powder bed fusion. Adv. Powder Mater. 1(4) (2022), 100056, https://doi.org/10.1016/j.apmate.2022.100056

[528] K. Li, Z. Wang, K. Song, K. Khanlari, X.-S. Yang, Q. Shi, X. Liu, X. Mao: Additive manufacturing of a Co-Cr-W alloy by selective laser melting: In-situ oxidation, precipitation and the corresponding strengthening effects. J. Mater. Sci. & Techn. (in press), https://doi.org/10.1016/j.jmst.2022.01.036

[529] M. Song, X. Lin, F. Liu, H. Yang, W. Huang: Effect of environmental oxygen content on the oxide inclusion in laser solid formed AISI 420 stainless steel. Mater. & Des. 90 (2016), 459 – 467, http://dx.doi.org/10.1016/j.matdes.2015.11.003

[530] D. Wang, D. Cheng, Z. Zhou, W. Wang, B. Hu, Y. Xie, Z. Xiong, D. Hu: Effect of laser power on the microstructure and properties of additive manufactured 17-4 PH stainless steel in different fabrication atmosphere. Mater. Sci. & Eng. A 839 (2022), 142846, https://doi.org/10.1016/j.msea.2022.142846

[531] D. Wang, C. T. Chi, W. Q. Wang, Y. L. Li, M. S. Wang, X. G. Chen, Z. H. Chen, X. P. Cheng, Y. J. Xie: The effects of fabrication atmosphere condition on the microstructural and mechanical properties of laser direct manufactured stainless steel 17-4 PH. J. Mater. Sci. & Techn. 35(7) (2019), 1315 – 1322, https://doi.org/10.1016/j.jmst.2019.03.009

[532] L. Palmeira Belotti, J. A. W. van Dommelen, M. G. D. Geers, C. Goulas, W. Ya, J. P. M. Hoefnagels: Microstructural characterisation of thick walled wire arc additively manufactured stainless steel. J. Mater. Proc. Techn. 299 (2022), 117373, https://doi.org/10.1016/j.jmatprotec.2021.117373

[533] S. Miran, P. Franke, A. Möslang, H. J. Seifert: Casting technology for ODS steels – the internal oxidation approach. IOP Conf. Ser.: Mater. Sci. & Eng. 228 (2017), 012021, https://doi.org/10.1088/1757-899X/228/1/012021

[534] K. Sato, N. Sekido, K. Yoshimi: Fabrication of oxide dispersion strengthened alloys through solid-state reactions between Fe-Al and Fe_2O_3 powders. Mater. Sci. & Eng. A 754 (2019), 68 – 74, https://doi.org/10.1016/j.msea.2019.03.060

[535] Z. Hong, X. Zhang, Q. Yan, Y. Chen: A new method for preparing 9Cr-ODS steels using elemental yttrium and Fe_2O_3 oxygen carrier. J. All. & Comp. 770 (2019), 831 – 839, https://doi.org/10.1016/j.jallcom.2018.08.196

[536] B. Stegman, B. Yang, Z. Shang, J. Ding, T. Sun, J. Lopez, W. Jarosinski, H. Wang, X. Zhang: Reactive introduction of oxide nanoparticles in additively manufactured 718 Ni alloys with improved high temperature performance. J. All. & comp. 920 (2022), 165846, https://doi.org/10.1016/j.jallcom.2022.165846

[537] Z. Shi, F. Han: The microstructure and mechanical properties of micro-scale Y_2O_3 strengthened 9Cr steel fabricated by vacuum casting. Mater. & Des. 66 A (2015), 304 – 308, https://doi.org/10.1016/j.matdes.2014.10.075

[538] S. Dadbakhsh, L. Hao: Effect of Al alloys on selective laser melting behaviour and microstructure of in situ formed particle reinforced composites. J. All. & Comp. 541 (2012), 328 – 334, http://dx.doi.org/10.1016/j.jallcom.2012.06.097

[539] S. Dadbakhsh, L. Hao: Effect of layer thickness in selective laser melting on microstructure of Al/5 wt.% Fe_2O_3 powder consolidated parts. Sci. World J. 6 (2014), 106129, https://doi.org/10.1155/2014/106129

[540] S. Dadbakhsh, R. Mertens, K. Vanmeensel, J. Vleugels, J. van Humbeeck, J.-P. Kruth: In situ alloying and reinforcing of Al6061 during selective laser melting. Proc. CIRP 74 (2018), 39 – 43, https://doi.org/10.1016/j.procir.2018.08.009

[541] F. Hinrichs, A. Kauffmann, D. Schliephake, S. Seils, S. Obert, K. Ratschbacher, M. Allen, A. Pundt, M. Heilmaier: Flexible powder production for additive manufacturing of refractory metal-based alloys. Metals 11(11) (2021), 1723, https://doi.org/10.3390/met11111723

[542] J. Schmelzer, S.-K. Rittinghaus, A. Weisheit, M. Stobik, J. Paulus, K. Gruber, E. Wessel, C. Heinze, M. Krüger: Printability of gas atomized Mo-Si-B powders by laser metal deposition. Int. J. Refract. Met. & Hard Mater. 78 (2019), 123 – 126, https://doi.org/10.1016/j.ijrmhm.2018.08.016

[543] M. A. Spurek, L. Haferkamp, C. Weiss, A. B. Spierings, J. H. Schleifenbaum, K. Wegener: Influence of the particle size distribution of monomodal 316L powder on its flowability and processability in powder bed fusion. Progr. Addit. Manuf. (2021), https://doi.org/10.1007/s40964-021-00240-z

[544] A. Kini: Laser Additive Manufacturing of Oxide Dispersion Strengthened Steels and Cu-Cr-Nb Alloys. PhD Thesis (2019) RWTH Aachen University, https://doi.org/10.18154/RWTH-2019-07341

[545] C. F. Burmeister, A. Kwade: Process engineering with planetary mills. Chem. Soc. Rev. 42 (2013), 7660, https://doi.org/10.1039/c3cs35455e

[546] S. Jendrzej, B. Gökce, M. Epple, S. Barcikowski: How size determines the value of gold: Economic aspects of wet chemical and laser-based metal colloid synthesis. Chem. Phys. Rev. 18 (2017), 1012, https://doi.org/10.1002/cphc.201601139

[547] X. H. Wang, Y. Hirata: Colloidal Processing and Mechanical Properties of SiC with Al_2O_3 and Y_2O_3. J. Ceram. Soc. Jpn. 112 (2004), 22 – 28, https://doi.org/10.2109/jcersj.112.22

[548] G. Lefèvre, L. Čerović, S. Milonjić, M. Fédoroff, J. Finne, A. Jaubertie: Determination of isoelectric points of metals and metallic alloys by adhesion of latex particles. J. Colloid & Interf. Sci. 337(2) (2009), 449 – 455, https://doi.org/10.1016/j.jcis.2009.05.005

[549] G. Marzun, C. Streich, S. Jendrzej, S. Barcikowski, P. Wagener: Adsorption of colloidal platinum nanoparticles to supports: Charge transfer and effects of electrostatic and steric interactions. Langmuir 30 (2014), 11928 – 11936, https://doi.org/10.1021/la502588g

[550] M. Schneider: Laser cladding with powder. PhD Thesis (1998), University of Twente, https://ris.utwente.nl/ws/portalfiles/portal/6075114/t0000007.pdf, Accessed: 23.08.2022

[551] F. Caiazzo, V. Alfieri, G. Casalino: On the relevance of volumetric energy density in the investigation of Inconel 718 laser powder bed fusion. Mater. 13(3) (2020), 538. https://doi.org/10.3390/ma13030538

[552] H. G. Coe, S. Pasebani: Use of bimodal particle size distribution in selective laser melting of 316L stainless steel. J. Manuf. Mater. Proc. 4(1) (2020), 8, https://doi.org/10.3390/jmmp4010008

[553] M. S. Moyle. N. Haghdadi, S. P. Ringer, S. Primig: On the microstructure and texture evolution in 17-4 PH stainless steel during laser powder bed fusion: Towards textural design. J. Mater. Sci. & Techn. 117 (2022), 183 – 195, https://doi.org/10.1016/j.jmst.2021.12.015

[554] H. Zhou, C. Song, Y. Yang, C. Han, M. Wang, Y. Xiao, Z. Liu: The microstructure and properties evolution of SS316L fabricated by magnetic field-assisted laser powder bed fusion. Mater. Sci. & Eng. A 845 (2022), 143216, https://doi.org/10.1016/j.msea.2022.143216

[555] Q. Tan, A. Atrens, N. Mo, M.-X. Zhang: Oxidation of magnesium alloys at elevated temperatures in air: A review. Corr. Sci. 112 (2016), 734 – 759, https://doi.org/10.1016/j.corsci.2016.06.018

[556] K. Djebaili, Z. Mekhalif, A. Boumaza, A. Djelloul: XPS, FTIR, EDX, and XRD analysis of Al_2O_3 scales grown on PM2000 alloy. J. Spectroscopy (2015), 868109, http://dx.doi.org/10.1155/2015/868109

[557] Material data sheet Kanthal APMT alloy. https://www.kanthal.de/produkte-und-dienstleistungen/material-datasheets/wire/na/kanthal-apmt/?show=pdf. Accessed: 18.08.2022

[558] Y. Kong, L. Zhao, L. Zhu, H. Huang: The selection of laser beam diameter in directed energy deposition of austenitic stainless steel: A comprehensive assessment. Addit. Manuf. 52 (2022), 102646, https://doi.org/10.1016/j.addma.2022.102646

[559] K. G. Field, M. A. Snead, Y. Yamamoto, K. A. Terrani: Handbook on the material properties of FeCrAl alloys for nuclear power production applications. (FY Version: Revision 1), OSTI Technical Reports (2018), https://doi.org/10.2172/1474581

[560] D.-G. Ahn: Directed energy deposition (DED) Process: State of the art. Int. J. Prec. Eng. & Manuf. Green Techn. 8 (2021), 703 – 742, https://doi.org/10.1007/s40684-020-00302-7

[561] Y. Lee, M. Nordin, S. S. Babu, D. F. Farson: Effect of fluid convection on dendrite arm spacing in laser deposition. Met. & Mater. Trans. B 45 (2014), 1520 – 1529, https://doi.org/10.1007/s11663-014-0054-7

[562] S. Fetni, T. M. Enrici, T. Nicolini, H. S. Tran, O. Dedry, L. Duchêne, A. Mertens, A. M. Habraken: Thermal model for the directed energy deposition of composite coatings of 316L stainless steel enriched with tungsten carbides. Mater. & Des. 204 (2021), 109661, https://doi.org/10.1016/j.matdes.2021.109661

[563] S. Reisinger, G. Ressel, S. Eck, S. Marsoner: Differentiation of grain orientation with corrosive and colour etching on a granular bainitic steel. Micron 99 (2017), 67 – 73, https://doi.org/10.1016/j.micron.2017.04.002

[564] P. J. Szabó, A. Bonyár: Effect of grain orientation on chemical etching. Micron 43(2-3) (2012), 349 – 351, https://doi.org/10.1016/j.micron.2011.09.015

[565] H. L. Wei, J. Mazumder, T. DebRoy: Evolution of solidification texture during additive manufacturing. Sci. Rep. 5 (2015), 16446, https://doi.org/10.1038/srep16446

[566] T. Schopphoven, A. Gasser, G. Backes: EHLA: Extreme high-speed laser material deposition. Laser-Technik J. 14(4) (2017), 26 – 29, https://doi.org/10.1002/latj.201700020

[567] S. Koß, S. Ewald, M.-N. Bold, J. H. Koch, M. Voshage, S. Ziegler, J. H. Schleifenbaum: Comparison of the EHLA and LPBF process in context of new alloy design methods for LPBF. Adv. Mater. Res. 1161 (2021), 13 – 25, https://doi.org/10.4028/www.scientific.net/AMR.1161.13

[568] N. Pirch, S. Keutgen, A. Gasser, K. Wissenbach, I. Kelbassa: Modeling of coaxial single- and overlap-pass cladding with laser radiation. Proc. 37th MATADOR Conf. (2017), Manchester, UK. https://doi.org/10.1007/978-1-4471-4480-9_11

[569] N. Pirch, S. Linnenbrink, A. Gasser, K. Wissenbach, R. Poprawe: Analysis of track formation during laser metal deposition. J. Laser Appl. 29 (2017), 022506, https://doi.org/10.2351/1.4983231

[570] S. Mokadem, C. Bezençon, A. Hauert, A. Jacot, W. Kurz: Laser repair of superalloy single crystals with varying substrate orientations. Met. Mater. Trans. A 38 (2007), 1500 – 1510, https://doi.org/10.1007/s11661-007-9172-z

[571] J. B. Ferguson, G. Kaptay, B. F. Schultz, P. K. Rohatgi, K. Cho, C. S. Kim: Brownian motion effects on particle pushing and engulfment during solidification in metal-matrix composites. Met. & Mater. Trans A 45 (2014), 4635 – 4645, https://doi.org/10.1007/s11661-014-2379-x

[572] M. Klimenkov, R. Lindau, A. Möslang: Study of oxide precipitates in PM2000 steel. Microsc. & Microanal. 13 (2007), 296 – 297, https://doi.org/10.1017/S1431927607081482

[573] Z. B. Zhang, N. R. Tao, O. V. Mishin, W. Pantleon: Oxide dispersion-strengthened steel PM2000 after dynamic plastic deformation: Nanostructure and annealing behaviour. J. Mater. Sci. 51 (2016), 5545 – 5555, https://doi.org/10.1007/s10853-016-9859-x

[574] S.-K. Rittinghaus, V. R. Molina Ramirez, J. Zielinski, U. Hecht: Oxygen gain and aluminum loss during laser metal deposition of intermetallic TiAl. J. Laser Appl. 31 (2019), 042005, https://doi.org/10.2351/1.5096974

[575] J. Liu, P. Wen: Metal vaporization and its influence during laser powder bed fusion process. Mater. & Des. 215 (2022), 110505, https://doi.org/10.1016/j.matdes.2022.110505

[576] T. Mukherjee, J. S. Zuback, T. DebRoy: Printability of alloys for additive manufacturing. Sci. Rep. 6 (2016), 19717, https://doi.org/10.1038/srep19717

[577] W. Hearn, R. Steinlechner, E. Hryha: Laser-based powder bed fusion of non-weldable low-alloy steels. Powder Met. 65(2) (2022), https://doi.org/10.1080/00325899.2021.1959695

[578] W. Hearn, E. Hryha: Effect of carbon content on the processability of Fe-C alloys produced by laser based powder bed fusion. Front. Mater. 8 (2022), 800021, https://doi.org/10.3389/fmats.2021.800021

[579] J. Platl, D. Rainer, H. Leitner, C. Turk, F. Galbusera, A. G. Demir, B. Previtali, R. Schnitzer: Potential causes for cracking of a laser powder bed fused carbon-free FeCoMo alloy. BHM 167 (2022), 325 – 331, https://doi.org/10.1007/s00501-022-01238-y

[580] K. Kempen, B. Vrancken, S. Buls, L. Thijs, J. van Humbeeck, J.-P. Kruth: Selective laser melting of crack-free high density M2 high speed steel parts by base plate preheating. J. Manuf. Sci. & Eng. 136(6) (2014), 061026, https://doi.org/10.1115/1.4028513

[581] J. Platl, S. Bodner, C. Hofer, A. Landefeld, H. Leitner, C. Turk, M.-A. Nielsen, A. G. Demir, B. Previtali, J. Keckes, R. Schnitzer: Cracking mechanism in a laser powder bed fused cold-work tool steel: The role of residual stresses, microstructure and local elemental concentrations. Acta Mater. 225 (2022), 117570, https://doi.org/10.1016/j.actamat.2021.117570

[582] J. Platl, H. Leitner, C. Turk, A. G. Demir, B. Previtali, R. Schnitzer: Defects in a laser powder bed fused tool steel. Adv. Eng. Mater. 23(12) (2021), 2000833, https://doi.org/10.1002/adem.202000833

[583] A. Haghshenas, M. M. Khonsari: Damage accumulation and crack initiation detection based on the evolution of surface roughness parameters. Int. J. Fatigue 107 (2018), 130 – 144, https://doi.org/10.1016/j.ijfatigue.2017.10.009

[584] J. Wang, L. Li, W. Tao: Crack initiation and propagation behavior of WC particles reinforced Fe-based metal matrix composite produced by laser melting deposition. Opt. & Laser Techn. 82 (2016), 170 – 182, https://doi.org/10.1016/j.optlastec.2016.03.008

[585] A. Bergsmo, F. P. E. Dunne: Competing mechanisms of particle fracture, decohesion and slip-driven fatigue crack nucleation in a PM nickel superalloy. Int. J. Fatigue 135 (2020), 105573, https://doi.org/10.1016/j.ijfatigue.2020.105573

[586] J. Munk, E. Breitbarth, T. Siemer, N. Pirch, C. Häfner: Geometry effect on microstructure and mechanical properties in laser powder bed fusion of Ti-6Al-4V. Metals 12(3) (2022), 482, https://doi.org/10.3390/met12030482

[587] J. B. Ferguson, H. Lopez, D. Kongschaug, B. Schultz, P. Rohatgi: Revised orowan strengthening: Effective interparticle spacing and strain field considerations. Met. & Mater. Trans. A 43 (2012), 2110 – 2115, https://doi.org/10.1007/s11661-011-1029-9

[588] M. Awd, J. Tenkamp, M. Hirtler, S. Siddique, M. Bambach, F. Walther: Comparison of microstructure and mechanical properties of Scalmalloy® produced by selective laser melting and laser metal deposition. Mater. 11(1) (2018), 17, https://doi.org/10.3390/ma11010017

[589] C. Hatzoglou, B. Radiguet, P. Pareige: Experimental artefacts occurring during atom probe tomography analysis of oxide nanoparticles in metallic matrix: Quantification and correction. J. Nucl. Mater. 492 (2017), 279 – 291, https://doi.org/10.1016/j.jnucmat.2017.05.008

[590] B. Gault, D. W. Saxey, M. W. Ashton, S. B. Sinnott, A. N. Chiaramonti, M. P. Moody, D. K. Schreiber: Behavior of molecules and molecular ions near a field emitter. New J. Phys. 18 (2016), 033031, https://doi.org/10.1088/1367-2630/18/3/033031

[591] H. Sakasegawa, L. Chaffron, F. Legendre, L. Boulanger, T. Cozzika, M. Brocq, Y. de Carlan: Correlation between chemical composition and size of very small oxide particles in the MA957 ODS ferritic alloy. J. Nucl. Mater. 384 (2009), 115 – 118, https://doi.org/10.1016/j.jnucmat.2008.11.001

[592] C. Capdevila, M. K. Miller, K. F. Russell, J. Chao, J. L. González-Carrasco: Phase separation in PM 2000™ Fe-base ODS alloy: Experimental study at the atomic level. Mater. Sci. & Eng. A 490(1-2) (2008), 277 – 288, https://doi.org/10.1016/j.msea.2008.01.029

[593] J. Chao, J. González-Carrasco, C. Capdevila: Influence of annealing at 1100°C and 475°C on the mechanical properties at room temperature of an iron base ODS alloy. ISIJ Int. 47(8) (2007), 1214 – 1220, https://doi.org/10.2355/isijinternational.47.1214

[594] J. H. Schneibel, M. Heilmaier, W. Blum, G. Hasemann, T. Shanmugasundaram: Temperature dependence of the strength of fine- and ultrafine-grained materials. Acta Mater. 59 (2011), 1300 – 1308, https://doi.org/10.1016/j.actamat.2010.10.062

[595] J. Wunder: Mikrostrukturelle Beschreibung der Warmfestigkeit ferritischer Superlegierungen. VDI, Reihe 5: Grund- und Werkstoffe, Nr. 510, 1997, ISBN 3-18-351005-7.

[596] R. L. Klueh, J. P. Shingledecker, R. W. Swindeman, D. T. Hoelzer: Oxide dispersion-strengthened steels: A comparison of some commercial and experimental alloys. J. Nucl. Mater. 341 (2005), 103 – 114, https://doi.org/10.1016/j.jnucmat.2005.01.017

[597] J. H. Schneibel, M. Heilmaier: Hall-Petch breakdown at elevated temperatures. Mater. Trans. 55(1) (2014), 44 – 51, https://doi.org/10.2320/matertrans.MA201309

[598] M. De Sanctis, A. Fava, G. Lovicu, R. Montanari, M. Richetta, C. Testani, A. Varone: Temperature dependent mechanical behaviour of ODS steels. Mater. Sci. For. 941 (2018), 257 – 262, https://doi.org/10.4028/www.scientific.net/MSF.941.257

[599] G. Monnet, S. Naamane, B. Devincre: Orowan strengthening at low temperatures in bcc materials studied by dislocation dynamics simulations. Acta Mater. 59 (2011), 451 – 461, https://doi.org/10.1016/j.actamat.2010.09.039

[600] S.-K. Rittinghaus, J. Zielinski: Influence of process conditions on the local solidification and microstructure during laser metal deposition of an intermetallic TiAl alloy (GE4822). Met. & Mater. Trans. A 52 (2021), https://doi.org/10.1007/s11661-021-06139-2

[601] S.-K. Rittinghaus, A. Weisheit, M. Mathes, W. Garcia Vargas: Laser metal deposition of titanium aluminides – a future repair technology for jet engine blades? Proc. 13th World Conf. on Titanium, https://doi.org/10.1002/9781119296126.ch205

[602] V. Lindström, O. Liashenko, K. Zweiacker, S. Derevianko, V. Morozovych, J. Lyashenko, C. Leinenbach: Laser powder bed fusion of metal coated copper powders. Mater. 13(16) (2020), 3493, https://doi.org/10.3390/ma13163493

[603] T. Q. Tran, A. Chinnappan, J. K. Y. Lee, N. H. Loc, L. T. Tran, G. Wang, V. V. Kumar, W. A. D. M. Jayathilaka, D. Ji, M. Doddamani, S. Ramakrishna: 3D printing of highly pure copper. Metals 9(7) (2019), 756, https://doi.org/10.3390/met9070756

[604] Q. Jiang, P. Zhang, Z. Yu, H. shi, D. Wu, H. Yan, X. Ye, Q. Lu, Y. Tian: A review on additive manufacturing of pure copper. Coatings 11(6) (2021), 740, https://doi.org/10.3390/coatings11060740

[605] A. Bor, B. Jargalsaikhan, K. Uranchimeg, J. Lee, H. Choi: Particle morphology control of metal powder with various experimental conditions using ball milling. Powder Techn. 394 (2021), 181–190. https://doi.org/10.1016/j.powtec.2021.08.053

[606] D. Tiberto, U. E. Klotz, F. Held, G. Wolf: Additive manufacturing of copper alloys: Influence of process parameters and alloying elements. Mater. Sci. & Techn. 35(8) (2019), 969 – 977, https://doi.org/10.1080/02670836.2019.1600840

[607] O. A. Tertuliano, P. J. DePond, D. Doan, M. J. Matthews, X. W. Gu, W. Cai: Nanoparticle-enhanced absorptivity of copper during laser powder bed fusion. Addit. Manuf. 51 (2022), 102562, https://doi.org/10.1016/j.addma.2021.102562

[608] J. P. Kruth, X. Wang, T. Laoui, L. Froyen: Lasers and materials in selective laser sintering. Assembly Autom. 23(4) (2003), 357 – 371, https://doi.org/10.1108/01445150310698652

[609] A. H. Seltzman, S. J. Wukitch: Fracture characteristics and heat treatment of laser powder bed fusion additively manufactured GRCop-84 copper. Mater. Sci. & Eng. A 827 (2021), 141690, https://doi.org/10.1016/j.msea.2021.141690

[610] A. H. Seltzman, S. J. Wukitch: Precipitate size in GRCop-84 gas atomized powder and laser powder bed fusion additively manufactured material. Fus. Sci. & Techn. 77(7–8) (2021), 641 – 646, https://doi.org/10.1080/15361055.2021.1913030

[611] J. Fu, T. P. Davis, A. Kumar, I. M. Richardson, M. J. M. Hermans: Characterisation of the influence of vanadium and tantalum on yttrium-based nano-oxides in ODS Eurofer steel. Mater. Charact. 175 (2021), 111072, https://doi.org/10.1016/j.matchar.2021.111072

[612] H. Xu, Z. Lu, D. Wang, C. Liu: Microstructure refinement and strengthening mechanisms of a 9Cr oxide dispersion strengthened steel by zirconium addition. Nucl. Eng. & Techn. 49(1) (2017), 178 – 188, https://doi.org/10.1016/j.net.2017.01.002

[613] J. J. Park, S. M. Hong, E. K. Park, M. K. Lee, C. K. Rhee: Synthesis of Fe based ODS alloys by a very high speed planetary milling process. J. Nucl. Mater. 428(1–3) (2012), 35 – 39, https://doi.org/10.1016/j.jnucmat.2011.12.027

[614] K. R. Anderson, J. R. Groza, R. L. Dreshfield, D. Ellis: High-performance alloy dispersion-strengthened Cu-8Cr-4Nb alloy. Met. & Mater. Trans. A 26 (1995), 2197 – 2206, https://doi.org/10.1007/BF02671235

[615] K. R. Anderson, J. R. Groza: Microstructural size effects in high-strength high-conductivity Cu-Cr-Nb alloys. Met. & Mater. Trans A 32 (2001), 1211 – 1224, https://doi.org/10.1007/s11661-001-0130-x

[616] A. R. Kini, D. Maischner, A. Weisheit, D. Ponge, B. Gault, E. A. Jägle, D. Raabe: In-situ synthesis via laser metal deposition of a lean Cu-3.4Cr-0.6Nb (at.%) conductive alloy hardened by Cr nano-scale precipitates and by laves phase mi-cro-particles. Acta Mater. 197 (2020), 330 – 340, https://doi.org/10.1016/j.actamat.2020.07.035

[617] D. Maischner, U. Fritsching, A. Kini, A. Weisheit, V. Uhlenwinkel, J. H. Schleifenbaum, T. Biermann: Laser additive manufacturing of copper-chromium-niobium alloys using gas atomized powder. Int. J. Mater. Res. 111(7) (2020), 587 – 593, https://doi.org/10.3139/146.111912

[618] P. Kürnsteiner, P. Bajaj, A. Gupta, M. B. Wilms, A. Weisheit, X. Li, C. Leinenbach, B. Gault, E. A. Jägle, D. Raabe: Control of thermally stable core-shell nano-precipitates in additively manufactured Al-Sc-Zr alloys. Addit. Manuf. 32 (2020), 100910, https://doi.org/10.1016/j.addma.2019.100910

[619] S.-K. Rittinghaus, A. Amr, U. Hecht: Intrinsic heat treatment of an additively manufactured medium entropy $AlCrFe_2Ni_2$-alloy. Met. Mater. Int. (2022), https://doi.org/10.1007/s12540-022-01246-0

[620] C. Meier, S. L. Fuchs, N. Much, J. Nitzler, R. W. Penny, P. M. Pregla, S. D. Proell, Y. Sun, R. Weissbach, M. Schreter, N. E. Hodge, A. J. Hart, W. A. Wall: Physics-based modeling and predictive simulation of powder bed fusion additive manufacturing across length scales. GAMM-Mitteilungen 44 (2021), e202100014, https://doi.org/10.1002/gamm.202100014

[621] H. Xie, M. Hong, E. M. Hitz, X. Wang, M. Cui, D. J. Kline, M. R. Zachariah, L. Hu: High-temperature pulse method for nanoparticle redispersion. J. Am. Chem. Soc. 142(42) (2020), 17364 – 17371, https://doi.org/10.1021/jacs.0c04887

[622] M. Lervåg, C. Sørensen, A. Robertstad, B. M. Brønstad, B. Nyhus, M. Eriksson, R. Aune, X. Ren, O. M. Akselsen, I. Bunaziv: Additive manufacturing with superduplex stainless steel wire by CMT Process. Metals 10(2) (2020), 272, https://doi.org/10.3390/met10020272

[623] A. Priyadarshi, M. Khavari, T. Subroto, P. Prentice, K. Pericleous, D. Eskin, J. Durodola, I. Tzanakis: Mechanisms of ultrasonic de-agglomeration of oxides through in-situ high-speed observations and acoustic measurements. Ultras. Sonochem. 79 (2021), 105792, https://doi.org/10.1016/j.ultsonch.2021.105792

[624] J. Lv, J. Zhou, T. Zhang, X. Meng, P. Li, S. Huang: Microstructure and wear properties of IN718/WC composite coating fabricated by ultrasonic vibration-assisted laser cladding. Coatings 12(3) (2022), 412, https://doi.org/10.3390/coatings12030412

[625] D. Yuan, S. Shao, C. Guo, F. Jiang, J. Wang: Grain refining of Ti-6Al-4V alloy fabricated by laser and wire additive manufacturing assisted with ultrasonic vibration. Ultras. Sonochem. 73 (2021), 105472, https://doi.org/10.1016/j.ultsonch.2021.105472

[626] Z. Yi, C. Song, G. Zhang, T. Tong, G. Ma, D. Wu: Microstructure and wear property of ZrO_2-added NiCrAlY prepared by ultrasonic-assisted direct laser deposition. Mater. 14(19) (2021), 5785, https://doi.org/10.3390/ma14195785

[627] C. J. Todaro, M. A. Easton, D. Qiu, D. Zhang, M. J. Bermingham, E. W. Lui, M. Brandt, D. H. StJohn, M. Qian: Grain structure control during metal 3D printing by high-intensity ultrasound. Nature Comm. 11 (2020), 142, https://doi.org/10.1038/s41467-019-13874-z

[628] D. Zhang, L. Nastac: Numerical modeling of the nanodispersion during ultrasonic and electromagnetic stirring processing of Al-based nanocomposites. 8th Int. Conf. Electromag. Proc. Mater. (2015), Cannes, France. https://hal.archives-ouvertes.fr/hal-01333879

[629] S. Pradhan, J. Hedberg, E. Blomberg, S. Wold, I. O. Wallinder: Effect of sonification on particle dispersion, administered dose and metal release of non-functionalized, non-inert metal nanoparticles. J. Nanoparticle Res. 18 (2016), 285, https://doi.org/10.1007/s11051-016-3597-5

[630] D. G. Eskin, I. Tzanakis, F. Wang, G. S. B. Lebon, T. Subroto, K. Pericleous, J. Mi: Fundamental strudies of ultrasonic melt processing. Ultras. Sonochem. 52 (2019), 455 – 467, https://doi.org/10.1016/j.ultsonch.2018.12.028

[631] R. Shi, S. A. Khairallah, T. T. Roehling, T. W. Heo, J. T. McKeown, M. J. Matthews: Microstructural control in metal laser powder fusion additive manufacturing using laser beam shaping strategy. Acta Mater. 184 (2020), 284 – 305, https://doi.org/10.1016/j.actamat.2019.11.053

B. Supplementary

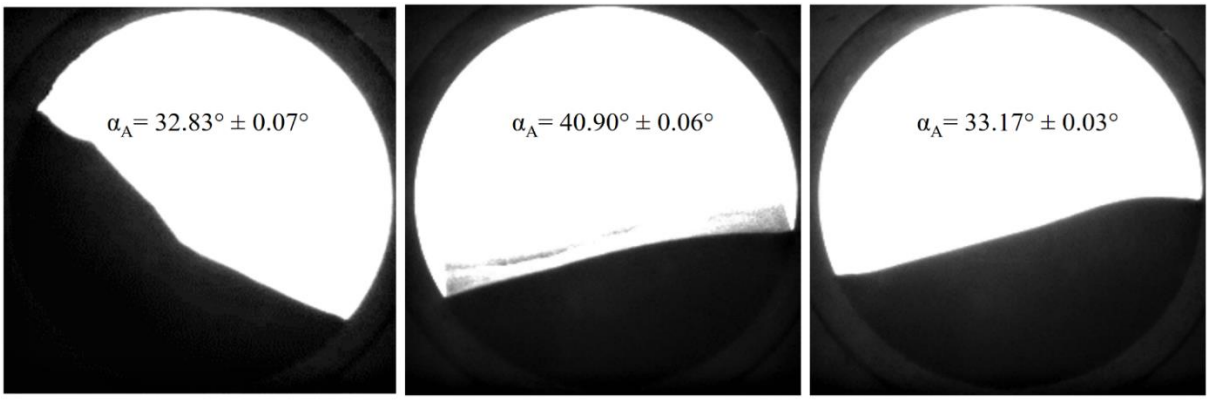

Fig. S1: Photographs from the flowability measurement in the revolution powder analyser. a) Raw stainless steel powder material. b) MA manufactured powder material. c) LSPC-generated powder material showing different surface fractals.

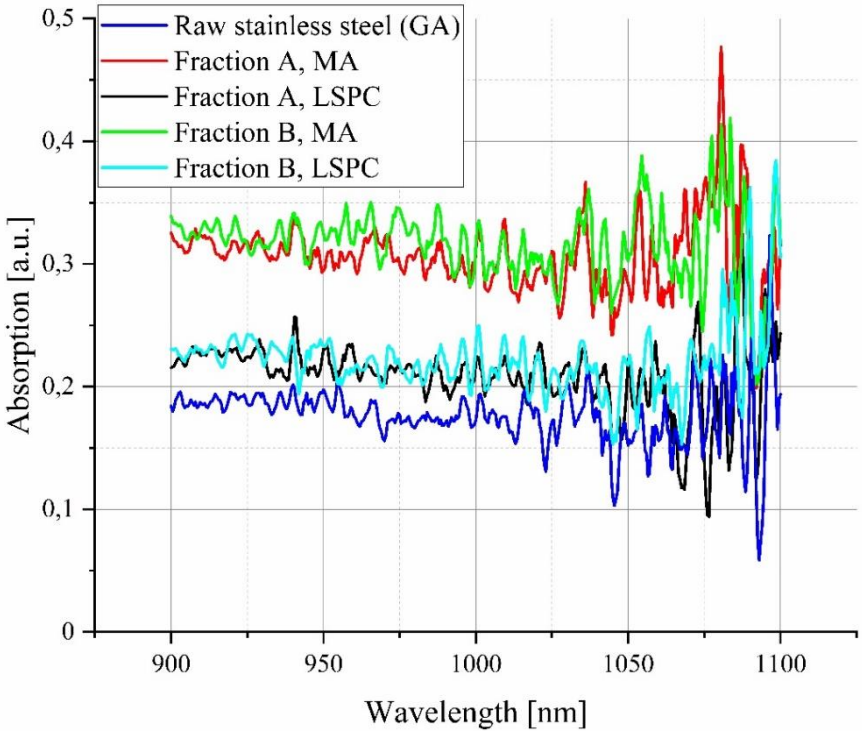

Fig. S2: Absorption curves for GA raw stainless steel Fe20Cr4.5Al0.5Ti (wt.%) and the manufactured powder composites by MA and LSPC for powder fraction A (< 45 µm) and B (45 – 90 µm) for wavelengths from 900 – 1100 nm.

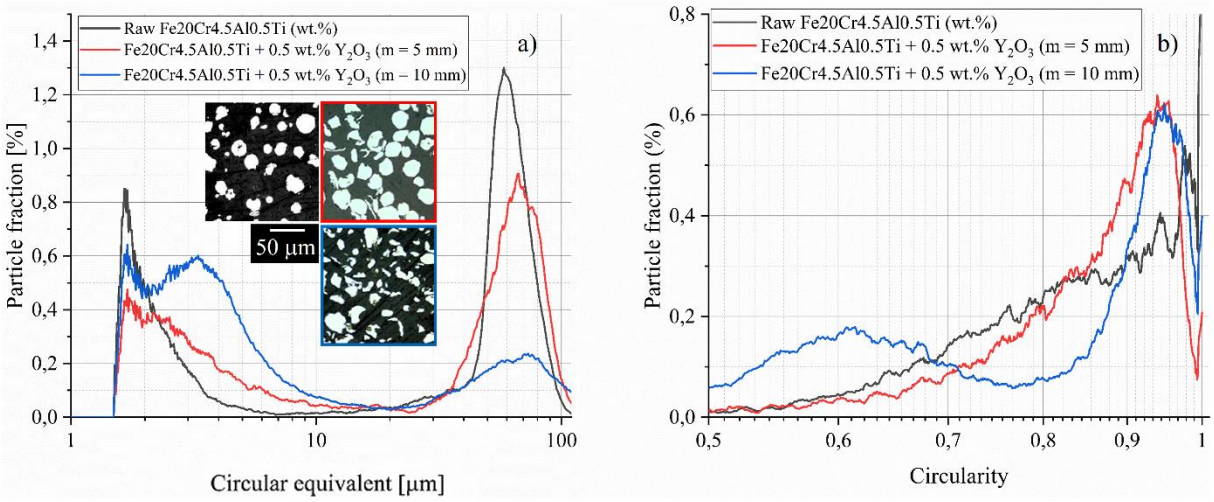

Fig. S3: a) Particle size distribution of gas atomized stainless steel powder (black curve) and milled powder material with 5 mm (red curve) and 10 mm (blue curve) grinding balls. b) Corresponding circularity distribution of the powder materials examined in a).

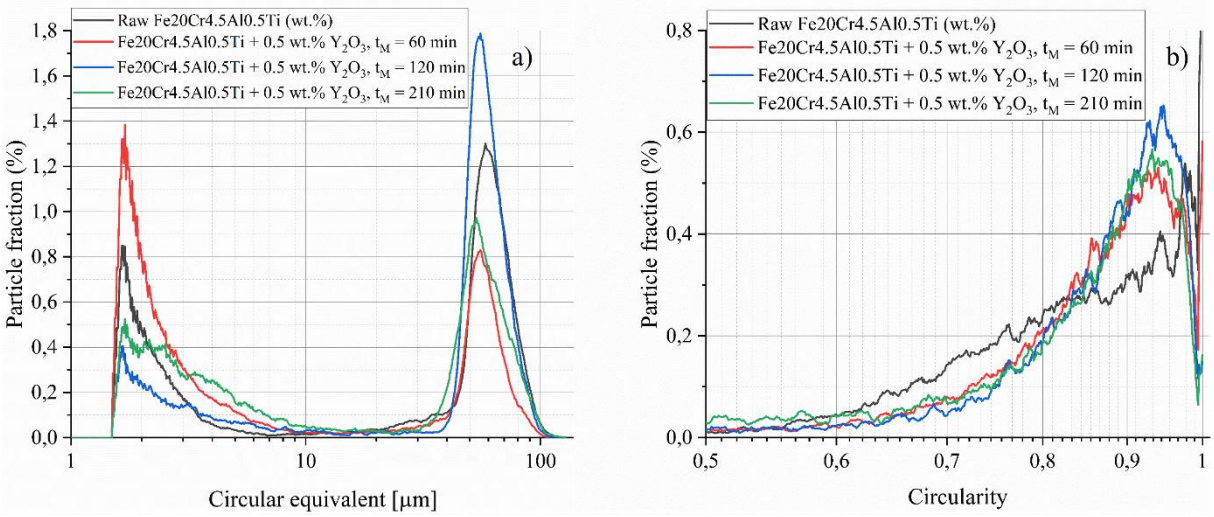

Fig. S4: a) Particle size distribution of gas atomized stainless steel powder and mechanically alloyed powder materials with varied cumulative milling time using grinding ball diameters of 5 mm and a rotation speed of 150 min^{-1}. b) Corresponding circularity distribution of the powder materials examined in a).

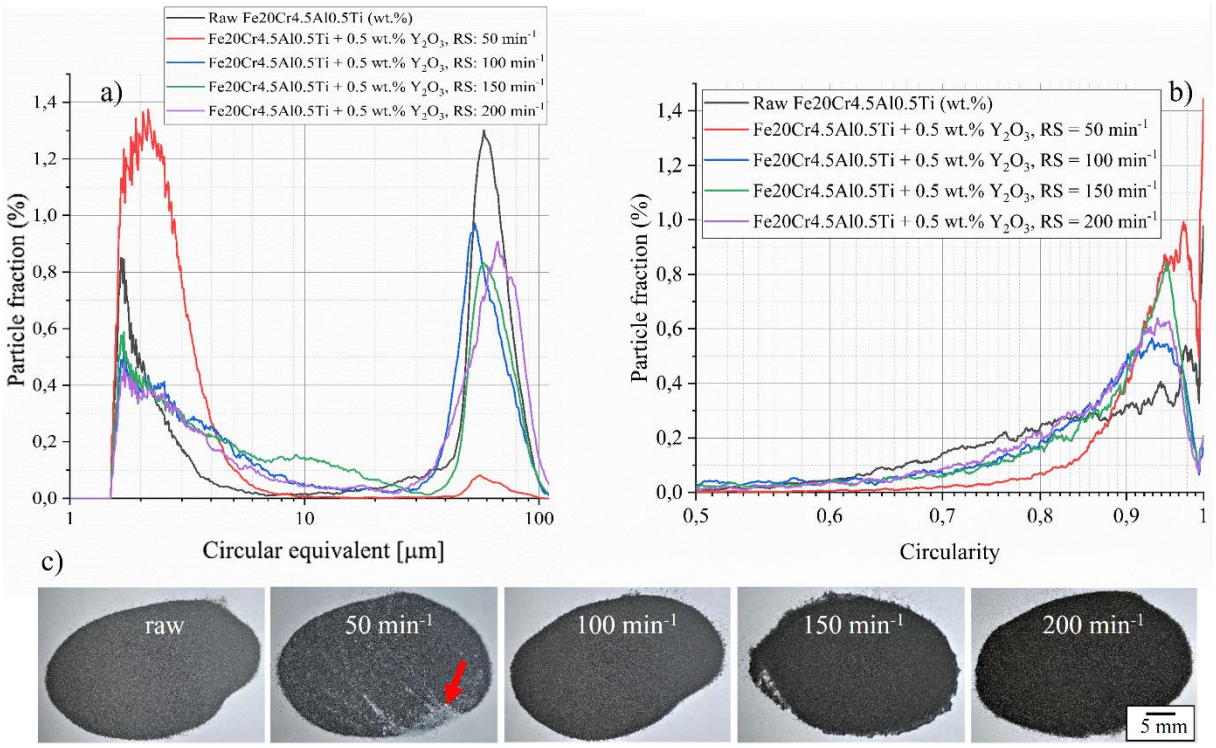

Fig. S5: a) Particle size distribution of gas atomized “raw” stainless steel powder and mechanically alloyed powder materials with varied rotation speed (RS) of the planetary mill using grinding ball diameters of 5 mm and a cumulative milling time of 120 min. b) Corresponding circularity distribution of the powder materials examined in a). c) Photographic images of the gas atomized stainless steel powder (“raw”) and composite powders after mechanical alloying procedure at different rotation speeds.

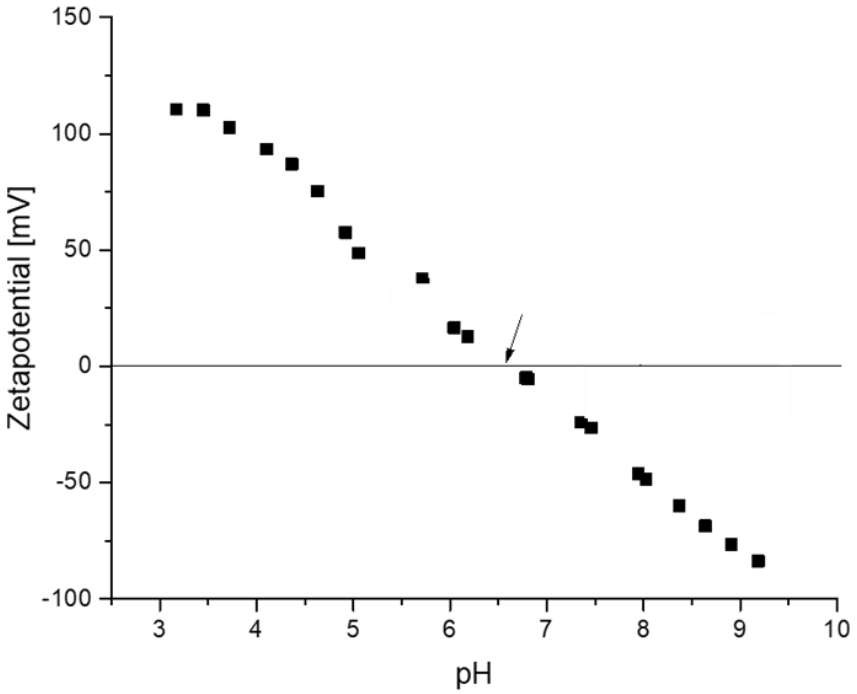

Fig. S6: Measured IEP of the stainless steel powder by evaluating the zeta potential of the colloidal powder at different pH values by DLS. The arrow denotes the IEP at a pH of approx. 6.5. [13]

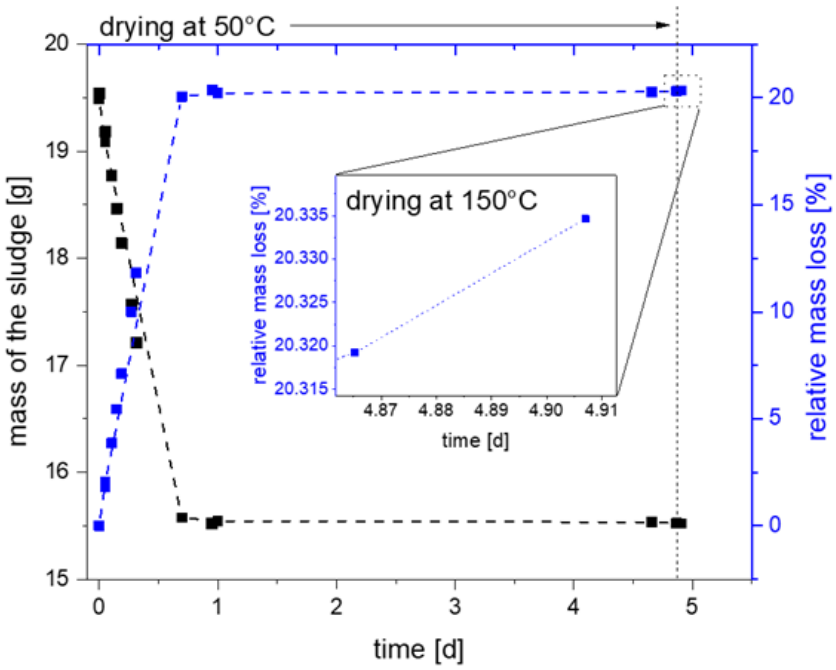

Fig. S7: Weight of the sludge after sedimentation and removal of the supernatant and relative mass loss relative to the weight of the sludge at the beginning of the drying procedure. The initial powder amount is 15.5 g. [16]

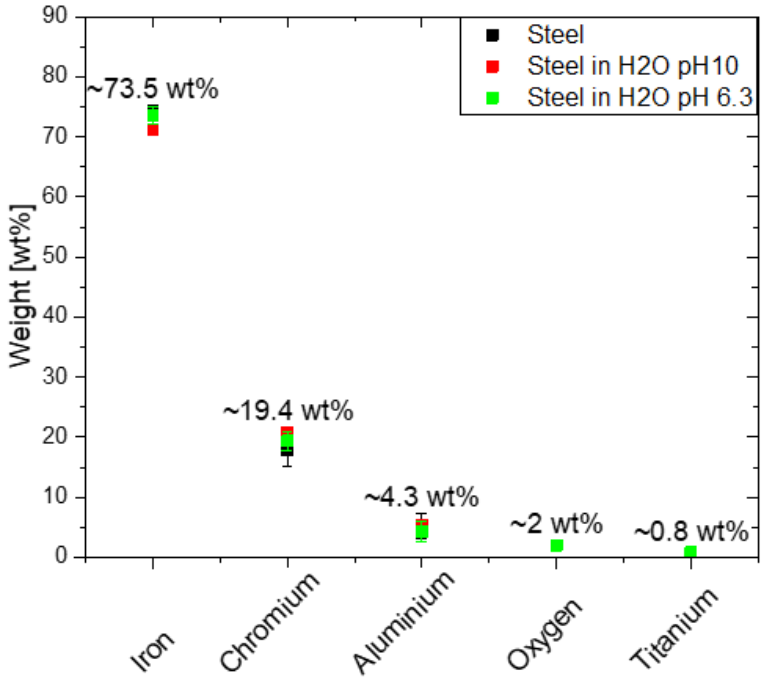

Fig. S8: EDS measurements of the stainless steel powder exposed to water environment with different pH values (in red and green) compared to the untreated stainless steel powder in black. Both "Steel in H_2O" samples were treated with water for 2 hours at the given pH values. Afterwards the supernatant was separated and the stainless steel powder was dried before the EDS measurement was performed. [16]

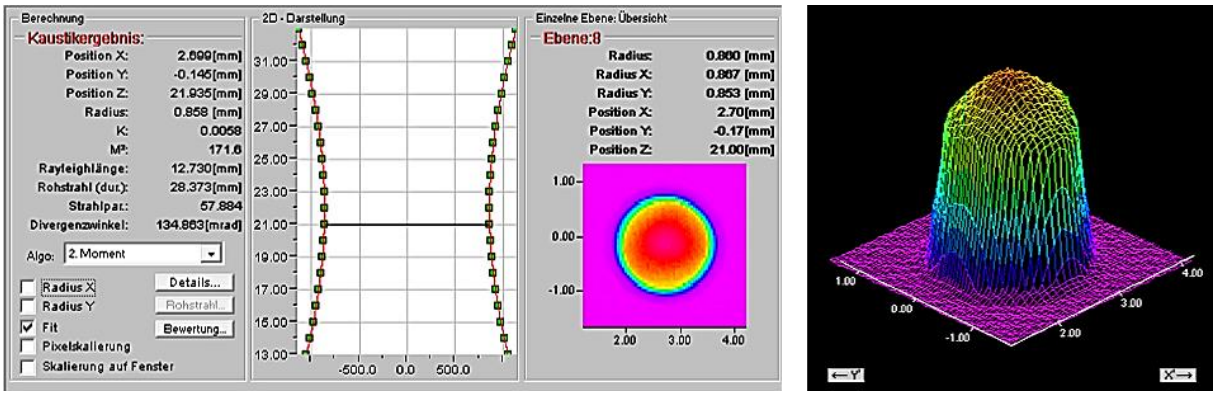

Fig. S9: Laser beam caustic with a TopHat beam intensity distribution in the focal plane of the LDM 3000-60 laser system used in L-DED machine 1 (beam diameter: 1.8 mm).

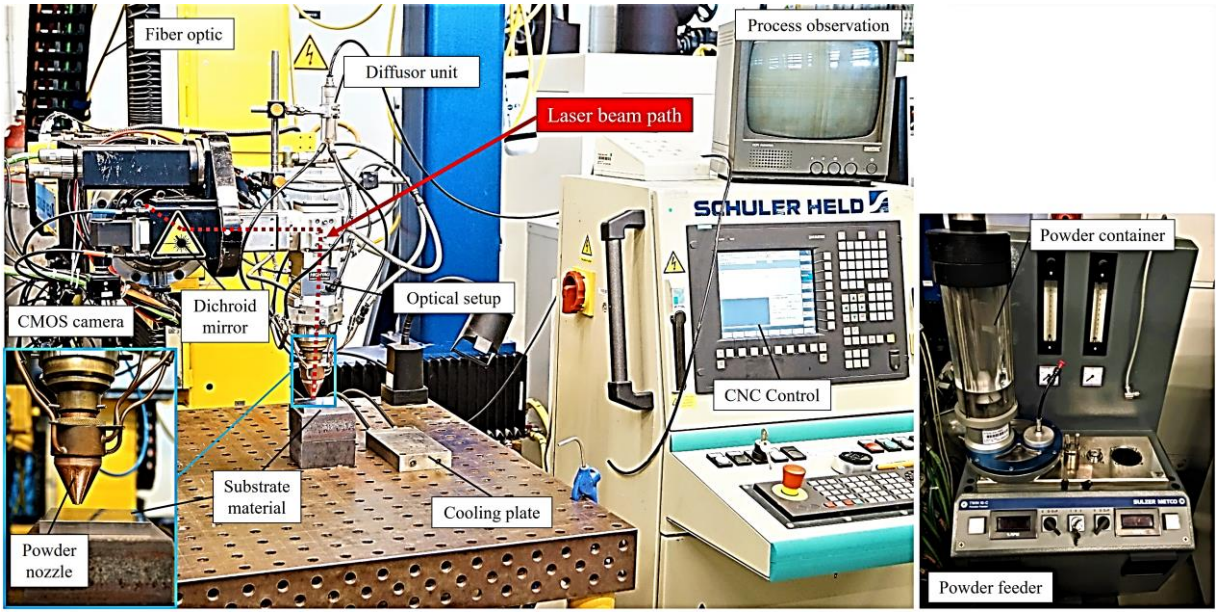

Fig. S10: Photographic depiction of L-DED machine 1.

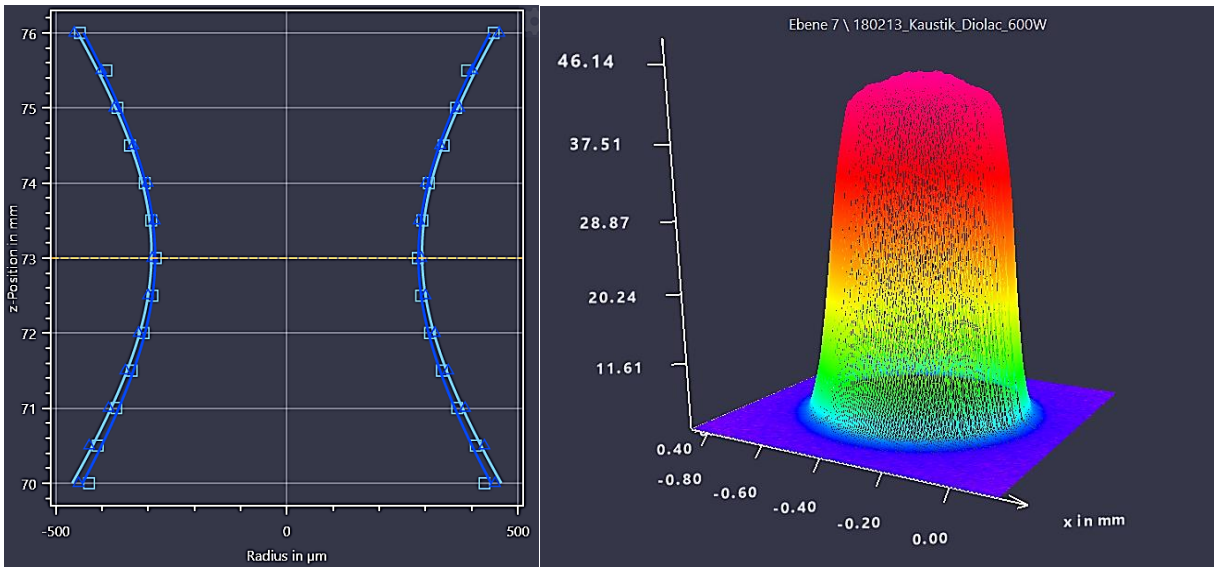

Fig. S11: Laser caustic with the beam intensity distribution in the focal plane of the LDF 2000-30 laser system used in L-DED machine 2 (beam diameter: 0.6 mm).

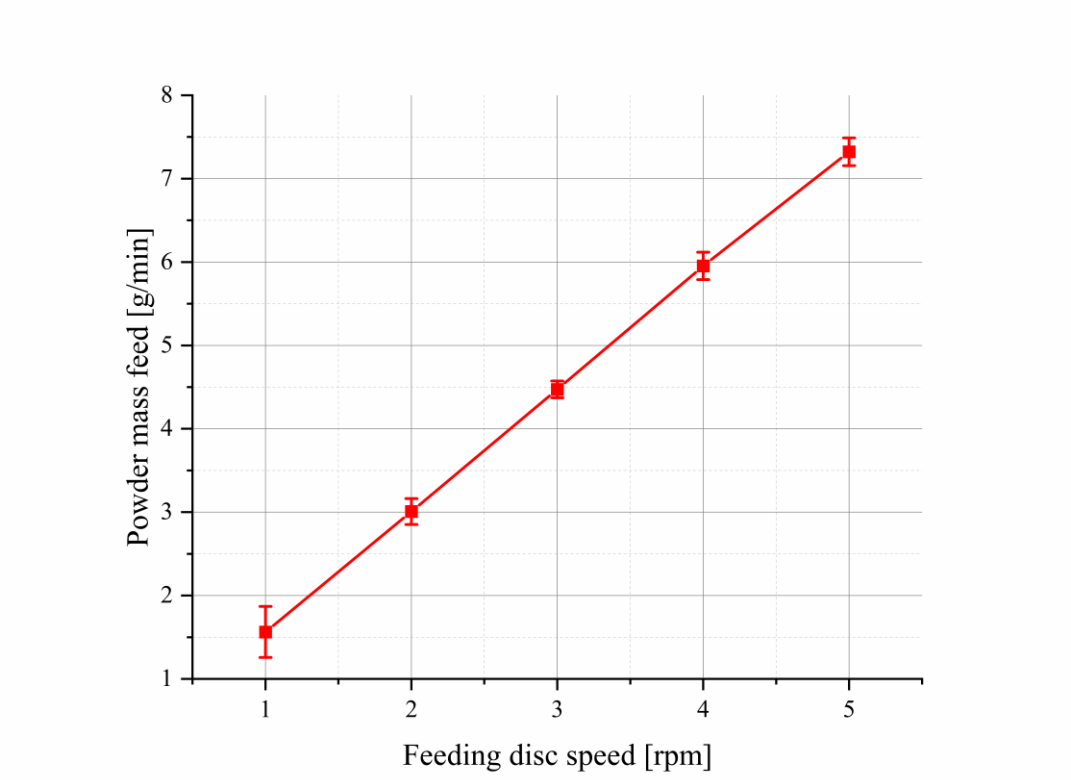

Fig. S12: Plot of the powder material feed as a function of the rotation speed of the disc in the powder feeding system. The groove of the feeding disc has a dimension of 3.5 mm x 0.6 mm.

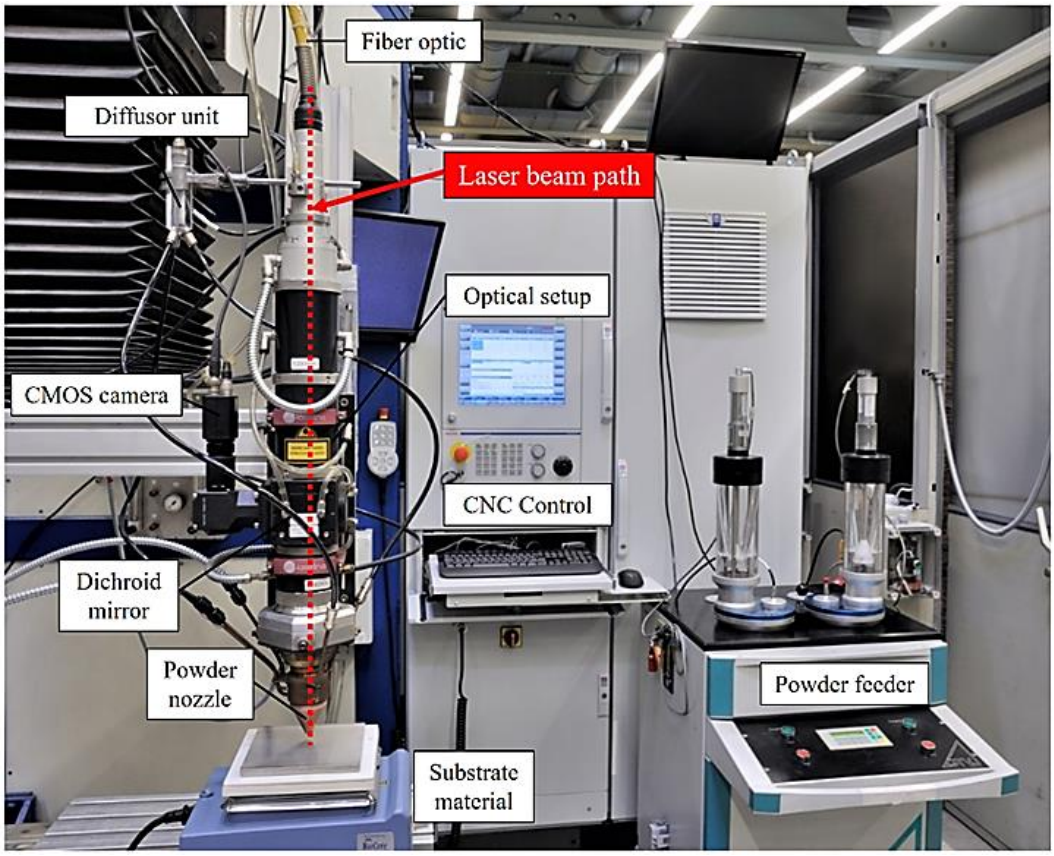

Fig. S13: Photographic depiction of L-DED machine 2.

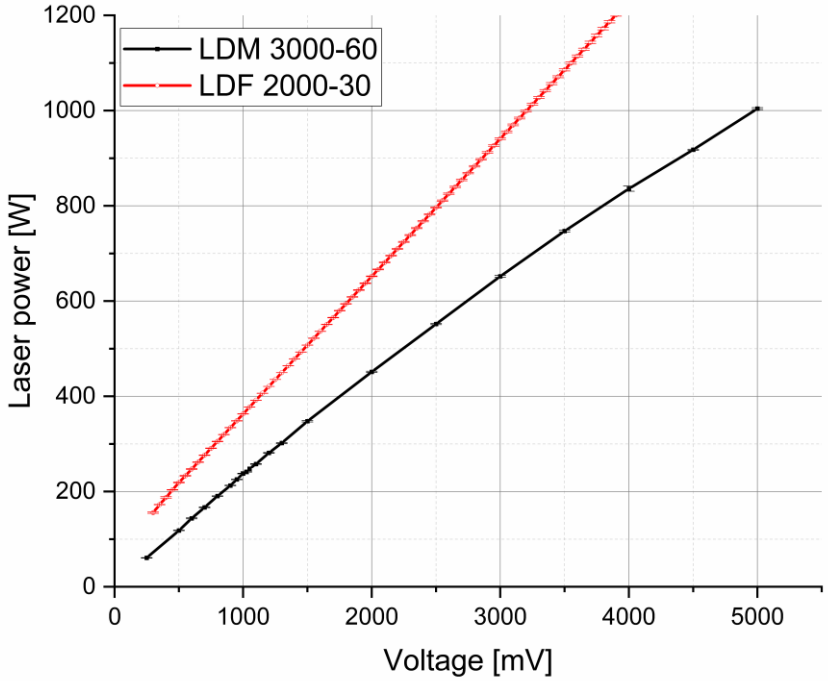

Fig. S14: Laser power calibration curve of the laser systems LDM 3000-60 (black curve) and LDF 2000-30 (red curve) used, showing the output power (after beam shaping by the optical alignment) as a function of the voltage.

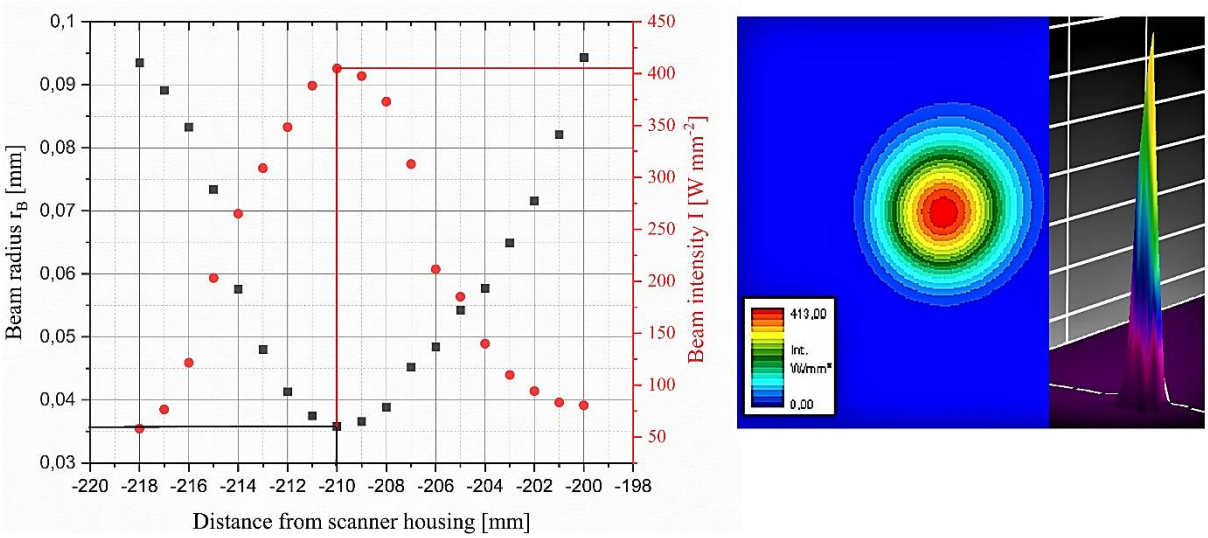

Fig. S15: Laser caustic with a gaussian beam intensity distribution in the focal plane of the YLR-1000WC laser system used for L-PBF.

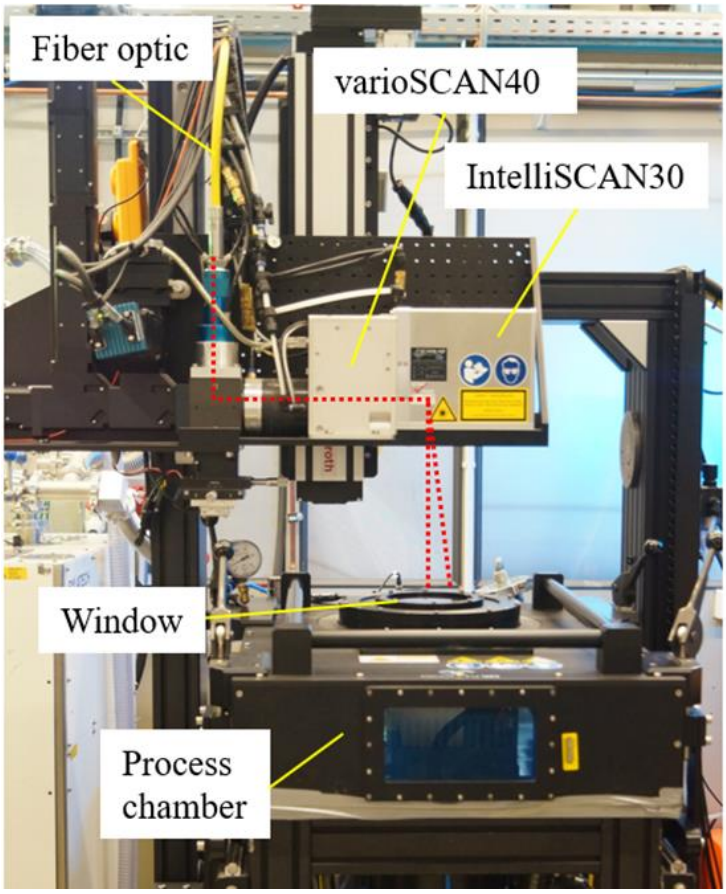

Fig. S16: Photographic depiction of L-PBF machine AconityMIDI used for L-PBF processing.

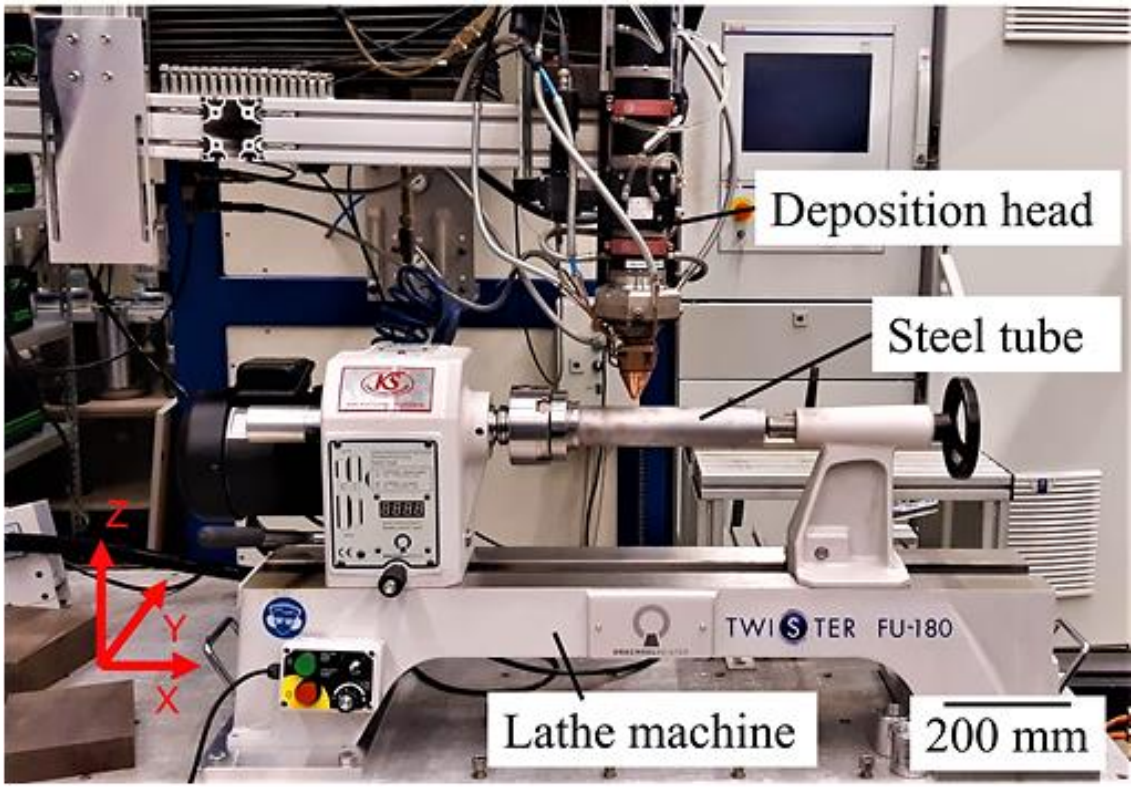

Fig. S17: Photographic depiction of HSLC machine setup, integrated in L-DED machine 2.

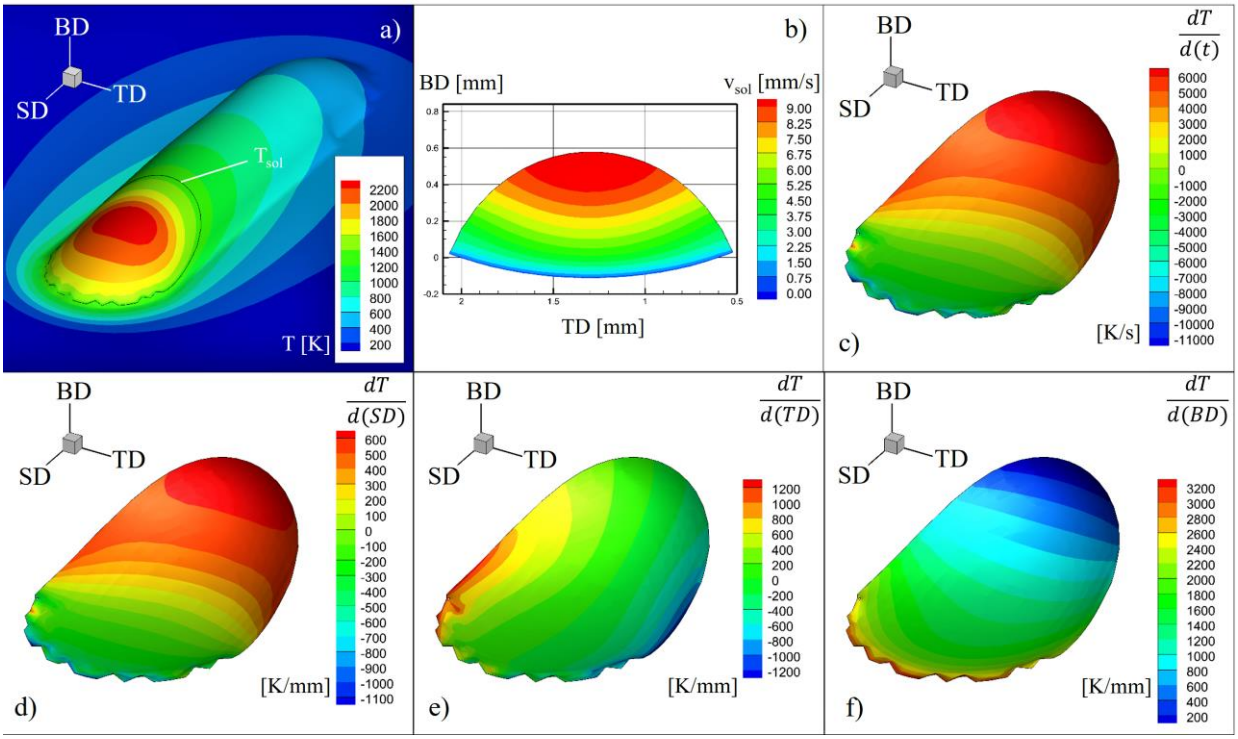

Fig. S18: FEM melt pool solidification simulations for L-DED manufactured material using a large beam diameter (1.8 mm): a) Melt pool temperature with solidus line (T_{sol}). b) Velocity of the solidification front v_{sol}. c) Cooling rate along the solidification front. Negative cooling rates can be considered as heating rates generated by the laser irradiation. d-f) The temperature gradients plotted in every direction in space $\frac{dT}{d(SD)}$ (d), $\frac{dT}{d(TD)}$ (e) and $\frac{dT}{d(BD)}$ (f).

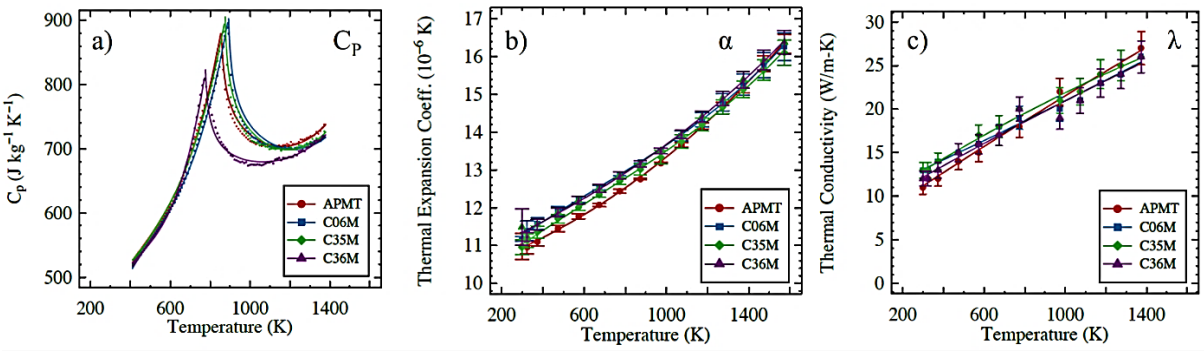

Fig. S19: Temperature dependent thermo-physical data of heat capacity C_P (a), thermal expansion α (b) and thermal conductivity λ (c) for the FEM modelling of cooling rate, solidification rate and thermal gradients of the melt pool of L-DED, HSLC and L-PBF processing of Fe20Cr4.5Al0.5Ti (wt.%) stainless steel. [559]

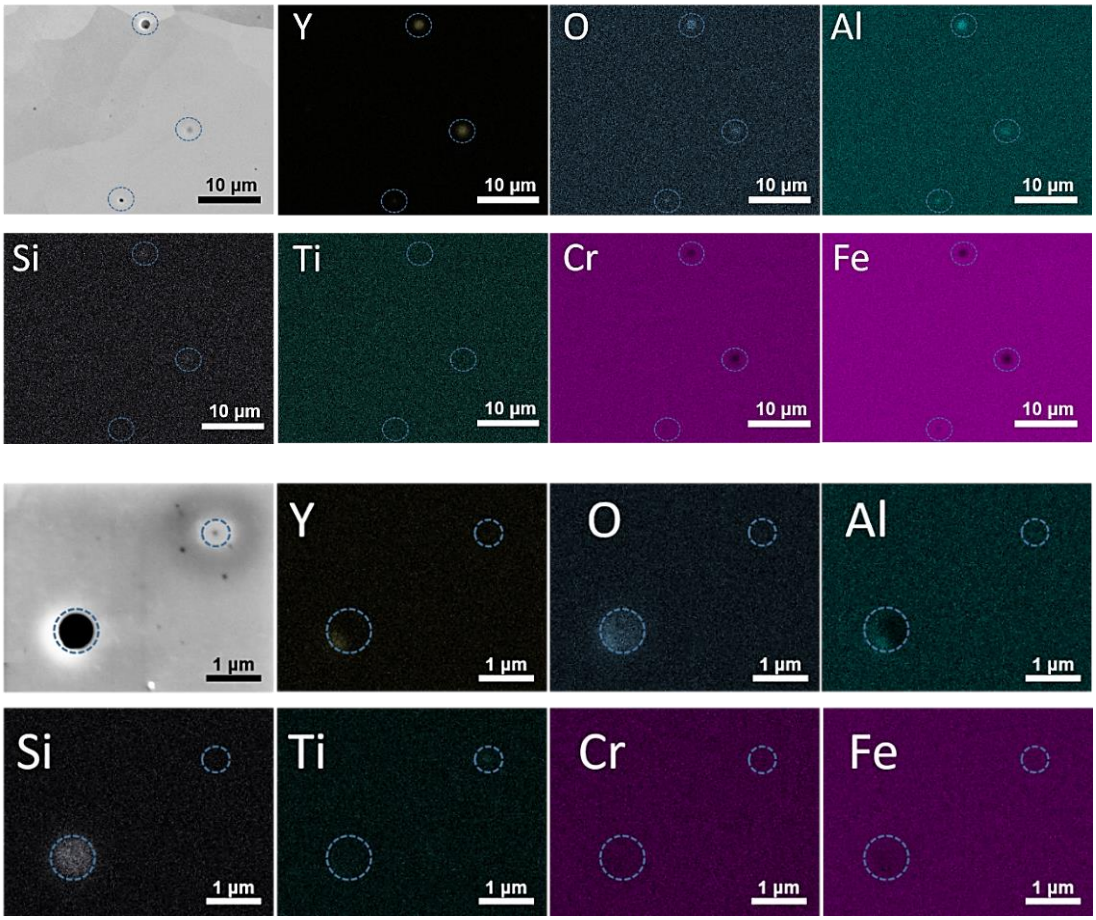

Fig. S20: SEM backscatter electron (BSE) micrographs and the corresponding EDS maps of the L-DED ODS steel with the elemental Y, O, Al and Si content of the observed particles with two different magnifications. [13]

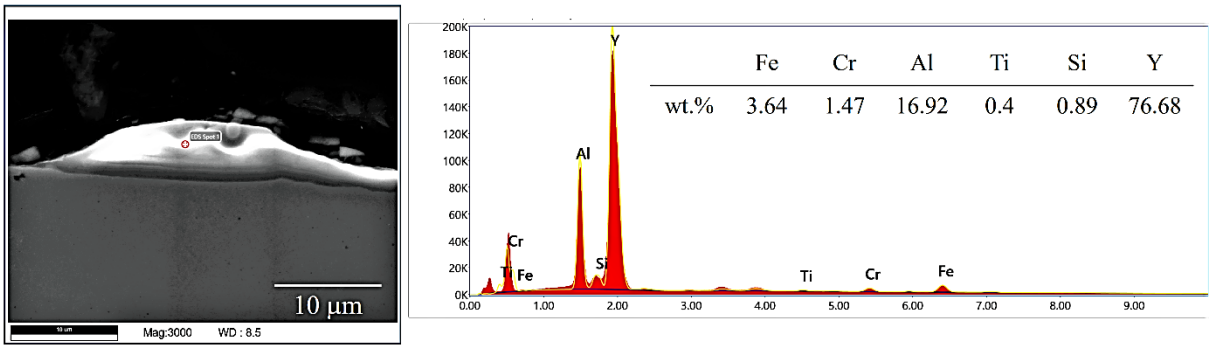

Fig. S21: SEM image (SE mode) and corresponding EDS measurement of a slag layer deposit on the surface of a L-PBF manufactured specimen using MA powder material, showing high content of yttrium and aluminium.

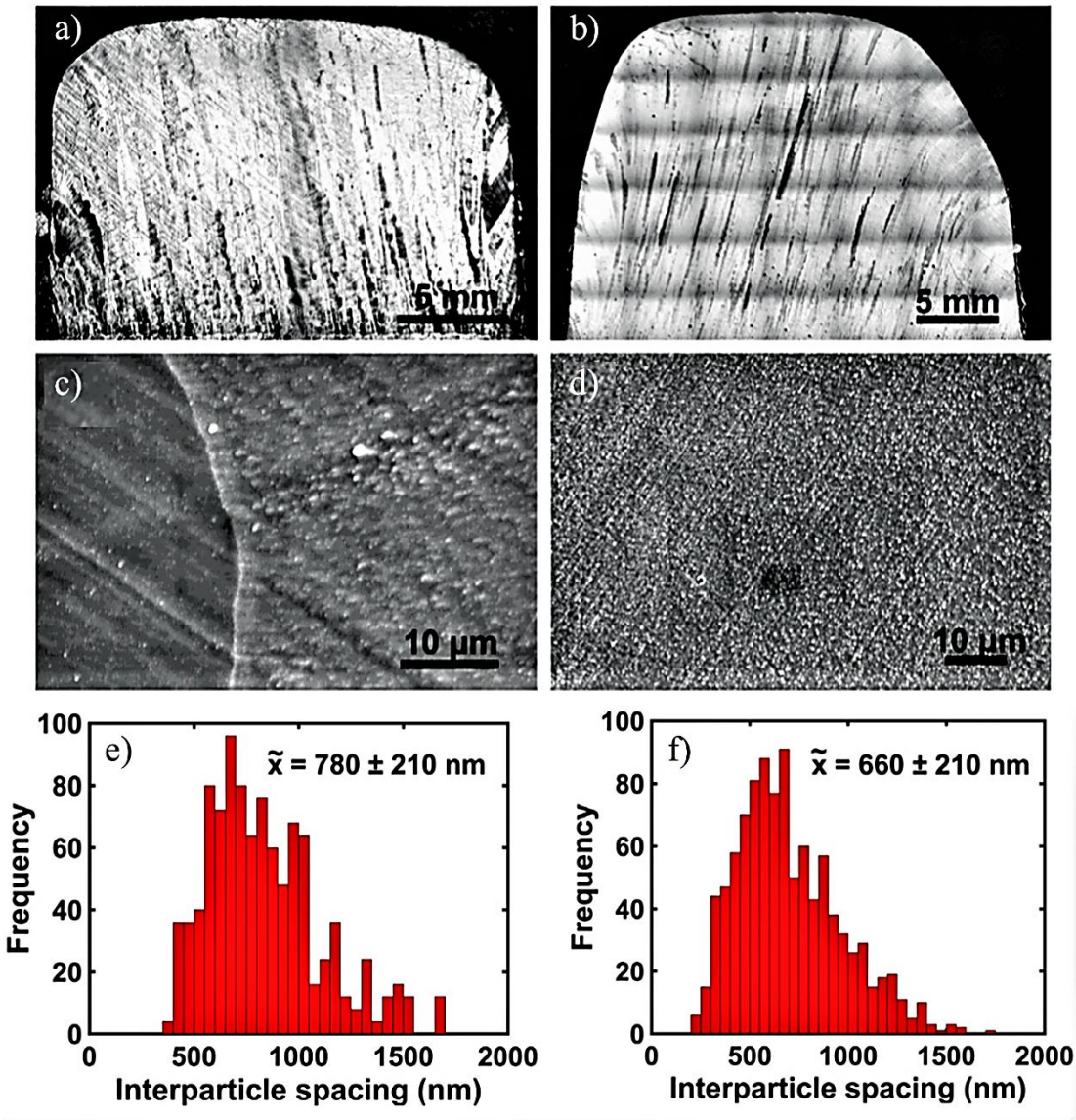

Fig. S22: Light optical microscopy images of cross sections of the L-DED-built specimens: a) Parts built from non-irradiated Y_2O_3 decorated stainless steel powder. b) Part built from steel powder decorated with Y_2O_3 nanoparticles. c) SEM image (SE-mode) of a cross section of the specimen depicted in a), showing distributed oxide particles (white structures). d) SEM image

(SE-mode) of a cross section of the specimen depicted in b), showing distributed oxide particles (white structures). e) Histogram of the interparticle spacing extracted from c). Histogram of the interparticle spacing extracted from d). [16]

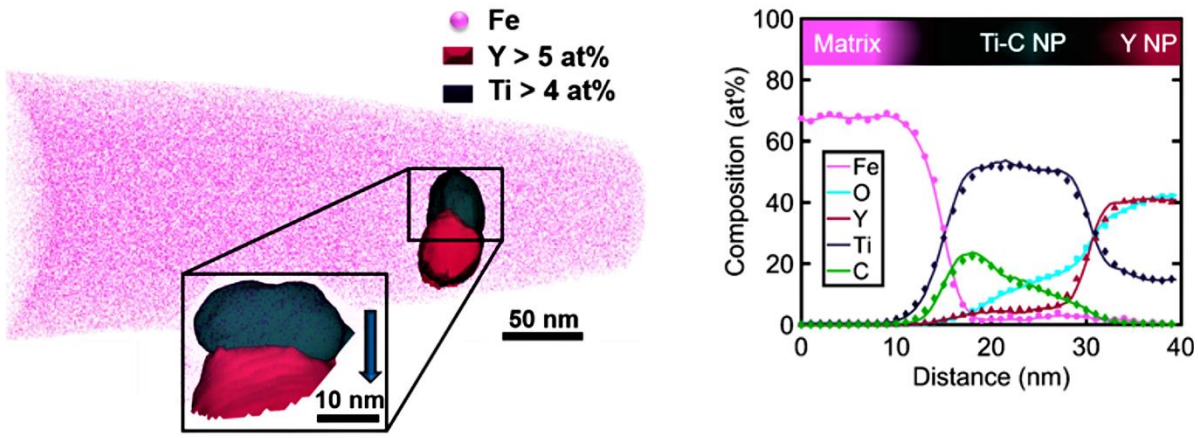

Fig. S23: APT results from L-PBF produced ODS steel. The left shows the reconstructed volume with co-nucleated yttrium-rich oxide (red) with a titanium-rich carbide (black). Co-nucleation of carbides and oxide nanoparticles is also observed in conventionally manufactured aluminium-rich ODS steels. [151] The corresponding proximity histogram for the isocomposition surfaces in the APT reconstruction shows a composition profile through both particles, the Y-oxide and the Ti-carbide, along the direction represented by the arrow in zoomed part of the left image, indicating a substantial content of titanium in the yttrium-rich oxide nanoparticle. [13]

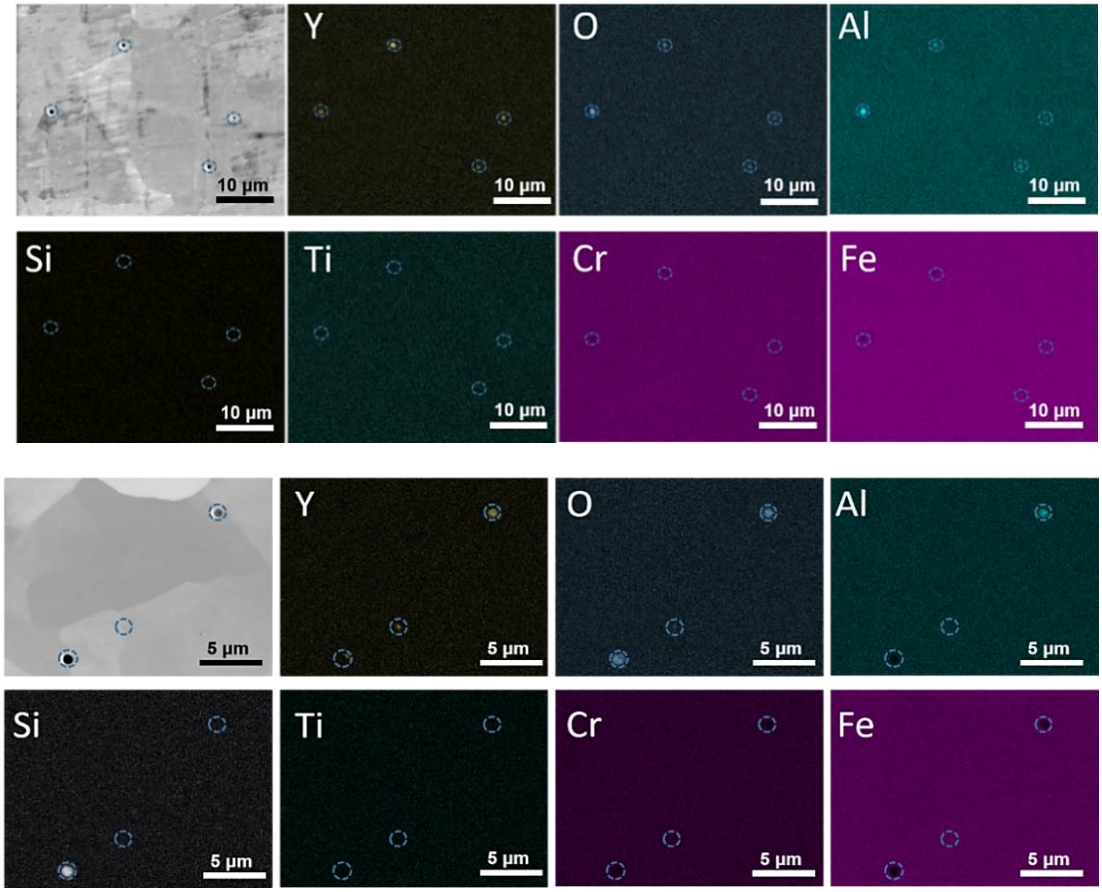

Fig. S24. SEM backscatter electron (BSE) micrographs and the corresponding EDS maps of the L-PBF ODS steel with the elemental Y, O, Al and Si content of the observed particles with two different magnifications. [13]

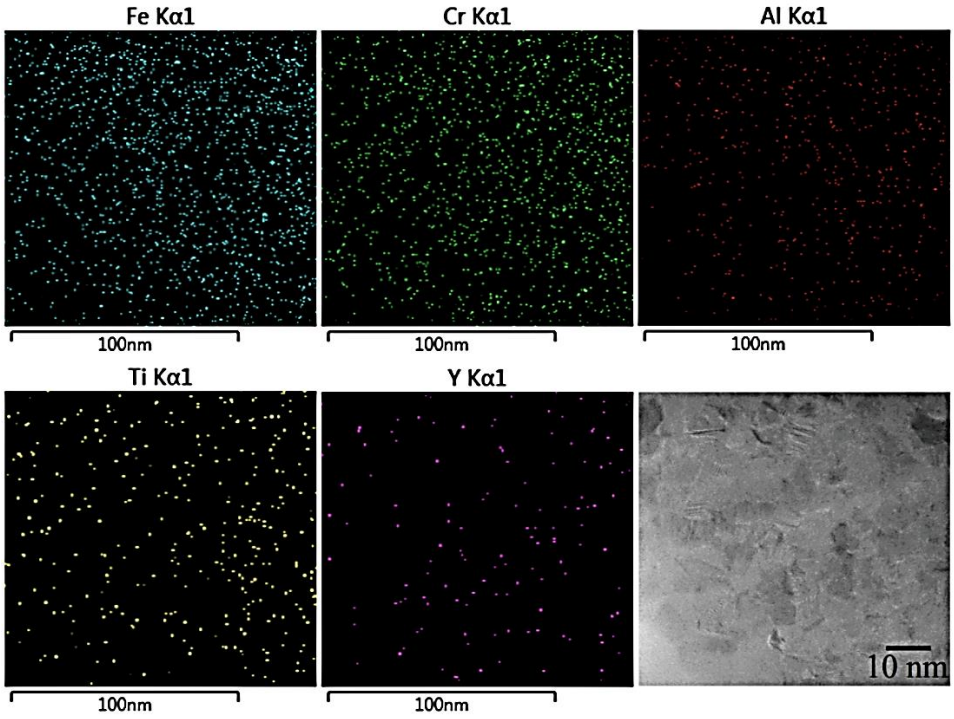

Fig. S25: EDS maps from TEM-examinations and corresponding BFTEM image confirming the presence of Y-Al-O and Y-Ti-O structures in L-PBF printed ODS steel, manufactured from LSPC-generated powder material.

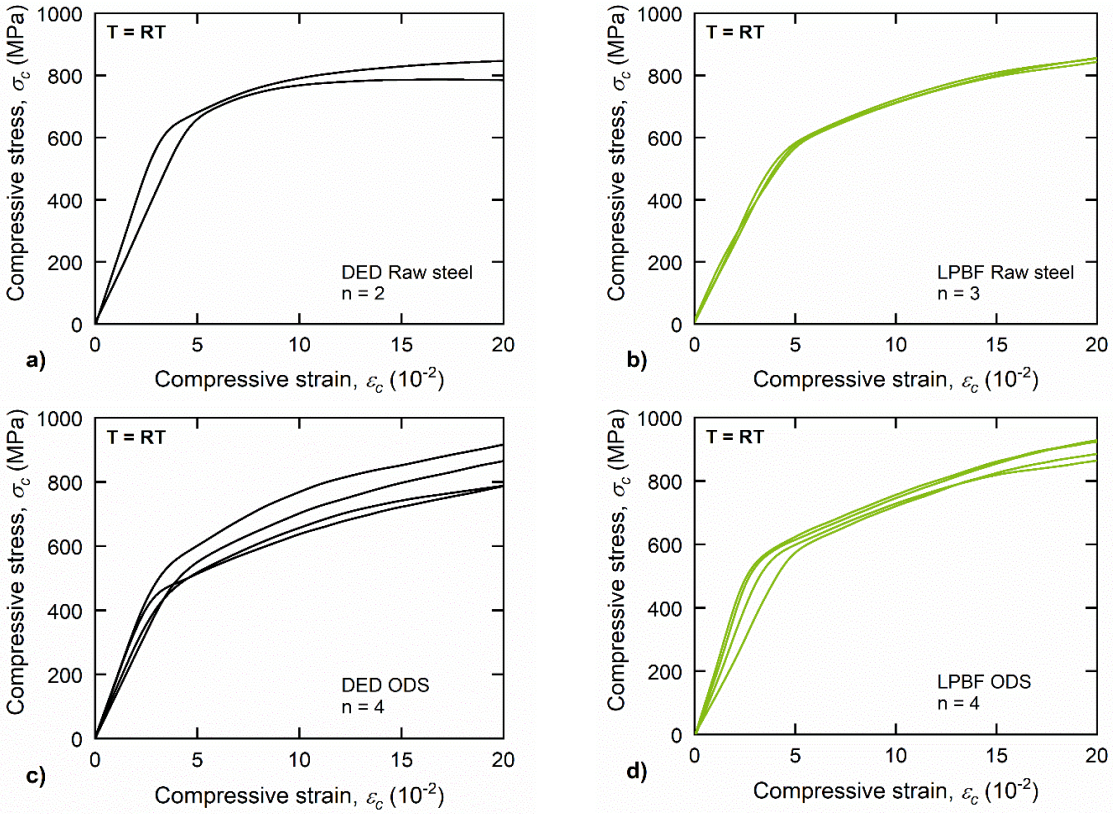

Fig. S26: Compressive stress σ_c of every tested as-built a) raw L-DED steel, b) raw L-PBF steel and c) ODS L-DED, d) ODS L-PBF processed as a function of the compressive strain ε_c at RT (23°C). The ODS powder material used was manufactured by LSPC. [13]

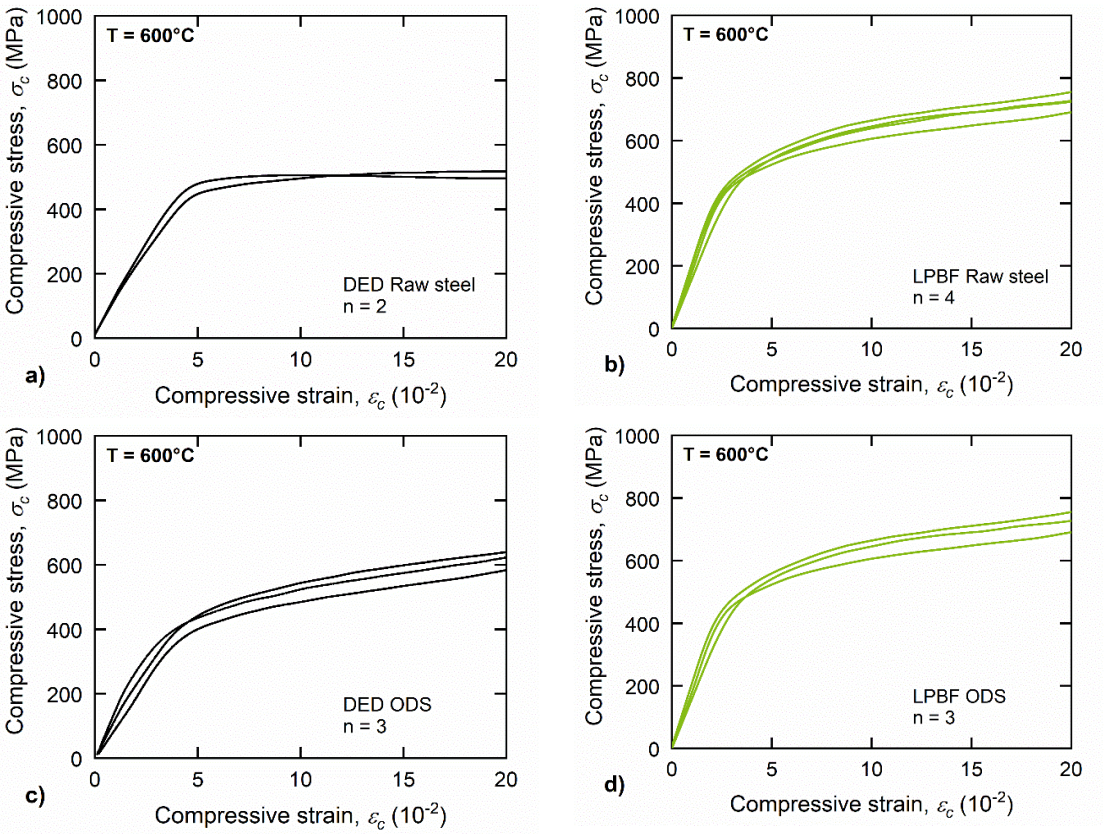

Fig. S27: Compressive stress σ_c of every tested as-built a) raw L-DED steel, b) raw L-PBF steel and c) ODS L-DED, d) ODS L-PBF as a function of the compressive strain ε_c at 600°C. The ODS powder material used was manufactured by LSPC. [13]

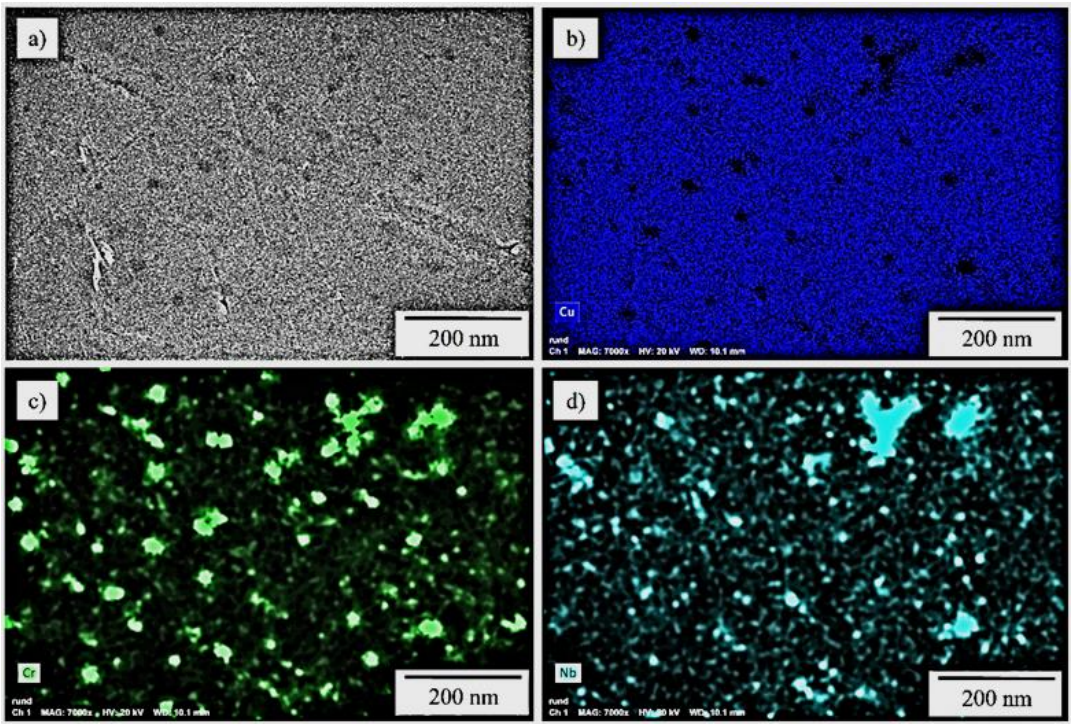

Fig. S28: EDS maps of cross sections of randomly selected Cu-3.3Cr-1.5Nb (wt.%) powder particles in gas atomized state: a) BSE image showing the presence of darker appearing particles indicating local enrichment of elements with higher atomic number. EDS maps of copper (b), chromium (c) and niobium (d) confirm the local enrichment of chromium and niobium of dark appearing areas from (a).

C. List of scientific papers related to this thesis

[I] H. Springer, C. Baron, A. Szczepaniak, E. A. Jägle, **M. B. Wilms**, A. Weisheit, D. Raabe: Precipitation reactions in age-hardenable alloys during laser additive manufacturing. Materials & Design 111 (2016), 60 – 69, https://doi.org/10.1016/j.matdes.2016.08.084

[II] R. Streubel, **M. B. Wilms**, C. Doñate-Buendía, A. Weisheit, S. Barcikowski, J. H. Schleifenbaum, B. Gökce: Depositing laser-generated nanoparticles on powders for additive manufacturing of oxide dispersed strengthened alloy parts via laser metal deposition. Japanese Journal of Applied Physics 57 (2018), 040310, https://doi.org/10.7567/JJAP.57.040310

[III] C. Doñate-Buendia, F. Frömel, **M. B. Wilms**, R. Streubel, J. Tenkamp, T. Hupfeld, M. Nachev, E. Gökce, A. Weisheit, S. Barcikowski, F. Walther, J. H. Schleifenbaum, B. Gökce: Oxide dispersion-strengthened alloy generated by laser metal deposition of laser-generated nanoparticle-metal powder composites. Materials & Design 154 (2018), 360 – 369, https://doi.org/10.1016/j.matdes.2018.05.044

[IV] **M. B. Wilms**, R. Streubel, F. Frömel, A. Weisheit, J. Tenkamp, F. Walther, S. Barcikowski, J. H. Schleifenbaum: Laser additive manufacturing of oxide dispersion strengthened steels using laser-generated nanoparticle-metal composite powders. Procedia CIRP 74 (2018), 196 – 200, https://doi.org/10.1016/j.procir.2018.08.093

[V] S.-K. Rittinghaus, **M. B. Wilms**: Oxide dispersion strengthening of γ-TiAl by laser additive manufacturing. Journal of Alloys & Compounds 804 (2019), 457 – 460, https://doi.org/10.1016/j.jallcom.2019.07.024

[VI] C. Doñate-Buendia, P. Kürnsteiner, F. Stern, **M. B. Wilms**, R. Streubel, I. M. Kusoglu, J. Tenkamp, E. Bruder, S. Barcikowski, K. Durst, J. H. Schleifenbaum, F. Walther, B. Gault, B. Gökce: Microstructure formation and mechanical properties of ODS steels built by laser additive manufacturing of nanoparticle coated iron-chromium powders. Acta Materialia 206 (2020), 116566, https://doi.org/10.1016/j.actamat.2020.116566

[VII] C. Doñate-Buendia, R. Streubel, P. Kürnsteiner, **M. B. Wilms**, F. Stern, J. Tenkamp, E. Bruder, S. Barcikowski, B. Gault, K. Durst, J. H. Schleifenbaum, F. Walther, B. Gökce: Effect of nanoparticle additivation on properties of oxide dispersion strengthened steels produced by laser powder bed fusion and directed energy deposition. Procedia CIRP 94 (2020), 41 – 45, https://doi.org/10.1016/j.procir.2020.09.009

[VIII] J. Schmelzer, S.-K. Rittinghaus, **M. B. Wilms**, O. Michael, M. Krüger: Strengthening of additively manufactured Me-Si-B (Me = Mo, V) by Y_2O_3 particles. Journal of Refractory Metals & Hard Materials 101 (2021), 105623, https://doi.org/10.1016/j.ijrmhm.2021.105623

[IX] **M. B. Wilms**, N. Pirch, B. Gökce: Manufacturing oxide dispersion strengthened steels using the advanced directed energy deposition process of high-speed laser cladding. Progress in Additive Manufacturing (2022), https://doi.org/10.1007/s40964-022-00319-1

[X] **M. B. Wilms**, S.-K. Rittinghaus: Laser additive manufacturing of oxide dispersion strengthened copper-chromium-niobium alloys. Journal of Manufacturing & Materials Processing 6(5) (2022), 102, https://doi.org/10.3390/jmmp6050102

[XI] **M. B. Wilms**, S.-K. Rittinghaus, M. Goßling, B. Gökce: Additive manufacturing of oxide-dispersion strengthened alloys: materials, synthesis and manufacturing. Progress in Materials Science 133 (2023), 101049, https://doi.org/10.1016/j.pmatsci.2022.101049

D. Complete list of publications

Peer-reviewed Journals

[1] H. Springer, C. Baron, A. Szczepaniak, E. A. Jägle, **M. B. Wilms**, A. Weisheit, D. Raabe: Precipitation reactions in age-hardenable alloys during laser additive manufacturing. Materials & Design 111 (2016), 60 – 69, https://doi.org/10.1016/j.matdes.2016.08.084

[2] **M. B. Wilms**, T. Biermann, G. Rolink, A. Weisheit, R. Poprawe: Growing of bulk sapphire single crystals using laser material deposition. Journal of Laser Applications 29(2) (2017), https://doi.org/10.2351/1.4983638

[3] C. Haase, F. Tang, **M. B. Wilms**, A. Weisheit, B. Hallstedt: Combining thermodynamic modeling and 3D printing of elemental powder blends for high-throughput investigation of high-entropy alloys – Towards rapid alloy screening and design. Materials Science & Engineering A 688 (2017), 180 – 189, https://doi.org/10.1016/j.msea.2017.01.099

[4] P. Kürnsteiner, **M. B. Wilms**, A. Weisheit, P. Barriobero-Vila, B. Gault, E. A. Jägle, D. Raabe: In-process precipitation during laser additive manufacturing investigated by atom probe tomography. Microscopy & Microanalysis 23(1) (2017), 694 – 695, https://doi.org/10.1017/S1431927617004135

[5] P. Kürnsteiner, **M. B. Wilms**, A. Weisheit, P. Barriobero-Vila, E. A. Jägle, D. Raabe: Massive nanoprecipitation in an Fe-19Ni-xAl maraging steel triggered by the intrinsic heat treatment during laser metal deposition. Acta Materialia 129 (2017), 52 – 60, https://doi.org/10.1016/j.actamat.2017.02.069

[6] R. Streubel, **M. B. Wilms**, C. Doñate-Buendía, A. Weisheit, S. Barcikowski, J. H. Schleifenbaum, B. Gökce: Depositing laser-generated nanoparticles on powders for additive manufacturing of oxide dispersed strengthened alloy parts via laser metal deposition. Japanese Journal of Applied Physics 57 (2018), 040310, https://doi.org/10.7567/JJAP.57.040310

[7] F. Kies, P. Köhnen, **M. B. Wilms**, F. Brasche, K. G. Pradeep, A. Schwedt, S. Richter, A. Weisheit, J. H. Schleifenbaum, C. Haase: Design of high-manganese steels for additive manufacturing applications with energy-absorption functionality. Materials & Design 160 (2018), 1250 – 1264, https://doi.org/10.1016/j.matdes.2018.10.051

[8] C. Doñate-Buendia, F. Frömel, **M. B. Wilms**, R. Streubel, J. Tenkamp, T. Hupfeld, M. Nachev, E. Gökce, A. Weisheit, S. Barcikowski, F. Walther, J. H. Schleifenbaum, B. Gökce: Oxide dispersion-strengthened alloy generated by laser metal deposition of laser-generated nanoparticle-metal powder composites. Materials & Design 154 (2018), 360 – 369, https://doi.org/10.1016/j.matdes.2018.05.044

[9] **M. B. Wilms**, R. Streubel, F. Frömel, A. Weisheit, J. Tenkamp, F. Walther, S. Barcikowski, J. H. Schleifenbaum: Laser additive manufacturing of oxide dispersion strengthened steels using laser-generated nanoparticle-metal composite powders. Procedia CIRP 74 (2018), 196 – 200, https://doi.org/10.1016/j.procir.2018.08.093

[10] P. Kürnsteiner, A. Hariharan, H. Y. Jung, N. Peter, **M. B. Wilms**, A. Weisheit, P. Barriobero-Vila, B. Gault, D. Raabe, E. A. Jägle: Application of atom probe tomography to complex microstructures of laser additively manufactured samples. Microscopy & Microanalysis 25(2) (2019), 2514 – 2515, https://doi.org/10.1017/S1431927619013308

[11] O. Stryzhyboroda, U. Hecht, V. T. Witusiewicz, G. Laplanche, A. Asabre, **M. B. Wilms**, A. Weisheit: Precipitation hardenable high entropy alloy for tooling applications. MRS Advances 4 (2019), 1427 – 1433, https://doi.org/10.1557/adv.2019.146

[12] S.-K. Rittinghaus, **M. B. Wilms**: Oxide dispersion strengthening of γ-TiAl by laser additive manufacturing. Journal of Alloys & Compounds 804 (2019), 457 – 460, https://doi.org/10.1016/j.jallcom.2019.07.024

[13] P. Kürnsteiner, P. Bajaj, A. Gupta, **M. B. Wilms**, A. Weisheit, X. Li, C. Leinenbach, B. Gault, E. A. Jägle, D. Raabe: Control of thermally stable core-shell nano-precipitates in additively manufactured Al-Sc-Zr alloys. Additive Manufacturing 32 (2020), 100910, https://doi.org/10.1016/j.addma.2019.100910

[14] F. Kies, **M. B. Wilms**, N. Pirch, K. G. Pradeep, J. H. Schleifenbaum, C. Haase: Defect formation and prevention in directed energy deposition of high-manganese steels and the effect on mechanical properties. Materials Science & Engineering A 772 (2020), 138688, https://doi.org/10.1016/j.msea.2019.138688

[15] P. Kürnsteiner, P. Bajaj, **M. B. Wilms**, A. Weisheit, B. Gault, E. A. Jägle, D. Raabe: High strength damascus steel by additive manufacturing. Nature 582 (2020), 515 – 519, https://doi.org/10.1038/s41586-020-2409-3

[16] T. Fischer, B. Kuhn, D. Rieck, A. Schulz, R. Trieglaff, **M. B. Wilms**: Fatigue cracking of additively manufactured materials- process and material perspectives. Applied Sciences 10(16) (2020), 5556, https://doi.org/10.3390/app10165556

[17] C. Doñate-Buendia, P. Kürnsteiner, F. Stern, **M. B. Wilms**, R. Streubel, I. M. Kusoglu, J. Tenkamp, E. Bruder, S. Barcikowski, K. Durst, J. H. Schleifenbaum, F. Walther, B. Gault, B. Gökce: Microstructure formation and mechanical properties of ODS steels built by laser additive manufacturing of nanoparticle coated iron-chromium powders. Acta Materialia 206 (2020), 116566, https://doi.org/10.1016/j.actamat.2020.116566

[18] S. Fries, S. Genilke, **M. B. Wilms**, M. Seimann, A. Weisheit, A. Kaletsch, T. Bergs, J. H. Schleifenbaum, C. Broeckmann: Laser-based additive manufacturing of WC–Co with high-temperature powder bed preheating. Steel Research International 91(5) (2020), https://doi.org/10.1002/srin.201900511

[19] C. Doñate-Buendia, R. Streubel, P. Kürnsteiner, **M. B. Wilms**, F. Stern, J. Tenkamp, E. Bruder, S. Barcikowski, B. Gault, K. Durst, J. H. Schleifenbaum, F. Walther, B. Gökce: Effect of nanoparticle additivation on properties of oxide dispersion strengthened steels produced by laser powder bed fusion and directed energy deposition. Procedia CIRP 94 (2020), 41 – 45, https://doi.org/10.1016/j.procir.2020.09.009

[20] A. Asabre, **M. B. Wilms**, A. Kostka, P. Gemagami, A. Weisheit, J. Pfetzing-Micklich, G. Laplanche: Laser metal deposition on a tool steel of an $Al_{0.6}$CoCrFeNi compositionally complex alloy with Ti & C additions using elemental powder blends. Surface & Coatings Technology 418 (2021), 127233, https://doi.org/10.1016/j.surfcoat.2021.127233

[21] J. Schmelzer, S.-K. Rittinghaus, **M. B. Wilms**, O. Michael, M. Krüger: Strengthening of additively manufactured Me-Si-B (Me = Mo, V) by Y_2O_3 particles. Journal of Refractory Metals & Hard Materials 101 (2021), 105623, https://doi.org/10.1016/j.ijrmhm.2021.105623

[22] A. K. Singh, Y. Mundada, P. Bajaj, **M. B. Wilms**, J. P. Patil, S. Kumar Mishra, E. A. Jägle, A. Arora: Investigation of temperature distribution and solidification morphology in multilayered directed energy deposition of Al-0.5Sc-0.5Si alloy. International Journal of Heat and Mass Transfer 186 (2022), 122492, https://doi.org/10.1016/j.ijheatmasstransfer.2021.122492

[23] T. Fischer, B. Kuhn, X. Fan, **M. B. Wilms**: Additive manufacturing potentials of high performance ferritic (HiperFer) steels. Applied Sciences 12(14) (2022), 7234, https://doi.org/10.3390/app12147234

[24] **M. B. Wilms**, N. Pirch, B. Gökce: Manufacturing oxide dispersion strengthened steels using the advanced directed energy deposition process of high-speed laser cladding. Progress in Additive Manufacturing (2022), https://doi.org/10.1007/s40964-022-00319-1

[25] **M. B. Wilms**, S.-K. Rittinghaus: Laser additive manufacturing of oxide dispersion strengthened copper-niobium alloys. Journal of Manufacturing and Materials Processing 6(5) (2022), 102, https://doi.org/10.3390/jmmp6050102

[26] S.-K. Rittinghaus, F. Throm, **M. B. Wilms**, R. Hama-Saleh, M. W. Rackel: Laser Fusion of Powder and Foil (LFPF) – a multi material approach to AM. Lasers in Manufacturing & Materials Processing (2022), https://doi.org/10.1007/s40516-022-00190-6

[27] **M. B. Wilms**, S.-K. Rittinghaus, M. Goßling, B. Gökce: Additive manufacturing of oxide-dispersion strengthened alloys: Materials, synthesis and manufacturing. Progress in Materials Science (2022), 101049, https://doi.org/10.1016/j.pmatsci.2022.101049

[28] A. K. Singh, Y. Mundada, P. Bajaj, **M. B. Wilms**, J. P. Patil, S. Kumar Mishra, A. Arora: Microstructure engineering during directed energy deposition of Al-0.5Sc-0.5Si alloy using heated build platform. International Journal of Heat and Mass Transfer 202 (2023), 123679, https://doi.org/10.1016/j.ijheatmasstransfer.2022.123679

[29] P. Kürnsteiner, P. Barriobero-Vila, P. Bajaj, F. De Geuser, **M. B. Wilms**, E. A. Jägle, D. Raabe: Designing an Fe-Ni-Ti maraging steel tailored for laser additive manufacturing. Additive Manufacturing 73 (2023), 103647, https://doi.org/10.1016/j.addma.2023.103647

Journals / Conference Proceedings

[1] S. Fries, **M. B. Wilms**, A. Weisheit, A. Kaletsch, J. H. Schleifenbaum, C. Broeckmann: Influence of laser energy input on the microstructure development of additively manufactured WC-Co hardmetal. Proceedings of the EuroPM2019, Maastricht, Netherlands.

[2] S.-K. Rittinghaus, J. Schmelzer, **M. B. Wilms**, M. Krüger: Laser Additive Manufacturing of intermetallic alloys for high-temperature applications. Proceedings of the Materials for Additive Manufacturing Conference (MAMC) 2019, Örebro, Sweden.

[3] J. Saewe, **M. B. Wilms**, L. Jauer, J. H. Schleifenbaum: Influence of preheating temperature on hardness and microstructure of high-speed steel HS6-5-3-8 manufactured by laser powder bed fusion. Proceedings of the Materials for Additive Manufacturing Conference (MAMC) 2019, Örebro, Sweden.

[4] S. Genilke, **M. B. Wilms**, M. Seimann, A. Weisheit, S. Fries, A. Kaletsch, T. Bergs, J. H. Schleifenbaum, C. Broeckmann: Laser based additive manufacturing of WC-Co with high temperature powder bed pre-heating. Tooling Conference 2019, Aachen, Germany.

[5] C. Doñate-Buendia, P. Kürnsteiner, **M. B. Wilms**, B. Gault, B. Gökce: Oxide dispersion strengthened steel manufactured by laser powder bed fusion and directed energy deposition. Laser in Manufacturing Conference (LIM) 2021, Munich, Germany.

[6] S. Fries, A. Kaletsch, **M. B. Wilms**, C. Broeckmann: Additive manufacturing of WC-Co hard metals using laser powder bed fusion. Ceramic Forum International (CFI) 98(5-6) (2021), 26 – 32, ISSN 01739913.

Regular Conference Talks

Please note, that the presenting author is underlined.

[1] P. Kürnsteiner, **M. B. Wilms**, A. Weisheit, E. A. Jägle, D. Raabe: Precipitation reaction in a maraging steel during laser additive manufacturing triggered by intrinsic heat treatment. Materials Science and Engineering Congress (MSE) 2016, Darmstadt, Germany.

[2] **M. B. Wilms**, A. Kini, A. Weisheit, E. A. Jägle, D. Raabe: Laser additive manufacturing as an alternative near net shaped fabrication method for the production of ODS Materials. 4th International Workshop on ODS Materials "ODISSEUS" 2017, Dresden, Germany.

[3] **M. B. Wilms**, C. Haase, A. Weisheit, J. H. Schleifenbaum: Rapid alloy development of high-entropy alloys via laser additive manufacturing. Alloys for Additive Manufacturing Symposium (AAMS) 2017, Dübendorf, Switzerland.

[4] P. Kürnsteiner, **M. B. Wilms**, A. Weisheit, E. A. Jägle, D. Raabe: In-process precipitation strengthening in Al–Sc during laser metal deposition by exploiting the intrinsic heat treatment. Alloys for Additive Manufacturing Symposium (AAMS) 2017, Dübendorf, Switzerland.

[5] P. Kürnsteiner, **M. B. Wilms**, A. Weisheit, P. Barriobero-Vila, E. A. Jägle, D. Raabe: Designing a novel Fe–Ni–Al maraging steel optimised for laser metal deposition. Alloys for Additive Manufacturing Symposium (AAMS) 2017, Dübendorf, Switzerland.

[6] P. Kürnsteiner, **M. B. Wilms**, A. Weisheit, P. Barriobero-Vila, E. A. Jägle, D. Raabe: Designing a novel Fe–Ni–Al maraging steel for laser metal deposition exploiting intrinsic heat treatment. EUROMAT 2017, Thessaloniki, Greece.

[7] P. Kürnsteiner, **M. B. Wilms**, A. Weisheit, E. A. Jägle, D. Raabe: In-process precipitation strengthening during laser metal deposition of aluminum alloys by Al_3(Sc,Zr) nano-precipitates. EUROMAT 2017, Thessaloniki, Greece.

[8] P. Kürnsteiner, **M. B. Wilms**, A. Weisheit, P. Barriobero-Vila, E. A. Jägle, D. Raabe: Designing a novel maraging steel for laser metal deposition exploiting intrinsic heat treatment. Advances in Materials & Processing: Challenges & Opportunities (AMPCO17), Roorkee, India.

[9] E. A. Jägle, A. Kini, M. Haines, **M. B. Wilms**, C. Baron, H. Springer, N. Nakada, D. Raabe: Impact of the process gas atmosphere in laser additive manufacturing–desired and undesired effects. Alloys for Additive Manufacturing Symposium (AAMS) 2018, Sheffield, UK.

[10] P. Kürnsteiner, **M. B. Wilms**, A. Weisheit, P. Bajaj, X. Li, C. Leinenbach, E. A. Jägle, D. Raabe: Preventing the coarsening of Al_3Sc precipitates by the formation of a Zr-rich shell during laser metal deposition. Alloys for Additive Manufacturing Symposium (AAMS) 2018, Sheffield, UK.

[11] P. Kürnsteiner, **M. B. Wilms**, A. Weisheit, P. Barriobero-Vila, E. A. Jägle, D. Raabe: Designing a novel Fe–Ni–Al–Ti maraging steel tailor-made for laser metal deposition. Metal Additive Manufacturing Conference (MAMC) 2018, Vienna, Austria.

[12] P. Kürnsteiner, **M. B. Wilms**, A. Weisheit, P. Bajaj, X. Li, C. Leinenbach, E. A. Jägle, D. Raabe: Process and alloy design for in-Situ precipitation strengthening of Al–Sc alloys during laser metal deposition. Metal Additive Manufacturing Conference (MAMC) 2018, Vienna, Austria.

[13] P. Kürnsteiner, **M. B. Wilms**, A. Weisheit, P. Barriobero-Vila, E. A. Jägle, D. Raabe: Design eines Fe–Ni–Ti–Al Maraging Stahls optimiert für in-situ Ausscheidungshärtung während des Laserauftragschweißens. Fachtagung Werkstoffe und Additive Fertigung 2018, Potsdam, Germany.

[14] P. Kürnsteiner, **M. B. Wilms**, A. Weisheit, P. Barriobero-Vila, E. A. Jägle, D. Raabe: Designing Fe–Ni–Al and Fe–Ni–Ti maraging steels for in-situ precipitation hardening during laser metal deposition. TMS 2018, Phoenix, Arizona, USA.

[15] E. A. Jägle, P. Kürnsteiner, P. Bajaj, **M. B. Wilms**, P. Barriobero-Vila, D. Raabe: Controlling phase transformations during Laser AM – The intrinsic heat treatment effect and beyond. Alloys for Additive Manufacturing Symposium (AAMS) 2019, Gothenburg, Sweden.

[16] P. Bajaj, P. Kürnsteiner, **M. B. Wilms**, A. Gupta, T. Hickel, A. Weisheit, E. A. Jägle, D. Raabe: Intrinsic heat treatment in a model Al-Sc alloy during laser metal deposition – Driving factors, kinetics and effect of impurities. Alloys for Metal Additive Manufacturing Conference (MAMC) 2019, Örebro, Sweden.

[17] J. K. Saewe, **M. B. Wilms**: Additive Manufacturing of high-speed steel by applying preheating temperatures during Laser Powder bed Fusion. Alloys for Additive Manufacturing Symposium (AAMS) 2019, Gothenburg, Sweden.

[18] S.-K. Rittinghaus, J. Schmelzer, **M. B. Wilms**, M. Krüger: Laser Additive Manufacturing of intermetallic alloys for high-temperature applications. Metals for Additive Manufacturing Conference (MAMC) 2019, Örebro, Sweden.

[19] P. Kürnsteiner, **M. B. Wilms**, A. Weisheit, P. Barriobero-Vila, P. Bajaj, E. A. Jägle, D. Raabe: Exploiting intrinsic heat treatment to trigger precipitation reactions in maraging steels during laser additive manufacturing. Metals for Additive Manufacturing Conference (MAMC) 2019, Örebro, Sweden.

[20] B. Gökce, R. Streubel, **M. B. Wilms**, J. H. Schleifenbaum, S. Barcikowski: Laser additive manufacturing of oxide dispersion strengthened steels. Proceedings SPIE 2019, San Francisco, California, USA.

[21] J. K. Saewe, **M. B. Wilms**: Influence of preheating temperature on hardness and microstructure of high-speed steel HS 6-5-3-8 manufactured by laser powder bed fusion. 10th International Conference on Materials for Advanced Technologies (ICMAT) 2019, Singapore.

[22] S. Fries, S. Genilke, **M. B. Wilms**, M. Seimann, A. Weisheit, A. Kaletsch, T. Bergs, J. H. Schleifenbaum, C. Broeckmann: Laser-based additive manufacturing of WC–Co with high-temperature powder bed preheating. Tooling Conference 2019, Aachen, Germany.

[23] S. Fries, **M. B. Wilms**, A. Weisheit, A. Kaletsch, J. H. Schleifenbaum, C. Broeckmann: Influence of laser energy input on the microstructure development of additively manufactured WC-Co hardmetal. EuroPM2019, Maastricht, Netherlands.

[24] E. Jägle, P. Kürnsteiner, P. Barriobero-Vila, **M. B. Wilms**, F. de Geuser, D. Raabe: Combining atom-probe tomography and synchroton methods to investigate in-situ precipitation in AM-produced alloys. TMS 2020, San Diego, California, USA.

[25] **M. B. Wilms**, S.-K. Rittinghaus, B. Gökce: Laser Additive Manufacturing of oxide dispersion-strengthened steels. A comparative study. Alloys for Additive Manufacturing Symposium (AAMS) 2022, Munich, Germany.

Conference posters

[1] P. Kürnsteiner, **M. B. Wilms**, A. Weisheit, P. Barriobero-Vila, E. A. Jägle, D. Raabe: Designing a novel Fe-Ni-Al maraging steel for laser metal deposition exploiting intrinsic heat treatment. EUROMAT Conference 2017. Thessaloniki, Greece.

[2] A. Kini, **M. B. Wilms**, E. A. Jägle, A. Weisheit, D. Raabe: Synthesis of oxide dispersion strengthened (ODS) steels by laser additive manufacturing. 4th International Workshop on ODS Materials “ODISSEUS” 2017, Dresden, Germany.

[3] P. Kürnsteiner, P. Bajaj, **M. B. Wilms**, X. Li, C. Leinenbach, B. Gault, E. A. Jägle, D. Raabe: Preventing the coarsening of Al_3Sc precipitates by the formation of a Zr-rich shell during laser metal deposition. Alloys for Additive Manufacturing Symposium (AAMS) 2018, Sheffield, UK.

[4] **M. B. Wilms**, N. Pirch, B. Gökce: Manufacturing oxide dispersion strengthened steels using the advanced directed energy deposition process of high-speed laser cladding. MATFRAME Conference 2022, Montabaur, Germany.